Imperial College London
Department of Department of Physics

B-spline ADC: Many-body *ab initio* theory for electron dynamics in strong laser fields

Marco Ruberti

10 August

Submitted in partial fulfilment of the requirements for the degree of
Doctor of Philosophy in Department of Physics of Imperial College London
and the Diploma of Imperial College London

Declaration of Originality

I herewith certify that all the results presented in this thesis are my own and that all else has been appropriately referenced.

Marco Ruberti

Copyright Declaration

Marco Ruberti

Abstract

This thesis is focused on the development of an efficient first-principles theoretical and numerical method based on the many-electron algebraic diagrammatic construction [ADC(n)] schemes, in order to describe the correlated ionisation dynamics in atomic and molecular systems interacting with perturbative and non-perturbative laser fields.

The first line of research has focused on the calculation of total single-photon photoionisation cross-sections, applying the Stieltjes-Imaging theory to Lanczos pseudospectra of the ADC Hamiltonian in Gaussian basis. We have established the accuracy of this technique by comparing the ADC-Lanczos-Stieltjes ground-state cross-sections obtained using different levels of many-body theory to the experimental ones for a series of organic molecules. We have extended this method to excited states cross-sections showing that a theoretical modelling of photoionisation from excited states requires an intrinsically double excitation theory. However, above 80 eV photon energy all three methods lead to inaccurate results due to the limitations of the Gaussian basis to describe continuum wave-functions of ionised electrons.

The second, main line of research, has therefore been dedicated to constructing and computationally optimising the first implementation of the single [ADC(1)] and double excitations [ADC(2)] schemes in the B-spline basis, which is able to accurately describe the strongly oscillating continuum orbitals. As first application of this new method, we have calculated the photoionisation cross-sections of noble gas atoms showing that the features that pose a challenge for the GTO calculations are reproduced in a very good agreement with the experiment. We also have developed a time-dependent version with which we have calculated the HHG spectra of Ar, reproducing the effect of the Cooper minimum, and CO_2, quantitatively investigating the multi-channel effects on its dynamical minimum. Finally we have provided a numerical answer to the highly topical question of coherence and

ionic wavepacket formation in short pulse photoionisation.

I would like to thank my supervisor, Dr. Vitali Averbukh, for the precious support and the valuable suggestions that he has made during my PhD. He has motivated me and, at the same time, he has given me the freedom to explore new ideas and to increase my experience. I would like to thank Professor Piero Decleva, who has kindly hosted me several times in the Chemistry department at University of Trieste and has been extremely supportive during the implementation of the B-spline ADC method, dedicating a lot of his time to explain me how B-spline functions work, to answer my questions, to solve my doubts and to constructively debate about the possible ways of implementing the code. I would like to thank Professor Misha Ivanov for the numerous wise suggestions and the stimulating discussions. I would like to thank Renjie Yun for having collaborated with me in the GTO calculations. I would like to thank all the people of the theory office and all the members of the Laser Consortium for having made my PhD experience extremely pleasant not only from a professional point of view, but also from a sociable and human point of view.
Finally I would like to thank my family, as without them I would not be here right now writing this dedication. Their support has been my fuel during all these years and will definitely continue to be so.

Contents

List of Figures

6.15. Top panel – central frequency dependence of the final degrees of coherence $G_{\pi_g-\pi_u}$ and $G_{\sigma_g-\sigma_u}$ between the final ionic states produced during the ionisation of CO_2 by an ultra-short IR laser pulse. Bottom panel – Absolute value of the normalised coefficients C_{Π_g} and C_{Π_u} for the Π symmetry ionic wave-function (left figure); Absolute value of the normalised coefficients C_{Σ_u} and C_{Σ_g} for the Σ symmetry ionic wave-function (central figure); Relative phases $\phi_{\pi_g-\pi_u}$ and $\phi_{\Sigma_u-\Sigma_g}$, in units of π, for the Π and Σ symmetry ionic wave-functions (right figure). The IR peak intensity and the pulse duration used in the calculation are respectively $0.8 \times 10^{14}\,\mathrm{W/cm^2}$ and 5.2 fs. 207

List of Tables

1. Introduction

The understanding of how a quantum system evolves in time and the possibility of visualising or even controlling the underlying correlated quantum dynamics on its natural length- and time-scale are subjects in the very focus of modern atomic, molecular and optical physics, and they inevitably move into the field of view of other research areas as well, ranging from solid-state physics over materials science to quantum chemistry and molecular biology. Physical and chemical changes that occur in atomic and molecular systems, including structural deformations and electronic motion, typically occur at femtosecond (10^{-15} s) and attosecond (10^{-18} s) timescales.

The interaction of matter with light is a key process in physical systems on any length scale. The absorption of light promotes electrons into excited states. If enough energy is absorbed by an atom or a molecule, one or more electrons can leave the system (i.e., ionization takes place). The most common types of ionisation are single-photon and few-photon ionisations [1, 2, 3], above-threshold ionisation [4, 5], and tunnel ionisation [6, 7, 8, 9].

In the last decade the remarkable progress in high harmonic generation [4, 10, 11, 12, 13], made possible by the revolutionary advances in IR laser-technology which allow one to produce sub-10 fs IR laser pulses with peak intensities of more than 10^{16} W/cm^2, has allowed one to generate ultrashort (as short as 80 as [14]) VUV and XUV light pulses with broad spectral bandwidths [15, 16, 17].

The laser pulses used in the HHG experiments are so intense that their time-dependent electric fields are on the scale of the fields that valence electrons experience in molecules and solids. Therefore, these laser pulses distort significantly the potential of the electrons such that it is possible for the electron to tunnel through or even travel over the barrier out of the system (i.e., tunnel-ionization or barrier-suppression regime, respectively). High harmonic emission occurs when an electron, liberated from a molecule by an incident intense laser field, gains energy from the field and recom-

bines with the parent molecular ion. The emission provides a snapshot of the structure and dynamics of the recombining system, encoded in the amplitudes, phases and polarization of the harmonic light. The HHG spectroscopy technique, which relies upon measuring the spectrum of coherent radiation emitted by molecules aligned in space when interacting with the intense laser fields, has proven to be a promising tool in revealing the structure as well as the electronic and nuclear dynamics in diatomic molecules, with the potential for subangstrom spatial resolution and subfemtosecond temporal resolution [18].

The groundbreaking development of the attosecond laser pulse [19] in the extreme ultraviolet (XUV) spectrum where atoms and molecules can be ionised has enabled the experimental study of attosecond physics [20], i.e. the real-time study of most fundamental ultrafast motions of electrons in atoms, molecules and condensed matter, which can be resolved on a femtosecond or attosecond timescale. Time-domain studies of electronic motion in atoms, molecules and the condensed phase offer new approaches to understanding electronic structure and electronic correlations [21, 22, 23, 24, 25, 26, 27]. For instance, the generation of attosecond pulses was utilized to determine spatial structures of molecular orbitals [28] and an interferometric technique using attosecond pulses was used to characterize attosecond electron wave packets [29]. Moreover, attosecond technology demonstrated the ability to follow, on a sub-femtosecond time scale, processes such as photoionization [30], Auger decay [31], and valence electron motion driven by relativistic spin-orbit coupling [32]. Furthermore, the availability of attosecond pulses fueled a broad interest in exploring charge transfer dynamics following photoexcitation or photoionization [3].

When studying the electron motion and the corresponding hole-creation dynamics during the ionisation process [23, 33] it is in general possible to distinguish between two different types of electron dynamics: the bound-free dynamics which happens when one electron is freed from the parent system and the bound-bound electron dynamic which happens when the electronic system has been excited in a bound non-stationary state. From the experimental point of view, one of the techniques which has been very successful to study in the time domain the bound-free dynamics in ionised atoms and molecules such as Auger decay [31] and ICD [34] is the attosecond streaking technique [31]. However, attosecond streaking is unable to trace

the corresponding bound-bound dynamics such as hole migration [35, 36], in which no secondary electron is emitted.

The measurement of bound electronic wave packets has recently attracted widespread interest. One necessary condition for creating electronic motion is the population of multiple electronic states. For example, after photoionization, the state of the molecular ion can consist of a superposition of different ionic eigenstates and can therefore undergo an internal non-trivial dynamical evolution, which may take the form of hole-migration [35, 36, 37] or hole decay typically with some non-exponential (oscillatory) behaviour [38]. Other attosecond techniques have been introduced recently, such as attosecond transient absorption [32, 33, 39], but so far it is limited to electron dynamics in the valence shell, because the initial ionization happens through tunneling effect. Electronic wave packets have also been measured in the valence-shell of atomic ions using sequential double ionization [40, 7] and in the valence shell of neutral molecules using high-harmonic generation spectroscopy [41, 42, 43].

In the last decade, much work has been done in the realm of ultrafast hole migration following sudden ionization or excitation [36], which is believed to be a universal response of extended molecules. This process occurs due to the electron correlations within many-electron systems, and is predicted to take place typically on the timescale from few to sub-femtosecond (i.e. into the attosecond time domain) that is short with respect to the timescale of nuclear motion [44]. It is currently a prominent goal in attosecond science [20] to observe and fully characterise the hole migration process in order to improve the understanding of the process and ascertain the role of hole migration in determining photochemical and photophysical outcomes and to prove that experimental methods based on attosecond measurement can address correlation driven dynamics in extended quantum systems such as biomolecules. The hole migration dynamic has not been clearly observed yet, even though first promising experiments have been performed on amino-acids molecules [45].

Recent experiments [46, 47] have demonstrated that electronically excited ionic states can modify site-selective reactivity within tens of femtoseconds, making hole migration processes a promising tool to control chemical reactions. Up to now, theoretical calculations [36] investigating hole migration phenomena have neglected the interaction between the parent ion and the

photoelectron and assumed a perfectly coherent hole wave packet.

Moreover, the crucial requirement for creating bound electronic motion is to create a coherent superposition between the prepared electronic states. The coherence of the resulting ionic system is crucial to the theoretical interpretation of the dynamical informations that can be obtained in time-resolved (pump-probe) experiments [48], especially for applying strong field ionisation to initiate charge migration [35, 36, 37] which is usually discussed in the context of single-photon ionization in the sudden limit. The question about the coherence of the ionic wavepacket formed after ionization is especially relevant for molecules, where the much smaller energy separation between the eigenstates of the cation system with respect to the case of atomic systems could in principle favour the establishment of a higher degree of coherence. However, no quantitative studies have been performed so far on molecules and therefore a theoretical method for predicting the degree of coherence created by strong field ionisation or single photon XUV ionisation in molecular systems is desirable.

The advancement of attosecond physics requires new theoretical computational tools in order to be able to simulate and predict the correlated electron dynamics in atoms and molecules on the attosecond time-scale and to interpret the experimental observations of atomic-scale electron dynamics. The theoretical framework for the description of the electronic dynamics on the ultra-fast time-scale is based on the time-dependent Schrödinger equation (TDSE) [49]

$$+i\,\hbar\,\frac{\partial \mid \Psi\,(t)\rangle}{\partial t} \;=\; \hat{H} \;\mid \Psi\,(t)\rangle\,, \tag{1.1}$$

which describes the time evolution driven by the Hamiltonian operator $\hat{H}$ of a quantum system represented by the wavefunction $\mid \Psi\,(t)\rangle$.

While many well-developed theoretical techniques exist for the description of atomic photoionisation [50], the multi-centre molecular problem still poses a formidable challenge to the theory. Even for the calculation of the most basic single-photon molecular photoionisation cross-sections, the state of the art theoretical methods either do not take into account sufficiently the electronic correlation, see e.g. Refs. [51], or treat the photoionisation continuum rather approximately, see e.g. Ref. [52]. Highly accurate many-electron wave-functions and transition matrix elements are routinely ob-

tained by the post-Hartree-Fock (post-HF) methods of *ab-initio* quantum chemistry [49, 53, 54]. These methods are based on the use of finite sets of square-integrable (typically Gaussian) single-electron basis functions.

The main focus of research in my PhD has been dedicated to constructing and implementing the time-dependent (TD) B-spline ADC [55] *ab-initio* method, which allows to obtain accurate solutions of the TDSE for the ionisation dynamics of correlated electrons in molecules. TD B-spline ADC is a theoretical method that describes the temporal evolution of the electronic wavefunction combining a detailed description of the electron correlation [56] with an accurate representation of the electronic continuum states [57]. Having a detailed description of electron correlation is very important as both molecular structure and dynamics emerge under the influence of interatomic interactions between the electrons. In atoms and molecules each electron moves in the combined potential created by the ion core and all other electrons. The electrons are usually entangled with each other while they move and interact on the attosecond timescale. Therefore, multi-electron dynamics, whose description requires a theoretical method which goes beyond the single-electron approximation, is a natural area of research for attosecond science. For example, population of multiple electronic states of the cation is well known to be achieved in molecular strong-field ionization [58, 59, 60, 61, 62, 63]; this motivates the interest in studing the effect of the interchannel electron-electron interactions on the resulting HHG spectra. Successfully constructing and computationally optimising the first B-spline implementation of the first- [ADC(1)] and second-order [ADC(2)] schemes for electronic excitations enables one to mantain the same level of accuracy for the description of many-electron effects that is common to bound states in quantum chemistry and, at the same time, to overcome the difficulty of representing the ionisation continuum inherent to the use of the Gaussian Type Orbitals (GTO) basis set. Such an achievement allows the possibility to accurately describe, with a completely *ab-initio* method, a series of many-electron phenomena such as strong field multiphoton ionisation, creation of ionic state wavepackets by sudden single-photon ionisation, high-order harmonic generation, above-threshold ionisation and electron correlation-driven hole migration in the time-resolved fashion on the atto-second scale, not only in atoms but also in molecular systems and beyond single excitation theory (e.g., TDCIS [64]).

1.1. Personal contributions to the work

The contributions I have made to the following work are:

- I wrote the code for the ADC-Lanczos-Stieltjes excited states photoionisation cross-sections, see Chapter 4.
- I wrote the entire B-spline ADC code, both the time-independent and the time-dependent parts, including the two-electron integral transformation between the primitive B-splines basis functions and the Hartree-Fock (HF) basis functions and its optimisation (see Chapter 5). The only thing which was already available was a program for calculating the two-electron integrals between monocentric primitive B-splines basis functions; therefore these integrals were used as input for the newly-implemented B-spline ADC code.
- I produced and interpreted all the results which are presented in this thesis, see Chapters 3, 4, 5, 6.

1.2. Outline

This thesis is organised as follows.

In Chapter 2 the theory is presented.

Section 2.1 is devoted to the definition and the description of the single-photon ionisation cross-section observable for atomic and molecular systems.

In Section 2.2 the polarisation propagator is introduced in the context of the many-body Green's functions approach to calculate molecular excited states.

A specific way of calculating the polarisation propagator for many-electron systems, namely the algebraic diagrammatic construction (ADC) schemes, is introduced in Section 2.3. The derivation of this *ab-initio* method to calculate the electronic structure from the original diagrammatic approach for the polarisation propagator is illustrated.

The complementary derivation of the ADC methods, via the Intermediate State Representation of the electronic Hamiltonian, and the relevant aspects of the ADC approach to excited states are presented in Section 2.4. An emphasis will be put on the theoretical and computational advantages

provided by the ADC methods and an illustration of the wider application range of the method in the ISR formulation will be provided.

Section 2.5 will concern the problem of treating electronic states which lie in the electronic continuum, above the ionisation threshold. The Stieltjes moment theory will be introduced and an explanation will be given on the calculation possibilities that it offers, in addition to its own limitations.

The Lanczos iterative diagonalisation method is reviewed in Section 2.6. This technique is used to diagonalise high dimension effective Hamiltonian matrices with a recursive algorithm; Large-size Hamiltonian matrices naturally occur for even medium-sized organic molecules such as the ones considered in Chapter 3.

The B-spline basis set is introduced and a generic description of its properties is given in Section 2.7.

The Arnoldi-Lanczos numerical algorithm for the wavepacket time propagation calculations is discussed in Section 2.8.

Sections 2.9 and 2.10 will introduce two observables which will be calculated in this thesis, namely the high-order harmonic generation spectrum and the reduced ionic density matrix respectively.

Chapter 3 will present the application of ADC-Lanczos-Stieltjes method to the calculation of total single-photon photoionisation cross-sections. The accuracy of this technique will be established by comparing the theoretical ground-state cross-sections obtained using different levels of many-body theory to the experimental ones for a series of organic molecules.

Chapter 4 will present the extension of the ADC-Lanczos-Stieltjes method to excited states cross-sections showing that a theoretical modelling of photoionisation from excited states requires an intrinsically double excitation theory.

Chapter 5 will present the implementation of the single [ADC(1)] and double excitations [ADC(2)] schemes in the B-spline basis, which is able to accurately describe the strongly oscillating continuum orbitals, together with a first static application of the new method, i.e. the calculation of a series of photoionisation cross-sections of noble gas atoms.

Chapter 6 will present the first applications of the time-dependent version of B-spline ADC. In Section 6.1 the calculation of the HHG spectrum of the Ar atom will be presented, reproducing the effect of the Cooper minimum. In Section 6.2, the multi-channel effects on the dynamical minimum present

Atomic unit (a.u.)	SI value	Name (symbol)
Energy ($\frac{m_e\, e^4}{\hbar^2}$)	4.35975×10^{-18} J	Hartree (E_h)
Length ($\frac{\hbar^2}{m_e\, e^2}$)	5.29177×10^{-11} m	Bohr radius (a_0)
Time ($\frac{\hbar^3}{m_e\, e^4}$)	24.1888×10^{-18} s	Jiffy

Table 1.1.: Conversion Factors from Atomic to SI Units.

in the CO_2 HHG spectrum will be quantitatively investigated. Finally, section 6.3 will provide a numerical answer to the highly topical question of coherence and ionic wavepacket formation in short pulse photoionisation.

In this thesis atomic units (a.u.) are used. In Table 1.1 conversion factors from a.u. to SI units are provided.

Part I.

Theory

2. Theory

2.1. One-photon ionisation cross-section

The main basic observable describing the electron dynamics of an atom or molecule interacting with an ionising electric field and which can be measured in experiments and predicted theoretically at the same time, is the single photon total photoionisation cross-section. Knowledge and understanding of this measurable quantity permits us to gain insight into the electronic structure of the atomic and molecular systems. The total molecular single-photon ionisation cross-section is defined as the probability per unit time and per unit incident photon flux density, of ionising a molecule by absorbing a photon [1]. This quantity describes the probability of the physical process in which a molecule absorbs energy (one photon) from the radiation field and as a consequence undergoes a transition between its initial electronic bound state and some final state in the electronic continuum, i.e. one electron is emitted from the molecular region creating an electronic hole with respect to the neutral system. Electron emission is one of the most efficient decay mechanisms for molecules excited a few eV and higher above the ionisation limit, such that decay patterns other than ionisation are negligible and, consequently, the photoabsorption and photoionisation cross-sections become nearly coincident in this energy range (the ionisation yield is approximately 100%). Hence the measurement of the photoionisation cross-section provides one of the most sensitive probes to study the photoabsorption process in atoms and molecules.

The expression for the n-th excited state photoionisation cross-section in SI units is given, in the case of randomly oriented molecules, by [1]

$$\sigma_n(E) = \frac{\pi e^2 \hbar}{2\epsilon_0 m_e c} \frac{df_n(E)}{dE} = \frac{\pi e^2 \hbar}{2\epsilon_0 m_e c} g(E) \ , \tag{2.1}$$

where the function $g(E) = \frac{df_n(E)}{dE}$ represents the oscillator strength density

of the system and $E = \hbar\omega$ stands for the photon energy (the energy difference between the final and the initial states involved in the absorption process).

Within the dipole approximation and adopting the length gauge form for the light-matter interaction Hamiltonian, namely

$$\hat{H}_{int} = -\hat{\mathbf{D}} \cdot \mathcal{E}(t) \tag{2.2}$$

where $\mathcal{E}(t)$ is the electric field, the oscillator strength density function is given by the dipole matrix element between the n-th excited state (Ψ_n, where $n = 0$ indicates the ground state of the system Ψ_0) and the final continuum state (Ψ_E) of the N-electron system:

$$\frac{df_n(E)}{dE} = \frac{2m_e E}{3\hbar^2} \left| \left\langle \Psi_E \left| \sum_j^N \vec{r}_j \right| \Psi_n \right\rangle \right|^2 = g(E) \ . \tag{2.3}$$

In cgs units the expression for the photoionisation cross-section is

$$\sigma(E) = \frac{2\pi^2}{c} g(E) \ . \tag{2.4}$$

Since in the photoionisation process the final states are in the electronic continuum part of the spectrum, they are not $\mathcal{L}^2$ integrable [65] and they can be instead normalised to δ-function in energy:

$$\langle \Psi_E \mid \Psi_{E'} \rangle = \delta\left(E - E'\right) \ . \tag{2.5}$$

From this formula it is possible to see that the continuum states have the units of $[E]^{-\frac{1}{2}}$. This definition of the electronic continuum states carries the information about the exact density of states of the system in the continuum range of the energy spectrum.

The cross-section can also be defined in terms of the electronic dynamical (frequency-dependent) polarisabilty $\alpha(E)$

$$\sigma(E) = \frac{4\pi E}{c} \Im\left[\alpha(E)\right] \tag{2.6}$$

This formula states that the cross-section is, for real values of the energy E, proportional to the imaginary part of the polarisability. In fact, the

polarisability as a function of a complex energy z can be expressed as the following Riemann-Stieltjes integral

$$\alpha(z) = \int_{\varepsilon_0}^{\infty} \frac{df(\varepsilon)}{\varepsilon^2 - z^2} \tag{2.7}$$

where

$$\frac{df(\varepsilon)}{d\varepsilon} = \sum_j f_j \delta(\varepsilon_j - \varepsilon) + g(\varepsilon) \geq 0 \tag{2.8}$$

represents the generalised expression for the oscillator-strength density function including the contribution from the discrete (bound states) part of the energy spectrum. Therefore, by performing the integration and taking the pole contribution it is possible to see that the imaginary part of $\alpha(E)$ on the real E axis is given by

$$\Im[\alpha(E)] = \frac{\pi}{2E} \frac{df(E)}{dE} \tag{2.9}$$

and therefore Eq. (2.4) follows immediately.

The formulas presented in this Section are written within the vertical transition approximation (or fixed-nuclei approximation) which, for photon energies sufficiently higher than the first ionisation threshold of the molecule, may represent an acceptable simplification. This means that the nuclear degrees of freedom are ignored throughout the calculation and the nuclear geometry is frozen, i.e. it is assumed not to change in the course of the electronic transition. The neutral equilibrium geometry is assumed for both the initial neutral system and the final ionic system and the states appearing in the formulas of this Section are the electronic states calculated making use of the Born-Oppenheimer approximation [49].

The photoionisation cross-sections are characterised by a very complicated and rich structure. This structure can show characteristic features such as Cooper minima [1], Giant resonances, very narrow peaks corresponding to Fano-shape resonances, Feshbach resonances and 'many-electron' effects [66]. Therefore, their theoretical interpretation represents a powerful tool for investigating the molecular electronic structure and dynamics. Having an efficient and accurate theoretical method in order to be able to calculate and predict molecular photoionisation cross-sections is naturally important especially in the cases where either the cross-sections are diffi-

cult to be measured experimentally or a theoretical prediction is required beforehand, as is the case for astrophysics applications [67]. As an example, the photoionisation cross-section is an important parameter in the strong field approximation (SFA) theory of high harmonic generation (HHG) [68].

2.2. The polarisation propagator

There are two possible strategies to calculate cross-sections starting from Eq. (2.1): the first one is to use methods which directly provide a description of the initial and final states of the system, and subsequently use these states to compute their transition dipole matrix element (wave-function methods) [49, 53, 54]; the second one is to rely on methods that directly give the squared transition dipole matrix elements between the states, without explicitly passing through the description of the states involved (propagator methods, linear response methods) [69, 70, 71].

The polarisation propagator is the key-quantity needed to describe the neutral excitation of a system, i.e. the excitations which do not change the number of interacting particles in the system. It can be derived starting from the two-particle Green's function [72, 73, 74, 75, 76, 77, 78], which is defined in the coordinate representation as follows:

$$G_2\left(x_1,x_2,x_3,x_4\right) = (-i)^2 \left\langle \Psi_0 \right| \mathcal{T}\left[\hat{\Psi}\left(x_1\right)\hat{\Psi}\left(x_2\right)\hat{\Psi}^{\dagger}\left(x_4\right)\hat{\Psi}^{\dagger}\left(x_3\right)\right] \left|\Psi_0\right\rangle . \tag{2.10}$$

Here $\hat{\Psi}\left(x\right), \hat{\Psi}^{\dagger}\left(x\right)$ represent the fermionic field annihilation and creation operators, that respectively annihilate and create a fermionic particle (electron) at the space-time point $x = (\mathbf{r}, t)$. In this Section, all the operators are intended to be expressed in the Heisenberg picture, $\hat{a}\left(t\right) = e^{+\imath \hat{H} t} \hat{a} e^{-\imath \hat{H} t}$, and are therefore time-dependent.

The symbol $\mathcal{T}$ in Eq. (2.10) stands for the time-ordering Wick operator, whose action consists of ordering the time-dependent field operators on which it operates accordingly to their time argument in decreasing time order. Additionally, by definition of $\mathcal{T}$, in cases where both operators $\hat{\Psi}^{\dagger}\left(x\right)$ and $\hat{\Psi}\left(x^{'}\right)$ have equal time argument $t = t^{'}$ the creation operator $\hat{\Psi}^{\dagger}\left(x\right)$ always has to stand to the left of the corresponding annihilation operator $\hat{\Psi}\left(x\right)$.

Introducing a single-particle basis set of functions $\{\phi_n\left(\mathbf{r}\right)\}$, the annihila-

tion and creation field operators can be expressed in the following way:

$$\hat{\Psi}(x) = \sum_n \phi_n(\mathbf{r})\,\hat{a}_n(t) \quad \hat{\Psi}^\dagger(x) = \sum_n \phi_n^*(\mathbf{r})\,\hat{a}_n^\dagger(t)\ . \tag{2.11}$$

The single-particle basis functions are usually chosen as the solutions of some mean-field equations such as the Hartree-Fock equations.

By substituting these expressions for the field operators in Eq. (2.10), one arrives at the so-called number representation for the two particle Green's function:

$$G^{(2)}_{pq,rs}(t_1,t_2,t_3,t_4) = (-i)^2 \langle\Psi_0|\,\mathcal{T}\left[\hat{a}_p(t_1)\,\hat{a}_q(t_2)\,\hat{a}_s^\dagger(t_4)\,\hat{a}_r^\dagger(t_3)\right]|\,\Psi_0\rangle \tag{2.12}$$

where the indices p, q, r, s run over the single-particle basis states.

Starting from the two-particle Green's function $G^{(2)}_{pq,rs}(t_1,t_2,t_3,t_4)$, it is then possible to define the following quantity

$$R_{pq,rs}(t_1,t_2,t_3,t_4) = G^{(2)}_{pq,rs}(t_1,t_2,t_3,t_4) - G_{pr}(t_1,t_3)\,G_{qs}(t_2,t_4) \tag{2.13}$$

where the quantity $G_{pq}(t_1,t_2)$ represents the one-particle Green's function (or one-particle propagator) written in the number representation and it is defined as follows

$$G_{pq}(t_1,t_2) = -\imath\langle\Psi_0|\,\mathcal{T}\left[\hat{a}_p(t_1)\,\hat{a}_q^\dagger(t_2)\right]|\,\Psi_0\rangle\,. \tag{2.14}$$

One way of calculating $G_{pq}(t_1,t_2)$ is by solving the Dyson's equation, which allows one to express the exact one-particle Green's function in terms of the non-interacting (mean-field) one via the quantity $\Sigma_{pq}\left(t,t'\right)$, which is called the irreducible self-energy. The Dyson's equation for the one-particle Green's function reads

$$G_{pq}(t_1,t_2) = G^0_{pq}(t_1,t_2) + G^0_{pr}(t_1,t_3)\,\Sigma_{rs}(t_3,t_4)\,G_{sq}(t_4,t_2)\,. \tag{2.15}$$

In Eq. (2.15) summation and time integration for repeated indices are implied.

In a completely analogous way, $R_{pq,rs}(t_1,t_2,t_3,t_4)$ can be expressed in terms of the simplified quantity

$$R^0_{pq,rs}(t_1,t_2,t_3,t_4) = G_{ps}(t_1,t_4)\,G_{qr}(t_2,t_3) \tag{2.16}$$

by means of the so-called Bethe-Salpeter equation [79]:

$$R_{pq,rs}\left(t_1,t_2,t_3,t_4\right) \;=\; -R^0_{pq,rs}\left(t_1,t_2,t_3,t_4\right)$$

$$-\imath R^0_{pu,rt}\left(t_1,t_6,t_3,t_5\right)\; K^{p-h}_{uv,tz}\left(t_6,t_7,t_5,t_8\right)\; R_{vq,zs}\left(t_7,t_2,t_8,t_4\right)$$

. (2.17)

The kernel $K^{p-h}_{uv,tz}\left(t_6,t_7,t_5,t_8\right)$ is called the effective particle-hole (p-h) interaction, or alternatively, the irreducible p-h vertex and it is defined as the functional derivative of the self-energy $\Sigma_{pq}\left(t,t^{'}\right)$ with respect to the one-particle Green's function of Eq.(2.14). The quantities $G^{(2)}, R$ and K^{p-h} all depend of four time arguments (or, in the case of a time-independent Hamiltonian, on three time-differences).

The polarisation propagator, or time-ordered density correlation function, can be defined as the following limit

$$\Pi_{pq,rs}\left(t,t^{'}\right) = lim_{t_1,t_3\rightarrow t}\; limt_2,t_4 \rightarrow t^{'}\; \imath R_{ps,qr}\left(t_1,t_2,t_3,t_4\right) \tag{2.18}$$

and it is therefore a two-point quantity, depending only on two time variables (or, in the case of a time-independent Hamiltonian, on one time-difference). In the coordinate representation it can be expressed as

$$\Pi\left(x,x^{'}\right) = -\imath\left\langle\Psi_0\right|\mathcal{T}\left[\hat{\Psi}^{\dagger}\left(x\right)\hat{\Psi}\left(x\right)\hat{\Psi}^{\dagger}\left(x^{'}\right)\hat{\Psi}\left(x^{'}\right)\right]\left|\Psi_0\right\rangle +$$

$$\imath\left\langle\Psi_0\right|\hat{\Psi}^{\dagger}\left(x\right)\hat{\Psi}\left(x\right)\left|\Psi_0\right\rangle\left\langle\Psi_0\right|\hat{\Psi}^{\dagger}\left(x^{'}\right)\hat{\Psi}\left(x^{'}\right)\left|\Psi_0\right\rangle .$$

(2.19)

In order to understand the physical meaning of the polarisation propagator, it is useful to write it in the following form:

$$\Pi\left(x,x^{'}\right) = -\imath\left\langle\Psi_0\right|\mathcal{T}\left[\hat{\rho}\left(x\right)\hat{\rho}^{\dagger}\left(x^{'}\right)\right]\left|\Psi_0\right\rangle + \imath\left\langle\Psi_0\right|\hat{\rho}\left(x\right)\left|\Psi_0\right\rangle\left\langle\Psi_0\right|\hat{\rho}^{\dagger}\left(x^{'}\right)\left|\Psi_0\right\rangle . \tag{2.20}$$

In Eq. (2.20) the quantity $\hat{\rho}(x) = \hat{\rho}^{\dagger}(x) = \hat{\Psi}^{\dagger}(\mathbf{r})\,\hat{\Psi}(\mathbf{r})$ has been introduced: it is the density field operator at point $x = (\mathbf{r}, t)$ and it can be explicitly written as $\hat{\rho}(\mathbf{r}) = \sum_{i=1}^{N} \delta(\mathbf{r} - \hat{\mathbf{r}}_i)$. It is now possible to see from Eq. (2.20) that the polarisation propagator $\Pi\left(x, x^{'}\right)$ is a quantity which describes the propagation of a density disturbance from one point in space-time to another (i.e. it creates a density disturbance at point $x = (\mathbf{r}, t)$ and propagates it to $x^{'} = \left(\mathbf{r}^{'}, t^{'}\right)$. (In a way analogous to the one the one-particle propagator $G_{pq}(t_1, t_2)$ propagates either a single particle added to the system or a single hole created in the system).

The polarisation propagator in the number representation can be written, in compact notation, as:

$$\Pi\left(x, x^{'}\right) = \sum_{pqrs} \phi_q^*(\mathbf{r})\,\phi_p(\mathbf{r})\,\phi_r^*\left(\mathbf{r}^{'}\right)\phi_s\left(\mathbf{r}^{'}\right)\Pi_{pq,rs}(t) \tag{2.21}$$

$$\mathbf{\Pi}(t) = \mathbf{\Pi}^{+}(t) + \mathbf{\Pi}^{-}(t) \tag{2.22}$$

$$\Pi^{+}_{pq,rs}(t) = -i\langle\Psi_0|\,\hat{a}_q^{\dagger}\hat{a}_p\left[\hat{Q}^{(0)}e^{-i\left(\hat{H}-E_0\right)t}\hat{Q}^{(0)}\right]\hat{a}_r^{\dagger}\hat{a}_s\,|\,\Psi_0\rangle \tag{2.23}$$

The operator $\hat{Q}^{(0)} = \hat{1} - \hat{P}^{(0)}$ represents the projector onto the ground state orthonormal complement (i.e. the projector onto the excited states space). Its presence in Eq. (2.21) takes into account, in a compact way, the product term on the right-hand side of Eq. (2.20). Moreover, equation (2.21) makes it evident that the polarisation propagator describes the time-evolution of a neutral excitation on top of the exact ground state.

Due to the fact that a generic one-particle operator $\hat{O}$ can be written as $\hat{O} = \sum_{rs} o_{rs}\hat{a_r}^{\dagger}\hat{a_s}$, the quantity $\Pi_{pq,rs}(t)$ can also be used to define any time-ordered correlation function $T(t)$ in the following way:

$$T(t) = \sum_{pqrs} o_{pq}^{*} o_{rs}\Pi_{pq,rs}(t) = \mathbf{D}^{\dagger}\mathbf{\Pi}(t)\,\mathbf{D}\,. \tag{2.24}$$

The part $T^{+}(t) = \mathbf{D}^{\dagger}\mathbf{\Pi}^{+}(t)\,\mathbf{D}$ is also defined as the transition function corresponding to the operator $\hat{O}$.

When going into the spectral (frequency ω) domain

$$\Pi^{+}_{pq,rs}(\omega) = \int_{-\infty}^{+\infty} dt\; e^{+\imath(\omega+\imath\eta)t}\Pi^{+}_{pq,rs}(t) \tag{2.25}$$

it can be immediately noted that $\Pi^{+}_{pq,rs}(\omega)$ can be written as a matrix of resolvent-type matrix elements:

$$\Pi^{+}_{pq,rs}(\omega) = \langle \Psi_0 |\, \hat{a_q}^{\dagger} \hat{a_p} \left[\omega - \hat{H} + E_0 + i\eta \right]^{-1} \hat{a_r}^{\dagger} \hat{a_s} \,|\, \Psi_0 \rangle' \,. \tag{2.26}$$

In Eq. (2.25) the imaginary positive infinitesimal $+\imath\eta$ is introduced to guarantee the convergence of the Fourier transform between time and energy representations. The prime in Eq. (2.26) indicates that the undesired contribution

$$\Pi^{+}_{pq,rs} = + \langle \Psi_0 |\, \hat{a_q}^{\dagger} \hat{a_p} \mid \Psi_0 \rangle \langle \Psi_0 \mid \hat{a_r}^{\dagger} \hat{a_s} \,|\, \Psi_0 \rangle \, (\omega + i\eta)^{-1} \tag{2.27}$$

must be subtracted.

Repeating the same procedure for the Π^{-} part, it is possible to see that

$$\Pi^{-}_{pq,rs}(\omega) = \Pi^{+}_{sr,qp}(-\omega) \,. \tag{2.28}$$

Accordingly to this equation the two parts $\mathbf{\Pi}^{+}(\omega)$ and $\mathbf{\Pi}^{-}(\omega)$ contain the same physical information and it is therefore sufficient to calculate the former part.

Inserting the resolution of identity, expressed in terms of the exact excited states of the system $\mid \Psi_m \rangle$, into Eq. (2.26), leads to the so-called Lehnman representation of the polarisation propagator:

$$\Pi^{+}_{pq,rs}(\omega) = + \sum_{m \neq 0} \frac{\langle \Psi_0 |\, \hat{a}^{\dagger}_q \hat{a}_p \mid \Psi_m \rangle \langle \Psi_m \mid \hat{a}^{\dagger}_r \hat{a}_s \,|\, \Psi_0 \rangle}{\omega - (E_m - E_0) + i\eta} \tag{2.29}$$

$$\Pi^{-}_{pq,rs}(\omega) = - \sum_{m \neq 0} \frac{\langle \Psi_0 |\, \hat{a}^{\dagger}_r \hat{a}_s \mid \Psi_m \rangle \langle \Psi_m \mid \hat{a}^{\dagger}_q \hat{a}_p \,|\, \Psi_0 \rangle}{\omega + (E_m - E_0) - i\eta} \,. \tag{2.30}$$

Consistent with the fact that the polarisation propagator only describes density fluctuations, the term $m = 0$ corresponding to the ground state is not included in the summation.

Equation (2.29) makes the physical content of the polarisation propagator manifest even more; as it is clear from the analytical structure of its spectral representation, $\Pi^{+}_{pq,rs}(\omega)$ provides informations on the excitation energies of the system and on the squared transition moments $\langle \Psi_m \mid \hat{a}^{\dagger}_r \hat{a}_s \,|\, \Psi_0 \rangle$ of the corresponding excited eigenstates. More precisely, it has simple poles at the

discrete excitation energies, and the corresponding residues are related to the transition matrix element between the ground state and the respective excited eigenstates. This means that the integration of the polarisation propagator in the complex ω plane, around a closed path that includes only a specific isolated pole, gives direct information about the squared transition matrix elements from the ground state to the corresponding eigenspace of $\hat{H}$.

One of the ways in which the polarisation propagator can be calculated is via its diagrammatic perturbation expansion, which is based on the following partition for the total Hamiltonian of the system:

$$\hat{H} = \hat{H}_0 + \hat{W} \,. \tag{2.31}$$

Here $\hat{H}_0$ is chosen to be the mean-field Hamiltonian, while $\hat{W}$ contains the two-particle interaction part of the Hamiltonian. The diagrammatic perturbation expansion can be obtained by making use of the Dyson's expansion for the time evolution operator in the interaction picture [72]

$$\hat{U}\left(t,t^{'}\right) = T\, e^{-\imath \int_{t'}^{t} \hat{W}_I(\tau) d\tau} \; =$$

$$= \sum_{n=0}^{\infty} \frac{(-\imath)^n}{n!} \int_{t'}^{t} dt_1 \int_{t'}^{t} dt_2 \cdots \int_{t'}^{t} dt_n T \left[\hat{W}_I\left(t_1\right) \hat{W}_I\left(t_2\right) \cdots \hat{W}_I\left(t_n\right)\right]$$

(2.32)

and of the Gell-Mann and Low theorem for representing the exact ground state [72, 73, 74, 75, 76, 77]. This theorem relates the ground state of the non-interacting system $\mid \Phi_0 \rangle$ with an eigenstate of the interacting one

$$\mid \Psi_0^{'} \rangle = \frac{\hat{U}\left(0, \pm\infty\right) \mid \Phi_0 \rangle}{\langle \Phi_0 \mid \hat{U}\left(0, \pm\infty\right) \mid \Phi_0 \rangle} \qquad \langle \Phi_0 \mid \Psi_0^{'} \rangle = 1 \,. \tag{2.33}$$

This relation is obtained assuming an adiabatic evolution of the $\mid \Phi_0 \rangle$ state under an adiabatic switching on ($\hat{H}\left(t\right) = \hat{H}_0 + e^{-\varepsilon|t|}\hat{W}$) of the perturbation term $\hat{W}$ in the total Hamiltonian $\hat{H}$. If we look at time as a parameter and we assume that the local eigenvalues of the Hamiltonian do not show

crossing, we can say that the result of the adiabatic evolution of the non-interacting ground state will be the interacting one; therefore the following expression $\frac{|\Psi_0^{'}\rangle}{\langle\Psi_0^{'}|\Psi_0^{'}\rangle}$ can be substituted for the exact interacting ground state $|\Psi_0\rangle$ in the formula for the time-ordered polarisation propagator (Eq. (2.19)).

Doing so leads to an expression where $\Pi\left(x,x^{'}\right)$ is written in terms of expectation values of time-ordered products of creation and annihilation operators on the non-interacting ground state $|\Phi_0\rangle$; these are exactly the type of matrix elements for which Wick's theorem [72] holds, allowing the expansion of the polarisation propagator Π to be evaluated by means of the Feynman diagrammatic techniques.

Moreover, by expanding both the numerator and the denominator of Eq. (2.33) with the use of the Dyson's formula (Eq. (2.32)), it is possible to see that the only contributions to the polarisation propagator are those coming from the terms that can be represented by connected Feynman diagrams (linked cluster theorem) [72, 76, 77]. Consequently, the perturbation expansion of the time-ordered polarisation propagator can be expressed in diagrammatic ways as:

$$\Pi_{pq,rs}\left(t-t^{'}\right)=-\imath\sum_{n=0}^{\infty}\frac{(-\imath)^n}{n!}\int_{-\infty}^{+\infty}dt_1\int_{-\infty}^{+\infty}dt_2\cdots\int_{-\infty}^{+\infty}dt_n$$

$$\langle\Phi_0\mid T\left[\hat{W}_I\left(t_1\right)\hat{W}_I\left(t_2\right)\cdots\hat{W}_I\left(t_n\right)\hat{a}_q^{\dagger}\left(t\right)\hat{a}_p\left(t\right)\hat{a}_r^{\dagger}\left(t^{'}\right)\hat{a}_s\left(t^{'}\right)\right]\mid\Phi_0\rangle_{connected}\,. \tag{2.34}$$

In the next Section the algebraic diagrammatic construction (ADC(n)) schemes for the polarisation propagator will be presented. Since the ADC approximations for the time-ordered polarisation propagator are based on its diagrammatic perturbation expansion, they assume the validity of the Gell-Mann and Low theorem. This is only valid if there is no crossing, and therefore if there is no changing in the symmetry of the ground state when the perturbation is adiabatically switched on. Moreover, they also assume both the non-interacting and the interacting ground states to be non-degenerate (closed shell systems). In fact, in general for open shell systems the adiabatic limit does not hold for a single Slater determinant state

but the initial state that adiabatically converges to the exact interacting ground state consists of a linear combination of different Slater determinants instead. Therefore, the ADC theory presented in the following Section is intended to be strictly valid only for closed-shell systems.

2.3. ADC(n) approximation schemes for the polarisation propagator

The *ab-initio* many-body Green's function ADC(n) methods have been first introduced for calculation of excitation and ionisation energies of closed shell species [56, 80] and since then generalised for the description of double [81] and triple [82] ionisation energies. In this thesis the relevant ADC(n) schemes are the ones for the calculation of closed-shell systems excitations; these schemes have been originally derived as approximations to the polarisation propagator, based on an algebraic reformulation of its diagrammatic perturbation theory [56].

In this Section I am going to describe how this derivation was performed; I will consider the transition function $T_D(\omega)$ for the one-particle dipole operator $\hat{D}$, which is given by:

$$T(\omega) = \mathbf{D}^{\dagger}\mathbf{\Pi}^{+}(\omega)\,\mathbf{D}\,. \tag{2.35}$$

The same final results will apply to the transition function associated to any one-particle operator $\hat{O}$ or pairs of operators, being valid for $\Pi^{+}(\omega)$ itself.

It is important to note the following detail: consistent with the fact that in the perturbation expansion of the polarisation propagator, obtained by means of the Dyson and Gell-Man and Low formulas, the unperturbed zeroth-order non-interacting ground state is chosen to be the single Slater-determinant ground state of some mean-field zeroth-order theory, the orbital basis set chosen to represent the field operator $\hat{\Psi}(x)$, which also are associated with the creation ($\hat{a}_r^{\dagger}$) and annihilation ($\hat{a}_s$) operators, must be taken to be the eigenbasis of the same mean-field Hamiltonian. Therefore the one-particle indices appearing in the formal expression of Eq. (2.26) and in the diagrams expressions can be divided into two groups representing occupied mean-filed orbitals and virtual mean-field orbitals. Within the ADC framework the mean-field Hamiltonian chosen as zeroth-order Hamiltonian

is the Hartree-Fock Hamiltonian.

The ADC construction starts with the formulation of a specific guess for the algebraic form of the polarisation propagator and/or the corresponding transition functions. In particular, the way the transition function is written in the ADC formulation is the following:

$$T(\omega) = \mathbf{F}^{\dagger} \left[\omega \mathbf{1} - \mathbf{K} - \mathbf{C}\right]^{-1} \mathbf{F} \,. \tag{2.36}$$

In Eq. (2.36) the square matrices $\mathbf{K}$ and $\mathbf{C}$ are assumed to be ω-independent Hermitian matrices and in principle their dimensionality is given by the dimension of the entire excited state space, which I will denote by X; they are therefore defined within the configuration space consisting of all the possible p-h, 2p-2h, 3p-3h etc. excitations with respect to the HF mean-field ground state. The same applies to the vector $\mathbf{F}$.

The quantities $\mathbf{C}$ and $\mathbf{F}$ are respectively called the modified/effective interaction matrix and transition moments. The matrix $\mathbf{K}$ denotes the diagonal matrix of zeroth-order excitation energies

$$K_{ai,bj} = \delta_{ab}\delta_{ij} \left(\varepsilon_a - \varepsilon_i\right) \quad \bar{n}_a n_i = 1 \tag{2.37}$$

$$K_{abij,cdkl} = \delta_{ac}\delta_{bd}\delta_{ik}\delta_{jl} \left(\varepsilon_a + \varepsilon_b - \varepsilon_i - \varepsilon_j\right) \quad \bar{n}_a \bar{n}_b n_i n_j = 1 \tag{2.38}$$

etc., where n_k denotes the occupation number of the one-electron spin-orbital k in the HF meanfield ground state and $\bar{n}_k = 1 - n_k$. From the partition in Eq. (2.36) it can be noted that this contribution has been explicitely separated from the, so far unknown, matrix $\mathbf{C}$.

Moreover, it is useful to note that the vector $\mathbf{F}$ can also be expressed as

$$\mathbf{F} = \mathbf{f} \cdot \mathbf{D} = \sum_{rs} d_{rs} \mathbf{f}_{rs} \,, \tag{2.39}$$

where $\mathbf{f}_{rs}$ is a rectangular matrix of dimension $(X) \times (N^2)$ called the effective transition amplitudes matrix and N is the dimension of the one-particle Hilbert space.

Inserting the expression of Eq. (2.39) into the general ADC formula for the polarisation propagator (see Eq. (2.36)), it is possible to see that the

latter can be written as

$$\Pi^{+}_{pqrs}(\omega) = \mathbf{f}^{\dagger}_{pq}\left[\omega\mathbf{1} - \mathbf{K} - \mathbf{C}\right]^{-1}\mathbf{f}_{rs}\,. \tag{2.40}$$

Therefore, obtaining the expression for the quantity $\mathbf{f}$, it is possible to work out the vector $\mathbf{F}$ relative to every one-particle operator $\hat{O}$, including the one corresponding to the dipole moment operator $\hat{D}$.

From now on I will consider only the $\mathbf{\Pi}^{+}(\omega)$ part of the polarisation propagator because, as previously mentioned in Sec. 2.2, $\mathbf{\Pi}^{+}(\omega)$ and $\mathbf{\Pi}^{-}(\omega)$ contain the same physical information.

Having written the propagator in the ADC formal algebraic form, the key assumption to be made as the basis of the ADC approach is that the quantities $\mathbf{C}$ and $\mathbf{F}$ possess a well defined perturbation expansion:

$$\mathbf{F}(n) = \sum_{l=0}^{n}\mathbf{F}^{[l]} \tag{2.41}$$

$$\mathbf{C}(n) = \sum_{l=1}^{n}\mathbf{C}^{[l]}\,. \tag{2.42}$$

The perturbation is again defined, see Eq. (2.31), as the difference between the full interacting Hamiltonian $\hat{H}$ and the independent-particles mean-field Hamiltonian $\hat{H}^{M.F.}$:

$$\hat{W} = \hat{H} - \hat{H}^{M.F.}\,. \tag{2.43}$$

The ADC(n) propagator is built using the quantities $C(n)$ and $F(n)$ and takes the following form

$$T_n(\omega) = \mathbf{F}^{\dagger}(n)\left[\omega\mathbf{1} - \mathbf{K} - \mathbf{C}(n)\right]^{-1}\mathbf{F}(n)\,. \tag{2.44}$$

The physical informations are extracted from the exact or approximate ADC quantities $\mathbf{C}$ and $\mathbf{F}$ as follows: the vertical excitation energies are given by the eigenvalues of the Hermitian $\mathbf{M} = \mathbf{K} + \mathbf{C}$ matrix, because these are the poles of the propagator. The corresponding eigenvalue problem can be written in compact matrix notation as

$$\mathbf{MV} = \omega\mathbf{V} \tag{2.45}$$

where ω and $\mathbf{V}$ denote respectively the diagonal matrix of eigenvalues and

the matrix of the corresponding column eigenvectors. The transition moments are given by

$$\langle \Psi_m \mid \hat{D} \mid \Psi_0 \rangle = \mathbf{V}_m^\dagger \cdot \mathbf{F} = \sum_{rs} d_{rs} \mathbf{V}_m^\dagger \cdot \mathbf{f}_{rs} \,. \tag{2.46}$$

In order to obtain explicit expressions for the ADC(n) effective quantities $\mathbf{C}$ and $\mathbf{F}$ it is useful to substitute their formal perturbative expansions in the ADC form of the polarisation propagator and to explicitly expand the resulting total expression in powers on the perturbation. By doing so, a formal perturbation expansion for the polarisation propagator in powers of n is obtained; this formal algebraic expansion is not complete, because it misses the terms of order greater than n arising from $\mathbf{F}^{[l]}$ $l \geq n+1$ and/or $\mathbf{C}^{[l]}$ $l \geq n+1$, but it nevertheless includes all the terms up to order n. Indeed, all the terms that can give rise to nth-order contributions in the propagator algebraic perturbation expansion are contained in $\mathbf{F}(n)$ and $\mathbf{C}(n)$.

The algebraic expansion is therefore complete up to order n and can in turn be compared to the alternative, but in principle equivalent, diagrammatic perturbation expansion up to the same order n. In other words, the basic assumption is that the perturbation expansion of T through the quantities F and C must be the same as the one already known from diagrammatic perturbation theory. This procedure, performing this comparison through a sequence of definite orders n of perturbation theory, allows to successfully determine subsequent higher order contributions to the $\mathbf{M}$ and $\mathbf{F}$ ADC quantities and thus generate, in a systematic way, a hierarchy of consistent nth-order approximations schemes referred to as ADC(n) schemes.

The required equivalence of the perturbation expansions, diagrammatic and algebraic, at every order can be formally written as

$$T_n(\omega) = \sum_{l=0}^{n} T_n^{[l]}(\omega) + O(n+1) \tag{2.47}$$

$$T^{[n]}(\omega) = \underline{D}^\dagger \Pi^{+[n]}(\omega)\, \underline{D} \tag{2.48}$$

where the quantity $T^{[n]}(\omega) = D^\dagger \Pi^{+[n]}(\omega)\, D$ is obtained form the respective Feynman diagrams. For example, for second order ADC scheme,

namely ADC(2), the defining equations are the following:

$$T_2^{[0]}(\omega) = T^{[0]}(\omega) \tag{2.49}$$

$$T_2^{[1]}(\omega) = T^{[1]}(\omega) \tag{2.50}$$

$$T_2^{[2]}(\omega) = T^{[2]}(\omega) \tag{2.51}$$

where

$$T_2^{[0]}(\omega) = \underline{F}^{\dagger[0]}\left[\omega 1 - K\right]^{-1}\underline{F}^{[0]} \tag{2.52}$$

$$T_2^{[1]}(\omega) = \underline{F}^{\dagger[1]}\left[\omega 1 - K\right]^{-1}\underline{F}^{[0]} + \underline{F}^{\dagger[0]}(0)\left[\omega 1 - K\right]^{-1}\underline{F}^{[1]} +$$

$$+\underline{F}^{\dagger[0]}\left[\omega 1 - K\right]^{-1}C^{[1]}\left[\omega 1 - K\right]^{-1}\underline{F}^{[0]}$$

(2.53)

and

$$T_2^{[2]}(\omega) = \underline{F}^{\dagger[2]}\left[\omega 1 - K\right]^{-1}\underline{F}^{[0]} + \underline{F}^{\dagger[0]}\left[\omega 1 - K\right]^{-1}\underline{F}^{[2]} + \underline{F}^{\dagger[1]}\left[\omega 1 - K\right]^{-1}\underline{F}^{[1]} +$$

$$+\underline{F}^{\dagger[1]}[\omega 1 - K]^{-1}C^{[1]}[\omega 1 - K]^{-1}\underline{F}^{[0]} + \underline{F}^{\dagger[0]}[\omega 1 - K]^{-1}C^{[1]}[\omega 1 - K]^{-1}\underline{F}^{[1]} +$$

$$+\underline{F}^{\dagger[0]}\left[\omega 1 - K\right]^{-1}C^{[2]}\left[\omega 1 - K\right]^{-1}\underline{F}^{[0]} +$$

$$+\underline{F}^{\dagger[0]}[\omega 1 - K]^{-1}C^{[1]}[\omega 1 - K]^{-1}C^{[1]}[\omega 1 - K]^{-1}\underline{F}^{[0]}$$

. (2.54)

From a technical point of view it is important to note that Feynman di-

agrams describe the whole polarisation propagator. This means that after having performed all the associated time integrations and Fourier transforms, in order to obtain the diagrammatic perturbation expansion contributing only to the Π^+ part, the contribution of each Feyman diagram of order n must be expressed as the sum of the contributions of the corresponding $(n+2)!$ time-ordered Goldstone diagrams [72]. Goldstone diagrams are obtained starting from a definite Feynman diagram, which is drawn by convention with a specified ordering of the point vertices, by drawing all the possible different orderings of the $n+2$ time vertices $t, t_1, t_2, \ldots, t_n, t^{'}$. The Goldstone diagrams can therefore be divided into two classes according to the ordering of the external times, $t > t^{'}$ and $t < t^{'}$ respectively. The first class $t > t^{'}$ of Goldstone diagrams contributes only to the $\Pi^+(\omega)$ part of the polarisation propagator while the second class $(t < t^{'})$ to the $\Pi^-(\omega)$ part; mixed terms are not present and hence it is possible to calculate the two parts independently, as expected from the fact that they contain identical physical information.

In Fig. 2.1 the Feynman diagrams for the polarisation propagator in Abrikosov notation [72] are reported up to second order. The Abrikosov notation differs from the usual Goldstone-Feynman notation in the fact that the interaction wiggle lines are replaced by interaction points to which the antisymmetrised interaction matrix element $V_{ij[kl]} = V_{ijkl} - V_{ijlk}$ is associated and therefore, in this notation, the total number of diagrams is considerably reduced. At second order the number of Goldstone diagrams contributing to $\Pi^+(\omega)$ per each Feynman diagram is 12; at first order the number is 3. In total there is one Goldstone diagram at zeroth order, three Goldstone diagrams contributing at first order, and sixty at second order.

The determination of an explicit expression for the ADC quantities gives rise to an explicit expression for the ADC(n) polarisation propagator itself which is complete up to order n in perturbation theory with respect to the electron-electron interaction (it includes all the Feynman diagrams up to order n) and also includes higher-order diagrams in the form of infinite partial (incomplete) summations.

As an example, this procedure for the zeroth and the first non-trivial order (ADC(1)) is presented in the following. The diagrams for $T(\omega)$ are obtained from the Goldstone diagrams for $\Pi^+(\omega)$ by associating the transition matrix elements d^*_{pq} and d_{rs} with the upper and lower external vertex respectively

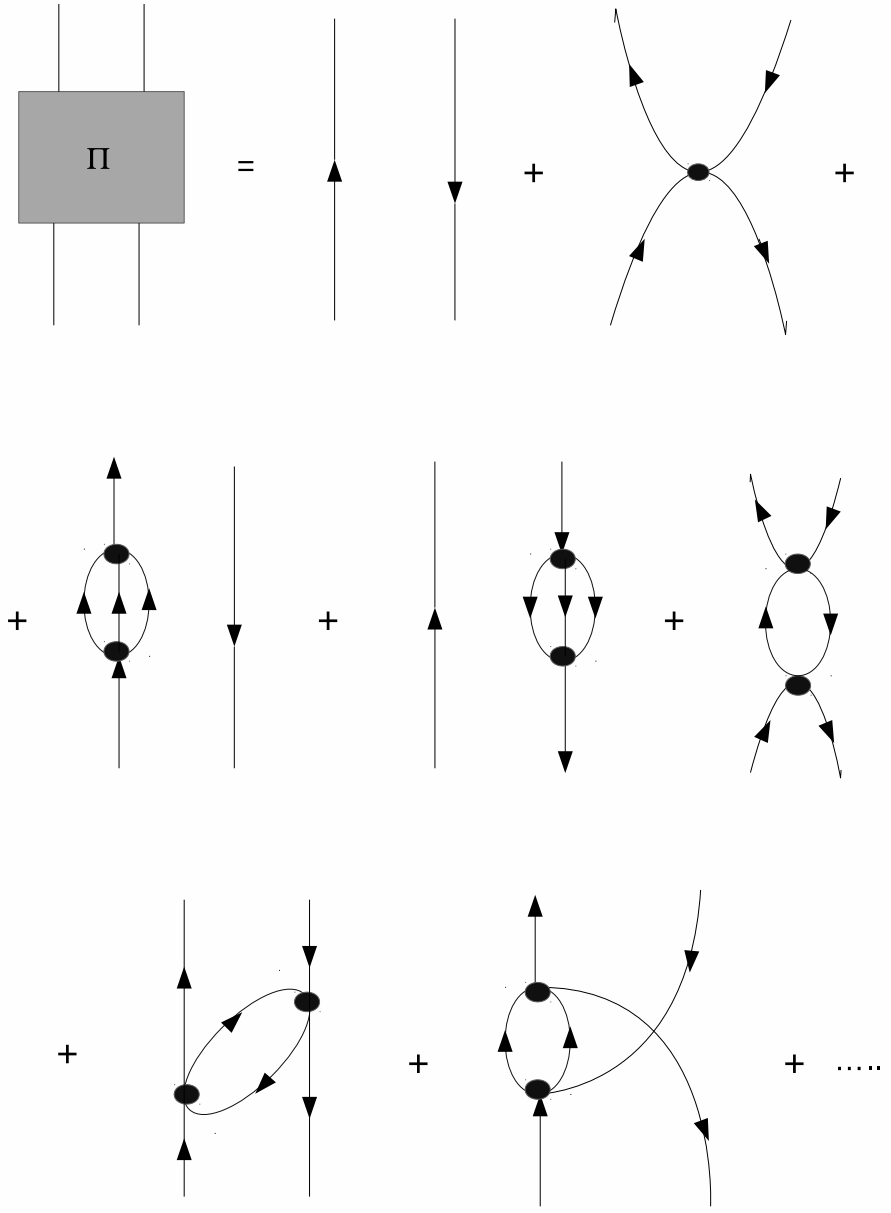

Figure 2.1.: Feynman diagrams up to second order for the polarisation propagator in Abrikosov notation [72].

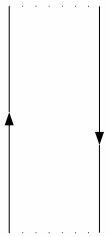

Figure 2.2.: Zeroth order Goldstone diagram for the $\Pi^{+}(\omega)$ part of the polarisation propagator.

and summing over all the p,q,r,s indices.

At zeroth order there is only one Goldstone diagram, represented in Fig. 2.2. The expression corresponding to this diagram is

$$X(1) = \sum_{ai} (d^{*}_{ai}) \frac{\bar{n}_a n_i}{(\omega + \varepsilon_i - \varepsilon_a)} (d_{ai}) \; . \tag{2.55}$$

Thus we immediately have the identification

$$K_{ai,bj} = \delta_{ab}\delta_{ij} (\varepsilon_a - \varepsilon_i) \tag{2.56}$$

$$F^{[0]}_{ai} = d_{ai} \, . \tag{2.57}$$

In Fig. 2.3 the three first order Goldstone diagrams corresponding to the first order Feynman diagram contributing to the $\Pi^{+}(\omega)$ part of the polarisation propagator, and therefore to $T(\omega)$, are represented. In every diagram the dotted lines indicate the external vertices. Naming them $X(1)$, $X(2)$ and $X(3)$ respectively, the explicit expressions for these diagrams read as follows:

$$X(1) = \sum_{a,i} \sum_{b,j} (d^{*}_{ai}) \frac{\bar{n}_a n_i}{(\omega + \varepsilon_i - \varepsilon_a)} \left(-V_{aj[bi]}\right) \frac{\bar{n}_b n_j}{(\omega + \varepsilon_j - \varepsilon_b)} (d_{bj}) \tag{2.58}$$

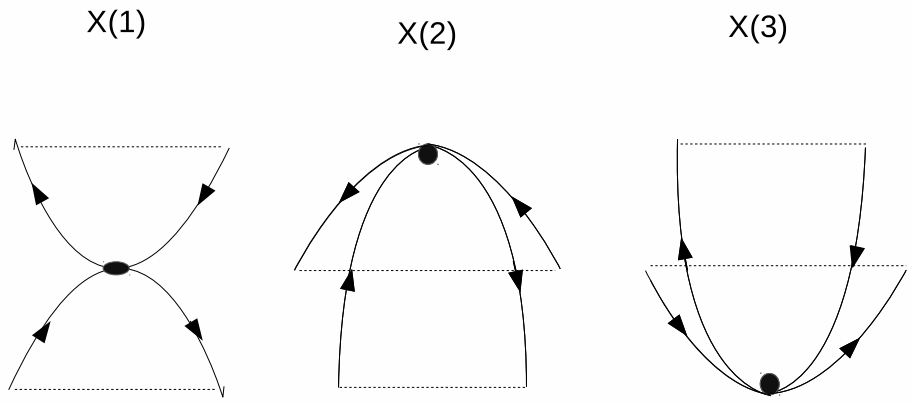

Figure 2.3.: First order Goldstone diagrams for the $\Pi^{+}(\omega)$ part of the polarisation propagator.

$$X(2) = \sum_{a,i} \sum_{c,k} \left[\frac{d^{*}_{kc} V^{*}_{ac[ki]} \bar{n}_c n_k}{(\varepsilon_a + \varepsilon_c - \varepsilon_k - \varepsilon_i)} \right] \frac{\bar{n}_a n_i}{(\omega + \varepsilon_i - \varepsilon_a)} (d_{ai}) \tag{2.59}$$

$$X(3) = \sum_{a,i} \sum_{c,k} (d^{*}_{ai}) \frac{\bar{n}_a n_i}{(\omega + \varepsilon_i - \varepsilon_a)} \left[\frac{d_{kc} V_{ac[ki]} \bar{n}_c n_k}{(\varepsilon_a + \varepsilon_c - \varepsilon_k - \varepsilon_i)} \right] \tag{2.60}$$

These terms fit directly into the algebraic expansion terms giving rise to the following identification:

$$C^{[1]}_{ai,bj} \equiv C_{ai,bj}(1) = -V_{aj[bi]} = -\langle aj \mid\mid bi \rangle \tag{2.61}$$

$$F^{[1]}_{ai} = \sum_{c,k} \frac{d_{kc} V_{ac[ki]}}{(\varepsilon_a + \varepsilon_c - \varepsilon_k - \varepsilon_i)} \ , \tag{2.62}$$

where the convention that occupied (hole) and non-occupied (virtual) orbitals in the mean-field reference state are denoted respectively by the letters

$i, j, k, l, m, n, \ldots$ and $a, b, c, d, e, f, \ldots$ has been adopted. All the quantities are expressed in terms of spin-orbitals.

Of course it is possbile to transform these expressions rearranging the products of two ω denominators into a sum of single ω denominators, consequently obtaining a different identification of the various algebraic terms. However, even though there is no uniqueness, it is not possible to transfer contributions from $\mathbf{F}$ to $\mathbf{C}$, whatever identification is used. In this sense the modified interaction matrix $\mathbf{C}$ is maximal and thereby uniquely determined.

As is clear from the expressions of Eq. (2.61) and Eq. (2.62), at the ADC(1) level of theory the explicit excited states manifold is the one consisting of all the p-h excitations on top of the mean-field ground state, and therefore only the p-h part of both $\mathbf{C}(1)$ and $\mathbf{F}^{[1]}$ is obtained when performing the comparison procedure at first order. The first order terms corresponding to higher excitation configurations (2h-2p, 3h-3p, etc.) do not contribute to the polarisation propagator at first order, but only at higher orders.

Of particular interest is the second order ADC(2) level of theory, where the dimension of the secular matrix coincides with the excitation manifold spanned by all the p-h and 2p-2h excitations with respect to the mean-field reference state. The number of Goldstone diagrams for the second order part $\Pi^{+}(\omega)$ is 60.

Within ADC(2), the perturbation expansion order of the secular matrix elements extend through second, first and zeroth order respectively in the one-hole-one-particle (1h1p) block, the 1h1p-two-hole-two-particle (2h2p) coupling block and the diagonal 2h2p block. In a similar way the p-h and 2p-2h parts of the effective transition amplitudes have perturbation expansions respectively through first and second order. An extension of the ADC scheme, not strictly consistent with the polarisation propagator and referred to as ADC(2) extended, is obtained by using the first-order expansion for the 2p-2h block; in the strict ADC(2) level of approximation the 2h-2p block of the secular matrix M [2] is diagonal and no couplings between 2h-2p excitations are included. In the extended version called ADC(2)x this block is augmented with the first order couplings stemming from the higher-order ADC(3) scheme [83]. This is an *ad-hoc* extension and certainly introduces some imbalances in the description of the excited states and the ground state generally leading to an underestimation of excitation energies; however, as

a main result, this improves the treatment of doubly excited states and in general of states with a strong admixture of double excitations (strongly double-excitation character states).

At the third order level ADC(3) the expansion manifold is the same as at the ADC(2) level (the dimension of the secular matrix **M** and of the effective transition amplitudes vector **F** does not change), while the perturbation expansions of the matrix elements extend through the next order of perturbation theory (3,2,1 respectively for the blocks of **M** and 3,2 for those of **F**).

The ADC(2) matrix can be therefore concisely written as

$$\mathbf{M}\left(2\right)^{ADC[2]} \equiv \mathbf{M}^{ADC[2]} = \begin{pmatrix} M_{11}\left(2\right) & M_{12}\left(1\right) \\ M_{21}\left(1\right) & M_{22}\left(0\right) \end{pmatrix} \tag{2.63}$$

and the effective amplitudes F as

$$\mathbf{F}\left(2\right)^{ADC[2]} \equiv \mathbf{F}^{ADC[2]} = \begin{pmatrix} F_1\left(2\right) \\ F_2\left(1\right) \end{pmatrix} , \tag{2.64}$$

where the numbers in square brackets indicate the maximum order of perturbation theory up to which the various matrix elements extend.

The explicit analytic expressions for the matrix elements of the 1h-1p block of **M**, found by a procedure analogous to the one performed before for the ADC(1) level, are given by

$$M_{ia,jb}^{ADC[2]} = M_{ia,jb}^{[0]} + M_{ia,jb}^{[1]} + M_{ia,jb}^{[2]} , \tag{2.65}$$

where again the numbers in square brackets indicate the perturbation order of the matrix elements. The second, first and zeroth order contribution are respectively:

$$M_{ia,jb}^{[0]} = \delta_{ij}\delta_{ab}\left(\varepsilon_a - \varepsilon_i\right) = K_{ia,jb} \tag{2.66}$$

$$M_{ia,jb}^{[1]} = -\langle aj \mid\mid bi\rangle \tag{2.67}$$

$$M_{ia,jb}^{[2]} = M\left(2\right)_{ia,jb}^{[2]A} + M\left(2\right)_{ia,jb}^{[2]B} + M\left(2\right)_{ia,jb}^{[2]C} \tag{2.68}$$

$$M^{[2]A}_{ia,jb} = -\frac{1}{4}\delta_{ij}\sum_{c,kl}\left[t^{ac}_{kl}\langle kl \,||\, bc\rangle + \left(t^{bc}_{kl}\right)^{*}\langle ac \,||\, kl\rangle\right] \tag{2.69}$$

$$M^{[2]B}_{ia,jb} = -\frac{1}{4}\delta_{ab}\sum_{cd,k}\left[t^{cd}_{ik}\langle jk \,||\, cd\rangle + \left(t^{cd}_{jk}\right)^{*}\langle cd \,||\, ik\rangle\right] \tag{2.70}$$

$$M^{[2]C}_{ia,jb} = +\frac{1}{2}\sum_{c,k}\left[t^{ac}_{ik}\langle jk \,||\, bc\rangle + \left(t^{bc}_{jk}\right)^{*}\langle ac \,||\, ik\rangle\right] \tag{2.71}$$

The first order coupling 1h1p-2h2p block is given by

$$M^{[1]}_{ia,menf} = +\delta_{ae}\langle mn \,||\, if\rangle - \delta_{af}\langle mn \,||\, ie\rangle + \delta_{im}\langle an \,||\, ef\rangle - \delta_{in}\langle am \,||\, ef\rangle \tag{2.72}$$

where $m < n$, $e < f$ is assumed and finally the zeroth order diagonal 2h-2p block is given by

$$M^{[0]}_{kcld,menf} = \delta_{ce}\delta_{df}\delta_{km}\delta_{ln}\left(\varepsilon_c - \varepsilon_k + \varepsilon_d - \varepsilon_l\right) = K_{kcld,menf} \tag{2.73}$$

where $m < n$, $e < f$ and $k < l$, $c < d$ is assumed.

In these expressions the quantity t^{ac}_{ik} stands for

$$t^{ac}_{ik} = \frac{\langle ac \,||\, ik\rangle}{\varepsilon_i + \varepsilon_k - \varepsilon_a - \varepsilon_c} \tag{2.74}$$

and $\langle ac \,||\, ik\rangle = \langle ac \mid ik\rangle - \langle ac \mid ki\rangle$ represents the antisymmetrised matrix element of the electron-electron Coulomb interaction, in terms of spin-orbitals $\chi\left(\sigma, \mathbf{r}\right)$

$$\langle ac \mid ik\rangle =$$

$$= \int d\sigma_1 d\sigma_2 \int d^3r_1 d^3r_2 \chi^{*}_a\left(\sigma_1, \mathbf{r}_1\right)\chi^{*}_c\left(\sigma_2, \mathbf{r}_2\right)\frac{1}{\mid \mathbf{r}_1 - \mathbf{r}_2 \mid}\chi_i\left(\sigma_1, \mathbf{r}_1\right)\chi_k\left(\sigma_2, \mathbf{r}_2\right) \,. \tag{2.75}$$

The expression for the effective transition matrix element are given by

$$F_{ai}^{ADC[2]} = d_{ai} + \sum_{c,k} t_{ik}^{ac} d_{kc} + F\left(2\right)_{ai}^{[2]A} + F\left(2\right)_{ai}^{[2]B} + F\left(2\right)_{ai}^{[2]C} + \sum_{I=1}^{10} F\left(2\right)_{ai}^{[2]I} \tag{2.76}$$

for the 1h1p block, where the second order part consists of 13 different contributions and by

$$F_{abij}^{ADC[2]} = \sum_{k} \left[t_{kj}^{ab} d_{ki} - t_{ki}^{ab} d_{kj} \right] - \sum_{c} \left[t_{ij}^{cb} d_{ac} - t_{ij}^{ca} d_{bc} \right] \tag{2.77}$$

for the first order contribution to the 2h-2p block where $a < b\,,\, i < j$ is assumed.

From a computational point of view in an ADC(2) calculation the scaling with respect to the number N of orbitals is N^6 for the generation of the p-h block and N^5 for any iteration step in the diagonalising procedure.

Finally it should be noted that the algebraic form of Eq. (2.36) for the polarisation propagator in the frequency domain results automatically, if instead of inserting in Eq. (2.26) the resolution of identity in terms of the ground state and the exact excited states of the system, one inserts the resolution of the identity in terms of $\mid \Psi_0\rangle$ and of some generic basis set $\{\mid \Psi_I\rangle\}$ in the excited states space called intermediate states, i.e.

$$\mathbf{1} = \mid \Psi_0\rangle\langle\Psi_0 \mid + \sum_{I} \mid \Psi_I\rangle\langle\Psi_I \mid \ . \tag{2.78}$$

Of course the explicit form of the secular matrix $\mathbf{M}$ and of $\mathbf{F}$ depends on the particular set $\{\mid \Psi_I\rangle\}$ chosen and the ADC form requires a specific set of intermediate states.

2.4. Intermediate State Representation (ISR) approach to ADC

Although the ADC(n) schemes for excited states of closed-shell systems were originally derived as approximations to the polarisation propagator, based on an algebraic reformulation of its diagrammatic perturbation theory [56], they were later recognised [84] as being interpretable as wave-function methods as well. In fact, ADC establishes a connection between propaga-

tor and wave-function methods. The latter interpretation comes from the explicit identification and construction of the intermediate states representation (ISR) that gives rise to the ADC form of the propagator, providing an alternative and direct approach to the hierarchy of the ADC schemes [84, 85].

The starting point of the ISR-ADC approach is the construction of the so called correlated excited states (CES), defined as

$$\mid \Psi_I^0\rangle = \hat{C}_I^\dagger \mid \Psi_0\rangle \,, \tag{2.79}$$

where the operators $\hat{C}_I^\dagger$ denote the physical excitation operators corresponding respectively to 1p1h, 2p2h etc. excitations,

$$\hat{C}_I^\dagger = \left\{ \hat{a}_a^\dagger \hat{a}_i \,;\, \hat{a}_a^\dagger \hat{a}_b^\dagger \hat{a}_j \hat{a}_k \quad (a<b, j<k) \,;\, \hat{a}_a^\dagger \hat{a}_b^\dagger \hat{a}_c^\dagger \hat{a}_j \hat{a}_k \hat{a}_l \quad (a<b<c, j<k<l) \,;\ldots \right\}, \tag{2.80}$$

and $\mid \Psi_0\rangle$ is the exact correlated ground state of the system.

Here, as before, the formulas are written adopting the familiar notation in which the subscripts $a, b, c, ...$ refer to unoccupied virtual orbitals (with respect to the mean-field single Slater determinant ground state), and $i, j, k, ...$ to the occupied orbitals. Physical excitation operators are intended to be those operators which remove electrons from the occupied orbitals of the zeroth order state and create electrons in the virtual orbitals only. These intermediate states are divided in classes according to the number of excitations they involve; thus $\hat{a}_a^\dagger \hat{a}_i \mid \Psi_0\rangle$ represent the first excitation class, $\hat{a}_a^\dagger \hat{a}_b^\dagger \hat{a}_c^\dagger \hat{a}_j \hat{a}_k \hat{a}_l \mid \Psi_0\rangle$ the second and so on. In general the states will be denoted as $\mid \Psi_y^m\rangle$ where the index m represents the class to which they pertain, while the index y identifies the specific state in that class.

This non-orthogonal CES basis set is complete in the space of the excited states of the N-electron system [86]. Including the ground state as a zeroth order class one obtains a basis set for the entire Hilbert space of the system. The advantage of using this basis set instead of the traditional configuration (CI) states (physical excitations with respect to the zeroth order ground state) is that ground state correlation is already built into every basis vector, making it an ideal set to describe fluctuations of small particles number away from the ground state. The price that one pays is the lack of orthogonality of the N-electron basis states. However since the basis

set is not linearly dependent, it may be straigthforwardly orthonormalised. The orthonormalisation procedure affects the final basis and therefore any related matrix representation of operators, but the spectra and the eigenstates will remain invariant. The orthonormalisation procedure that gives the intermediate basis representation reproducing the ADC quantities is called Excitation Class Orthonormalisation (ECO).

ECO is a two-step procedure which consists firstly in Gram-Schmidt orthogonalisation of the excitation class under consideration with respect to all the lower excitation classes and secondly in symmetric orthonormalisation within the excitation class itself. The states $\mid \Psi_y^{m\#}\rangle$ formed in this first step are referred to as precursor states. Subsequently a symmetric orthonormalisation of the resulting precursor states is performed within the given excitation class under consideration. The algorithm is sequential in the sense that this procedure is applied consecutively to all the excitation classes starting from the first.

As an example the procedure for the first (1h1p) excitation class gives the following precursor states:

$$\mid \Psi_{ai}^{1\#}\rangle = \hat{a}_a^\dagger \hat{a}_i \mid \Psi_0\rangle - \mid \Psi_0\rangle\langle\Psi_0 \mid \hat{a}_a^\dagger \hat{a}_i \mid \Psi_0\rangle \,. \tag{2.81}$$

The second step gives

$$\mid \tilde{\Psi}_{ai}^{1}\rangle = \sum_{bj} \mid \Psi_{bj}^{1\#}\rangle \left(S^{-\frac{1}{2}}\right)_{bj,ai} , \tag{2.82}$$

where $\mathbf{S}$ is the overlap matrix of the first excitation class precursor states, i.e.

$$S_{bj,ai} = \langle \Psi_{bj}^{1\#} \mid \Psi_{ai}^{1\#}\rangle = \langle\Psi_0 \mid \hat{a}_j^\dagger \hat{a}_b \hat{a}_a^\dagger \hat{a}_i \mid \Psi_0\rangle - \langle\Psi_0 \mid \hat{a}_j^\dagger \hat{a}_b \mid \Psi_0\rangle\langle\Psi_0 \mid \hat{a}_a^\dagger \hat{a}_i \mid \Psi_0\rangle \tag{2.83}$$

In a compact notation the excitation class orthogonalised (ECO) states can be written as

$$\mid \tilde{\Psi}_x^m\rangle = \hat{Q}^{m-1} \sum_y \mid \Psi_y^m\rangle \left(S_{yx}^m\right)^{-\frac{1}{2}} , \tag{2.84}$$

where S_{yx}^m is defined as

$$S_{yx}^m = \langle \Psi_y^m \mid \hat{Q}^{m-1} \mid \Psi_x^m\rangle \tag{2.85}$$

and

$$\hat{Q}^m = \hat{1} - \sum_{l=0}^{m} \hat{P}^l \tag{2.86}$$

is the projector operator onto the space orthogonal to the first m excitation classes. Finally, every intermediate state can be expressed as

$$\mid \tilde{\Psi}_I \rangle = \tilde{C}_I^\dagger \mid \Psi_0 \rangle \,, \tag{2.87}$$

where all the effects of the consecutive orthonormalisations are encoded in the new creation operators $\tilde{C}_I^\dagger$.

The orthonormalisation procedure is bijective in the sense that there is a one-to-one correspondence between the initial states and the final orthonormal states. Hence, since both the projective and the symmetric othonormalisation steps preserve the association of the final states with the indices of the original overlapping correlated excited states, each of the orthonormal ECO-CES states is largely characterised, as the initial states, by specific hole and particle indices and by a specific excitation class index. The Gram-Schmidt procedure leads to formal expansions in terms of the correlated ground state for the successive classes of intermediate states and becomes rather lengthy for higher excitation classes.

Inserting these expansions in the respective sub-blocks of the ISR/ADC matrices, one obtains closed form expressions depending on the exact ground state wave-function and energy. The representation of the shifted electronic Hamiltonian operator $\hat{H} - E_0$ in the ECO-CES space reads:

$$\mathcal{H}_{IJ} = \langle \tilde{\Psi}_I \mid \hat{H} - E_0 \mid \tilde{\Psi}_J \rangle = \langle \Psi_0 \mid \tilde{C}_I \left[\hat{H}, \tilde{C}_J^\dagger \right] \mid \Psi_0 \rangle \,. \tag{2.88}$$

At this point Møller-Plesset (MP) Rayleigh-Schrödinger (RS) perturbation theory is introduced to describe the ground state correlation, i.e. $\mid \Psi_0 \rangle$

$$\mid \Psi_0^{'} \rangle = \mid \Phi_0^{HF} \rangle + \mid \Psi_0^{[1]^{'}} \rangle + \mid \Psi_0^{[2]^{'}} \rangle + \mid \Psi_0^{[3]^{'}} \rangle + \ldots \,, \tag{2.89}$$

in which the first order correction $\mid \Psi_0^{[1]^{'}} \rangle$ contains only double excitations (2h2p) with respect to the Hartree-Fock (HF) ground state, $\mid \Phi_0^{HF} \rangle$, while $\mid \Psi_0^{[2]^{'}} \rangle$ contains single, double, triple and quadruple excitations, and E_0:

$$E_0 = \langle \Phi_0^{HF} \mid \hat{H} \mid \Psi_0^{'} \rangle = E_0^{[0]} + \langle \Phi_0^{HF} \mid \hat{W} \mid \Psi_0^{'} \rangle$$

$$E_0^{[n]} = \langle \Phi_0^{HF} \mid \hat{W} \mid \Psi_0^{[n-1]'} \rangle. \tag{2.90}$$

In these formulas the ground state is denoted with the prime superscript as $\mid \Psi_0^{'} \rangle$ to remember that, in RS perturbation theory, intermediate normalisation is assumed for the ground state in the sense that it satisfies the following relation

$$1 = \langle \Phi_0^{HF} \mid \Psi_0^{'} \rangle \, . \tag{2.91}$$

It is important to realise that in the expressions for the intermediate ADC states the normalised ground state

$$\mid \Psi_0 \rangle = \frac{\mid \Psi_0^{'} \rangle}{\left[\langle \Psi_0^{'} \mid \Psi_0^{'} \rangle \right]^{\frac{1}{2}}} \tag{2.92}$$

must be used in conjunction with its own perturbation expansion that is simply recovered from the perturbation expansion for $\mid \Psi_0^{'} \rangle$ as reads up to third order as

$$\mid \Psi_0 \rangle = \mid \Phi_0^{HF} \rangle + \mid \Psi_0^{[1]'} \rangle + \mid \Psi_0^{[2]'} \rangle - \frac{1}{2} \mid \Phi_0^{HF} \rangle \left(\langle \Psi_0^{'} \mid \Psi_0^{'} \rangle \right)^{[2]} +$$

$$+ \mid \Psi_0^{[3]'} \rangle - \frac{1}{2} \mid \Phi_0^{HF} \rangle \left(\langle \Psi_0^{'} \mid \Psi_0^{'} \rangle \right)^{[3]} - \frac{1}{2} \mid \Psi_0^{[1]'} \rangle \left(\langle \Psi_0^{'} \mid \Psi_0^{'} \rangle \right)^{[2]} + O\left[4\right] \, . \tag{2.93}$$

For example, the expansion of the first excitation class states up to second order reads

$$\mid \tilde{\Psi}_{ai}^{1} \rangle = \hat{a}_a^{\dagger} \hat{a}_i \mid \Phi_0^{HF} \rangle + \hat{a}_a^{\dagger} \hat{a}_i \mid \Psi_0^{[1]'} \rangle + \hat{a}_a^{\dagger} \hat{a}_i \mid \Psi_0^{[2]'} \rangle - \mid \Phi_0^{HF} \rangle \langle \Psi_0^{[2]'} \mid \hat{a}_a^{\dagger} \hat{a}_i \mid \Phi_0^{HF} \rangle -$$

$$- \frac{1}{2} \sum_{bj} \hat{a}_b^{\dagger} \hat{a}_j \mid \Phi_0^{HF} \rangle \langle \Psi_0^{[1]'} \mid \hat{a}_j^{\dagger} \hat{a}_b \hat{a}_a^{\dagger} \hat{a}_i \mid \Psi_0^{[1]'} \rangle + O\left[3\right] \tag{2.94}$$

while the second excitation class states up to first order are given by:

$$\mid \tilde{\Psi}_{aibj}^{2} \rangle = \hat{a}_a^{\dagger} \hat{a}_b^{\dagger} \hat{a}_j \hat{a}_k \mid \Phi_0^{HF} \rangle \, + \, \hat{a}_a^{\dagger} \hat{a}_b^{\dagger} \hat{a}_j \hat{a}_k \mid \Psi_0^{[1]'} \rangle -$$

$$- \mid \Phi_0^{HF} \rangle \langle \Psi_0^{[1]'} \mid \hat{a}_a^{\dagger} \hat{a}_b^{\dagger} \hat{a}_j \hat{a}_k \mid \Phi_0^{HF} \rangle \, + \, O\left[2\right] \, .$$

(2.95)

We see from these expressions how for each intermediate state there exists a correspondence between the excitation class to which it belongs and the configuration (CI) states from which it receives the major contribution.

In this new perspective the ADC secular matrix M is defined as the representation $\mathcal{H}$ of the shifted electronic Hamiltonian $\hat{H} - E_0$ in the space of these intermediate correlated excited states

$$M_{IJ}^{ADC} = \langle \tilde{\Psi}_I \mid \hat{H} - E_0 \mid \tilde{\Psi}_J \rangle \,. \tag{2.96}$$

The vertical excitation energies are obtained by solving the eigenvalue problem $\mathbf{HV} = \omega\mathbf{V}$ and the excited eigenstates of the system are therefore given in the basis of the intermediate states:

$$\mid \Psi_n \rangle = \sum_I V_{I,n} \mid \tilde{\Psi}_I \rangle \,. \tag{2.97}$$

Thus, basically, explicit construction of the eigenstate wave-function becomes possible in the ISR approach. Having this explicit expression for the excited states of the system the transition moments of the type $\langle \Psi_m \mid \hat{D} \mid \Psi_0 \rangle$ are given by

$$\langle \Psi_m \mid \hat{D} \mid \Psi_0 \rangle = \mathbf{V}_m^\dagger \cdot \mathbf{F} = \sum_{rs} d_{rs} \mathbf{V}_m^\dagger \cdot \mathbf{f}_{rs} \,, \tag{2.98}$$

where d_{rs} are the matrix elements of the dipole operator on the one particle orbitals choosen as basis set functions. The matrix of effective transition amplitudes $\mathbf{f}$ and the associated vector $\mathbf{F}$ are defined correspondingly by:

$$f_{I,rs} = \langle \tilde{\Psi}_I \mid \hat{a}_r^\dagger \hat{a}_s \mid \Psi_0 \rangle \,, \quad F_I = \langle \tilde{\Psi}_I \mid \hat{D} \mid \Psi_0 \rangle \,. \tag{2.99}$$

Once we have established the way these intermediate states are constructed and perturbatively expanded, we can recover the hierarchy of ADC(n) approximations exactly at each order n by truncating the ECO intermediate states manifold at some limiting excitation class and simultaneously truncating the resulting perturbation expansions for the included classes in a way consistent with the polarisation propagator results. In general a method

that is consistent with the ADC form of the polarisation propagator to a certain order n needs only the 1h1p-1h1p block expanded to that order. It is sufficient to use lower orders for the higher excitation blocks included. The orders up to which each sub-block must be calculated is of course the same as the orders appearing in the $\mathbf{M}$ matrix. The orthonormal complement of the truncated manifold is by definition expanded at zeroth order, the corresponding states reducing to configurations states, and every diagonal or coupling block involving them is evaluated with the mean-field zeroth-order Hamiltonian with the result that this space becomes completely uncoupled, in the Hamiltonian matrix, to the effective truncated space. By definition the couplings between the ground state and all other intermediate states are exactly zero at all orders, and consideration of both the ground state and the spaces of uncoupled higher excitations are therefore removed from the computation altogether.

In the ADC(1) scheme the Hamiltonian matrix reduces to the Configuration Interaction Singles (CIS) one, while the transition moment with respect to the ground state are improved and are expressed as

$$\langle \tilde{\Psi}_i^a \mid \hat{D} \mid \Psi_0 \rangle = d_{ai} + \sum_v \sum_o \frac{\langle va \mid\mid oi \rangle}{\epsilon_o + \epsilon_i - \epsilon_v - \epsilon_a} d_{ov} \tag{2.100}$$

where $\langle va \mid\mid oi \rangle$ is the antisymmetrised two-particle Coulomb integral in physicists' notation and the two indices v and o run over the virtual and the occupied canonical (Hartree-Fock) orbitals respectively. Therefore ADC(1) can be already considered as an improved version of CIS.

At the ADC(2) level the matrix in the whole space of the system can be represented as

$$\mathcal{H}^{\mathrm{ADC[2]}} = \mathcal{H}^{[0]} + \mathcal{H}^{1,1[1]} + \mathcal{H}^{1,1[2]} + \mathcal{H}^{1,2[1]} + \mathcal{H}^{2,1[1]}. \tag{2.101}$$

where $\mathcal{H}^{i,j[n]}$ represents the n-th order term in the expansion of the ihip-jhjp block of the ADC Hamiltonian matrix. The ADC(2) secular matrix can also be expressed in the following closed form expression [87]

$$\mathbf{M}^{ADC[2]} = \begin{pmatrix} \langle \Psi_0 \mid \hat{\tau}_{\mu 1} \left[\hat{H} + \frac{1}{2} \left(\hat{W} \hat{T}_2^{[1]\dagger} + \hat{T}_2^{[1]} \hat{W} \right) \right] \hat{\tau}_{\nu 1}^\dagger \mid \Psi_0 \rangle & \langle \Psi_0 \mid \hat{\tau}_{\mu 1} \hat{W} \hat{\tau}_{\nu 2}^\dagger \mid \Psi_0 \rangle \\ \langle \Psi_0 \mid \hat{\tau}_{\mu 2} \hat{W} \hat{\tau}_{\nu 1}^\dagger \mid \Psi_0 \rangle & \langle \Psi_0 \mid \hat{\tau}_{\mu 2} \hat{F} \hat{\tau}_{\nu 2}^\dagger \mid \Psi_0 \rangle \end{pmatrix} \tag{2.102}$$

where the operator $\hat{T}_2^{[1]\dagger}$ defines the first order correction to the HF ground state in the sense that $\mid \Psi_0^{[1]'} \rangle = \hat{T}_2^{[1]\dagger} \mid \Phi_0^{HF} \rangle$ (the subscript 2 indicates that the correction consists of double excitations) and the operators $\hat{\tau}_{\mu 1}$ and $\hat{\tau}_{\mu 2}$ respectively represent the single and double excitations operators in a compact way. The ADC(2) secular matrix has also been recognised [88] to be the symmetrised version of the secular matrix resulting within the configuration interaction singles with perturbative doubles correction CIS(D_∞) method, i.e.

$$\mathbf{M}^{ADC[2]} = \frac{1}{2}\mathbf{M}^{CIS(D_\infty)} + \frac{1}{2}\left(\mathbf{M}^{CIS(D_\infty)}\right)^\dagger . \tag{2.103}$$

One of the peculiar features of ADC is that the ADC matrices have the property that ground state correlation is built into each matrix element via perturbation theory, and the extent to which this is done is described by the ADC order n. In the ADC ground state correlation is estimated in a size consistent manner, via perturbation theory. Excitations on top of the ground state feel a dressed interaction, due to the local ground state correlation, but the ground and excited states have the exact same correlation character away from this region. Furthermore, much of the intrinsic error of ground state RS perturbation theory is cancelled out since only the energy differences between the ground and the excited states of the system are directly computed. While correlation is treated in a balanced way between ground and excited states, excitations of different classes are handled differently. The scheme discussed above, i.e. ADC(2), is most accurate for excitations of mainly p-h character (the qualitative definition of such a state can be made independent of methodology by the use of reduced density matrices [89])). These should be the most experimentally relevant excitations of a system, although excitations of 2h-2p character are an important manifestation of electron correlation, and this effective truncation is closely related to the efficiency of the scheme.

One of the main advantages of ADC(n) methods is that the basic computational procedure consists in the diagonalisation of a Hermitian secular matrix using RS perturbation theory to evaluate the secular matrix elements. While at second order there are the same number of degrees of freedom as in either the Configuration Interaction with Single and Double excitations (CISD) [49] and the Equation Of Motion Coupled Cluster with Single and

Double excitations (EOM-CC-SD) methods [54], the equation to be solved for excited states energies is a Hermitian eigenvalue problem and, at the same time, the method is size-consistent, therefore obtaining two of the primary advantages of the CISD and EOM-CCSD methods respectively. The ADC equations are indeed separable in the sense that local and nonlocal excitations are strictly decoupled, and the ADC results for both energies and for transition moments are size-consistent (size-intensivity property) [90]. Moreover the ADC(n) schemes are compact relative to the corresponding truncated CI expansions [90], i.e. the dimension of explicit configurations space required in the ADC(n) secular problem, in order for the energies of the resulting principal (1h-1p character) eigenstates to satisfy a certain level of perturbation theoretical accuracy, is systematically smaller than the dimension needed in CI expansions of comparable accuracy. As an example the ADC truncation error resulting from restricting the configuration space to singles and doubles excitation classes (in ADC(3)) is of order 4 (for the excitation energies of single excitations) as compared to a second order error for the same truncation in the CI case. In this respect the ADC schemes are also superior to the Coupled Cluster (CC) methods where the corresponding truncation error is of order 3.

While the results are obviously the same as in the polarisation propagator approach, in the original ADC procedure explicit expressions for the matrix elements of $\mathbf{M}$ and $\mathbf{f}$ are obtained without the need to specify the intermediate state representation. Even though the ISR approach to the derivation of explicit ADC expressions becomes quite cumbersome beyond second order and here the original diagrammatic derivation is more advantageous, within the ISR formalism it is possible to define the ADC representations of other operators other than the Hamiltonian, because we have the explicit expression for the basis set giving rise to ADC representation.

Moreover, using the expansion in terms of ECO intermediate states, the ADC approximation forms can also be derived for quantities which have no direct diagrammatic perturbation expansion, such as high order (quadratic, cubic, etc.) response functions.

The reformulation of the ADC methods as wave-function methods using the intermediate state representation (ISR) has led to applications of the ADC-ISR technique to the calculation of properties of and transition moments between excited [85], singly ionised [91] and doubly ionised [92]

bound states.

In the excited states context, the ADC-ISR representation of any one-particle operator was recently derived at the second order level [85]. This has opened the possibility of calculating the transition dipole moments between any pair of electronic excited states of the system (i.e. the dipole matrix in the system's excited states Hilbert space) at the ADC(2) level:

$$\langle \Psi_m \mid \hat{D} \mid \Psi_n \rangle = \mathbf{V}_m^{\dagger} \cdot \mathbf{D} \cdot \mathbf{V}_n = \sum_{ij} V_{m,i}^{*} \mathcal{D}_{IJ} V_{n,j} \tag{2.104}$$

where $\mathcal{D}_{IJ}$ are the matrix elements of the dipole operator on the ISR many-electron basis set functions [85]:

$$\mathcal{D}_{IJ} = \langle \tilde{\Psi}_I \mid \hat{D} \mid \tilde{\Psi}_J \rangle = \langle \Psi_0 \mid \tilde{C}_I \hat{D} \tilde{C}_J^{\dagger} \mid \Psi_0 \rangle \,. \tag{2.105}$$

The perturbative theoretical consistency of the results depends on the excitation class of the states considered. At the ADC(2) level the properties and the transition moments between excited states with mainly single excitations contribution are treated consistently through second order. The representation of the dipole operator at the ADC(2) level has the following structure

$$D^{ADC[2]} = D^{[0]} + D^{1,1[2]} + D^{1,2[1]} + D^{2,1[1]}. \tag{2.106}$$

The matrix elements of the hp-hp block of this matrix in spin-orbital form can be expressed by:

$$D_{ai,bj} = D_{ai,bj}^{[0]} + D_{ai,bj}^{[2]} = \delta_{ij} d_{ab} - \delta_{ab} d_{ji} + \sum_{k=1}^{7} D_{ai,bj}^{[2],k}. \tag{2.107}$$

There is indeed no first-order contribution to this block. Considering this part of the matrix: the first second-order part, $D_{ai,bj}^{[2],1}$, contains the second order contributions to the one-particle density matrix elements $\rho_{ia}^{[2]}$

$$D_{ai,bj}^{[2],1} = -\delta_{ij} \sum_{l} \rho_{lb}^{[2]} d_{al} - \delta_{ab} \sum_{c} \rho_{jc}^{[2]} d_{ci} + h.c. \tag{2.108}$$

Therefore a strictly consistent treatment of $D^{1,1[2]}$ at the ADC(2) level would require one to evaluate the ground state one-particle density matrix at least through second-order in perturbation theory (through its strict second order

expression)

$$\rho_{ia}^{[2]} = \langle \Psi_0 \mid \hat{a}_a^\dagger \hat{a}_i \mid \Psi_0 \rangle^{[2]} = \langle \Psi_0^{[2]} \mid \hat{a}_a^\dagger \hat{a}_i \mid \Phi_0^{HF} \rangle. \tag{2.109}$$

Finally another remarkable advantage of the ISR approach to ADC is that, having access to both energetic information in the ADC effective Hamiltonian and a state space resolution for the wave-function via the ISR, now makes it possible, in the ADC formalism, to numerically time-propagate a state [i.e. to solve the time-dependent Schrödinger equation (TDSE)] and to consequently analyse the state of the system as a function of time, having direct access to it via its expansion coefficients in the ECO-ISR basis [93].

2.5. The Stieltjes moment theory technique for the bound-continuum matrix elements

The calculation of photoionisation cross-sections requires the knowledge of many-electron wave-functions belonging to the continuum part of the spectrum. The basic computational problem one faces here is taking into account both the scattering character of the photoionised state wave-function and the electron correlation. In the previous sections the ADC(n) methods used to calculate excited states and excitation energies of electronic atomic and/or molecular systems have been highlighted. However, many-electrons states calculated using Gaussians as single particle basis functions can not be used directly in Eq. (2.3) to compute an approximation to the oscillator-strength density in the electronic continuum $\frac{df(E)}{dE}$. The reason is that, due to the use of finite sets of square-integrable (typically Gaussian) single-electron basis functions, the computed molecular eigenstates in the continuum energy region are discrete and $\mathcal{L}^2$-normalised. These states will therefore give an inaccurate result because of the incorrect way they take into account the molecular continuum density of states.

Having the proper description of the continuum ionised states is important and essential in order to compute differential cross-sections and recover the angular distribution of the emitted electrons (for example to calculate the asymmetry parameter β_2, or to compute partial differential cross-sections, in which the state of the produced ion is exactly identified). For this aim it is important to know the asymptotic behaviour of the continuum wave-

functions far from the nuclear framework and therefore to have a detailed representation of the matrix elements between bound states and the degenerate states in the continuum. This is not given by any standard $\mathcal{L}^2$ calculation based on Gaussian one-electron basis functions.

However, in order to compute the total integral cross-section, dependent only on the energy of the photon absorbed by the system, for which the less demanding oscillator strength density as a function of the excitation energy in the electronic continuum is required, common quantum chemistry single-particle basis functions, such as the Gaussian basis functions, can be successfully used. In other words, in order to obtain this physical quantity it is possible to use the same basis sets that have been widely applied to the calculation of bound states in quantum chemistry.

In the $\mathcal{L}^2$ basis-set approach to the continuum a lot of use is made of the Stieltjes-Chebyshev imaging (SI) technique [94] that is implemented to avoid the construction of the electronic continuum scattering functions $\mid \Psi_E^f \rangle$. The SI technique can be seen as a practical and mathematically well defined procedure to obtain the correct continuum normalisation starting from a general discretised spectrum formed by energies and oscillator strengths obtained from an $\mathcal{L}^2$ calculation. It is, in fact, not directly concerned with the computation of states in the continuum, its aim being to extract from an $\mathcal{L}^2$ basis-set calculation of transition probabilities the oscillator-strength density in the energy region properly belonging to the continuum excitations. Thus it may be applied either to the results yielded by separate calculations of initial and final states, or to those arising from a direct evaluation of the transition matrix elements. Moreover it can be used at different levels of accuracy in the description of the initial and final states.

With the purpose of making the most out of purely $\mathcal{L}^2$ basis-set results, $\mathcal{L}^2$ pseudostates are introduced to provide a representation of both the discrete and continuum portions of the photoionisation spectra. The information to create photoionisation spectra is contained in the pseudo-frequencies and oscillator strengths, $\{\varepsilon_i, f_i\} \quad i = 1, ..., N$.

The ε_i values represent the difference between the energy of the i-th final state and the energy of the initial state and the f_i are given by the squared transition dipole moments between the initial and the final states; both set of quantities can be directly obtained from an $\mathcal{L}^2$ ADC(1) or ADC(2) calculation.

Basically a finite set of eigenstates with eigenvalues larger than the ionisation energy will offer a discretised description of the electronic continuum. These discretised states in the continuum do not have the correct continuum degeneracy, but are used to calculate approximate excitation energies from a bound initial state and the related oscillator strengths that altogether will form the discretised variational spectrum of interest. Additionally, as these final states are variationally determined, the distribution of the discretised oscillator strengths on the energy axis is strongly dependent on the $\mathcal{L}^2$ basis set employed.

The SI approach to photoionisation cross-sections is based on the hypothesis that this variational discretised $\mathcal{L}^2$ spectrum above the ionisation threshold, even if clearly inadequate to describe the exact structure of the continuum, allows one to obtain good converging approximations for at least the lowest spectral moments, $S(n)$, of the oscillator-strength density, $g(\omega)$.

These type of spectral moments are defined as

$$S(n) = \langle \Psi_0 \mid \hat{D}^\dagger \hat{H}^{n+1} \hat{D} \mid \Psi_0 \rangle , \tag{2.110}$$

where n is the order of the spectral moment.

It is possible to express the spectral moments (2.110) in terms of the exact bound $\{\Psi_j\}$ and continuum $\{\Psi_E\}$ eigenstates of the Hamiltonian using the resolution of identity:

$$\begin{aligned} S(n) &= \sum_j E_j^{n+1} \mid \langle \Psi_0 \mid \hat{D} \mid \Psi_j \rangle \mid^2 + \\ &+ \int_{E_{\text{threshold}}}^{\infty} E^{n+1} \mid \langle \Psi_0 \mid \hat{D} \mid \Psi_E \rangle \mid^2 dE . \end{aligned} \tag{2.111}$$

From this equation it is clear that these are spectral moments of the oscillator-strength density function $g(E) \propto E \mid \langle \Psi_0 \mid \hat{D} \mid \Psi_E \rangle \mid^2$. The calculation of $g(E)$ and hence of $\sigma(E)$ is directly connected to the knowledge of the lowest spectral moments which, as already mentioned, are supposed to be obtained with sufficient accuracy by $\mathcal{L}^2$ calculations.

Indeed, looking carefully at $g(E)$ it is immediately recognisable that the only part of the continuum wave-function actually needed in order to compute the matrix element is the one that has a non-zero overlap with the localised function $\hat{D} \mid \Psi_0 \rangle$. Assuming that this function is non-zero only

within a finite interaction region, one can express the spectral moments using the resolution of identity in terms of the variationally calculated discrete $\mathcal{L}^2$ eigenstates $\{\Phi_\alpha\}$ spanning this region:

$$S(n) \approx \sum_\alpha E_\alpha^{n+1} \mid \langle \Psi_0 \mid \hat{D} \mid \Phi_\alpha \rangle \mid^2 . \tag{2.112}$$

Thus it becomes clear that if there is an $\mathcal{L}^2$ variationally calculated set of states which forms a complete basis set spanning the interaction region, then the spectral moments can be calculated exactly.

The moment problem consists of recovering the continuous function $\frac{df(E)}{dE} \equiv g(E) \propto E \mid \langle \Psi_0 \mid \hat{D} \mid \Psi_E \rangle \mid^2$ from a finite number of its spectral moments obtained within the $\mathcal{L}^2$ approximation (2.112). It is important to note that within the non-relativistic theory the spectral moments diverge for $n > 1$ [95], and thus the SI approach must rely on the use of negative spectral moments.

The starting point is to find some Stieltjes integral expressed in terms of the measure $df(\varepsilon)$. The formula in Eq. (2.7) for the complex polarisability is perfect for this purpose. According to the Stieltjes approach, convergent approximations to the polarisability that are valid in the entire complex plane, including the real axis, are given in the form

$$\alpha(z) = \int_{\varepsilon_0}^{\infty} \frac{dF^{(n)}(\varepsilon)}{\varepsilon^2 - z^2} + R_n\left(z^2\right) \quad n = 1, 2, \ldots\ldots .$$

The functions $F^{(n)}(\varepsilon)$ are cumulative histogram-like oscillator-strength multistep functions built with the so-called principal quadrature pseudospectra $\left\{\varepsilon_i^{(n)}, f_i^{(n)}\right\}$ $i = 1, \ldots\ldots, n$ and are defined as

$$\begin{gathered} F^{(n)}(\varepsilon) = 0 \quad 0 < \varepsilon < \varepsilon_1^{(n)} , \\ F^{(n)}(\varepsilon) = \sum_{l=1}^{i} f_l^{(n)} \quad \varepsilon_i^{(n)} < \varepsilon < \varepsilon_{i+1}^{(n)} , \\ F^{(n)}(\varepsilon) = \sum_{l=1}^{n} f_l^{(n)} \quad \varepsilon_n^{(n)} < \varepsilon . \end{gathered}$$

(2.113)

The cumulative oscillator strength obtained in this way approximates the exact oscillator strength density function, converging to it for large values of n if the first $2n$ moments are accurately reproduced by the $\mathcal{L}^2$ calculation. This is formally expressed by the Chebyshev relation [94, 96]

$$F^{(n)}(\varepsilon - 0) < F^{(n+1)}(\varepsilon - 0) \leq f(\varepsilon) \leq F^{(n+1)}(\varepsilon + 0) < F^{(n)}(\varepsilon + 0) \tag{2.114}$$

which shows that $F^{(n)}(\varepsilon)$ gives upper and lower bounds on $F(\varepsilon)$ at the points $\varepsilon_i^{(n)}$.

Although, as already mentioned, variational $\mathcal{L}^2$ calculations will, in general, produce a variational spectrum that is strongly basis-set dependent in the continuum portion of the spectrum, the corresponding quadrature pseudospectrum is virtually independent of the basis, as long as the approximated spectral moments can be considered to converge to the correct ones.

The quadrature pseudo-excitation energies and pseudo-oscillator strengths correspond to the abscissae and weights of a generalised quadrature of order n for the polarisability integral taking $\frac{df(\varepsilon)}{d\varepsilon}$ as a weight function.

The SI computational procedure [96] includes construction of the quadrature pseudospectrum, which is defined by the following 2n equations:

$$S(-2k) = \sum_{i=1}^{n} \frac{f_i^{(n)}}{\left[\varepsilon_i^{(n)}\right]^{2k}}, \quad k = 1, 2, \ldots, 2n. \tag{2.115}$$

Thus, the first 2n moments reconstructed from the $\mathcal{L}^2$ variational calculation give rise to an n-term smoothed ($n \ll N$) principal pseudospectra $\left\{\varepsilon_i^{(n)}, f_i^{(n)}\right\}$ $i = 1, ..., n$. These quadrature pseudospectra are then used to determine the cumulative oscillator strength function, $F^{(n)}(\varepsilon)$.

The SI approximation to the oscillator strength density is found by differentiating the Stieltjes-Chebyshev cumulative function, according to the Stieltjes derivative definition (different from the Dirac convention for stepwise functions).

For the polarisability on the real axis, differentiating this approximate cumulative function according to the Stieltjes derivative definition, one finds

$$g^{(n)}(\varepsilon) = 0 \quad 0 < \varepsilon < \varepsilon_1^{(n)}$$

$$g^{(n)}(\varepsilon) = \frac{1}{2}\frac{\left(f_{i+1}^{(n)} + f_i^{(n)}\right)}{\left(\varepsilon_{i+1}^{(n)} - \varepsilon_i^{(n)}\right)} \quad \varepsilon_i^{(n)} < \varepsilon < \varepsilon_{i+1}^{(n)}$$

$$g^{(n)}(\varepsilon) = 0 \quad \varepsilon_n^{(n)} < \varepsilon\,. \tag{2.116}$$

Therefore we obtain the following formulas for the polarisability on the real axis

$$\Im\left[\alpha(\omega)\right] = \frac{\pi}{2\omega} g^{(n)}(\omega) + \Im\left[R_n\left(\omega^2\right)\right]$$

$$\Re\left[\alpha(\omega)\right] = \Re\left[R_n\left(\omega^2\right)\right] + P\int_{\varepsilon_0}^{\infty} \frac{g^{(n)}(\varepsilon)}{\varepsilon^2 - z^2} d\varepsilon\,.$$

The functions $g^{(n)}(\varepsilon)$ provide convergent approximations to the oscillator-strength density in the continuum that will converge to the correct value with increasing order n of the quadrature pseudospectrum. It should be noted that differentiating according to the Stieltjes approach (differently from the Dirac convention approach) is essential in order to obtain the proper energy unit normalisation (and the correct density of states factor).

The Stieltjes derivative of these cumulative oscillator-strength distributions converges to the correct oscillator-strength density in the limit of large n independently of the particular one-electron basis set used, if this is sufficient to reproduce accurately the first 2n moments, and consequently the photoabsorption cross-section profile in the electronic continuum spectrum of the system (photoionisation cross-section) converges to the exact one

$$\sigma^{(n)}(\omega) = \frac{2\pi^2}{c}\, g^{(n)}(\omega) \to \sigma(\omega)\ . \tag{2.117}$$

The reason for using the most advanced correlation methods available is to have a better convergence of the calculated spectral moments to the correct ones, at least for the lower moments. Hence the problem finally consists of calculating the n-order quadrature pseudospectrum given the first 2n spectral moments. In order to do this, the moment problem of Eq. (2.115) can be linearised by a Padé aprroximant to give the polarisability integral as

$$\alpha(z) = \sum_{i=1}^{n} S(-2k)\, z^{2(k-1)} + R_n\left(z^2\right) = \sum_{i=1}^{n} \frac{f_i^{(n)}}{\left[\varepsilon_i^{(n)}\right]^2 - z^2} + R_n\left(z^2\right) =$$

$$= \frac{P_{n-1}\left(z^2\right)}{Q_n\left(z^2\right)} + R_n\left(z^2\right) \tag{2.118}$$

$$P_{n-1}\left(z^2\right) = \sum_{i=0}^{n-1} a_i^{(n)} z^{2i}, \quad Q_n\left(z^2\right) = 1 + \sum_{i=1}^{n} b_i^{(n)} z^{2i} \tag{2.119}$$

and the pseudospectrum is then obtained from the roots and residues of the Padé approximant.

The coefficients $a_i^{(n)}$ and $b_i^{(n)}$ can be obtained by solving a set of linear equations:

$$\sum_{i=1}^{n} S(-2m+2i-2)\, b_i^n = -S(-2M-2) \;\; for \;\; n \le m \le (2n-1)$$

$$a_m^n = \sum_{i=0}^{m} S(-2m+2i-2)\, b_i^n \;\; for \;\; 0 \le m \le (n-1)\,. \tag{2.120}$$

As long as the $S(-2k)$ are moments of a non-decreasing distribution, a nontrivial solution of Eq. (2.120) can always be found. However the numerical implementation of the resulting formulas for the coefficients in terms of the moments is not convenient if a very large number of moments are required, because the spectral moments are highly redundant and the required accuracy with which they must be computed in order to avoid numerical problems is high.

Thus, when the spectral moments are given by the variationally determined pseudospectra, it is preferable to employ algorithms which use more stable quantities, instead of the spectral moments themselves, to compute the Padé approximants. Most of the algorithms make direct use of the N term variational pseudospectral quantities $\{\varepsilon_i, f_i\} \quad i = 1, ..., N$, without using the spectral moments explicitely. The approach used in this thesis is the one suggested by Langhoff [97], which is based on the continued fraction approximation of a Stieltjes integral different from the polarisability,

namely

$$\beta(z) = \int_{\varepsilon_0}^{\infty} \frac{\varepsilon df(\varepsilon)}{\varepsilon - z} = S(0) + S(-1) z + S(-2) z^2 + ... + S(-2n+1) z^{(2n-1)}. \tag{2.121}$$

In this case both even and odd negative moments are involved in the Taylor expansion and can be used to compute the quadrature pseudospectra.

The most serious limitation of this technique is its energy resolution capability. In fact any discretised representation of the electronic continuum is in general characterised by a finite resolution that is proportional to the number of states per unit energy interval. The density can be quite different in different energy regions and is basis-set dependent. One can think to increase it by increasing the dimension of the basis set in order to have a better energy resolution. However, apart form the linear dependence problems that one usually encounters with Gaussians, the additional problem in this respect is that, as previously outlined, the discretised spectrum which is used to compute the approximate oscillator-strength density is the optimised quadrature pseudospectrum. Consequently, even though this pseudospectrum definitely offers a more uniform and basis-set independent representation of the continuum, it cannot unfortunately improve the energy resolution because, in general, its dimension will be much smaller than the dimension of the input variational spectrum. This is true in cases where only a limited number of the computed low order moments satisfactorily approximate the correct values and can consequently be employed in the SI calculation. Therefore it is only possible to obtain a discrete set of Stieltjes derivatives values (i.e. of oscillator-strength density values), that can be generally fitted or interpolated to get the correct continuum dependence of the oscillator-strength density on the energy. This will in general smooth out any narrow resonance structure eventually present in the spectrum. The only way to obtain better results is to make the pseudospectrum denser in the energy region around the resonance structure. This can be achieved by increasing the order of the pseudospectrum, i.e. the number of spectral moments employed. Nevertheless the resolution can be moderately improved, it has proved to be almost impossible to extract a reasonable continuum normalisation from an $\mathcal{L}^2$ discretised spectrum in the neighbourhood of a narrow resonance position.

The SI technique is in principle generalisable to any discretised spectrum

formed by energy values and intensities as long as these are positive quantities. It has been also effectively applied to the calculation of Auger intensities, shake-off intensities as well as two-photon ionisation cross-sections [94]. Additionally it has been used, in combination with $\mathcal{L}^2$ ADC calculations, to estimate the linewidth Γ_ε of a resonance structure in the photoionisation spectrum

$$\Gamma_\varepsilon = 2\pi \mid \langle \Phi_d \mid \hat{H} - E_d \mid \Phi_\varepsilon \rangle \mid^2$$

due for instance to the presence of a discrete state $\mid \Phi_d \rangle$ belonging to a closed channel, embedded and interacting with the continuum states $\mid \Phi_\varepsilon \rangle$ of other open channels both in the case of a neutral system (autoionisation widths) and an ionic system (Auger-decay widths) [98, 99].

All the Stieltjes calculations reported in this thesis have been performed in quadruple numerical precision.

2.6. Lanczos iterative diagonalisation method

The main computational bottleneck of SI in its original formulation [94] is that the direct application of the SI procedure requires a full diagonalisation of the many-electron [e.g. ADC(n)] Hamiltonian matrix, i.e. the calculation of the full variational pseudospectrum of discretised final states obtainable from the specific molecular *ab-initio* method adopted. The basis sets typically used consists of a part describing the near nuclei behaviour, such as cc-pCV(D-T-Q)Z basis, augmented with Kaufmann-Baumeister-Jungen (KBJ) Gaussian functions optimised for the representation of continuum wave-functions [100]. In the case of ADC(1), full diagonalisation is achievable because the dimension of the resulting Hamiltonian matrix scales as N^2, where N is the number of one-electron basis-functions used in the calculation. However, obtaining the full pseudospectrum is typically not feasible, not even for a typical small organic molecule such as C_2H_4, for *ab-initio* methods going beyond single electronic excitations, e.g. ADC(2). Indeed, Hamiltonian matrix dimensions for polyatomic molecules represented using high-quality single-electron basis sets in computational schemes going beyond single excitations easily exceed millions, making these Hamiltonians not amenable to full diagonalisation. This effectively restricts the use of the technique to either small systems (e.g. atoms, diatomics) or to low-accuracy

ab-initio approximations for the photoionised states (e.g. single-excitation schemes).

This drawback of the Stieltjes imaging technique was realised early on by Nesbet [101] and a number of methods for overcoming this problem have been proposed since then [101, 102, 103]. In Ref. [104], it was proposed that this difficulty can be overcome by applying the moment theory SI procedure to the relatively low-dimensional block-Lanczos pseudospectrum of the full ADC(n) electronic Hamiltonian. The so called ADC-Lanczos-Stieltjes approach has been proved efficient not only for the ground state photoionisation cross-sections, but also for the autoionisation widths of excited states [98]. Moreover, very recently, an analogous Lanczos-Stieltjes approach has been developed for the coupled cluster pseudospectra by Cukras *et al.* [105].

Within the Lanczos method [106, 107, 108], the Hamiltonian is represented in the basis of the so-called Lanczos states, $\mid \Phi_j \rangle$, which are obtained by Gram-Schmidt orthogonalisation of the Krylov states

$$\mid \psi_j \rangle = \hat{H}^j \mid \psi_0 \rangle \quad j = 0, 1, 2, \ldots, N-1 \,. \tag{2.122}$$

By the Gram-Schmidt procedure, after N steps, an orthonormal basis of the N-dimensional Krylov subspace is obtained, and the representation of the Hamiltonian projected on this subspace has the following tridiagonal form:

$$H_N = \begin{pmatrix} \alpha_0 & \beta_1 & 0 & 0 & 0 & 0 & 0 \\ \beta_1 & \ddots & \ddots & 0 & 0 & 0 & 0 \\ 0 & \ddots & \ddots & \ddots & 0 & 0 & 0 \\ 0 & 0 & \ddots & \ddots & \ddots & 0 & 0 \\ 0 & 0 & 0 & \ddots & \ddots & \ddots & 0 \\ 0 & 0 & 0 & 0 & \ddots & \ddots & \beta_{N-1} \\ 0 & 0 & 0 & 0 & 0 & \beta_{N-1} & \alpha_{N-1} \end{pmatrix} . \tag{2.123}$$

This tridiagonal matrix representation of the Hamiltonian in the Krylov subspace can also be directly constructed through the following general three-term recurrence relation:

$$H\Phi_j = \alpha_j \Phi_j + \beta_j \Phi_{j-1} + \beta_{j+1} \Phi_{j+1} \tag{2.124}$$

with

$$\alpha_j = \Phi_j^\dagger H \Phi_j \tag{2.125}$$

$$\tilde{\Phi}_{j+1} = H\Phi_j - \alpha_j \Phi_j - \beta_j \Phi_{j-1} \tag{2.126}$$

$$\beta_{j+1} = \| \tilde{\Phi}_{j+1} \| \tag{2.127}$$

and

$$\Phi_{j+1} = \frac{\tilde{\Phi}_{j+1}}{\beta_{j+1}} \,. \tag{2.128}$$

The initial normalised state $\mid \psi_0 \rangle$ in the Lanczos construction is usually chosen to have maximal overlap with the Hamiltonian eigenstates that are of interest in the given physical problem. Obviously, it is assumed that neither $\mid \psi_0 \rangle$ itself nor all the other Φ_j Krylov states are eigenvectors of H, otherwise the algorithm terminates.

The Lanczos states of successive orders can be used to construct a series of approximations to the Hamiltonian. The N-th order Lanczos approximation $\hat{H}^{(N)}$ to $\hat{H}$ is of the form

$$\hat{H}^{(N)} = \sum_{j,k=0}^{N} \mid \Phi_j \rangle \langle \Phi_j \mid \hat{H} \mid \Phi_k \rangle \langle \Phi_k \mid \tag{2.129}$$

and its eigenvalues and eigenvectors of the operator ,

$$\hat{H}^{(N)} \mid \chi_\alpha^{(N)} \rangle \; = \; E_\alpha^{(N)} \mid \chi_\alpha^{(N)} \rangle \,, \tag{2.130}$$

form the so-called Lanczos pseudospectrum. With increasing N, the Lanczos pseudospectrum becomes a subsequently better approximation to the spectrum of $\hat{H}$.

A generalisation of the Lanczos technique to the case of a set of initial states is called block-Lanczos method [107]. The Lanczos (block-Lanczos) method is useful not only for diagonalising Hamiltonian matrices of large dimensions, but also for calculating functionals of the Hamiltonians. Indeed, the following approximate relations hold:

$$F\left(\hat{H}\right) \approx F\left(\hat{H}^{(N)}\right) = \sum_{\alpha=0}^{N} \mid \chi_\alpha^{(N)} \rangle F\left(E_\alpha^{(N)}\right) \langle \chi_\alpha^{(N)} \mid \,. \tag{2.131}$$

Consequently it can also be used for the calculation of the spectral moments

of the type of (2.110). To this end, the original Hamiltonian has to be substituted by its Lanczos representation:

$$S_n \approx S_n^{(N)} = \sum_{\alpha=0}^{N} \left(E_\alpha^{(N)}\right)^n \mid \langle \Psi_0 \mid \hat{D} \mid \chi_\alpha^{(N)} \rangle \mid^2 . \tag{2.132}$$

While the non-negative moments of the order $0 \leq n \leq 2N$ can be calculated exactly by Eq. (2.132) with the appropriate choice of the initial Krylov state, i.e. $\mid \Phi_0\rangle = \hat{D} \mid \Psi_0\rangle$ in the case of photoionisation calculations, (or block of states) [107], the negative moments required for the Stieltjes imaging can be calculated only approximately. Since the Lanczos (block-Lanczos) algorithm approximates most effectively the eigenstate subspace spanned by the starting vector (or vectors), one has to consider the physical properties of the system when choosing the initial Krylov state. In the case of photoionisation cross-section the final states of the process that we wish to resolve are of 1h1p type and have the symmetry of the $\hat{D} \mid \Psi_0\rangle$ state. Therefore, we choose our starting vectors for the block-Lanczos iterations as the full set of 1h1p ADC intermediate states of the appropriate symmetry.

2.7. B-splines basis-set

With the aim of performing ionisation dynamical calculations, i.e. wavepacket time-propagation calculations where part of the electronic wave-function escapes from the atomic or molecular region, most of the work completed in my PhD has been devoted to the implementation of the B-splines basis set within the *ab-initio* ADC method.

The reason for employing B-splines as radial basis functions is that, with respect to our purpose, the description of the continuum states requires basis sets which could reproduce the oscillating behaviour of the electronic wave-function up to big distances from the molecular region. Traditional $\mathcal{L}^2$ basis functions, such as Slater Type Orbitals (STOs) or Gaussian Type Orbitals (GTOs), are not adequate to represent the rapidly oscillating continuum states of an ionised electron far away from the molecular region, since numerical linear dependencies rapidly occur as the basis set increases. B-splines, conversely, are very flexible functions and are able to provide a very accurate representation of both bound and continuum states with-

out running into numerical dependencies even for large bases. The use of such a pre-determined quasi-complete set of one-particle orbitals eliminates the need of any a priori procedure in selecting the parameters for the Gaussian-type or Slater-type functions required in the standard $\mathcal{L}^2$ quantum chemistry calculations which often depend upon non-trivial treatment to minimise the linear dependence embedded in the choice of basis functions. This feature makes them superior to the other more conventional $\mathcal{L}^2$ basis sets and computationally competitive with the "local" finite-difference methods [109]. B-splines produce smooth curves with continuous derivatives at every point. Since they are defined in a restricted space, usually referred to as a box, one has to define a certain knot sequence with which discretising the radial coordinate, depending on the target system. The continuum wave-functions can be correctly reproduced by using a linear grid of points and a sufficient density of B-splines.

The monocentric B-spline basis, used in the work reported in this thesis, is composed of spherical harmonics for the angular part and B-splines functions for the radial coordinate. Single particle orbitals are therefore expressed as linear combinations of products of B-splines and spherical harmonics

$$\psi_n = \sum_j \Phi_j C_{jn} \tag{2.133}$$

$$\Phi_{ilm} = \frac{1}{r} B_i(r) Y_{lm}(\theta, \phi) \tag{2.134}$$

The spherical harmonics are then defined by

$$Y_{l,m}(\theta, \phi) = \sqrt{\left(\frac{2l+1}{4\pi} \frac{(l-m)!}{(l+m)!}\right)} P_l^m(\cos\theta)\, e^{im\phi}, \tag{2.135}$$

where $P_l^m(x)$ is a generalised Legendre polynomial and the normalisation is chosen such that

$$\int_0^{2\pi} \int_0^{\pi} Y^*_{l_1,m_1}(\theta, \phi) Y_{l_2,m_2}(\theta, \phi) sin(\theta)\, d\theta d\phi = \delta_{m_1 m_2} \delta_{l_1 l_2}\,. \tag{2.136}$$

Here δ_{mn} represents the Kronecker delta. Spherical harmonics obey the

following relations

$$Y_{l,-l}(\theta,\phi) = \frac{1}{2^l l!}\sqrt{\left(\frac{(2l+1)!}{4\pi}\right)} sin^l(\theta)\, e^{-il\phi} \tag{2.137}$$

$$Y_{l,0}(\theta,\phi) = \sqrt{\left(\frac{2l+1}{4\pi}\right)} P_l(\cos\theta) \tag{2.138}$$

$$Y_{l,-m}(\theta,\phi) = (-1)^m Y^*_{l,m}(\theta,\phi)\,. \tag{2.139}$$

The use of B-splines in the atomic problem has been pioneered by Shore [110] and employed in the atomic and molecular context by several authors [111]. Although the first applications were to static properties, it has turned out that B-splines are possibly even more important for the calculation of dynamic properties such as multiphoton excitation, above-threshold ionisation (ATI) and high-order harmonic generation (HOHG) for atoms in the single-electron approximation [112]. Theory and computational aspects of B-splines are well documented in the literature [113]. In the following a brief review of the most relevant aspects and properties of the B-spline basis set will be given.

B-splines [57] are one-variable *piecewise polynomial functions* (pp-functions), characterised by their polynomial order k (maximum degree $k-1$), designed to generalise polynomials for the purpose of approximating arbitrary functions on some finite interval $[0, R_{max}]$. In order to completely describe the B-spline basis functions, the following set of quantities must be introduced: a radial interval $[0, R_{max}]$ divided into l adjacent subintervals $I_j = [\xi_j, \xi_{j+1}]$ by a sequence of $l+1$ points ξ_j in strict ascending order $0 = \xi_1 < \xi_2 < \ldots < \xi_{l+1} = R_{max}$; the ξ_j are usually called breakpoints (bps). A second sequence of non-negative integers $\nu_j,\ j = 2, ..., l$ is associated with interior bps $\xi_j,\ j = 2, ..., l$ and define continuity condition $C^{\nu_j - 1}$ at the associated bps ξ_j. Finally another sequence of points $\{t_i\}$ in ascending order, called knots, which are not necessarily distinct and may be in part coincident:

$$0 = t_1 \leq ... \leq t_n = R_{max}\,. \tag{2.140}$$

They are associated with the sequences ξ_j and ν_j in the following way:

$$t_1 = t_2 = \ldots = t_{\mu_1} = \xi_1$$

$$t_{\mu_1+1} = \ldots = t_{\mu_1+\mu_2} = \xi_2$$

$$\ldots$$

$$t_{\mu_1+\mu_2+\ldots+\mu_{i-1}+1} = \ldots = t_{\mu_1+\ldots+\mu_{i-1}+\mu_i} = \xi_i$$

$$\ldots$$

$$t_{n+1} = \ldots = t_{n+\mu_{l+1}} = \xi_{l+1} \ , \ n = \mu_1 + \ldots + \mu_l$$

where the integer μ_j defines the multiplicity of the knots t_i at ξ_j and are given by $\mu_j = k - \nu_j$. Note that in this Section $\{t_i\}$ identify the spatial position of the knot points and do not have to be confused with the time variable.

Given the knots sequence, a family of B-splines of order k can be defined at any specific point r, using the following Cox-de Boor recursion relation [113]

$$B_j^k(r) = \frac{r - t_j}{t_{j+k} - t_j} B_j^{k-1}(r) + \frac{t_{j+k+1} - r}{t_{j+k+1} - t_{j+1}} B_{j+1}^{k-1}(r) \tag{2.141}$$

together with the definition for the B-splines of order $k = 1$

$$B_j^1(r) = 1 \text{ if } t_j \leq r \leq t_{j+1}$$

$$B_j^1(r) = 0 \text{ otherwise}. \tag{2.142}$$

These formulas give rise to the algorithm employed for the practical evaluation of B-splines: given a point r, one generates by recursion the values

of all the k B-splines which are non-zero at r. Each B-spline is therefore a function made up of different polynomial pieces on adjacent subintervals, of a fixed order k, joined with a certain degree of continuity at the bps.

The polynomial continuity at the knots is controlled by the knot multiplicity. For $r = \xi_j$, $B(r)$ is $C^{k-\mu_j-1}$, where μ_j is the multiplicity at ξ_j (the class C^n specifies the maximum derivation order n for which the derivative function $D^n f$ is still continuous over a specified interval). The maximum multiplicity is k, giving discontinuous functions, the minimum is 1 (simple knots), giving C^{k-2} B-spline functions. There is no point in demanding more than C^{k-2} continuity, since otherwise $f(r)$ reduces to a single polynomial over all the interval and therefore some discontinuity is the essence of pp-functions.

A single B-spline function $B_i^k(r)$, defined by the order $k > 0$ and a set of $k+1$ consecutive knots (at most k adjacent subintervals), has the following properties:

- $B_i^k(r)$ is a pp-function of order k over $[t_i, t_{i+k}]$
- $B_i^k(r) > 0$ for $r \in]t_i, t_{i+k}[$
- $B_i^k(r) = 0$ for $r \notin]t_i, t_{i+k}[$
- The B-spline basis is not orthogonal. $B_i^k(r) \neq 0$ over $]t_j, t_{j+1}[$ for $i = j-k+1, \ldots, j$, which implies that there are exactly k non-zero B-splines on each interval I_j and that

$$\int B_i^k(r)\, B_j^k(r)\, dr = 0 \text{ for } |i-j| \geq k$$

$$\int B_i^k(r)\, B_j^k(r)\, dr \geq 0 \text{ for } |i-j| < k \quad (2.143)$$

- B-splines are normalised as $\int B_i^k(r)\, dr = 1$ over the whole interval $[t_k, t_{n+1}]$.

- Each B-spline is indexed by the index i of the left knot (t_i) corresponding to the first interval $I_j = [\xi_j, \xi_{j+1}]$ where the B-spline starts to be different from zero.

In order to have a complete polynomial basis over the entire interval, a maximum multiplicity is imposed at the extremes of the interval $\mu_1 = \mu_{l+1} = k$, namely $t_1 = \ldots = t_k = \xi_1$ and $t_{n+1} = \ldots = t_{n+k} = \xi_{l+1}$; this makes the first and last basis functions different from zero for $r = 0$ and $r = R_{max}$. Boundary conditions at the origin, $\psi(0) = 0$, are satisfied by simply removing the first B-spline from the basis set. Similarly, it is possible to enforce the same condition at the outer boundary by removing the last B-spline. If necessary, numerical stability can be improved by removing also the next-to-last B-spline, thereby forcing the first derivative to go to zero: $\psi'(R_{max}) = 0$. The most common choice for knot multiplicity at inner bps is unity, corresponding to maximum continuity, that is C^{k-2}, unless there is a known singularity at some point, where continuity may be reduced by suitably increasing the knot multiplicity. This choice is typical of the B-spline bases commonly employed and has also been made in the work described throughout this thesis. With this choice the total number of B-spline functions n is given by $n = l + k - 1$. Continuity may be relaxed at the inner bps by increasing the associated knot multiplicity there.

The derivative of a B-spline of order k, being a pp-function of order $k-1$, can also be expressed as a linear combination of B-splines of the same order:

$$DB_i^k(r) = \frac{k-1}{t_{i+k-1} - t_i} B_i^{k-1}(r) - \frac{k-1}{t_{i+k} - t_{i+1}} B_{i+1}^{k-1}(r) \; . \tag{2.144}$$

Once these definitions have been introduced, it is possible to express any function $f(r)$ in a B-spline basis set over an interval $[a, b]$:

$$f(r) = \sum_{i=1}^{n} C_i \, B_i(r) \tag{2.145}$$

Hence the pp-function $f(r)$ is a linear combination of B-splines, made of l polynomial pieces of order k, one for each subinterval I_j. In this expansion of an arbitrary function $f(r)$ in terms of B-splines the number of contributing terms is reduced to k, hence a minimal number of operations is needed.

Since the B-spline functions are non-negative definite and have a minimal

support, the expansion coefficients of an arbitrary function $f(r)$ are close to the function values at the knots. The main consequence is that wild oscillations in the coefficients are avoided, cancellation errors are minimal and numerical stability is maximal. In general, when approximating analytic functions, it is best to employ high-order splines, compatible with the numerical stability and roundoff errors, typically in the range $k = 7 - 10$. The error will be bound by [57]

$$\varepsilon \sim \frac{h_j^k |D^k f(\eta_j)|}{k!} \tag{2.146}$$

where h_j is the width of the interval I_j and η_j is contained in I_j. This is the main advantage of B-splines over global bases, in that the error can be controlled by the step size, in an analogous manner to finite-difference approaches, but retaining all the advantages of basis set expansions. The completeness property of the basis may be characterised by the fact that for a given threshold, ε, all sufficiently smooth functions will be approximated within ε, provided that the derivatives are conveniently limited, that is up to a cut-off on the maximum local value of the derivatives. B-splines are then capable of describing both bound and strongly oscillating continuum states with the important property that the limit on the maximum kinetic energy of the states represented can be tuned by the choice of the interval step $h_j = t_{j+1} - t_j$.

In practice calculations, stable evaluation of splines is accomplished by the recursion algorithm and is efficiently implemented in the subroutine BSPLVP [113], which requires as input values the spline order k, the knot sequence, the value of the abscissa r and the index of the 'left' knot t_i. The latter can be located given the abscissa and the knot sequence, by subroutine INTERV [113]. The routine returns the values of the k B-splines that are nonzero at r, that is $B_{i-k+1}(r), ..., B_i(r)$. Another subroutine, called BSPLVD [113], can also be used in order to obtain their derivatives, which are evaluated as combination of B-splines of lower order. In quantum mechanical applications mostly overlap and Hamiltonian matrix elements, i.e. definite integrals involving B-splines and their derivatives, are involved. These are best computed to machine accuracy employing Gauss-Legendre (GL) integration [114] of appropriate order over each subinterval I_j, which is essentially exact in high order. GL integration of order n (n points) is

indeed exact for a polynomial integrand of order $2n$ or less. Therefore k GL points integrate exactly the product $B_i B_j$, and a little more is usually completely accurate even for nonpolynomial integrands, provided there is no singularity present in the interior of I_i.

The evaluation of the B-spline radial two-electron integrals

$$R^l(pq,rs) = \int B_p(r_1)\, B_q(r_1)\, \frac{r_<^l}{r_>^{l+1}} B_r(r_2)\, B_s(r_2)\, dr_1 dr_2 \tag{2.147}$$

is carried out by direct two-dimensional numerical integration as reported in [115, 116]. Because of integrand singularity at $r_1 = r_2$ integration in the two $r_1 \leq r_2$ and $r_1 \geq r_2$ regions has to be performed separately. This gives very accurate results, close to machine precision. Computer time for two-electron B-spline integral evaluation, although sizeable, is not the major part of the total cost for the basis sets presently employed. Also, since B-splines separated by more than k intervals are disjoint, that is $B_i(r)B_j(r) = 0$ for $|i-j| > k$, the five-dimensional array $R^l(pq,rs)$ is strongly banded. If it is stored making maximum use of the integral symmetry, that is

$$p \geq q \;\;,\;\; r \geq s \;\;,\;\; pq \geq rs$$

$$p - q \leq k \;\;,\;\; r - s \leq k \tag{2.148}$$

the total storage needed scales approximately as

$$\left(\frac{1}{2} n^2 k^2\right) l_{max}\,, \tag{2.149}$$

where l_{max} is the maximum angular momentum included in the calculation. Therefore it is possible to keep the whole integral set in main memory even for quite sizeable radial basis size n.

The first step in the calculations reported in this thesis is the solution of the discretised closed-shell Hartree-Fock (HF) equations,

$$\hat{h}^{HF}\psi_n = \epsilon_n \psi_n\,, \tag{2.150}$$

where $\hat{h}^{HF}$ is the spin-free ground-state Fock operator of the neutral system,

$$\hat{h}^{HF} = \hat{h}_0 + \sum_{occ} (2\hat{J}_{occ} - \hat{K}_{occ}) \tag{2.151}$$

which consists of the sum of the kinetic energy part and the Coulomb potential due to the nuclei, i.e. $\hat{h}_0$, and of the direct $\hat{J}_{occ}$ and exchange $\hat{K}_{occ}$ Coulomb interactions between the electrons [49].

In the molecular case Eq. (2.150) is solved for every irreducible representation of the molecular point symmetry group, and the expansion of the wave-function ψ_n contains all the spherical harmonics angular functions $Y_{lm}(\theta, \phi)$ belonging to the particular irreducible representation. In the case of linear molecules with $D_{\infty h}$ as symmetry point group, such as N_2 or CO_2, the axial angular momentum m is a good quantum number for the system. This means that the number of spherical harmonics belonging to the irreducible representations, and therefore entering the expansion of the corresponding symmetric orbitals, is equal to $L_{max} + 1$ for σ_g and to L_{max} for all the other irreducible representations (σ_u, π_g, π_u, etc.), where L_{max} is the maximum angular momentum used in the calculation. In the atomic case, the HF equations can be projected upon the l-m spherical harmonic subspace and they simplify in the following way

$$\hat{h}_l^{HF} \psi_{lm,n}(r) = \epsilon_{l,n} \psi_{lm,n}(r)\,. \tag{2.152}$$

Solving Eq. (2.150) self-consistently, we obtain a quasi-complete set of discretised one-particle functions $\psi_{\lambda,n}$ corresponding to electronic orbitals with defined symmetry λ (in the atomic case λ stands for the pair of orbital angular momentum quantum numbers l, m) and variable energy (both negative and positive) defined by the Hartree-Fock effective one-particle Hamiltonian. Therefore, both the set of occupied HF orbitals and the full orthogonal complement of virtual orbitals, expressed in terms of B-splines basis functions, are obtained. These canonical orbitals are then used to construct the ADC many-body Hamiltonian. Therefore the *ab-initio* calculation is not performed working directly with primitive B-splines and as a consequence the one- and two-electron integral transformation from the original B-spline basis to the HF basis set must be computed. Computational details will be given in Sec. 5.1 of Chapter 5. Since ADC is formulated

as a perturbative theory with respect to the HF mean-field Hamiltonian, the canonical ADC(n) formulas are valid only in terms of HF orbitals. Apart from the case of the first order ADC(1) level of theory, they become much more complicated if a different orbital set is used.

Care has to be taken with the choice of the knot sequence defining the B-spline basis set. For simple equidistant knots each $B_i(r)$ is just a translation by one interval of the previous one. If the knots are not equidistant the shape of $B(r)$ changes smoothly with the change of the knot. In a bound-state calculation, the set of B-splines of order k and total number n is often defined with an exponentially increasing knot sequence [57],

$$\xi_i = r_{max} \frac{e^{\gamma \frac{i-1}{n-1}} - 1}{e^{\gamma} - 1}. \tag{2.153}$$

The choice of such a knot sequence satisfies the need for a more densely populated set of B splines near the nucleus in order to accommodate the fast rising inner s orbitals at small radius r. The short-range region, where the wave-function oscillates quickly and correlation effects are stronger, needs separate consideration since the optimal grid distribution requires an approximately exponential spacing between knots. On the other hand, a more evenly populated set of B-splines at larger r is required if the oscillating behaviour of the positive-energy orbitals at large distance has to be properly represented. Unlike bound states, continuum states are ever-oscillating functions and thus vary up to infinity. Therefore, there are no reasons for not choosing a linear breakpoint sequence which divides the radial coordinates into equally spaced grid points. The B-spline knot sequence we use is the parabolic-linear sequence, which is a mix of these two types of sequences: a short-range dense one which concentrates points near the nucleus with quadratically increasing knot spacing, which is better adapted to bound states, and a linear knot spacing sequence for larger values of r necessary for continuum states description. The connection between these two regions is made at an intermediate radial distance r_0, imposing continuity of the breaking point function ξ_i and of it's first derivative. The explicit parabolic-linear knot sequence formula is:

$$\xi_i = \alpha(i - i_0)^2 \text{ for } 1 \leq i < i_0 \;\; \xi_i = h(i - i_0) \text{ for } i_0 \leq i \leq n \tag{2.154}$$

Basis set Index	$R_{\max}$ (a.u.)	N_{splines}	23cm Linear Region step h (a.u.)	24cmQuadratic coefficient α (a.u.)	R_0 (a.u.)
Set 1	21.0	45	0.6	0.0295	2.392
Set 2	47.0	87	0.61	0.032	2.595
Set 3	33.0	97	0.367	–	0.0
Set 4	60.0	157	0.4	–	0.0
Set 5	120.0	200	0.6	–	0.0
Set 6	160.0	205	0.78	–	0.0
Set 7	320.0	410	0.78	–	0.0

Table 2.1.: B-splines basis sets employed in the calculations; for every basis set the dimension of the discretisation box, the number of B-spline functions and the step in the linear grid region are given.

The intermediate radius is defined by the index i_0 in the following way $r_0 = \xi_{i_0} = \frac{r_{max}(i_0-1)}{2n-i_0-1}$ and the quadratic and linear coefficients by $\alpha = \frac{r_0}{(i_0-1)^2}$ and $h = \frac{r_{max}}{(n-i_0)}$ respectively.

As already mentioned, the range of kinetic energies accurately described by the B-spline basis set can be tuned changing the knot spacing in the linear region. The long range knot spacing is related mainly to the minimum wavelength we want to describe for the photoelectron, considered as a free particle, which cannot be much smaller than the grid step otherwise the B-spline basis hardly describes the oscillating behaviour of the wave-function.

The maximum energy E_{max} of the discretised continuum states is set by both the B-spline order k and the breakpoint spacing. At large distance, a continuum wave-function oscillates with a wavelength given by $\frac{2\pi}{k}$, $k = \sqrt{2E}$ and the number of B-splines contained in one wavelength has to be large enough to fully reproduce the two sign switches. For B-splines of order 10, such as the ones used in the present work, it is sufficient to satisfy the following condition: $h_{max} \approx \frac{\lambda_{min}}{\pi} = \frac{2}{k}$. This condition leads to an error on the continuum wave-function phase that never exceeds 0.1 rad.

The basis sets used in the calculations presented in this thesis are listed in Table 2.1. The basis denoted as Set 1 and Set 2 are of the parabolic-linear type and they both present a knots spacing in the linear region of 0.6 a.u., much wider compared to the minimum spacing in the short range region of about 0.03 a.u. The B-spline basis denoted as Sets 3-7 are associated with linear knot sequences in the entire radial range instead. In the present total photoionisation cross-section Stieltjes calculations we are able to limit the size of the B-spline set to a modest n (e.g., $n = 45$ and $R_{max} = 21$

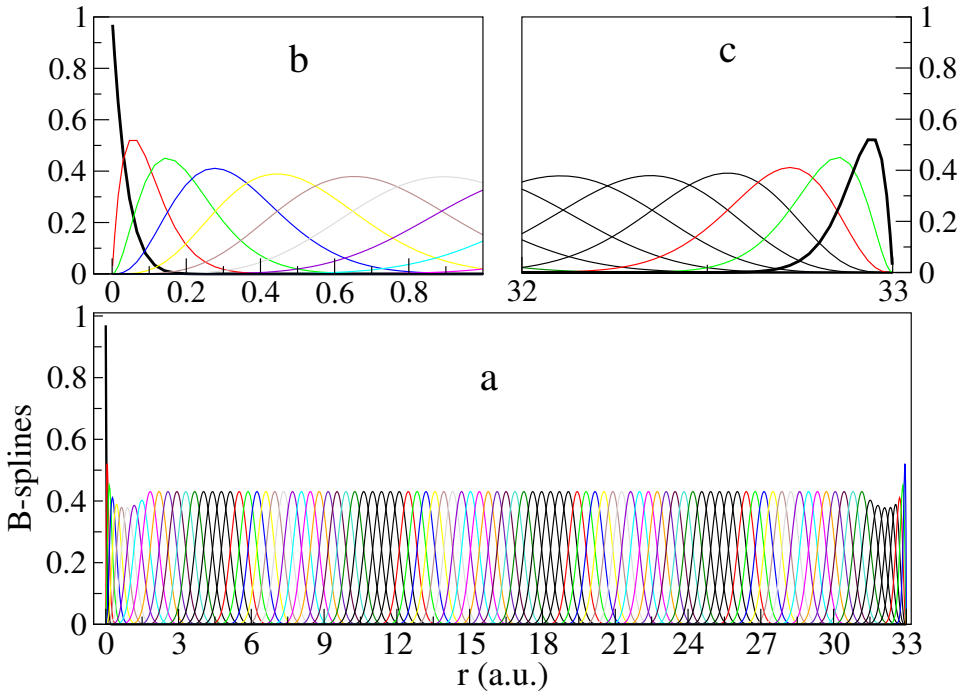

Figure 2.4.: a – graphical representation of B-spline basis Set 3, with $R_{max} = 33$ a.u.; the knot sequence is linear and the total number of B-spline functions is 97. b – magnification of the B-spline functions in the radial region close to the origin. c – magnification of the B-spline functions in the radial region close to the box boundary.

a.u. in our ADC(2) calculations), which is sufficiently large to take into account adequately the transition dipole moments of the excited states in the continuum with respect to the ground state. Set 4 is a linear basis set, and it has been used for the calculation of the Ar cross-section in the energy region of the core excitations from the 2p and 2s orbitals. In this case the linear spacing used is about 0.4 a.u. corresponding to the possibility of describing electrons with kinetic energy of about 300 eV. The B-spline Set 3 is represented graphically in Fig. 2.4.

Finally it must be mentioned that one of the most useful advantages of making use of B-spline functions is that they have the property of approaching completeness as much as desired by refining the corresponding knot sequence [57]. For example, the density of discretised continuum states represented by the basis can be increased arbitrarily by simply increasing the

extension of the grid, i.e. R_{max}, while maintaining at the same time fixed the spatial density of knots. This procedure can be done without being concerned about linear dependencies issues, which are commonly present with the use of Gaussian type orbitals instead.

In the approach used in this thesis, the ADC Hamiltonian diagonalisation procedure only provides a discrete set of many-electron wave-functions. These are the particular stationary solutions satisfying the boundary conditions $\Psi(r_i = R_{max}) = 0, i = 1, ..., N_e$, where N_e corresponds to the number of electrons, due to the fact that the problem has been restricted to a finite part of the space. Nevertheless, these functions can be interpreted as a discrete representation of the true electronic continuum with a different normalisation with respect to the energy unit one and with different asymptotic behaviour with respect to the scattering eigenstates of the system. Several techniques [117] have been developed in the last 20 years in order to correctly obtain, from a $\mathcal{L}^2$ B-spline calculation, normalised scattering states satisfying the correct asymptotic behaviour for photoionisation problems in the multi-channel case.

2.8. Time propagation scheme in the presence of attosecond laser pulses: Arnoldi-Lanczos algorithm

The focus of the second part of this thesis is on electronic-wavepacket time-propagation calculations where the atomic/molecular correlated electronic system, described by the B-spline ADC Hamiltonian, interacts with an ionising time-dependent electric field. Within TD-ADC, the time-dependent problem is solved making the following ansatz for the time-dependent electronic wave-function:

$$\mid \Psi(t)\rangle = C_0(t) \mid \Psi_0(t)\rangle + \sum_n C_n(t) \mid \Psi_n(t)\rangle \tag{2.155}$$

where the coefficients $C_0(t)$ and $C_n(t)$ refer to the ground-state and to the ECO-CES ADC configuration basis states respectively. Propagation of the B-spline ADC many-electron wave-function allows one to achieve a realistic *ab-initio* description of a series of many-electron phenomena in the

time-resolved fashion on the atto- and femto-second scale. In such numerical experiments, in which the electrons can reach very big distances from the molecular region ($\sim$ 1000 a.u.) during their interaction time with the laser electric field, the computational cost can become very high because of the dimension of the radial spherical box required. Indeed, the need of large numerical boxes in order to fully describe the electronic wavepacket throughout the interaction leads to a corresponding increase in the number of B-spline basis functions to be used and consequently to a final increase in the number of two-electron integrals to be calculated and in the dimension of the matrices to be propagated.

However, in many calculations one is interested in describing physical phenomena which happen within a limited region of space nearby the atomic or molecular system, not being influenced by the physics outside of that region. Therefore, in such circumstances the use of smaller boxes is desirable and convenient; however, although computationally cheaper, it introduces the problem of artificial reflections of the part of the wavepacket which reaches the box boundaries. This problem can be overcome with the implementation of absorbing boundary conditions, which is achieved in the work reported in this thesis by the use of the so-called complex absorbing potentials (CAPs) [118]. The use of a complex-absorbing potential has been demonstrated to be of practical value when dealing with ionisation or electronic decay processes, since it has the purpose of absorbing the emitted particle and allows one to limit the spatial extension of the basis-set. Indeed, CAPs artificially dampen those parts of the wave-function which penetrate the outer region of the grid, i.e. the region where the CAP itself is set different from zero, and ensure that the amplitude of the wave-function remains zero close to the edges of the box.

With the addition of the CAP term $-iW$ the form of the total time-dependent (no longer Hermitian) Hamiltonian of the system reads

$$\hat{\tilde{H}} = \hat{H}_0 + \hat{D}E(t) - i\hat{W} \tag{2.156}$$

where $\hat{H}_0$ is the field-free Hamiltonian and $\hat{D}E(t)$ is the laser-atom interaction in length form and within the dipole approximation. The $\hat{W}$ potential is a real non-negative function that vanishes in the inner region of space.

The form of the CAP used is this thesis is the following:

$$\hat{W} = 0 \quad \text{for} \quad r < r_{CAP}$$

$$\hat{W} = \eta(r - r_{CAP})^2 \quad \text{for} \quad r \geq r_{CAP}\,. \tag{2.157}$$

The CAP starts at a radius r_{CAP}, which defines the size of the inner region, and is characterised by a strength coefficient η which regulates the smoothness and steepness of the CAP profile. Small enough reflections can essentially be achieved by making the CAP strength η sufficiently small; therefore it is possible to propagate the initial wavepacket by $\tilde{H}$ rather than by the original Hamiltonian $\hat{H}$, without changing the values of the propagated wave-function at points where the CAP vanishes, i.e. for $r \leq r_{CAP}$. Due to the presence of the CAP the time-propagation is not unitary and therefore does not conserve the norm of the wave-function and the average energy of the system.

In this thesis the time-dependent Schrödinger equation (TDSE) for the unknown coefficients C_0, C_n of the B-spline ADC many-electron wave-function is solved with the use of the general complex Lanczos, or Arnoldi-Lanczos, algorithm [119, 120]. The Lanczos algorithm (Sec. 2.6) has been proved to be very efficient as a time propagation scheme for the non-relativistic Schrödinger equation [121] and is widely used in treating nuclear-dynamics problems [122, 123, 124]. The more general Arnoldi-Lanczos algorithm is suited to describe time-propagation with non-Hermitian Hamiltonians as well as the usual Hermitian ones. Indeed, it can be used efficiently when a complex-absorbing potential [118] is added to the Hamiltonian, which then becomes complex symmetric.

Using this algorithm, one actually replaces the full or partial diagonalisation of the large Hamiltonian matrix, in our case the ADC matrix, and the consecutive time propagation of the eigenvalues, with a repetitive diagonalisation of much smaller Hessenberg matrices. In this way, the time-propagation becomes applicable to large basis sets, which are practically inaccessible within approaches demanding a full diagonalisation of the secular matrix.

It is known that the time-dependent Schrödinger equation has a formal

solution

$$\mid \Psi(t)\rangle = \hat{U}(t,0) \mid \Psi(0)\rangle = T \exp\left(-\frac{i}{\hbar}\int_0^t \hat{H}(t')dt'\right) \mid \Psi(0)\rangle \,. \qquad (2.158)$$

where T exp is the so-called chronological exponent which represents the evolution operator $\hat{U}\,(t,0)$.

If the system Hamiltonian is time-independent, then the evolution operator describing the evolution of the system from time t to time $t+\Delta t$ is given by

$$\hat{U}\,(\Delta t) = \hat{U}\,(t+\Delta t, t) = \exp\left(-\frac{i}{\hbar}\hat{H}\Delta t\right) \,. \qquad (2.159)$$

The latter is also approximately true for a time-dependent Hamiltonian if, for a sufficiently small time increment Δt, the variation of the Hamiltonian is negligible. In that way, it is possible to represent the evolution operator as a product of such operators, propagating the wave-function from t to $t+\Delta t$, for which Eq. (2.159) is valid. In other words, a time interval can be divided into many small intervals with duration Δt and the evolution of the wave-function is represented as successive small steps.

It is obvious that if the initial state is an eigenfunction of H one gets $\mid \Psi\,(t)\rangle = \exp\left(-\frac{i}{\hbar}E_0 t\right) \mid \Psi\,(0)\rangle$, where E_0 is the eigenvalue of H corresponding to the eigenvector $\mid \Psi\,(0)\rangle$. In that way, if the eigenvalues and eigenvectors of the Hamiltonian are known, i.e. if the Hamiltonian matrix has been diagonalised, the time propagation is straightforward. Unfortunately, the full diagonalisation can be performed with reasonable expense only for relatively small systems or at a low level of approximation. Since the processes we want to treat result mainly from electronic correlation, the level of approximation should be as high as possible, which leads to large secular matrices even for small systems. It should be mentioned that if some knowledge of the system and the electronic process under study is available, one may encounter situations where not all the eigenstates are needed, i.e. a partial diagonalisation can be sufficient. Nevertheless, even in such cases the determination of the usually many eigenstates needed is very costly for multi-electron systems.

The Arnoldi-Lanczos algorithm leads to the following polynomial expansion of the exponential in the evolution operator:

$$\hat{U}(\Delta t) \approx \sum_{j=1}^{K} c_j P_j \left(-\frac{i}{\hbar}\hat{H}\Delta t\right) \tag{2.160}$$

where $P_j\left(-\frac{i}{\hbar}\hat{H}\Delta t\right)$ is a polynomial of degree j, and c_j are the expansion coefficients.

This polynomial expansion is obtained by projecting the Hamiltonian of the system at time t onto the Krylov subspace constructed starting from the normalised state vector of the system at the same time t, i.e. $V_0 = \psi(t)$, and spanned by the vectors $V_j = H^j\psi(t) \quad j = 0, 1, 2, \ldots, K-1$. Here H and $\psi(t)$ are respectively the matrix representations of $\hat{H}$ and $\mid \Psi(t)\rangle$ in some suitable basis.

Within the Arnoldi-Lanczos algorithm, in order to build the reduced Hamiltonian matrix H_K, the Krylov vectors are constructed recursively in the following way: assuming the set of the first, orthonormalised, j vectors, the Hamiltonian is applied to the j-th one and the resulting $(j+1)$th vector is first recursively orthogonalised with respect to the previous j vectors, starting from the first one, and then normalised. Obviously, it is assumed that none of the V_j is an eigenvector of H, otherwise the algorithm terminates immediately. Therefore, in this case, the recursive procedure for building the reduced Hamiltonian matrix H_K within the K-dimensional Krylov subspace, usually referred to as the modified Gram-Schmidt orthogonalisation scheme, reads as

$$\tilde{V}_{j+1}^{(1)} = HV_j$$

$$\text{for } \; i = 1, ..., j$$

$$\beta_{ij} = V_i^{\dagger}\tilde{V}_{j+1}^{(i)} \qquad \tilde{V}_{j+1}^{(i+1)} = \tilde{V}_{j+1}^{(i)} - \beta_{ij}V_i$$

$$V_{j+1} = \frac{\tilde{V}_{j+1}^{(j+1)}}{\beta_{j+1,j}} \qquad \beta_{j+1,j} = \| \, \tilde{V}_{j+1}^{(j+1)} \, \| \; .$$

(2.161)

In this way, starting with a normalised state $V_0 = \psi(0)$ one constructs an orthonormal basis $V_0, ..., V_{K-1}$ for the K-dimensional Krylov subspace, which represents a very good approximation to the Hilbert subspace to which the state of the system at time $t+\Delta t$ belongs and in which the reduced Hamiltonian H^K is represented as a complex upper Hessenberg matrix, i.e. a matrix which has zero entries only below the first subdiagonal,

$$H_{ij}^K \;=\; V_i^\dagger H V_j \;=$$

$$= \begin{pmatrix} \beta_{0,0} & \beta_{0,1} & \cdots & \cdots & \cdots & \cdots & \beta_{0,K-1} \\ \beta_{1,0} & \ddots & \ddots & \ddots & \ddots & \ddots & \vdots \\ 0 & \ddots & \ddots & \ddots & \ddots & \ddots & \vdots \\ 0 & 0 & \ddots & \ddots & \ddots & \ddots & \vdots \\ 0 & 0 & 0 & \ddots & \ddots & \ddots & \vdots \\ 0 & 0 & 0 & 0 & \ddots & \ddots & \beta_{K-2,K-1} \\ 0 & 0 & 0 & 0 & 0 & \beta_{K-1,K-2} & \beta_{K-1,K-1} \end{pmatrix} .$$

(2.162)

If the Hamiltonian is Hermitian, the matrix H_K becomes symmetric, and thus tridiagonal. In that sense, the Hermitian Lanczos discussed in Sec. 2.6 is just a special case of the more general complex Lanczos-Arnoldi algorithm.

In order to assure numerical orthogonality of the Krylov space basis set, at each step, each state vector is orthogonalised twice with respect to the previous ones. Therefore the final formulas for the reduced Hamiltonian matrix are:

$$\tilde{V}_{j+1}^{\text{new }(1)} = \tilde{V}_{j+1}^{(j+1)}$$

$$\text{for} \quad i = 1, ..., j$$

$$\beta_{ij}^{\text{correction}} = V_i^{\dagger} \tilde{V}_{j+1}^{\text{new }(i)} \quad \tilde{V}_{j+1}^{\text{new }(i+1)} = \tilde{V}_{j+1}^{\text{new }(i)} - \beta_{ij}^{\text{correction}} V_i$$

$$\beta_{ij}^{final} = \beta_{ij}^{standard} + \beta_{ij}^{\text{correction}} .$$

(2.163)

This re-orthogonalisation procedure is also known as the Kahan-Parlett "twice is enough" algorithm [106] and provides a very good accuracy for the orthogonality of the resulting Krylov basis states.

In the computational implementation of this scheme used in this thesis, it is possible to fix the maximum number of iterations requested, i.e. the maximum allowed dimension of the Krylov space. Moreover, the algorithm is stopped when the norm of the $(j+1)$-th Krylov vector candidate becomes smaller than a certain fixed threshold value, which, in this work, has been taken as the numerical precision of the calculator. If the norm condition is not violated the algorithm continues and therefore the new Krylov vector reads

$$\beta_{j+1,j} = || \tilde{V}_{j+1}^{\text{new }(j+1)} || \quad V_{j+1} = \frac{\tilde{V}_{j+1}^{\text{new }(j+1)}}{\beta_{j+1,j}} . \tag{2.164}$$

If instead the norm of the $(j+1)$-th Krylov vector candidate is smaller than the fixed threshold value, then the iterations are stopped and the dimension of the resulting Krylov space is smaller than the maximum allowed value. Then, the propagation operator $\hat{U}(\Delta t)$ can be approximated by its representation in the Krylov subspace:

$$\hat{U}_K(\Delta t) = \exp\left(-\frac{i}{\hbar} H_K \Delta t\right) . \tag{2.165}$$

Consequently the propagated vector we are interested in will be approximated by

$$\Psi(t) \approx \hat{U}_K(\Delta t)\, \Psi(0) . \tag{2.166}$$

The propagation of the initial wave-function is hence performed in the projected subspace by the upper Hessenberg Hamiltonian H_K, which is

much smaller than the full Hamiltonian and therefore much easier to diagonalise. After the diagonalisation the propagator can be expressed in the following form:

$$\hat{U}_K\left(\Delta t\right) = Z^{\dagger} \exp\left(-\frac{i}{\hbar} D_K \Delta t\right) Z\,, \tag{2.167}$$

where Z is the eigenvector matrix of H_K, and D_K is its diagonal matrix of eigenvalues. The propagated vector is constructed from the eigenvalues and eigenvectors of the matrix H_K and reads:

$$\Psi\left(t\right) = \exp\left(-\frac{i}{\hbar} H_K \Delta t\right) \Psi\left(0\right) = \sum_{j=1}^{K-1} a_j V_j\,, \tag{2.168}$$

where its coefficients onto the Krylov space basis vectors read

$$a_j = \sum_{n=0}^{K-1} Z_{jn} \exp\left(-\frac{i}{\hbar} \lambda_n \Delta t\right) \left(Z^{-1}\right)_{n0}\,. \tag{2.169}$$

In Eq. (2.169) the λ_n denote the eigenvalues of the matrix H_K. The propagated wave-function is then used as the initial vector for the next iteration, Eq. (2.161).

One has a very convenient estimate of the error, i.e., the difference between the propagated and exact wave-functions, when using the Lanczos integrator. This error is proportional to the magnitude of the first vector, V_K, lying outside of the Krylov space used [125]. This quantity can be used to adjust either the time-step size Δt or the maximum order K allowed. Since in all the time-dependent calculations reported in this thesis the Hamiltonian of the system is time-dependent, restrictions on the size of Δt can be important. All the results presented in this thesis have been obtained using a value, for both the time-step Δt and the maximum Krylov space dimension allowed K, at which the convergence of the calculated physical quantities has been achieved.

From the computational point of view this complex version of the Lanczos scheme is obviously more time consuming with respect to the Hermitian version, since in addition to the diagonalisation of the reduced Hamiltonian, in this case an upper Hessenberg matrix, one needs to perform an inversion of its eigenvector matrix, Z, which is now not unitary. Nevertheless, for non-Hermitian cases the Lanczos-Arnoldi algorithm appears to be very efficient.

The most important feature of the Arnoldi-Lanczos algorithm is that, when computing the tridiagonal matrix H_K, the full Hamiltonian matrix H is needed only for a simple matrix vector product and remains unchanged during the whole procedure. This allows the treatment of dynamical problems in which the size of the resulting system Hamiltonian is relatively large, for which the full diagonalisation is either very expensive or even impossible.

The time propagation can be performed representing the operators matrices both in the ECO-CES configuration basis set or in the Hamiltonian eigenvectors basis set. In the second scheme, after the Hamiltonian has been diagonalised, the dipole and CAP matrices are transformed to their representations in the basis of the Hamiltonian eigenvectors through the following formula:

$$D_{eigen} = Z^{\dagger} D_{ECO-CES} Z \,, \tag{2.170}$$

$$CAP_{eigen} = Z^{\dagger} CAP_{ECO-CES} Z \,, \tag{2.171}$$

where Z is the matrix of eigenvectors of the Hamiltonian.

The main advantages of this approach are that the dense Hamiltonian matrices do not have to be stored anymore, reducing the dynamical memory requirements of the calculation. However the CAP matrices will generally become dense and therefore will need to be fully stored. The second advantage of this scheme is that the basis states immediately have a clearer physical interpretation. Indeed, it becomes easier to calculate the rate of ionisation caused by the laser pulse, just by looking at the population of the bound eigenstates of the system at the end of the pulse. Therefore, it is not necessary to wait for all the outgoing ionised wavepacket to be absorbed by the CAP and to look at the resulting loss of norm of the wave-function, as is the case for the first scheme. However, the full diagonalisation can be performed with reasonable expense only for relatively small basis sets.

In order to guarantee the convergence of the Arnoldi-Lanczos algorithm, which depends crucially on the spectral radius of the Hamiltonian, in the first propagation scheme we removed from the numerical simulation the ECO-CES configurations with a zeroth-order energy higher than a certain threshold value. In an analogous way, in the second propagation scheme the unphysical high energy eigenstates have been removed from the prop-

agation. The threshold value for the cutoff energy which has been used in the calculations performed in this thesis is 40 a.u.; with this choice the Arnoldi-Lanczos algortihm converges well at each time step and, moreover, the removal of these high energy virtual orbitals does not change at all the physical results we are looking at.

2.9. High harmonic generation (HHG) spectrum

One of the observables that is calculated in this thesis is the high-order harmonic generation spectrum of atoms (Ar) and molecules (CO_2). High-order harmonic generation (HHG) spectroscopy has become a powerful tool to resolve ultrafast electron dynamics in atoms and molecules [126, 127] and also to investigate the geometric structure of molecules on an ultrafast time scale [128, 129, 130, 131, 132, 133, 60]. HHG occurs when an electron is removed from the parent molecule under the action of an intense infra-red (IR) laser field and is forced to recollide with the parent ion less than one period of the field oscillations later. High-harmonic generation can be described by the widely used three-step model [126]. The HHG process begins with strong-field ionisation, in which a high-intensity ($\approx 10^{14}$ W/cm^2) linearly polarised laser field distorts the molecular potential such that a portion of the bound electron wavepacket can tunnel-ionise. When an intense laser pulse ionises a molecule, its wave-function splits into two components: a free electron wavepacket and its associated ion, and the neutral molecule. The laser field pushes the liberated electron away from the ion and then drives it back [126]. There, if it has not drifted too far away from the parent ion, the electron can recombine with the ion, reforming the neutral molecule in its original state and producing coherent radiation in the form of high order harmonics of the incident light. The coherence in this quantum process comes from the fact that the final state of the system is the same as the initial one. The emission of radiation results from the recombination of an electron and a molecular ion and thus constitutes an inverse photoionisation process. Consequently, it is highly sensitive to the electronic structure of the target with the advantage that a broad range of photoelectron energies are probed simultaneously [134, 135, 136]. Moreover, different states of the molecular ion between ionisation and recombination provide different channels for this process. For each channel, specific elec-

tronic structure is encoded onto the harmonic amplitude and phase. These channels are different pathways that take the system from the same initial to the same final state via different states of the ion. They provide a basis for recording multielectron dynamics, including dynamics of electron rearrangement upon ionisation. Since the technique can be combined with nonadiabatic alignment, measurements can be performed in the molecular frame, revealing the detailed electronic structure of molecules [137]. High time resolution arises from the fact that different harmonics are emitted at different time-delays between ionisation and recombination, within a fraction of a laser cycle [131, 132, 133, 138, 139, 140]. Within the single-molecule response, several so-called 'quantum' trajectories of the liberated electron that return to the parent ion with the same kinetic energy but at different times t can be identified, see e.g. [141]. These trajectories can be grouped into 'short' and 'long', depending on whether they return to the parent ion before or after the highest-energy trajectory with the energy $3.17U_p$. Here $U_p = \frac{E^2}{4\omega^2}$ is the average electron oscillation energy, E and ω are the laser field strength and frequency [141]. The harmonic cutoff is determined by the maximum recollision energy of the ionised electron plus the ionisation potential I_p [68]:

$$\Omega_{\text{cutoff}} = 3.17U_p + 1.32I_p \tag{2.172}$$

Here $3.17U_p$ is the maximum energy that the liberated electron can gain between the ionisation and the recollision events [126]. The additional energy $0.32I_p$ is picked up by the returning electron in the strong-field regime, due to the offset of the point of tunnel ionisation from the origin of the Coulomb potential [68].

In this thesis, in order to compute the dipole acceleration which is required for describing high-harmonic generation, we first calculate the expectation value of the electric dipole moment $z(t)$ [142] and then we calculate its second time derivative. The HHG spectrum then reads

$$S_{\text{HHG}}(\omega) = \frac{1}{20}\frac{1}{3\pi c^3}\left|\int_{-\infty}^{\infty}\left[\frac{d^2}{dt^2}\langle z\rangle(t)\right]e^{-i\omega t}\,dt\right|^2 . \tag{2.173}$$

This quantity takes into account the contributions to the HHG spectrum from both the short and long trajectories, including the interference be-

tween the two. Differently, in a molecular gas macroscopic propagation of harmonic radiation associated with short and long trajectories is different in terms of both the phase-matching (which allows the harmonic field emitted from different molecules in the gas to sum coherently) and the divergence. In typical experiments on high harmonic generation, the geometry of the experimental setup suppresses the so-called 'long' trajectories and favours the short ones.

The expectation value of the electric dipole moment $z(t)$, as well as the one of any single-particle operator $\hat{O}$, onto the time-dependent wave-function of the system is calculated using the expansion of Eq. (2.155) and reads

$$\langle \hat{O} \rangle(t) = \sum_n \sum_m C_n(t) C_m^*(t) O_{m,n} \,. \tag{2.174}$$

The coefficients C_0 and C_n are known from the time propagation calculation. The matrices $O_{m,n}$ in the ECO-CES representation, as well as the transition moments from the ground state of the system to the ECO-CES states themselves, are evaluated consistently at the same level of the ADC(n) hierarchy as the one used to time propagate the state of the system.

2.10. Reduced ionic density matrix (R-IDM)

Another important quantity that is calculated in this work is the reduced ionic density matrix (R-IDM). Consider two systems A and B, with respective Hilbert spaces H_A and H_B. The Hilbert space of the composite system is defined as the tensor product

$$H_A \otimes H_B \,. \tag{2.175}$$

Denoting the state of the composite system AB by

$$\mid \Psi \rangle \in H_A \otimes H_B \,, \tag{2.176}$$

its density matrix $\hat{\rho}_{AB}$ is defined as the projection operator onto the state $\mid \Psi \rangle$ and reads as

$$\hat{\rho}_{AB} = \mid \Psi \rangle \, \langle \Psi \mid \,. \tag{2.177}$$

In general there is no way to associate a pure state with each component

subsystem A and B. However, it is possible to describe each subsystem with a reduced density matrix. The reduced density matrix of subsystem A, $\hat{\rho}_A$, is defined as the partial trace of ρ_{AB} over the basis states of system B:

$$\hat{\rho}_A \overset{\text{def}}{=} \sum_j \langle j \mid_B (\mid \Psi\rangle\langle\Psi \mid) \mid j\rangle_B = \mathrm{Tr}_B\, \hat{\rho}_{AB} \tag{2.178}$$

where the operator Tr_B represents the partial trace over system B. The reduced density matrix for an entangled pure ensemble is a mixed ensemble. On the other hand, if A and B are two distinct and independent systems, their total pure product state can be written as $\mid \Psi\rangle = \mid \psi\rangle_A \otimes \mid \phi\rangle_B$ and consequently, the density matrix of the composite system reads as

$$\hat{\rho}_{AB} = \hat{\rho}_A \otimes \hat{\rho}_B\,. \tag{2.179}$$

In this case the reduced density matrix of the A subsystem becomes

$$\hat{\rho}_A = \mid \psi\rangle_A\langle\psi \mid_A \tag{2.180}$$

and it is therefore possible to associate a pure state $\mid \psi\rangle_A$ to the subsystem A.

In the case where the two subsystems consist of a parent ion and a photoelectron, the time-dependent reduced ionic density matrix (R-IDM) $\rho^{Ionic}(t)$ is therefore constructed from the time-dependent N-electron state $\mid \Psi(t)\rangle$, by taking the trace of the total density matrix for the N-electron system

$$\hat{\rho}(t) = \mid \Psi(t)\rangle\langle\Psi(t) \mid \tag{2.181}$$

over the unobserved photoelectron:

$$\rho^{Ionic}(t) = Tr_a[\hat{\rho}(t)], \tag{2.182}$$

where Tr_a stands for the trace over all virtual orbitals.

Within the ADC(1) framework, where only explicit single excitations are allowed, $\rho^{Ionic}(t)$ can be espressed as

$$[\rho^{Ionic}(t)]_{i,j} = \sum_a \langle \tilde{\Phi}_i^a \mid \Psi(t)\rangle\langle\Psi(t) \mid \tilde{\Phi}_j^a\rangle = \sum_a C_i^a(t)[C_j^a(t)]^*\,. \tag{2.183}$$

The R-IDM diagonal matrix elements $\rho_{i,i}^{Ionic}$, $\rho_{j,j}^{Ionic}$ give the populations of the ionic states i and j respectively. Knowledge of the time dependence of these diagonal matrix elements reveals, for example, which ionic channels are populated during the interaction of a molecule with an intense IR laser pulse and therefore contribute more to the High-order Harmonic Generation process. Moreover they provide information about the nature of the ionic states populated after the end of the pulse.

The degree of coherence between the created hole states i and j is given by

$$G_{i,j}(t) = \frac{\mid \rho^{Ionic}(t)_{i,j} \mid}{\sqrt{\rho^{Ionic}(t)_{i,i}\rho^{Ionic}(t)_{j,j}}}\,. \tag{2.184}$$

Totally incoherent statistical mixtures result in $G_{i,j}(t) = 0$. The maximum achievable (perfect) coherence is given by $G_{i,j}(t) = 1$. Knowledge of the off-diagonal matrix elements $\rho^{Ionic}(t)_{i,j}$, gives quantitative information on the coherence degree $G_{i,j}(t)$ between pairs of final ionic channels i and j formed during the ionisation of the molecular system by the laser field and consequently reveals the coherence properties associated with the electronic wavepacket dynamics of the residual ion.

As we are interested in looking for the probability of ionising the system and to form ionic species, the bound excited part of the wave-function must be removed from the total wave-function before the trace is computed. This means that formally the formulas remain the same, but the coefficients on the single excited ECO-CES states, C_i^a, must now refer only to the ionised part of the wave-function:

$$\mid \Psi(t)^{ionised}\rangle = \mid \Psi(t)\rangle - \sum_n \langle \Psi_n^{bound} \mid \Psi(t)\rangle \mid \Psi_n^{bound}\rangle. \tag{2.185}$$

In the strong field regime the bound state excitation of the system is usually much smaller and negligible with respect to its ionisation; therefore this modification has a very small (negligible) effect onto the resulting R-IDM diagonal matrix elements. However the off-diagonal matrix elements can be very sensitive to the presence of a bound state component in the total wave-function; this is due to the fact that, in the bound excited states, the excited electron remains close to the ion causing the coherence factor to continue oscillating even a long time after the interaction of the system with the laser pulse is over.

The presence of the CAP has an impact on the dynamics of the reduced ionic density matrix. Indeed, the norm $\langle \Psi(t) \mid \Psi(t) \rangle = Tr[\hat{\rho}(t)]$ is not conserved, and this reflects itself into a modification of the evolution of the trace of the density matrix. With the introduction of a CAP the norm of the density matrix experiences a decay and, since the probabilities of leaving the atom in its ground state $\mid C_0(t) \mid^2$ and of creating 1h-1p excitations should add up to one at all times, $\rho^{Ionic}(t)$ must be corrected for the loss of norm.

The corrected ionic reduced density matrix that does not experience any damping has been calculated in [143] and reads

$$\rho_{i,j}^{Ionic}(t) = \sum_a C_i^a(t)[C_j^a(t)]^* +$$

$$+2e^{i(\epsilon_i - \epsilon_j)t} \int_{-\infty}^{t} \sum_{a,b} w_{b,a} C_i^a(t')[C_j^b(t')]^* e^{-i(\epsilon_i - \epsilon_j)t'} dt' \tag{2.186}$$

where ϵ_i and ϵ_j are the ionisation potentials of the ionic state i and j respectively.

Notice that the additional term on the right-hand side of Eq. (2.186) is not modified at all by the subtraction of the bound part of the wave-function as this part does not experience any loss of norm if the CAP starts sufficiently far from the radial origin. This means that evaluating this term with the coefficients of the total wave-function or the ones of its ionised part gives exactly the same numerical result.

Part II.

Results

3. Total molecular ground state photoionisation cross-sections by ADC-Stieltjes-Lanczos method: GTO-based Benchmark calculations

The calculation of photoionisation cross-sections requires the knowledge of many-electron wave-functions belonging to the continuum part of the spectrum. The main task here is to accurately take into account both the scattering character of the photoionised state wave-function and the electron correlation. While many well-developed theoretical techniques exist for the description of atomic photoionisation [50], the multi-centre molecular problem still poses a formidable challenge to the theory. The state of the art theoretical methods for calculation of molecular photoionisation cross-sections either do not take into account sufficiently the electronic correlation, see e.g. Refs. [51], or treat the photoionisation continuum rather approximately, see e.g. Ref. [52]. Highly accurate many-electron wave-functions and transition matrix elements are routinely obtained by the post-Hartree-Fock (post-HF) methods of *ab-initio* quantum chemistry [49, 53, 54]. These methods are based on the use of finite sets of square-integrable (typically Gaussian) single-electron basis functions.

In the work reported in this Chapter finite sets of square-integrable GTOs have been used as single-electron basis functions. Hence the ADC-Lanczos-Stieltjes scheme is used to compute the photoionisation cross-sections and a systematic study of the accuracy of the new technique at the ADC(1), ADC(2) and ADC(2)x levels of *ab-initio* theory is presented using a test set of molecules for which accurate experimental total ionisation cross-sections are available.

Hence in these calculations the ADC Hamiltonian is treated using the iterative block-Lanczos diagonalisation and the resulting Lanczos pseudospectrum is then used in the SI procedure to compute photoionisation cross-section. It is important to emphasise again that studies such as the following would be impossible without exploiting the convergence properties of the Lanczos pseudospectrum.

The *ab-initio* description of the discretised photoionised molecular states is based on the ADC many-electron Green's function approach. A hierarchy of *ab-initio* methods of the ADC type [80] is used. Construction of the ADC Hamiltonian matrices requires carrying out restricted HF calculations and transforming the electron repulsion integrals from the atomic orbital (AO) basis to the molecular orbital (MO) basis. Throughout this work, these tasks are performed using MOLCAS 7.6 quantum chemical program package [144]. The standard Gaussian basis sets used in the present study have been obtained from Ref. [145]. Kaufmann-Baumeister-Jungen (KBJ) continuum-like diffuse Gaussian functions [100] are systematically used in each calculation to augment the standard basis sets, for a strictly necessary better representation of the discretised electronic continuum.

The calculated cross-sections have been restricted to the energy range of up to 100 eV, thus including valence-type excitations but excluding excitations of the core electrons [146]. The Stieltjes imaging procedure is carried out in quadruple precision using the algorithm of Sec. 2.5. The photoionisation cross-sections presented are obtained as interpolation of the discrete points corresponding to several (up to a maximum of five) successive Stieltjes orders for which approximate stationarity of the results is achieved. The interpolation procedure analyses the points generated by each Stieltjes order and finds which orders and how many satisfy this stationarity condition and then interpolates them alltogether. The converged and interpolated Stieltjes orders are different in each case and their number varies between 3 and 5; nonetheless, for all of the molecules studied in this thesis, the reliable Stieltjes orders are typically from $n = 5$ up to $n = 15$. This gives an idea of the number of principal representation states and the energy resolution it is possible to achieve with the method presented. For all systems correlation consistent basis sets of the cc-pCVnZ type have been used, with n=T or n=Q depending on the system and on the specific atom within the molecule.

Molecule	Basis set	22cmADC(2) matrix dimension	22cmKrylov space dimension
H_2O	25.7cmO:cc-pCVQZ+(10s10p4d); H:cc-pVQZ+(5s5p5d)	157653	3390
HF	25.7cmF:UN-cc-pCVQZ+(10s10p10d4f); H:UN-cc-pVQZ+(6s6p6d2f)	181236	3800
NH_3	25.7cmN:UN-cc-pCVTZ+(5s5p5d); H:UN-cc-pVTZ+(3s3p)	121376	3920
CH_4	25.7cmC:UN-cc-pCVQZ+(6s6p6d2f); H:UN-cc-pVTZ+(4s4p2d)	209682	3980
C_2H_2	25.7cmC:cc-pCVTZ+(10s10p10d4f); H:cc-pVTZ+(6s6p6d2f)	252025	3170
C_2H_4	25.7cmC:cc-pCVTZ+(7s10p10d4f); H:cc-pVTZ+(3s3p3d)	411931	3870
CH_3OH	25.7cmC,O:UN-cc-pCVTZ+(2s4p3d); H:UN-cc-pVTZ+(1s1p)	182194	3960
CO_2	25.7cmC,O:cc-pCVTZ+(5s6p6d2f)	391838	3920

Table 3.1.: The basis sets employed, the dimension of the ADC(2) matrices and the dimension of the Lanczos pseudospectrum space, for which the converged cross-section has been obtained, are reported for each molecule studied in this thesis.

3.1. Molecular photoionisation cross-sections by ADC-Lanczos-Stieltjes method

The accuracy of the method is established by comparing the ADC-Lanczos-Stieltjes cross-sections in the valence ionisation region to the experimental ones for a series of eight molecules of first row elements for which high-quality experimental cross-sections are available in the literature: HF, NH_3, H_2O, CO_2, H_2CO, CH_4, C_2H_2, and C_2H_4.

The deviation of the ADC-Lanczos-Stieltjes cross-sections from the experimental ones has been quantified computing their energy-dependent and energy-averaged relative discrepancies over the photon energy region covered. It is found that the inclusion of large Gaussian exponents for the accurate description of the localised core electrons can lead to a significant improvement in the cross-section. In some cases uncontracting the basis set leads to an improvement in the cross-section, while in other cases it did not make a substantial difference. For every molecule the convergence of the results of the spectral moments and of the cross-section, with respect to the choice of the details of the basis sets, i.e. with respect to the choice

of the number of KBJ exponents and the number of angular momenta in the cc-type basis set, has been checked; only the results obtained using the basis set at which the convergence has been achieved are reported in the following. In Table 3.1 a fully uncontracted basis set is denoted by the prefix UN.

Experimental total photoionisation cross-section as well as a series of SI results obtained via full diagonalisation of the ADC(1) matrix and block Lanczos diagonalisation of the ADC(2) and ADC(2)x matrices are reported in Figs. 3.1- 3.8 for the molecules considered. The basis set employed, as well as the dimension of the ADC(2) (x) matrices and that of the Lanczos pseudospectrum space for which the convergence in the cross-section has been obtained are reported in Table 3.1. Also average relative deviations are reported in Table 3.2.

3.1.1. Water

Fig. 3.1 shows the experimental total photoionisation cross section of the H_2O molecule as well as a series of Stieltjes imaging results obtained via full diagonalisation of the ADC(1) matrix and block-Lanczos diagonalisation of the ADC(2) and ADC(2)x Hamiltonian matrices.

The details of the calculations can be found in Table 3.1. One can see that the agreement between the experimental and the theoretical cross sections improves dramatically from ADC(1) to ADC(2) level, but not nearly as much when going from ADC(2) to the ADC(2)x level. The experimental measurement in [147] were perfomed using the dipole (e,2e) electron scattering technique, in the more recent [148] the dipole (e,e) spectroscopy technique has been used, while in [149] the cross-section is measured directly with photoabsorption techniques, by use of a double ionisation chamber. The ADC(2) and the ADC(2)x results essentially coincide with the newer experimental data [149, 148] (apart from the sharp feature at 15 eV), but show visible deviation from the older experimental results around 20-30 eV [147]. In Table 3.2 relative deviations of the theoretical results from the newer experimental data are cited.

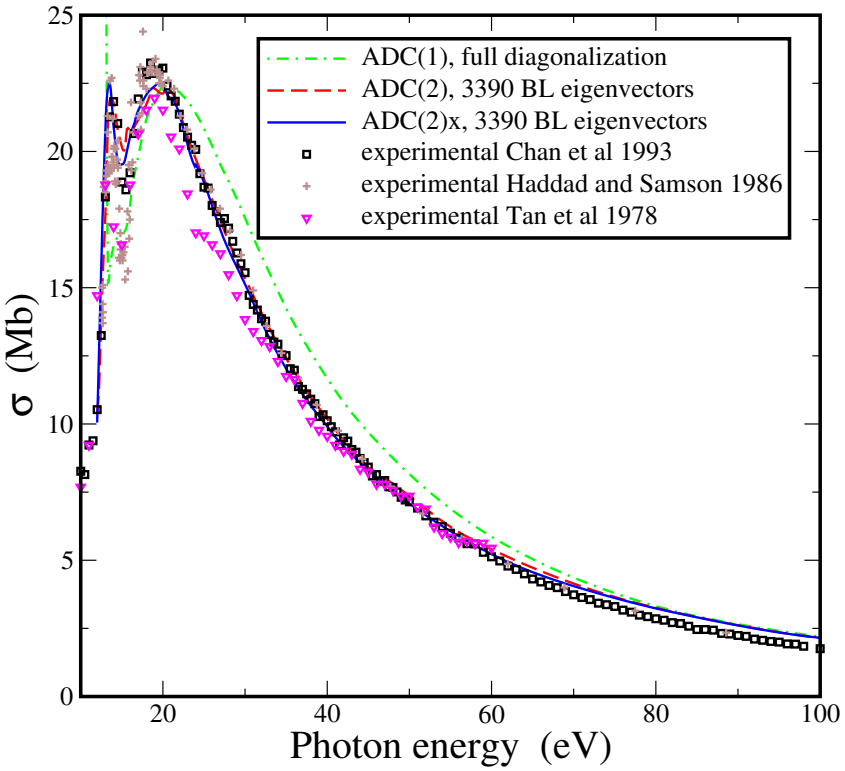

Figure 3.1.: Total photoionisation cross-section of H_2O. Triangles – experimental result of Ref. [147], crosses – experimental results of Ref. [149], squares – experimental result of Ref. [148], dashed-dotted line – ADC(1)-Stieltjes result, dashed line – ADC(2)-Lanczos-Stieltjes cross-section obtained using block-Lanczos pseudospectrum of 3390 eigenvalues and eigenvectors, full line – ADC(2)x-Lanczos-Stieltjes cross-section obtained using block-Lanczos pseudospectrum of 3390 eigenvalues and eigenvectors.

3.1.2. Hydrogen Fluoride

Fig. 3.2 shows the experimental total photoionisation cross section of the HF molecule as well as a series of Stieltjes imaging results obtained via full diagonalisation of the ADC(1) matrix and block-Lanczos diagonalisation of the ADC(2) and ADC(2)x Hamiltonian matrices. The details of the calculations can be found in Table 3.1. The most recent experimental result that is possible to find in the literature is from 1981 and the experimental method used in that work [150] is the magic-angle dipole (e,2e) spectroscopy technique. The theoretical ADC results reported here show that, although

ab-initio level	C_2H_4	C_2H_2	CH_4	CO_2	CH_2O	H_2O	HF	NH_3	average
ADC(1)	19.3 %	29.5 %	27.5 %	16.9 %	24.9 %	16.8 %	8.1 %	22.7 %	20.4 %
ADC(2)	15.8 %	18.6 %	22.5 %	7.3 %	17.5 %	7.9 %	7.2 %	19.0 %	14.0 %
ADC(2)x	12.4 %	14.6 %	17.7 %	7.3 %	16.4 %	7.8 %	7.6 %	17.6 %	12.1 %

Table 3.2.: Relative deviations of the ADC-Stieltjes photoionisation cross-sections from the experimental results across the energy range of ionisation threshold to 100 eV.

the higher-order schemes lead to a much improved peak position, they do not reproduce precisely the cross-section peak height and the cross-section shoulder above 40 eV (see Table 3.2 for the average relative deviations of the computed hydrogen fluoride cross-sections from the experimental one). However, these theoretical results are in good agreement with the previous theoretical multichannel random phase approximation (MC-RPA) results of Cacelli *et al.* [151]. This suggests a revision of the experimental cross-section for HF.

3.1.3. Ammonia

Fig. 3.3 shows the experimental total photoionisation cross section of the NH_3 molecule as well as a series of Stieltjes imaging results obtained via full diagonalisation of the ADC(1) matrix and block-Lanczos diagonalisation of the ADC(2) and ADC(2)x Hamiltonian matrices. The details of the calculations can be found in Table 3.1. As in the case of water and hydrogen fluoride, one can see that the agreement between the experimental and the theoretical cross sections improves with the order of the ADC scheme, with the difference between ADC(1) and ADC(2) being more critical than between ADC(2) and ADC(2)x. The experimental measurement in [152] were perfomed using the dipole (e,e) spectroscopy technique, while in [153] the cross-section is measured directly by use of a double ionisation chamber. Average relative deviations of the computed ammonia cross-sections from the experimental one [152] are given in Table 3.2. The main contribution to the deviation comes from the tail of the cross-section in the energy range above 60 eV.

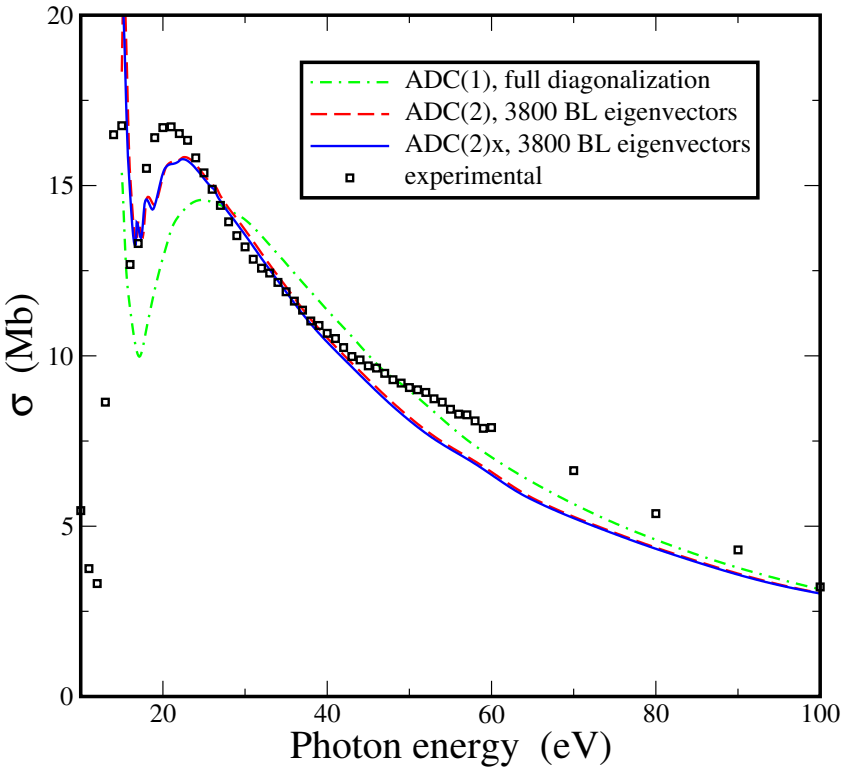

Figure 3.2.: Total photoionisation cross-section of HF. Squares – experimental result of Ref. [150], dashed-dotted line – ADC(1)-Stieltjes result, dashed line – ADC(2)-Lanczos-Stieltjes cross-section obtained using block-Lanczos pseudospectrum of 3800 eigenvalues and eigenvectors, full line – ADC(2)x-Lanczos-Stieltjes cross-section obtained using block-Lanczos pseudospectrum of 3800 eigenvalues and eigenvectors.

3.1.4. Methane

Fig. 3.4 shows the experimental total photoionisation cross section of the CH_4 molecule as well as a series of Stieltjes imaging results obtained via full diagonalisation of the ADC(1) matrix and block-Lanczos diagonalisation of the ADC(2) and ADC(2)x Hamiltonian matrices. The details of the calculations can be found in Table 3.1. The experimental measurement in [154] were perfomed using the dipole (e,e) spectroscopy technique. One can see that the agreement between the experimental and the theoretical cross sections improves with the order of the ADC scheme. The highest-order ADC(2)x result essentially coincides with the experimental one apart from

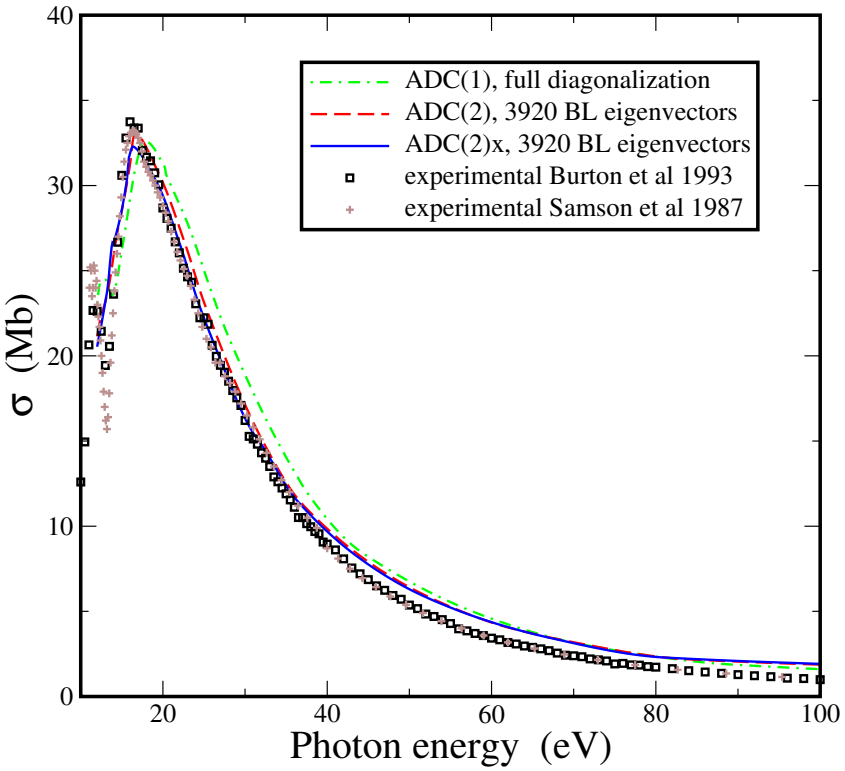

Figure 3.3.: Total photoionisation cross-section of NH_3. Squares – experimental result of Ref. [153], crosses – experimental result of Ref. [152] dashed-dotted line – ADC(1)-Stieltjes result, dashed line – ADC(2)-Lanczos-Stieltjes cross-section obtained using block-Lanczos pseudospectrum of 3920 eigenvalues and eigenvectors, full line – ADC(2)x-Lanczos-Stieltjes cross-section obtained using block-Lanczos pseudospectrum of 3920 eigenvalues and eigenvectors.

the value at the peak that is underestimated by about 5 Mb. This underestimation of the maximum height of the peak is characteristic to some degree of the computed photoabsorption cross-sections of acetylene and ethylene (see below). Average relative deviations of the computed methane cross-sections from the experimental one are given in Table 3.2.

3.1.5. Acetylene

Fig. 3.5 shows the experimental total photoionisation cross section of the C_2H_2 molecule as well as a series of Stieltjes imaging results obtained via

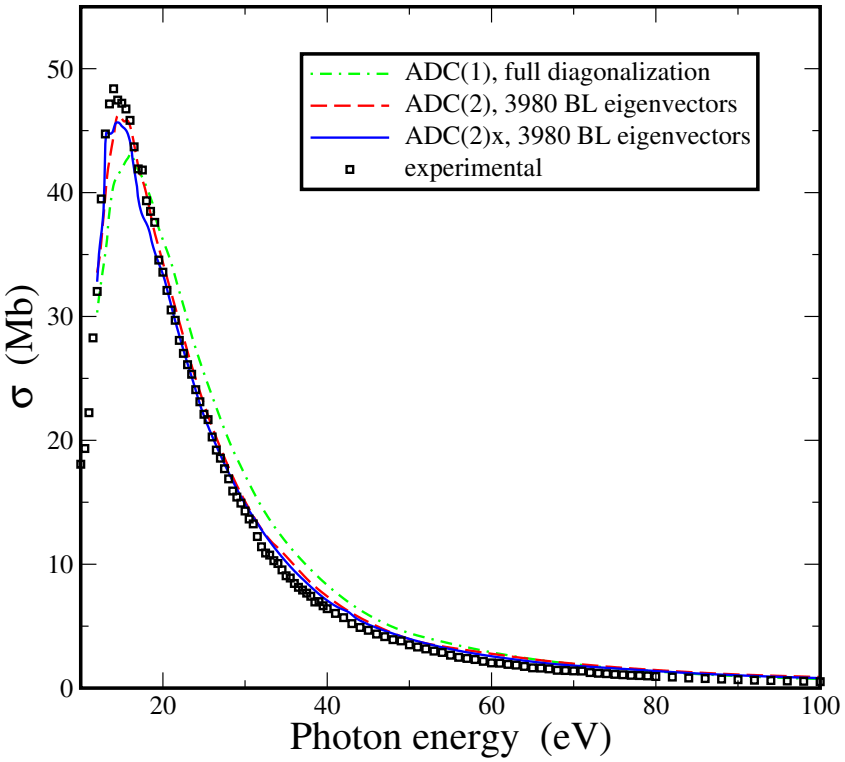

Figure 3.4.: Total photoionisation cross-section of CH_4. Squares – experimental result of Ref. [154], dashed-dotted line – ADC(1)-Stieltjes result, dashed line – ADC(2)-Lanczos-Stieltjes cross-section obtained using block-Lanczos pseudospectrum of 3980 eigenvalues and eigenvectors, full line – ADC(2)x-Lanczos-Stieltjes cross-section obtained using block-Lanczos pseudospectrum of 3980 eigenvalues and eigenvectors

full diagonalisation of the ADC(1) matrix and block-Lanczos diagonalisation of the ADC(2) and ADC(2)x Hamiltonian matrices. The details of the calculations can be found in Table 3.1. Acetylene photoionisation has been well studied theoretically, in particular sharp resonance features in the fixed-geometry valence cross-sections have been revealed [155]. The limited resolution of the SI procedure does not allow one to reproduce such fine structures, however due to vibrational broadening the experimental values can be directly compared to the SI results. Among the available experimental data, the most recent and extended set has been reported by Cooper *et al.* [156], who deduced it using dipole (e,e) and (e, e-ion) spectroscopies and these data have been choosen to compare the theoretical cross-section with.

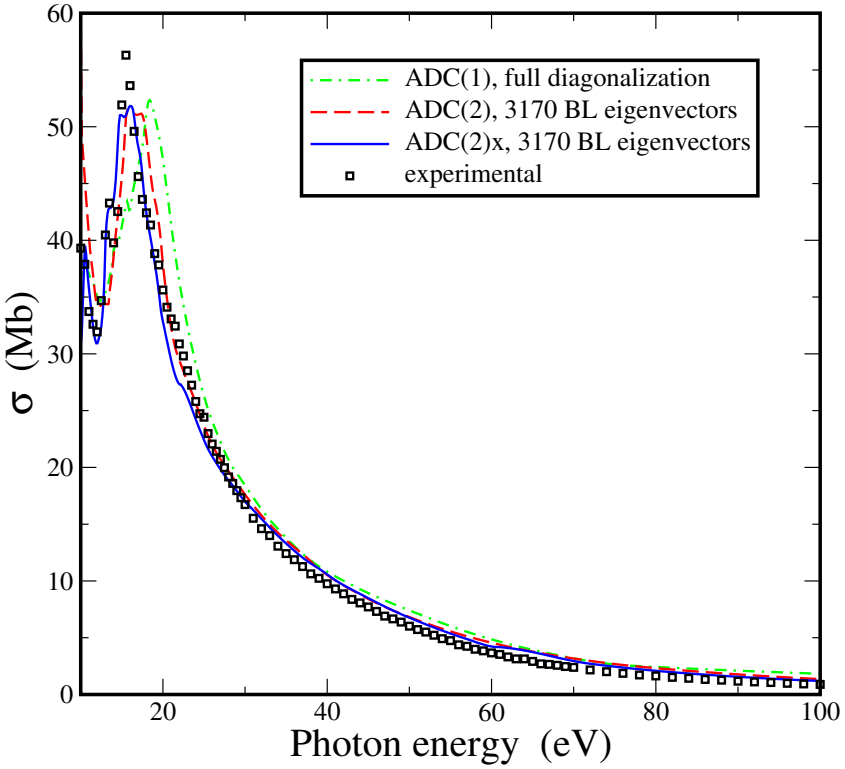

Figure 3.5.: Total photoionisation cross-section of C_2H_2. Squares – experimental results of Ref. [156], dashed-dotted line – ADC(1)-Stieltjes result, dashed line – ADC(2)-Lanczos-Stieltjes cross-section obtained using block-Lanczos pseudospectrum of 3170 eigenvalues and eigenvectors, full line – ADC(2)x-Lanczos-Stieltjes cross-section obtained using block-Lanczos pseudospectrum of 3170 eigenvalues and eigenvectors.

The same experimental method has been used by Cooper *et al.* to measure the photoabsorption cross-sections of ethylene and methane. One can see that the agreement between the experimental and the theoretical cross sections improves with the order of the ADC scheme. In particular, the position of the cross-section main peak at 15.5 eV is reproduced essentially exactly by the ADC(2)x scheme. The height of the peak is smaller with respect to the experimental measured value, being underestimated by about 5 Mb as in the case for methane. This difference is due to the energy resolution of the SI procedure. For the same reason also the double hump structure in the energy region between 13 eV and 16 eV is only aprroximately reproduced by

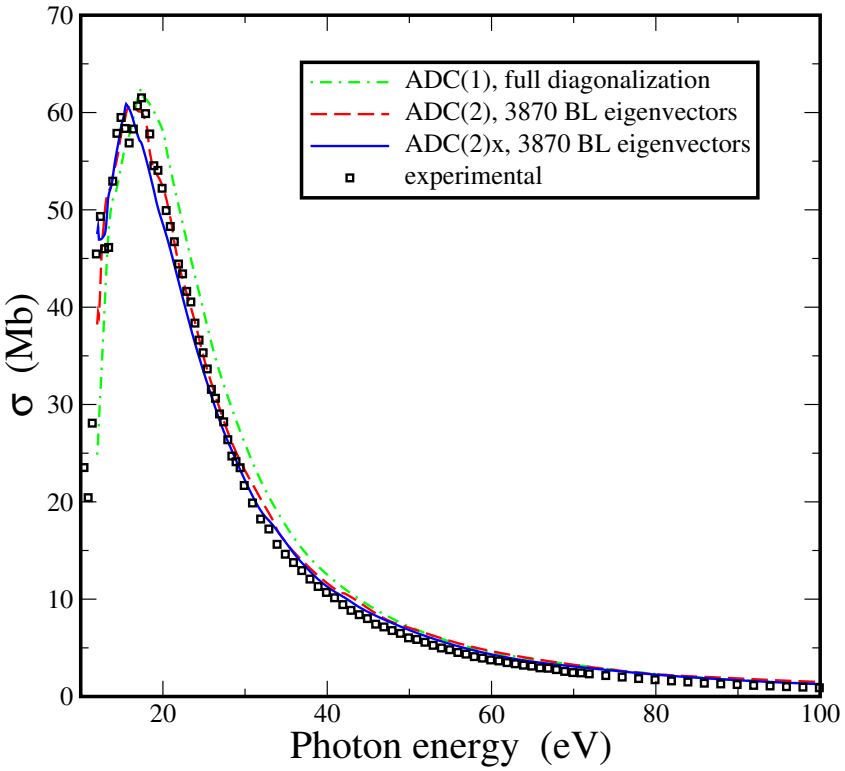

Figure 3.6.: Total photoionisation cross section of C_2H_4. Squares – experimental results of Ref. [157], dashed-dotted line – ADC(1)-Stieltjes result, dashed line – ADC(2)-Lanczos-Stieltjes cross-section obtained using block-Lanczos pseudospectrum of 3870 eigenvalues and eigenvectors; full line – ADC(2)x-Lanczos-Stieltjes cross-section obtained using block-Lanczos pseudospectrum of 3870 eigenvalues and eigenvectors.

the SI cross-section presented here, resulting in a small shoulder at 13 eV. Average relative deviations of the computed acetylene cross-sections from the experimental one are given in Table 3.2.

3.1.6. Ethylene

Fig. 3.6 shows the experimental total photoionisation cross section of the ethylene molecule as well as a series of Stieltjes imaging results obtained via full diagonalisation of the ADC(1) matrix and block-Lanczos diagonalisation of the ADC(2) and ADC(2)x Hamiltonian matrices. The details of the calculations can be found in Table 3.1. The experimental measurement in

[157] were perfomed using the dipole (e,e) spectroscopy technique. One can see that the agreement between the experimental and the theoretical cross sections improves significantly from the ADC(1) to the ADC(2) scheme. The highest-order ADC(2)x result, while more accurate in the tail region from 30 eV to 100 eV, does not improve the agreement with the experimental one in the main peak region. As in the case of acetylene, also the ethylene cross-section exhibit a sharp double hump structure in the energy region around 18 eV at the top of the peak, which is missed by both ADC(2) and ADC(2)x and is attributed to the resolution of the SI. On the contrary, the maximum value of the measured cross-section (≈ 61 Mb) is better reproduced, comparing to methane and acetylene. Average relative deviations of the computed ethylene cross-sections from the experimental one are given in Table 3.2.

3.1.7. Formaldehyde

Fig. 3.7 shows the experimental total photoionisation cross section of the H_2CO molecule as well as a series of Stieltjes imaging results obtained via full diagonalisation of the ADC(1) matrix and block-Lanczos diagonalisation of the ADC(2) and ADC(2)x Hamiltonian matrices. The details of the calculations can be found in Table 3.1. The experimental measurement in [158] were perfomed using the dipole (e,e) spectroscopy technique. One can see that the agreement between the experimental and the theoretical cross sections improves with the order of the ADC scheme. Both ADC(2) and ADC(2)x methods struggle to reproduce the very sharp peak near 13 eV and the structure of the main peak at 18-20 eV, but give a better representation of the tail of the cross-section than the ADC(1) result. Average relative deviations of the computed formaldehyde cross-sections from the experimental one are given in Table 3.2. As in the case of ammonia, the main contribution to the average deviation comes from the tail of the cross-section, in the energy range above 30 eV.

3.1.8. Carbon Dioxide

Fig. 3.8 shows the experimental total photoionisation cross section of the CO_2 molecule as well as a series of Stieltjes imaging results obtained via full diagonalisation of the ADC(1) matrix and block-Lanczos diagonalisation

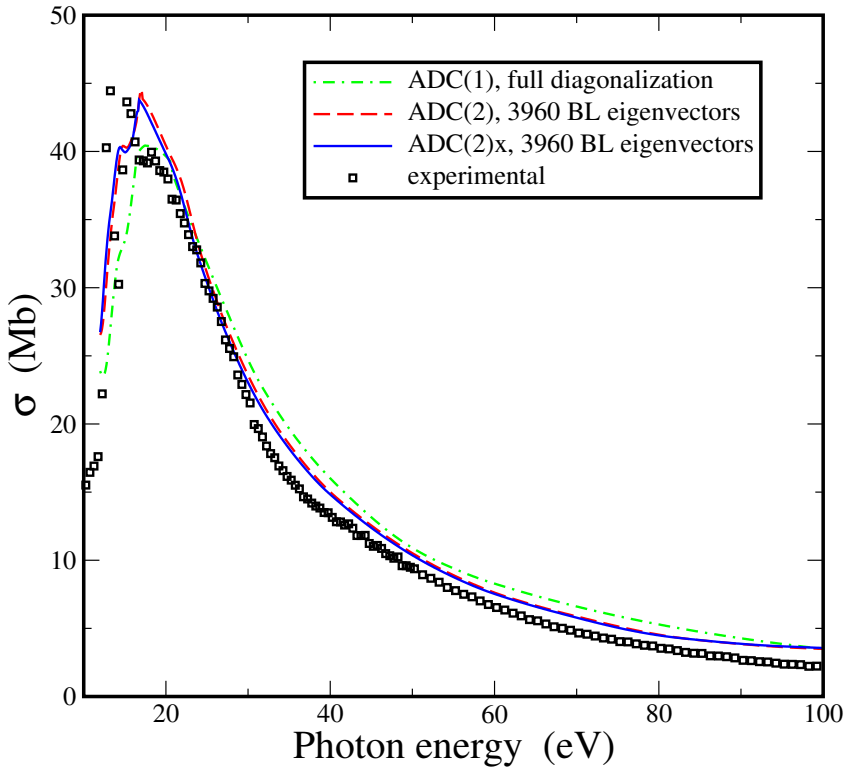

Figure 3.7.: Total photoionisation cross-section of CH_2O. Squares – experimental result of Ref. [158], Dashed-dotted line – ADC(1)-Stieltjes result, dashed line – ADC(2)-Lanczos-Stieltjes cross-section obtained using block-Lanczos pseudospectrum of 3960 eigenvalues and eigenvectors, full line – ADC(2)x-Lanczos-Stieltjes cross-section obtained using block-Lanczos pseudospectrum of 3960 eigenvalues and eigenvectors.

of the ADC(2) and ADC(2)x Hamiltonian matrices. The details of the calculations can be found in Table 3.1. The experimental measurement in [159] were perfomed using the dipole (e,e) spectroscopy technique. One can see that the agreement between the experimental and the theoretical cross sections improves with the order of the ADC scheme. The double narrow peak at near 20 eV is reproduced by Stieltjes imaging as a single peak. The main difference between the ADC(2) and ADC(2)x results is in the region of the cross-section minimum that is described more accurately by the ADC(2)x scheme.

Finally, the oscillations present in the experimental cross section in the

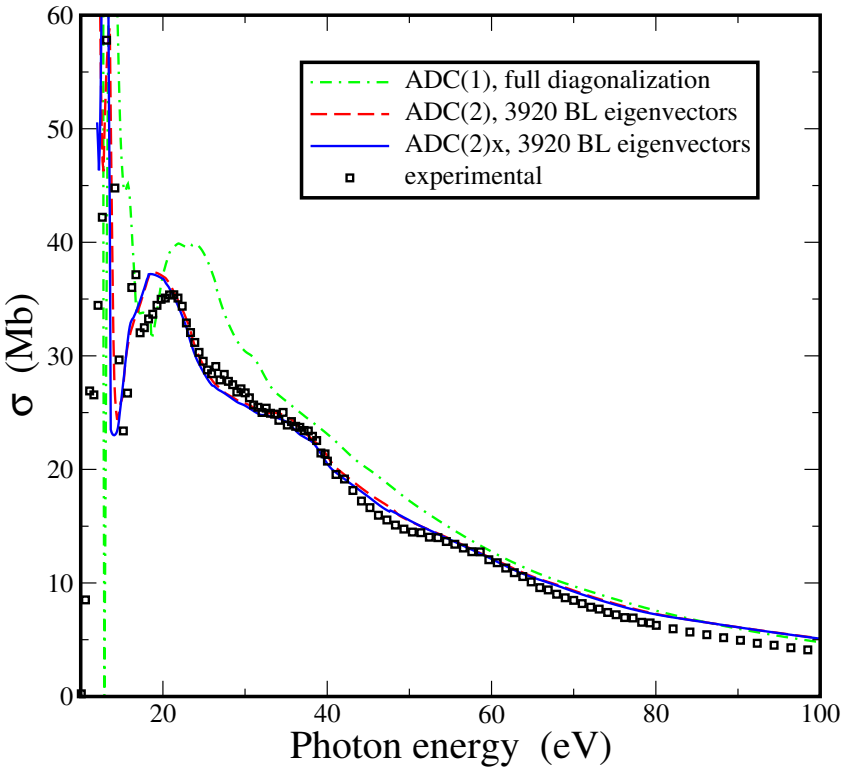

Figure 3.8.: Total photoionisation cross-section of CO_2. Squares – experimental result of Ref. [159], Dashed-dotted line – ADC(1)-Stieltjes result, dashed line – ADC(2)-Lanczos-Stieltjes cross-section obtained using block-Lanczos pseudospectrum of 3920 eigenvalues and eigenvectors, full line – ADC(2)x-Lanczos-Stieltjes cross-section obtained using block-Lanczos pseudospectrum of 3920 eigenvalues and eigenvectors.

30-60 eV range are missed completely by the ADC(1) result and they are not yet fully reproduced by the second order ADC(2) and ADC(2)x SI results. More specifically it is possible to abserve that the first plateau around 35 eV is well reproduced by both second order methods, while the second one at 55 eV is not. This is due to the low resolution of the converged Stieltjes orders, interpolated to obtain the cross-sections, in the 45-65 eV energy range. Average relative deviations of the computed carbon dioxide cross-sections from the experimental one are given in Table 3.2.

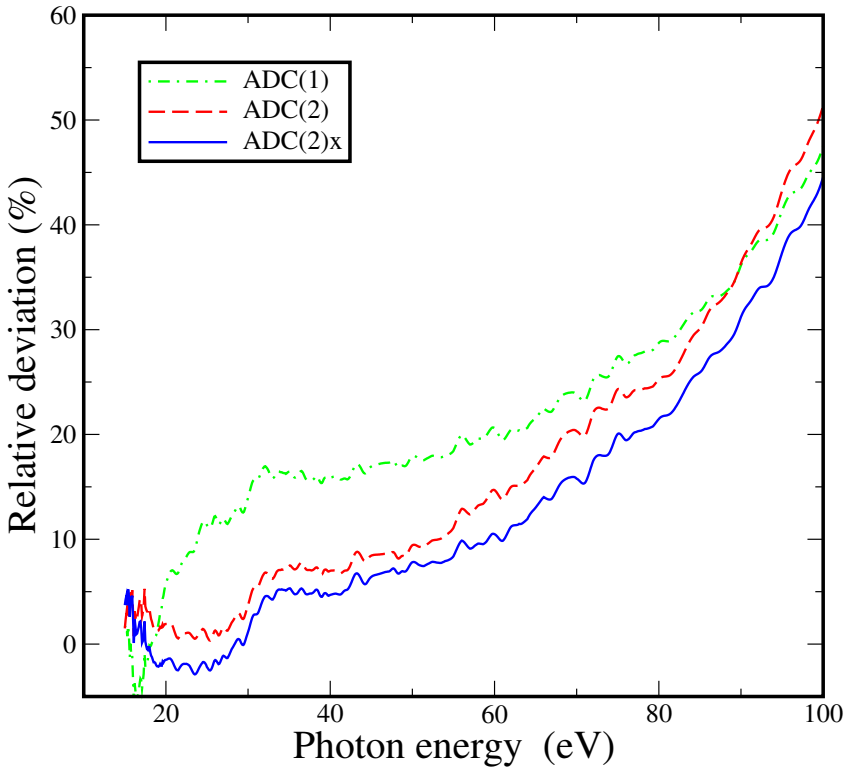

Figure 3.9.: Relative deviations of the ADC-Stieltjes photoionisation cross-sections from the experimental results averaged on the eight molecules calculated, as a function of the energy in the energy range of ionisation threshold to 100 eV. Dashed-dotted line – ADC(1)-Stieltjes result, dashed line – ADC(2)-Lanczos-Stieltjes cross-section, full line – ADC(2)x-Lanczos-Stieltjes cross-section.

3.2. Summary

Stieltjes imaging has been long established as an efficient way of calculation of total photoionisation cross-sections using discretised continuum pseudospectra of the final states. However, the accuracy of this technique is limited by both the ability of the chosen $\mathcal{L}^2$ basis set to represent continuum functions within the interaction volume and the numerical instability of the computational algorithm of the Stieltjes-Chebyshev moment theory. In view of these limitations, it could be doubted that improving the many-body theoretical description of the ionised system leads to significantly better cross-sections justifying the required higher numerical effort. Indeed,

the resulting difference in the calculated cross-sections might fall within the margins of the inaccuracy incurred by the basis set and the Stieltjes imaging procedure. The first results on ADC-Lanczos-Stieltjes method presented [104], indicated that this is actually not the case and full inclusion of double electronic excitations does lead to more accurate Stieltjes imaging cross-sections. However, the initial work dealt only with two atomic and one molecular system. In the present work, it has been shown beyond doubt that the trend seen in Ref. [104] is characteristic of molecules of first row atoms in the valence energy region. Within the specific family of post-HF many-electron methods used here (ADC), ADC(2) leads to clear, substantial improvement over the single-excitation ADC(1) theory for all molecules considered, while for some of them, even a more demanding ADC(2)x level of theory leads to better agreement with the available experimental data (see Table 3.2). On average, the precision gain achieved with ADC(2)x relative to ADC(2) in the considered energy window (from ionisation threshold up to 100 eV) is about twice smaller than the precision gain of ADC(2) relative to the single-excitation ADC(1) method.

It is instructive to analyse the relative deviations of the three *ab-initio* methods as function of photon energy (Fig. 3.9). Indeed, one observes that below 60 eV both ADC(2) and ADC(2)x methods lead to impressive agreement with experiment with the relative deviations below 10%. At higher photon energies inaccuracy of all the ADC schemes grows reaching 20% level around 80 eV. Since this behaviour does not does not depend on the level of *ab-initio* theory, it is concluded that it has to do with the limitations of the Gaussian single-electron basis sets.

The present work establishes the ADC-Lanczos-Stieltjes method as an efficient and reasonably accurate technique for molecular cross-sections in the valence region. Indeed, even within an unoptimised straightforward implementation of the method on the Intel Core i7-2600 processor, typical CPU time required for the cross-section calculations presented here is of the order of a few hours.

4. Total photoionisation cross-sections of molecular excited electronic states by algebraic diagrammatic construction-Stieltjes-Lanczos method

Photoionisation cross-sections from atoms and molecules in their electronic ground states have been widely studied and described in numerous experimental and theoretical works [50, 147, 149, 150, 151, 153, 152, 154, 155, 156, 157, 158, 159, 160]. On the other hand, experimental characterization of photoionisation processes starting from electronically bound excited states can be very demanding since the initial states in this case are usually unstable and their lifetime due to radiative [161] or non-radiative decay (vibrational relaxation of the excited electronic state to lower energy electronic states due to vibronic coupling, e.g. at conical intersections) [162] varies from nanoseconds to a few tens of femtoseconds respectively. Experimental measurements of total photoabsorption cross-sections of electronically excited systems are scarce and mostly concentrate on near-threshold atomic photoabsorption as well as do the theoretical calculations [163]. Recently, however, due to the advent of ultrashort laser sources in few-femtosecond and attosecond domains [19], it has become possible to perform pump-probe experiments with time resolution fully sufficient to "look inside" the shortest lifetimes of the molecular excited states [20]. This development opens the possibility of studying coherent electron dynamics in microscopic systems on its natural few-femtosecond or sub-femtosecond time-scale. A basic pump-probe experiment of such kind would consist of an excitation of a molecule

with a short pump pulse to form an electronic wavepacket of the ground and a series of excited states, which is probed with a delayed ionising XUV pulse. Broad-band XUV absorption by such a wavepacket is governed by interfering ionisations from distinct bound states into the same continuum state. As a result, the ionic yield (or the transient absorption strength) shows modulation as a function of the pump-probe pulses time delay, allowing one to follow the wavepacket dynamics. Very recently, an experiment of such kind has been indeed performed [164], and the interpretation of the experimental results was given using the time-dependent density functional theory (TDDFT). Modelling the pump-probe experiments of the type of Ref. [164] requires phase information for the description of interference between the excitation-ionisation pathways and cannot be achieved using cross-sections. However, calculation of cross-sections of the plausible intermediate (excited) states of these schemes can teach us a lot about the level of the *ab-initio* description required for the full modelling. To this end, in the present Chapter, the $\mathcal{L}^2$ *ab-initio* ADC-Lanczos-Stieltjes method for the molecular ground-state total photoionisation cross-section is extended to the calculation of photoionisation cross-sections of molecular electronically excited states [165] using the intermediate state representation (ISR) of the dipole operator in the ADC many-electron basis set in order to compute the dipole transition moments between the excited states of the molecule. The comparison between the results obtained using different levels of the many-body theory, i.e. ADC(1), ADC(2) and ADC(2)x is shown for the first two singlet excited states of CO, N_2 and H_2O both at the ground state and the excited state equilibrium nuclear geometries.

4.1. ADC-Lanczos-Stieltjes Photoionisation cross-sections of molecular excited states: application to H_2O, N_2 and CO.

The basic computational details of excited state cross-section calculations are analogous to the ones for the ground-state photoionisation calculations described in the previous Chapter. However, here the computational procedure presents some differences: it consists of building the ADC Hamiltonian matrix in the symmetry space to which the initial state belongs; block-

Davidson diagonalisation of the initial Hamiltonian to obtain the eigenvector of the initial state; construction of the ADC Hamiltonian matrix for the dipole-allowed final symmetry space; and finally the block-Lanczos diagonalisation to obtain the final space pseudo-spectra. The transition dipole moments are obtained according to Eq. (2.104) by contracting on the fly the ISR dipole matrix with the fixed initial state eigenvector and the final Lanczos pseudospectrum eigenvectors.

The basic physical difference between the ground state and the excited state photoionisation becomes apparent if one considers these processes qualitatively as transitions between single electronic configurations within the frozen orbital approach (see Fig. 4.1). Indeed, applying the Slater-Condon rules [49], one can easily see that the HF ground state can only be excited into a 1h1p configuration, while a 1h1p excited state can be excited both to another 1h1p and to a 2h2p configurations. This simple qualitative argument suggests that inclusion of the 2h2p configurations into the photoionisation theory is essential for the excited state processes. In what follows the validity of this conclusion has been tested quantitatively.

In order to investigate how the different levels of *ab-initio* theory work for the excited state photoionisation, calculations for different excited states of three molecules have been performed: N_2, CO and H_2O, one of which (N_2) has been investigated experimentally in Ref. [164]. The calculated vertical and (for CO and N_2) adiabatic ADC(2) and ADC(2)x excitation energies of the electronic states considered in this thesis are reported in Table 4.1, together with the corresponding experimental values (the basis sets used for the ADC calculations are reported further below). The lowest-lying singlet excited state of water, 1^1B_1 is a rapidly dissociating state, leading to the H(^2S) and OH($X^2\Pi$) formation as has been shown both experimentally [166, 167] and theoretically [168]. The next 1^1A_2 excited electronic state of water is dipole forbidden and has been identified by electron-impact energy-loss spectroscopy [169]. The 1^1A_2 state is also predicted to be dissociative and, similarly to the lower 1^1B_1 state, is thought to be involved in the predissociation processes of higher lying states [170, 168]. Thus, Table 4.1 gives no adiabatic excitation energies for the water excited states.

The results obtained for the vertical excitation energies are in a very good agreement with the experimental ones and constitute an improvement over the previously reported ADC results [171] due to the larger basis sets used

	24cmVertical excitation energies (eV)			24cmAdiabatic excitation energies (eV)		
State	ADC(2)	ADC(2)x	Exp.	ADC(2)	ADC(2)x	Exp.
H_2O 1^1B_1	7.18	6.98	7.40-7.46[a,b,c,d,e]	–	–	–
H_2O 1^1A_2	8.82	8.63	9.09 [b]	–	–	–
CO $1^1\Pi$	8.85	8.32	8.51 [f]	8.11	7.63	8.07 [h]
CO $1^1\Sigma^-$	10.15	9.64	9.88 [f]	7.57	7.12	8.07 [h]
N_2 $1^1\Pi_g$	9.55	8.98	9.31 [g]	8.58	8.10	8.59 [h]
N_2 $1^1\Sigma_u^-$	10.31	10.13	9.92 [g]	8.69	8.40	8.45 [h]

Table 4.1.: Comparison between the ADC(2) and ADC(2)x values and the experimental values for the vertical and adiabatic excitation energies of the 1^1B_1, 1^1A_2 excited states of water, the $1^1\Pi_g^+$ and $1^1\Sigma_u^-$ excited states of N_2 and the $1^1\Pi$ and $1^1\Sigma^-$ excited states of CO. [a] – Ref. [172], [b] – Ref. [169], [c] – Ref. [173], [d] – Ref. [174], [e] – Ref. [175] [f] – computed in Ref. [176] via numerical solution of the nuclear Schrödinger equation using the spectroscopic rovibronic constants given by Huber and Herzberg in Ref. [177]. [g] – calculated in Ref. [178] using the same procedure as in Ref. [176]. [h] – Ref. [177]. All the energy values are given in eV.

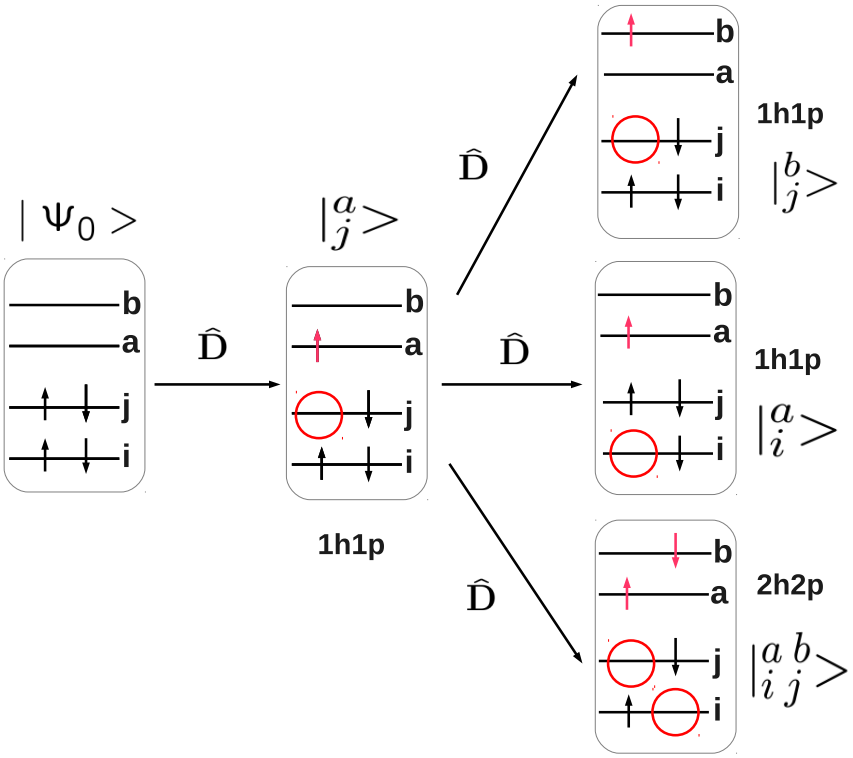

Figure 4.1.: Schematic representation of a two-step dipole excitation process within simple frozen orbital approach. In the first step, HF ground state is excited by dipole (i.e. a single-electron operator) to singly excited configurations (1h1p's), whereas in the second step each 1h1p can be excited to both 1h1p's and 2h2p's.

in these calculations. The calculated adiabatic excitation energies are also in a good agreement with the experimental values, apart from the CO $1^1\Sigma^-$ state, where a larger discrepancy is observed. It should be noted that ADC schemes are all based on HF solution of the ground state and their accuracy is expected to deteriorate at internuclear distances significantly larger than the ground state equilibrium geometry. Among the excited states considered here, CO $1^1\Sigma^-$ state shows the largest distortion of the excited state geometry relative to the ground state one, and the available precise computations of the corresponding adiabatic transition energy are based on the multiconfigurational and multireference approaches [179]. For almost all excited states considered, the extended ADC(2)x does not lead to a clear improvement over ADC(2), as could be expected for the states dominated by

single excitations. The experimental-theoretical discrepancies in the vertical excitation energies of water (see Table 4.1) partly result from the assignment of the experimental value as the maximum of the band rather than its centre of gravity (see Ref. [180] for the detailed analysis in the harmonic approximation). The discrepancies between the ADC and the experimental adiabatic excitation energies are affected by the lack of correction of the theoretical values for the zero point energy differences. Apart from the CO $1^1\Sigma^-$ state mentioned above, the ADC results reported in this thesis are found to be in a very good agreement with previous theoretical calculations of the vertical and adiabatic excitation energies in H_2O, N_2 and CO, see Refs. [181, 182].

Fig. 4.2 and Fig. 4.3 show the total photoionisation cross sections of the H_2O molecule in the first 1^1B_1 and the second 1^1A_2 electronically excited states, as a result of the Stieltjes imaging technique applied to the pseudospectra obtained via full diagonalisation of the ADC(1) matrix and block-Lanczos diagonalisation of the ADC(2) and ADC(2)x Hamiltonian matrices in the dipole-allowed final symmetry spaces. Every cross-section reported in this thesis is drawn as a function of the photon energy, starting from the calculated photoionisation threshold of the respective initial excited bound state.

The basis set employed, as well as the dimension of the ADC(2)x matrices and that of the Lanczos pseudospectrum space for which the convergence in the cross-section has been obtained are reported in Table 4.2. In both cases the cross-sections have been calculated for two different nuclear geometries: the equilibrium ground state geometry and the lowest energy C_{2v} geometries for the lowest excited states of H_2O as calculated in Ref [182]. The latter geometries correspond to the saddle points of the dissociative full potential energy hypersurfaces of the excited water molecule.

At the photon energies close to threshold, all three methods give similar results for the cross-section, with the quantitative differences being comparable to those obtained for ground state photoionisation [104, 146]. However, throughout the > 20 eV photon energy range, the ADC(1) cross-section represents, at both geometries, just a small fraction of the total one predicted by the ADC(2) and the ADC(2)x methods. The main cross-section peak is simply absent from the ADC(1) result. This inadequacy of the single excitation theory can be easily explained by the previous qualitative con-

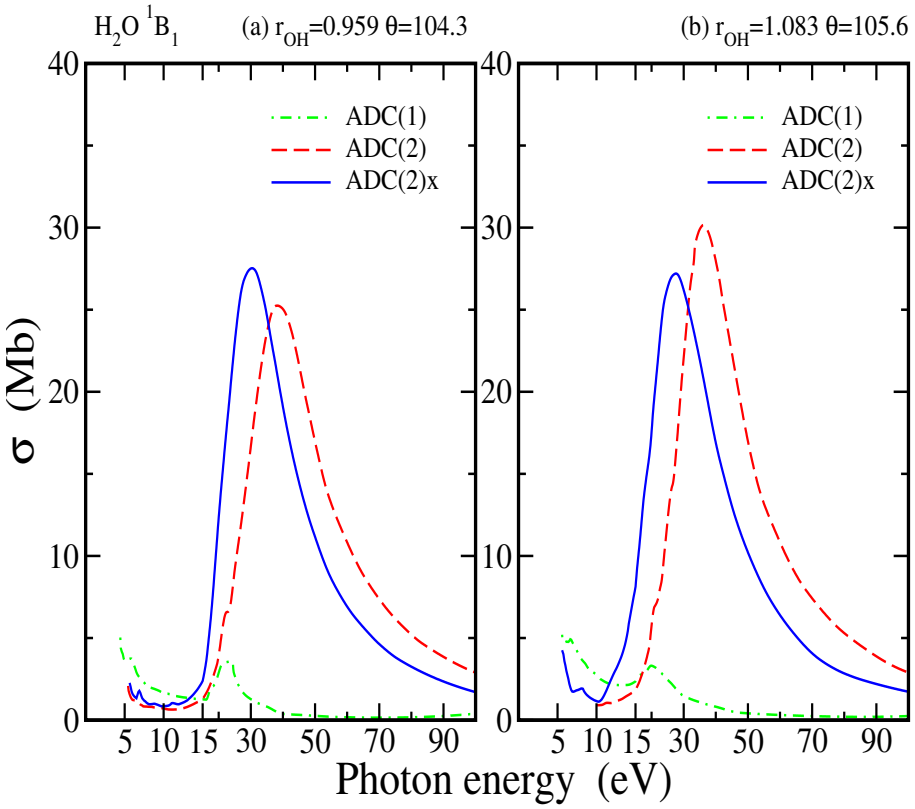

Figure 4.2.: Total photoionisation cross section of the H_2O molecule from the first 1^1B_1 electronically excited state at the ground state equilibrium geometry (a) and at the excited state saddle point geometry (b, see text for details). Dashed-dotted line – ADC(1)-Stieltjes, dashed line – ADC(2)-Lanczos-Stieltjes, full line – ADC(2)x-Lanczos-Stieltjes. See Table 4.2 for computational details.

siderations (see Fig. 4.1). Indeed the ADC(2) method produces a much larger cross-section because it takes into account the Slater-Condon-allowed transitions to the doubly excited final states. The dramatic change in the cross-section profile occurring when going from the single excitation to the double excitation methods tells us that the photoionisation channels leaving the molecular ion in an excited state are not only significantly, but are actually starting to be the dominant ones already about 10 eV above threshold.

Contrary to the situation with the ground state cross-sections [104, 146], the ADC(2) cross-sections differ quite strongly from the ADC(2)x ones. Once the 2h2p final states become important, the interactions between the

22cmMolecular state	22cmBasis set	22cmInitial dimension	22cmFinal dimension	22cmKrylov dimension
H_2O 1^1B_1	25cmcc-pVTZ + O(10*s*7*p*6*d*); H(3*s*3*p*2*d*)	46507	49785	6025
H_2O 1^1A_2	25cmcc-pVTZ + O(10*s*10*p*4*d*); H(3*s*3*p*2*d*)	45695	48665	8000
N_2 $1^1\Pi_g$	25cmN:cc-pCVTZ+(6*s*9*p*6*d*3*f*)	82777	87431	9600
N_2 $1^1\Sigma_u^-$	25cmN:cc-pCVTZ+(9*s*9*p*9*d*6*f*)	125292	131499	11580
CO $1^1\Pi$	25cmC,O:cc-pVDZ+(4*s*6*p*5*d*)	40749	44016	6700
CO $1^1\Sigma^-$	25cmC,O:cc-pVTZ+(4*s*6*p*5*d*2*f*)	88704	93744	10000

Table 4.2.: The basis sets employed, the dimension of the ADC(2)x matrices in the initial and in the final dipole-allowed symmetry spaces and the dimension of the final space Lanczos pseudospectrum, for which the converged cross-section has been obtained, are reported for each molecular initial excited state studied in this thesis.

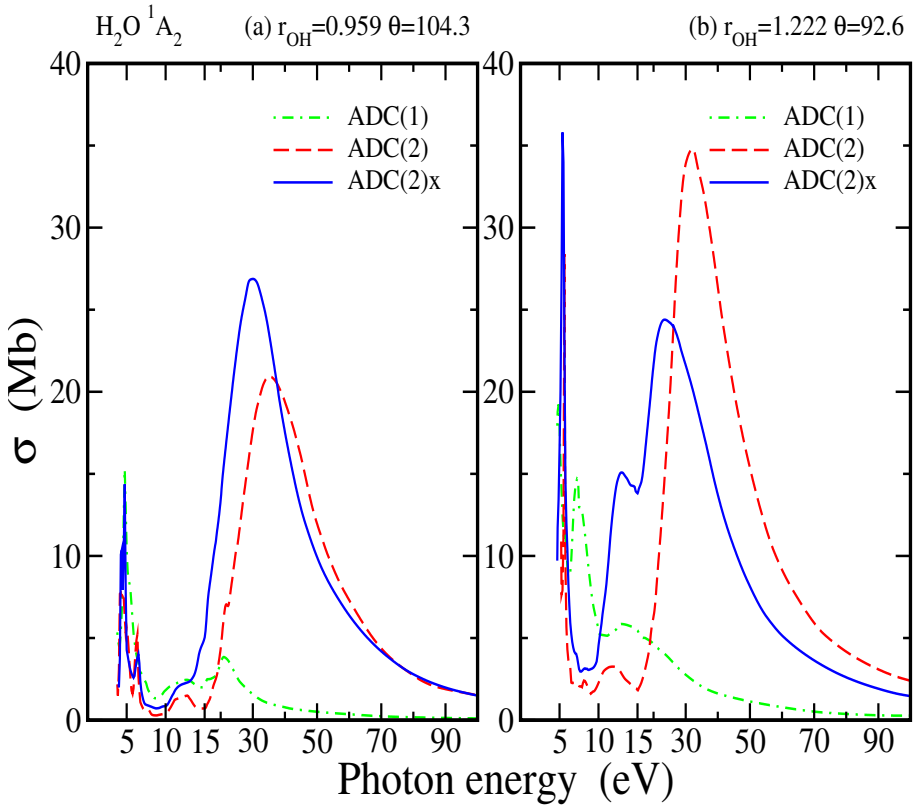

Figure 4.3.: Total photoionisation cross section of the H_2O molecule from the second 1^1A_2 electronically excited state at the ground state equilibrium geometry (a) and at the excited state saddle point geometry (b, see text for details). Dashed-dotted line – ADC(1)-Stieltjes, dashed line – ADC(2)-Lanczos-Stieltjes, full line – ADC(2)x-Lanczos-Stieltjes. See Table 4.2 for computational details.

2h2p configurations, first taken into account in the ADC(2)x method, start playing a role as well. Looking, for example, at the photoionisation cross-section from the 1^1B_1 state calculated at the ground state nuclear geometry it is possible to see that the ADC(2)x peak energy is shifted by around 8 eV with respect to the ADC(2) value. The difference is appreciable also in the 60-100 eV energy range in which the ADC(2)x cross-section is considerably lower than the ADC(2) prediction (see Fig. 4.2). The difference between the ADC(2) and the ADC(2)x results is even more appreciable in the cross-section from the 1^1A_2 state (see Fig. 4.3).

In the previous ground state calculations [146], we have used starting

Lanczos blocks consisting of all 1h1p intermediate states, $|\tilde{\Psi}_1\rangle$, see Eq. (2.87). In the present excited state calculations, this strategy is no longer the optimal one, because of the importance of the doubly-excited configurations in the final states of the absorption process. Instead, we have found it beneficial to use a bigger starting block consisting also of the N 2h2p configurations with the greatest dipole transition moments from the initial state, $\langle\tilde{\Psi}_2 \mid \hat{D} \mid \Psi_{In}\rangle$ calculated at the ADC(2) level. In the case of the first 1^1B_1 excited state of the H_2O molecule, the latter approach with $N = 100$ leads to convergence after only 25 iterations, i.e. with 6025 Lanczos vectors in contrast with the previous $N = 0$ approach where the Lanczos vectors used would be 15665 (more than twice as many iterations). Every calculation reported in this thesis was performed using both schemes for the initial block and it was checked that both cases lead to the same convergent cross-section. Unfortunately when the strict ADC(2) method is used, the scheme including the 2h2p's into the initial block is not applicable, because the nature of the Hamiltonian matrix leads in that case to exact linear dependencies in the Krylov space immediately after the first Lanczos iteration. This is due to the fact that the double excitations block in the strict ADC(2) method is diagonal, and therefore the result of the action of the Hamiltonian on any doubly excited state is a linear combination of this state and of all the 1h1p states it is coupled to. In other words, Hamiltonian action leads in this case to a state lying in the starting Krylov space.

Simple qualitative considerations (see Fig. 4.1) suggest that the central feature of the excited state cross-sections, namely the importance of the double excitations, should not depend crucially on the molecular geometry. The calculations performed at the saddle point geometry of the 1^1B_1 excited water molecule (see Fig. 4.2) show that this is indeed the case. The dramatic differences between the ADC(1) and the doubly excited ADC(2)-ADC(2)x calculated cross-sections are still present at the modified nuclear geometry. The same turns out to be true for all the excited states cross-sections studied in this thesis. Nevertheless, some modifications in the excited states ADC(2) and ADC(2)x cross-sections depending on the nuclear geometry can be observed; in the case of the water 1^1B_1 state the main peak shifts of about 3 eV with respect to the ground state equilibrium geometry energy position value, both in the ADC(2) and ADC(2)x cross-sections. Differently with respect to the ADC(2) cross-section, where the peak maximum

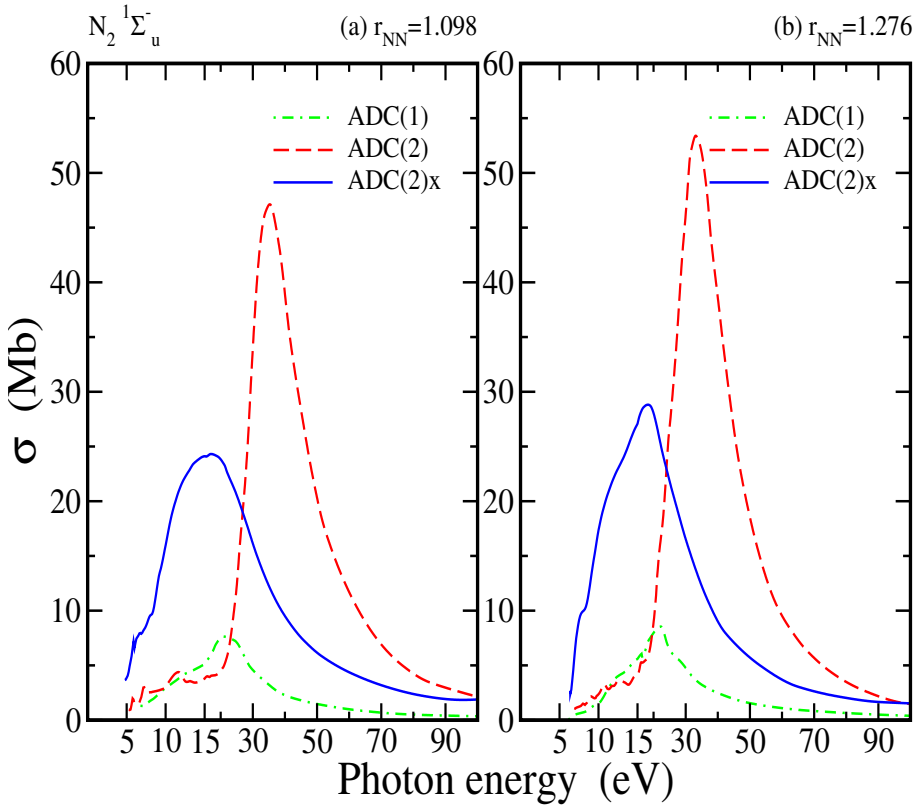

Figure 4.4.: Total photoionisation cross section of the N_2 molecule from the first $1^1\Sigma_u^-$ electronically excited state in the ground state (a) and excited state (b) equilibrium geometries. Dashed-dotted line – ADC(1)-Stieltjes, dashed line – ADC(2)-Lanczos-Stieltjes, full line – ADC(2)x-Lanczos-Stieltjes. See Table 4.2 for computational details.

increases by about 5 Mb, the height of the peak in the ADC(2)x result at the excited state equilibrium geometry shows a slight decrease. The cross-section dependencies on nuclear positions show up a bit stronger in the 1^1A_2 excited state, where both the ADC(2) and the ADC(2)x peaks are shifted of about 3 and 7 eV respectively, with the ADC(2) height being increased of about 14 Mb while the ADC(2)x one being decreased by about 3 Mb at the excited state saddle point geometry (Fig. 4.3).

In Figs. 4.4-4.7 the total photoionisation cross sections calculated fixing as the starting state for the absorption process respectively the first $1^1\Pi_g$ and the second $1^1\Sigma_u^-$ excited states of the N_2 molecule and the first $1^1\Pi$ and

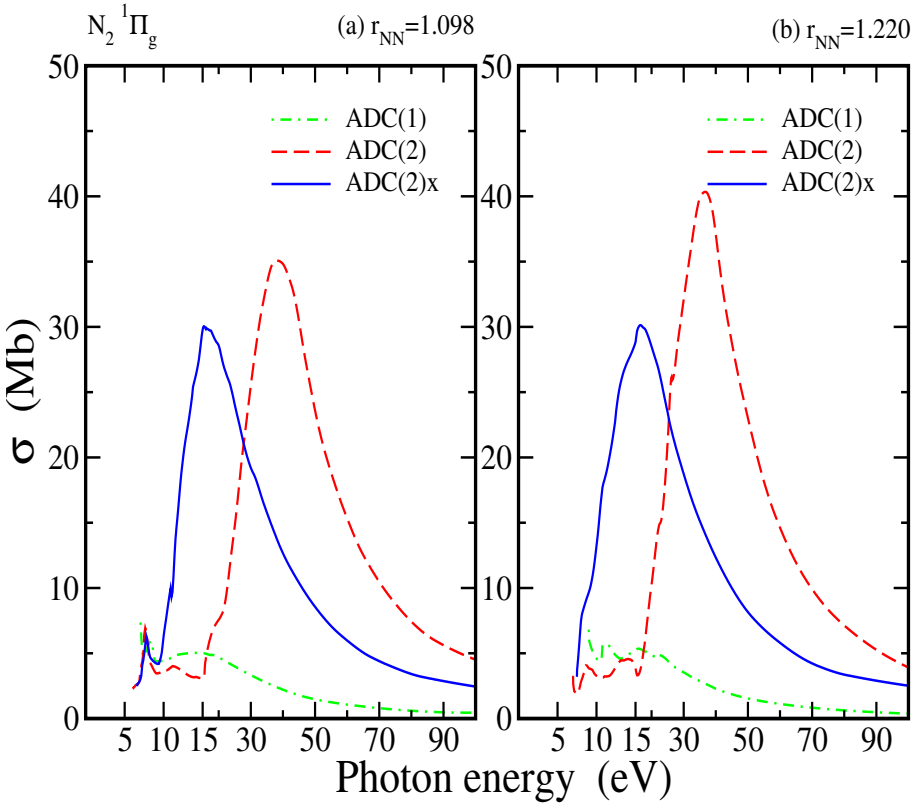

Figure 4.5.: Total photoionisation cross section of the N_2 molecule from the second $1^1\Pi_g$ electronically excited state in the ground state (a) and excited state (b) equilibrium geometries. Dashed-dotted line – ADC(1)-Stieltjes, dashed line – ADC(2)-Lanczos-Stieltjes, full line – ADC(2)x-Lanczos-Stieltjes. See Table 4.2 for computational details.

the second $1^1\Sigma^-$ excited states of the CO molecule, are reported. The basis set employed, as well as the dimension of the ADC(2)x matrices and that of the Lanczos pseudospectrum space for which the convergence in the cross-section has been obtained are reported in Table 4.2. For all of these excited states the calculations are computed at two different nuclear geometries, the ground state equilibrium one and the specific excited state equilibrium one as taken from Ref. [177].

The difference between the ADC(2) and the ADC(2)x cross-sections at the ground state nuclear equilibrium geometry is even more evident in the N_2 and CO molecules than in water. However in the excited states of the

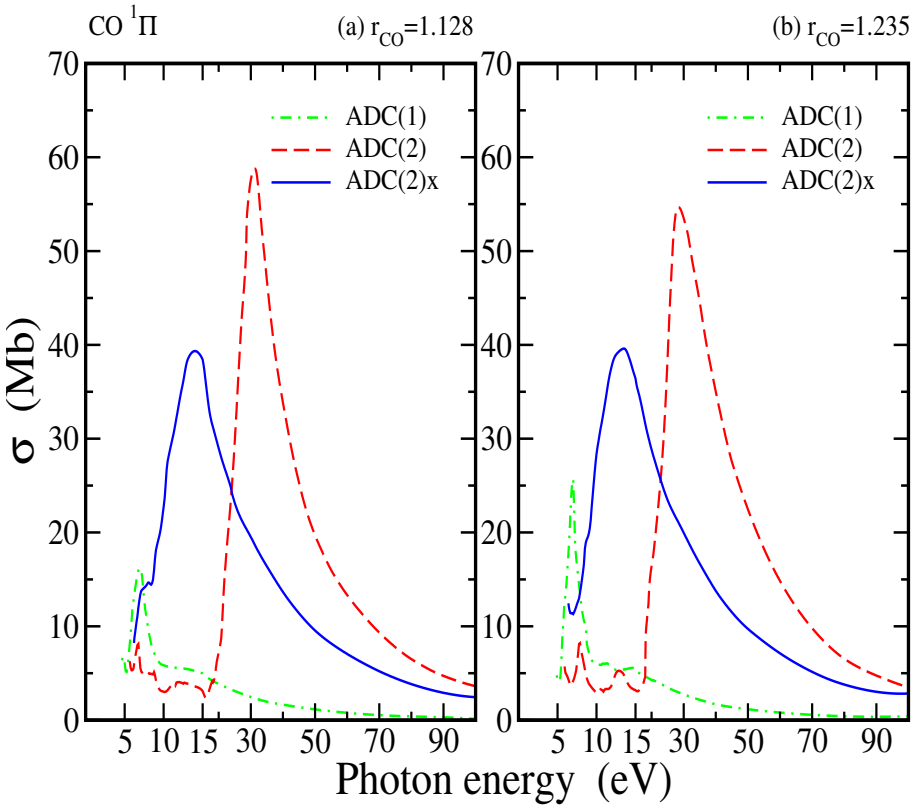

Figure 4.6.: Total photoionisation cross section of the CO molecule from the first $1^1\Pi$ electronically excited state in the ground state (a) and excited state (b) equilibrium geometries. Dashed-dotted line – ADC(1)-Stieltjes, dashed line – ADC(2)-Lanczos-Stieltjes, full line – ADC(2)x-Lanczos-Stieltjes. See Table 4.2 for computational details.

N_2 and CO molecules studied in this thesis it is possible to notice that, in general, the ADC(2)x cross-sections show smaller dependence, if any, with respect to the nuclear geometry in comparison to the strict ADC(2) ones. Therefore, the difference between the cross-sections calculated with the two methods tends to increase with distortion of the nuclear equilibrium geometry, even if not as much as it does in the case of the 1^1A_2 excited state cross-section of water molecule.

For all the four states considered, the ADC(2)x cross-section, in the nuclear ground state equilibrium geometry, exhibits a smaller peak at a lower energy with respect to the ADC(2) one, this behaviour being confirmed

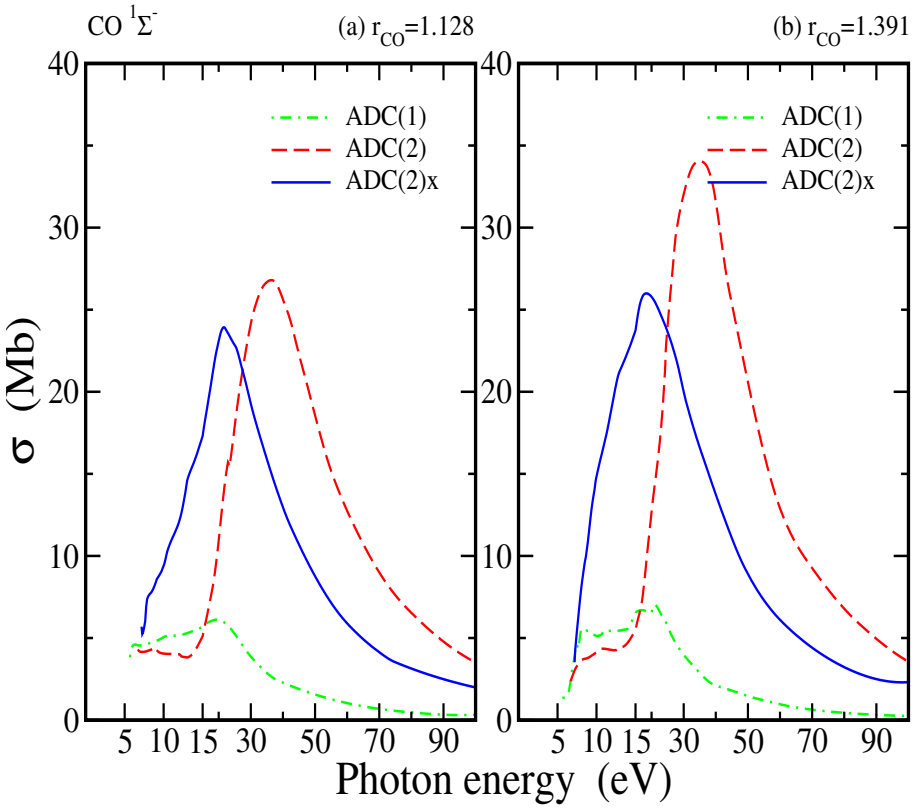

Figure 4.7.: Total photoionisation cross section of the CO molecule from the second $1^1\Sigma^-$ electronically excited state in the ground state (a) and excited state (b) nuclear equilibrium geometry. Dashed-dotted line – ADC(1)-Stieltjes, dashed line – ADC(2)-Lanczos-Stieltjes, full line – ADC(2)x-Lanczos-Stieltjes. See Table 4.2 for computational details.

at different nuclear geometries as well. Apart from the near-threshold energy region, the ADC(1) cross-sections are found to be strongly suppressed in comparison with the ones calculated using double excitation theories. Qualitatively, one could expect a single excitation theory to fail starting from the energy region of the first satellite (2h1p-like) states of the ionised system giving rise to the 2h2p-like final photoionisation states. For the molecules considered here, the satellites in the molecular ion spectra first appear about 10 eV above the ground state of the ion (see, e.g. Ref. [183]), and indeed in this energy region, the ADC(2)x results already differ strongly from the ADC(1) ones; on the other hand the strict ADC(2) results start to

considerably differ from the single excitation theory ones at slightly higher energies. (see Figs. 4.2-4.7).

4.2. Summary

In the present Chapter the ADC-Lanczos-Stieltjes method has been extended to compute photoionisation cross-sections of electronically excited molecular states. Comparison of the series of excited state cross-sections computed at the different levels of the *ab-initio* theory led us to conclude that the single excitation ADC(1) method is inadequate for the description of the excited state photoionisation even at the qualitative level. The reason for the inapplicability of the first-order scheme is the double excitation (2h2p) character of many of the final states of the process, which are consequently omitted by the single excitation method. While this feature is fully expected on the basis of the simple Slater-Condon rule analysis, the extent to which the double excitations change the cross-section could be seen only in a quantitative study such as the one performed here. The numerical results reported in this Chapter show beyond doubt that the full inclusion of double electronic excitations is absolutely necessary in order to produce even a qualitatively accurate photoionisation cross-section. Moreover, it is found that it is important to include the coupling between the double excitations into the theory. Indeed, within the ADC family of methods used here, ADC(2)x leads to a clear, substantial systematic difference with respect to the strictly second-order ADC(2) theory for all molecules and geometries considered. This is in sharp contrast to the case of the ground state cross-sections, where ADC(2) and ADC(2)x results were found to be in much better agreement [104, 146]. Since the doubly excited final states of the excited state photoionisation are much better described by the ADC(2)x theory, it has been assumed that the ADC(2)x cross-sections represent a major improvement over the ADC(2) results.

These calculations demonstrate that a theoretical modelling of photoionisation of excited states requires an intrinsically double excitation theory with respect to the ground state and can not be achieved by the standard single excitation methods. There is no reason to assume that the failure of the single-excitation theory for the excited state photoionisation is unique to the ADC(1) scheme. Indeed, these results imply that any method that

does not fully include the 2h2p final states, such as configuration interaction singles (CIS), Tamm-Dancoff approximation (TDA), random phase approximation (RPA), linear response TDDFT, etc. can not be expected to provide a correct description of the process. A separate issue is whether the non-perturbative TDDFT calculations, such as performed in Ref. [164] can describe ionisation of a many-electron wavepacket consisting of the ground and a series of excited states. For the exchange-correlation functionals used in Ref. [164], one would expect that in general the contribution of the double excitation relative to that of the singles is subject to non-physical constraints stemming from the single-determinant description and as a result the XUV ionisation probability should not be given correctly. Indeed, artefacts arising from the single determinant character of the wave-function have been extensively discussed in the context of the related time-dependent HF (TDHF) method [184]. However, in the cases where the exciting IR field can be considered as an adiabatic perturbation, the initial (approximately HF, i.e. single-determinant) ground state would physically evolve into a TDHF-like state under the influence of the IR field. XUV ionisation of such an adiabatic TDHF state should be given correctly by the TDHF or TDDFT theory as long as the XUV intensity is in the perturbative regime. These conditions are met by the experiment of Ref. [164]. From the cross-section analysis presented in this Chapter it is clear however that careful benchmarking of the performance of the non-perturbative TDDFT with various exchange-correlation functionals in the time-dependent modelling of excitation-ionisation schemes is highly warranted.

5. B-spline Algebraic Diagrammatic Construction: Application to Photoionisation Cross-Sections

In the previous two Chapters it has been shown that the ADC schemes in conjunction with iterative block-Lanczos (BL) diagonalisation [106, 107, 108] and the Stieltjes-Chebyshev moment theory [94] can be used also for accurate and efficient characterization of bound-continuum transitions, i.e. for calculations of photoionisation cross-sections [104, 146, 165]. In the bulk of the ADC work cited above and presented in Chapters 3 and 4, Gaussian type orbitals (GTOs) have been used as a single-electron basis as is indeed customary in the *ab-initio* quantum chemistry. However, the benchmark study [146] reported in Chapter 3 indicates that it is the use of the GTOs in the excitation ADC schemes that leads to the onset of major inaccuracies in molecular photoionisation cross-section calculations at about 70 eV above threshold. This trend has been shown to be general for a series of molecular species and independent of the order of the employed ADC scheme [146]. Moreover, GTO-based ADC-Lanczos-Stieltjes method fails to reproduce not only the narrow features of the cross-section due to excitation resonances (as is fully expected of a moment theory technique), but even the much broader features, such as Cooper minima, e.g. in argon photoionisation. Very similar behaviour has been observed in a recent implementation of the GTO/Stieltjes approach within linear response coupled cluster models for electronic excitations [105]. Even very careful GTO selection cannot yield converged high order moments, i.e high energy features and high resolution, without running into linear dependence problems [105]. The inadequacy of the GTO bases for the characterization of the molecular photoionisation calls for an introduction of new basis sets, better suited for the description

of the oscillatory continuum wave-functions across the interaction region. Several such basis sets have been already introduced in the nineties within the framework of the many-body methods that do not fully include double electronic excitations and were successfully used for the solution of the time-independent many-electron problems, e.g. for photoionisation cross-section calculations, see e.g. Ref. [185].

In the present Chapter the first implementation of the *ab-initio* many-body Green's function method, algebraic diagrammatic construction (ADC), in the B-spline single-electron basis [55], is presented. The work presented in this Chapter addresses the single-electron basis set issue by construction B-spline versions of ADC schemes explicitly treating not only single [ADC(1)], but also double [ADC(2)] excitations and applying them to the *ab-initio* calculation of static (photoionisation cross-sections) quantities. The single-electron basis employed is composed of the spherical harmonics for the angular part and a B-spline expansion for the radial coordinate. In order to calculate the total photoionisation cross-sections of nobel gas atoms and to perform a direct comparison of the performance of the B-spline basis against the Gaussian type one, the Stieltjes imaging (SI) [94, 104, 146, 165] technique, which allows one to obtain the correct continuum oscillator-strength density, without going through the direct calculation of the correctly energy-normalised wave-functions, has been used. The present development paves the way for the application of the B-spline ADC to both energy- and time-resolved theoretical studies of many-electron phenomena in atoms, molecules and clusters.

5.1. Computational details

While this choice of the single-particle basis functions leads to higher computational effort than in the GTO case, it at the same time simplifies tremendously the numerical algorithm mainly because of the absence of linear dependencies to take care of; moreover, the minimal localised support of the individual primitive B-spline basis functions allows to reduce the number of radial B-spline one-electron and two-electron integrals (Eq. (2.147)) to be calculated and dynamically stored in the RAM at the beginning of the calculation as already shown in Eqs. (2.148) and (2.149). Computer time for the evaluation of the radial two-electron integrals over the prim-

itive B-spline functions is a minor part of the total computational cost of the present calculations.

The main numerical procedure required in a B-spline-ADC calculation consist of four key steps, namely:

1. Solution of the B-spline HF equations.

2. One- and two-electron integral transformations with simultaneous calculation of the first order Hamiltonian and dipole matrix-elements on the fly.

3. Calculation of the second-order matrix elements in the ADC(2) method.

4. Full/iterative diagonalisation of the ADC Hamiltonian and calculation of the static physical quantity of interest (e.g. a cross-section) via the SI technique or time-propagation of an initial state in order to obtain the dynamic quantity of interest (e.g. HHG spectrum).

The first step consists of solving a set of one-particle integro-differential equations with non-local terms, i.e. the Hartree-Fock equations. These equations are solved iteratively, in each irreducible representation of the electronic Hamiltonian, in the standard way [49].

The second step makes the integrals transformation from the primitive B-spline basis set to the basis of the Hartree-Fock (HF) canonical orbitals. Two-electron integral transformation from primitive orbital sets to atomic/molecular working orbital sets is the most time consuming process for large-scale B-spline ADC calculations.

The two-electron integrals over the primitive monocentric basis set functions of Eq. (2.134), indeced with the integers 1,2,3,4, are defined as

$$(12 \mid 34) = \int \int \Phi_1 (\mathbf{r}) \, \Phi_2 (\mathbf{r}) \, \frac{1}{\mid \mathbf{r} - \mathbf{r}^{'} \mid} \Phi_3 \left(\mathbf{r}^{'} \right) \Phi_4 \left(\mathbf{r}^{'} \right) d^3\mathbf{r} d^3\mathbf{r}^{'} \, , \qquad (5.1)$$

where

$$\Phi_1 (\mathbf{r}) = \frac{1}{r} B_{i_1} (r) \, Y_{l_1, m_1} (\theta, \phi) \, . \qquad (5.2)$$

Two-electron integrals over the primitive monocentric basis set functions can be factorised, using Eq. (5.2), into products of radial and angular con-

tributions and consequently expressed as

$$(12 \mid 34) = \sum_{k=k_{min},2}^{k_{max}} ANG\,(k, l_1, m_1, l_2, m_2, l_3, m_3, l_4, m_4)\, R^k\,(i_1 i_2, i_3 i_4)\ , \tag{5.3}$$

where $R^k\,(i_1 i_2, i_3 i_4)$ is the radial two-electron integral over the primitive B-spline functions of Eq. (2.147), the two extremes of the summation over the k index are given by

$$k_{min} = max\,(\mid l_1 - l_2 \mid, \mid l_3 - l_4 \mid)$$

$$k_{max} = min\,(l_1 + l_2, l_3 + l_4) \tag{5.4}$$

and the function $ANG\,(k, l_1, m_1, l_2, m_2, l_3, m_3, l_4, m_4)$, which depends only on the angular momentum quantum numbers of the orbitals and is the result of the two-dimensional integration onto the angular variables, can be expressed as

$$ANG\,(k, l_1, m_1, l_2, m_2, l_3, m_3, l_4, m_4) =$$

$$\sum_{q=-k}^{+k} YYY\,(l_2, k, l_1, m_2, q, m_1)\, YYY\,(l_3, k, l_4, m_3, q, m_4)\ \frac{4\pi}{2k+1}\,. \tag{5.5}$$

Finally, here the quantity YYY stands for the integral of the product of three spherical harmonics and is given by

$$YYY\,(l_1, l_2, l_3, m_1, m_2, m_3) = \int_0^{2\pi} \int_0^{\pi} Y^*_{l_1,m_1}(\theta,\phi) Y_{l_2,m_2}(\theta,\phi) Y_{l_3,m_3}(\theta,\phi) \sin\theta d\theta d\phi =$$

$$(-1)^{m_1}\sqrt{\left(\frac{(2l_1+1)\,(2l_2+1)\,(2l_3+1)}{4\pi}\right)}\begin{pmatrix} l_1 & l_2 & l_3 \\ -m_1 & m_2 & m_3 \end{pmatrix}\begin{pmatrix} l_1 & l_2 & l_3 \\ 0 & 0 & 0 \end{pmatrix},$$

(5.6)

where $\begin{pmatrix} l_1 & l_2 & l_3 \\ -m_1 & m_2 & m_3 \end{pmatrix}$ is a Wigner 3j-symbol and is related to the Clebsch-Gordan coefficients $(l_1 l_2 m_1 m_2 \mid l_1 l_2 l m)$ through

$$\begin{pmatrix} l_1 & l_2 & l \\ m_1 & m_2 & m \end{pmatrix} = \frac{(-1)^{l_2-l_1+m}}{\sqrt{2l+1}}\;(l_1 l_2 m_1 m_2 \mid l_1 l_2 l-m)\;. \tag{5.7}$$

Using the relation between the canonical HF orbitals and the primitive monocentric basis functions, which reads explicitely as

$$\psi_n = \sum_j \Phi_j C_j^n = \sum_{(l,m)}\sum_i C_{l,m,i}^n Y_{l,m}(\theta,\phi)\frac{1}{r}B_i(r)\,, \tag{5.8}$$

the two-electron integrals over the primitive monocentric basis set are transformed to the HF canonical basis set as

$$(pq \mid rs) = \sum_{i_1=1}^{N}\sum_{i_2=1}^{N}\sum_{i_3=1}^{N}\sum_{i_4=1}^{N} C_{i_1}^p C_{i_2}^q\,(12 \mid 34)\,C_{i_3}^r C_{i_4}^s\,, \tag{5.9}$$

where N is the total number of HF orbitals.

However, a straightforward application of Eq. (5.9), simply looping over all p, q, r, s, and then looping over all the primitive indices 1,2,3,4, gives rise to a total number of numerical operations which scales as N^8, where N is the number of basis states. Indeed, this elementary approach would give eight nested loops which, with a basis size required for a realistic calculation, is beyond the power of present computers.

However, a careful analysis shows that the size of the problem can be reduced to N^5. Therefore a different sequential algorithm, which allows the $O\left(N^8\right)$ process to be converted into four $O\left(N^5\right)$ consecutive steps, has been implemented in major *ab-initio* quantum chemistry MO codes [49].

The trick is to convert one index at a time from the primitive orbitals to the final orbitals basis. That is, starting with the matrix (tensor) (12 | 34),

convert one of the indices (a "quarter transform"), then convert the next one, until a total of four quarter-transforms are accomplished. Therefore the total 4-indices transformation can be thought of in the following way

$$(pq \mid rs) = \left(\sum_{i_1=1}^{N} C_{i_1}^{p} \left(\sum_{i_2=1}^{N} C_{i_2}^{q} \left(\sum_{i_3=1}^{N} C_{i_3}^{r} \left(\sum_{i_4=1}^{N} C_{i_4}^{s} \left(12 \mid 34 \right) \right) \right) \right) \right) . \quad (5.10)$$

This is called factorizing the expression, and it helps reducing the cost immensely. Therefore the transformation is performed with this common four-step algorithm, giving a scaling of $4N^5$ with respect to the number of orbitals to be transformed. In the B-spline basis set case an N^5 scaling is still large. Further reductions are possible depending on the type of basis set, as discussed in the following for monocentric B-splines, and on the level of ADC theory used.

Indeed, the first transformation step reads:

$$(12 \mid 3s) = \sum_{(l_1,m_1)} \sum_{i_1} \sum_{(l_2,m_2)} \sum_{i_2} \sum_{(l_3,m_3)} \sum_{i_3} \sum_{d=1}^{N} \sum_{(l_4,m_4)} \sum_{i_4} C_{l_4,m_4,i_4}^{s} \langle 12 \mid 34 \rangle \quad (5.11)$$

and, with the monocentric B-splines as primitive basis set, scales therefore as $O\left(N_{ang}^4 N_{B-splines}^2 (2j_{ord}-1)^2 2l_{max} N\right)$. Here the factor $2l_{max}$ comes from the k loop in Eq. (5.3), l_{max} denotes the maximum angular momentum used in the monocentric expansion and j_{ord} stands for the order of the B-spline basis set used. Similar procedures are repeated three more times untill all the four indices have been transformed.

Due to the number of basis functions involved, both the memory requirements and the time of the transformation can quickly become unaffordable with the increase in the number of spherical harmonics and/or of the radial B-spline functions used in the monocentric expansion (Eq. (2.134)). This problem has been approached by calculating only the two-electron integral types required by the ADC Hamiltonian and dipole matrix elements: in the ADC(1) case only the integrals involving two virtual canonical orbitals indices are needed, namely integrals of the type (vv—oo) and (vo—vo). In the ADC(2) calculations two other types of integrals are required, namely the (vv—vv), (vv—vo) and the less demanding (vo—oo) types [56].

Furthermore, use has been made of the Hamiltonian symmetry group to

divide every type of integral calculation with respect to the quadruplet of orbital irreducible representations involved. While in the atomic and linear molecules calculations the full symmetry of the system is exploited, i.e. the full rotational symmetry and the full $D_{\infty h}$ or $C_{\infty v}$ point group symmetry respectively, in the general, non-linear, molecular case the biggest Abelian symmetry subgroup of the molecule has been used. Following this strategy it is possible to end up with an increased number of less demanding single calculations to be performed.

In the cases where one of the final orbital indices is restricted to the occupied HF orbitals, that is (vv—oo), (vo—vo), (vo—oo) and (vv—vo), this index is the first one to be transformed. Doing so allows the scaling of the first transformation to be considerably improved, as the loop over the final transformed index reduces to a smaller loop over the occupied orbitals in a certain symmetry space of the system, and to minimise the memory allocation requirements after the first step. Moreover, the scaling can be further improved noticing that the occupied orbitals are localised in space within the molecular region; therefore, the loop over the radial B-spline functions with the same radial argument as the transformed orbitals (i.e. i_3) can be truncated at an index value for which their overlap with the occupied orbital becomes smaller than a certain threshold value. Looping over higher indices would be useless as the resulting two-electron integrals would have a negligible value; the same argument allows to reduce the memory allocation requirements for the intermediate two-electron integrals vectors as a considerable number of integrals is not required anymore in the subsequent steps.

The scaling becomes then $O\left(N_{ang}^4\ N_{Bspl}\ N_{Bspl}^{R_{occ}}\ (2j_{ord}-1)^2\ 2l_{max}\ N_{occ}\right)$, where N_{occ} stands for the number of occupied HF orbitals and $N_{Bspl}^{R_{occ}}$ denotes the number of B-splines that overlap with the occupied orbitals. If extended radial grids are used, this can give a considerable gain (up to a factor of 10 with the B-spline basis sets used in this thesis). In Table 5.1 the scalings of the number of numerical operations required at any step of the two-electron integral transformation for the cases of the (vo—vo) and (vv—oo) types of integrals are reported.

However, even though these procedures considerably reduce the computational effort required by the transformation, the number of basis functions used in B-spline ADC is well above the standards of a typical *ab-initio* cal-

21.3cmTransf. step	(vo—vo)	(vv—oo)
1	$27.2cmO\left(N_{ang}^{4}\left(N_{Bspl}^{R_{occ}}\right)^{2}\left(2j_{ord}-1\right)^{2}2l_{max}N_{occ}\right)$	$27.4cmO\left(N_{ang}^{4}N_{Bspl}N_{Bspl}^{R_{occ}}\left(2j_{ord}-1\right)^{2}2l_{max}N_{occ}\right)$
2	$27cmO\left(N_{ang}^{3}\left(N_{Bspl}^{R_{occ}}\right)^{2}\left(2j_{ord}-1\right)N_{occ}N_{virt}\right)$	$27cmO\left(N_{ang}^{3}N_{Bspl}N_{Bspl}^{R_{occ}}\left(2j_{ord}-1\right)N_{occ}^{2}\right)$
3	$27cmO\left(N_{ang}^{2}N_{Bspl}^{R_{occ}}\left(2j_{ord}-1\right)N_{occ}^{2}N_{virt}\right)$	$27cmO\left(N_{ang}^{2}N_{Bspl}\left(2j_{ord}-1\right)N_{occ}^{2}N_{virt}\right)$
4	$27cmO\left(N_{ang}N_{Bspl}^{R_{occ}}N_{occ}^{2}N_{virt}^{2}\right)$	$27cmO\left(N_{ang}N_{Bspl}N_{occ}^{2}N_{virt}^{2}\right)$

Table 5.1.: Scaling of the number of numerical operations required at any step of the two-electron integral transformation for the cases of the (vo—vo) and (vv—oo) types of integrals. Here N_{virt} stands for the number of virtual HF orbitals. With the use parallel algorithm described in the text and schematically represented in Fig. 5.1, these scalings, for each transformation step, must be divided by a factor approximately equal to the number of cpu's used.

culation and as a result, the numerical algorithm has to be further highly optimised. Consequently, it becomes necessary to take advantage of the parallel computing environment [186, 187], which has become increasingly easy to manage, in order to minimise the computer time for the transformation.

Each of the reduced single calculations has been massively parallelised, both inter-nodes, with the standard MPI (message passing interface) technology in parallel computing environment, and intra-node with the OpenMP (shared memory) technology. Indeed, as is well recognised in HPC communities, parallelization is now key for large-scale simulations in any research field, no matter what kind of computers, vector or scalar parallel, are used. The parallel transformation algorithm presented here makes it possible to carry out large-scale calculations within the B-spline based post Hartree-Fock ADC(n) theories on parallel computers.

However it must be mentioned that in general, although the MPI technology allows to substantially reduce the memory requirement per single-node, substantial global amount of RAM (spread across a high number of nodes) is still needed for B-spline ADC calculations requiring a big dimension of the one-electron basis set expansion and that, for such basis sets, assembling the two-electron integrals is still a time-consuming task.

The parallel algorithm used in this work to perform the two-integral transformation is described in the following. In details, while the vector containing the radial two-electron integrals over the primitive B-spline basis functions (Eq. 2.147) is allocated in the RAM on each MPI node, since the first transformation step, the dynamical memory allocation of the transformed two-electron integrals vector is divided between the computational MPI nodes available. This division is performed onto the first index of the four-indices two-electron integral tensor V_{IJKL}. Each of these pieces of the two-electron integral vector undergoes the four indices transformations from V_{IJKL} to V_{PQRS} locally on every node in parallel; only after the fourth and last index transformation step is performed, the resulting partial contributions from every single node to the fully transformed vector of two-electron integrals are broadcasted among each node where they are summed up together. Therefore, at the end of the algorithm, every node has access to the fully transformed quadruple of two-electron integrals. The advantage of this algorithm is that it turns out to never be necessary, at any intermediate stage of the transformation, to have the full integral vector dynamically al-

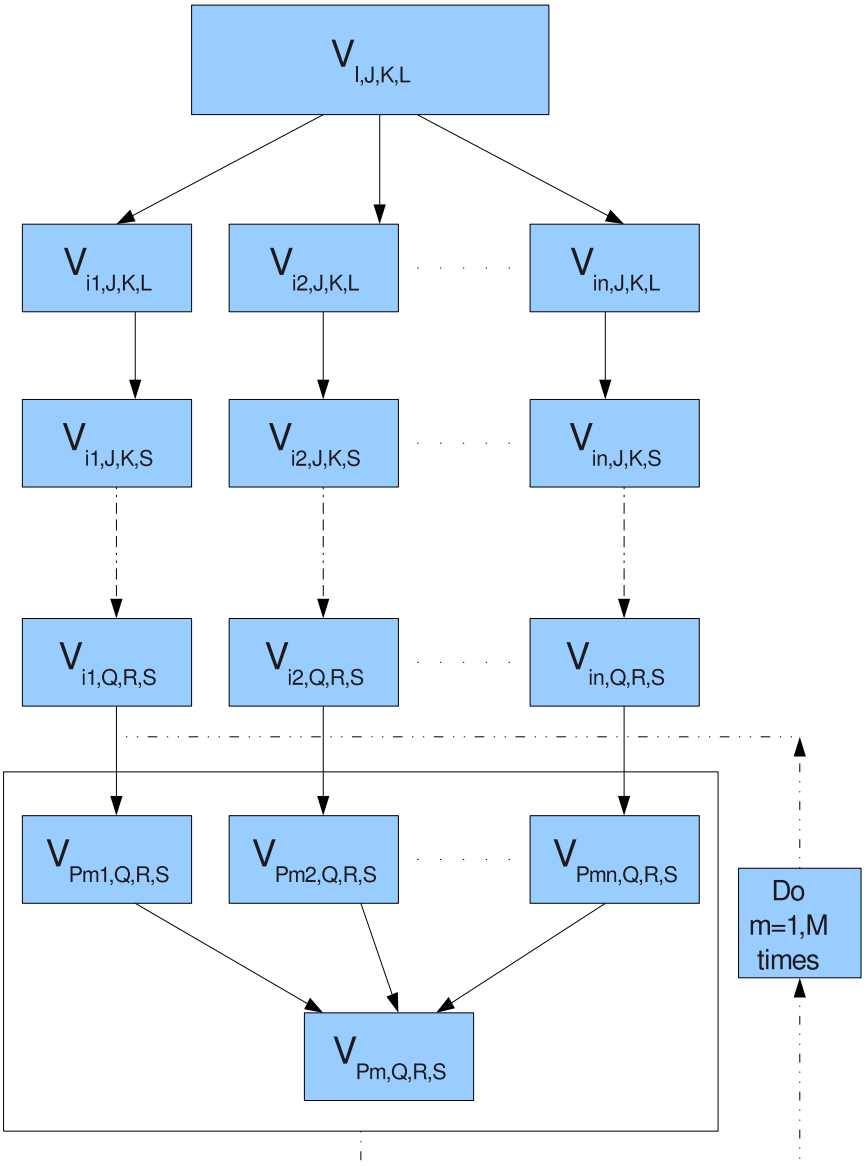

Figure 5.1.: Schematic representation of the way the two-electron integral transformation is parallelised. The indices I,J,K,L refer to the primitive basis functions of Eq. (5.2); the indices P,Q,R,S refer to the Hartree-Fock canonical orbitals.

located on a single node. The RAM allocation of every intermediate vector of two-electron integrals is equally shared among the computational nodes. Moreover, even if the full final transformed integrals vector can be bigger than the full partially-transformed intermediate ones, its complete allocation onto a single node is not required because it can be computed piece by piece sequentially. Additionally, the potentially serious bottleneck of heavy wall-to-wall transmissions among processors during the intermediate stages of the transformation, which arises from the need of all the primitive integrals for obtaining one single final integral over transformed orbitals, is completely solved with the use of this algorithm.

With the use of the parallel algorithm described in the text and schematically represented in Fig. 5.1, the scalings for each transformation step of Table 5.1, must be divided by a factor approximately equal to the number of cpu's used. A schematic representation of the way every specific quadruple of two-electron integrals undergoes the 4-indices transformation in parallel is given in Fig. 5.1.

The contributions to the first-order matrix elements of the ADC Hamiltonian and of the ADC transition moments are calculated on the fly at the last step of the integral transformation. The integrals involved in the second-order ADC matrix elements are instead stored on disk. The OpenMP technology is used to parallelise every intermediate transformation performed on every node, reducing therefore considerably the time of the computation.

The third step, in the case of the ADC(2) level of theory, evaluates the remaining terms of the ADC Hamiltonian matrix and transition moments using the relevant two-electron integrals stored on disk. The matrices to deal with in ADC(2) are of a size often up to 1,000,000 or greater. In ADC(1) the linear scaling with respect to the number of basis functions is however much more favourable. The value of the individual matrix element, which at the first-order ADC(1) level represents a two-variable integral over a two-body Coulomb interaction is in general small but non-zero and, as a result, the matrix is non-sparse. At the second-order level the 1h1p-2h2p coupling block is quite sparse, around 10/15%, while the 2h2p block is diagonal; this simplifies enormously the computation and actually makes such type of calculation possible.

The calculation is performed by dividing the matrix into a large number of sub-matrices of a size storable on a single node. Every sub-matrix is

calculated in parallel, with every node computing a partial contribution to it. The same process is repeated for every sub-matrices, the number of times this is done depending on the memory storage capabilities available and on the matrix dimension. Therefore for memory reasons the different sub-matrices are calculated sequentially one after the other, even if they are independent one of each other. Nevertheless the extension to the parallel computing environment speeds up substantially this step as well, because every node just calculates its own specific contribution to the given sub-matrix and moreover this calculation is OpenMP parallelised as well.

The fourth step involves the extraction of the relevant physical information from the ADC Hamiltonian. In the particular case of a total cross-section calculation, performed using the SI technique, the quantities of interest are the pseudospectrum of the Hamiltonian and the transition moments of the pseudo-eigenstates. A newly-implemented, parallelised, BL diagonalisation routine allows us to obtain a limited number of energy eigenvalues and their corresponding eigenvectors by diagonalising the ADC(2) sparse matrices generated in the third step. A direct diagonalisation is instead performed in the ADC(1) calculations presented here. This is possible because with the B-spline basis sets used the ADC(1) matrices have typically small enough dimension, being for example 1978 in the calculations on krypton atom reported in the following. The range of the B-spline and spherical harmonics expansions over which such a full diagonalisation procedure is still applicable, is quite large for the ADC(1) Hamiltonian, because of the linear scaling of its dimension with respect to the number of one-electron basis functions. Finally, given the pseudospectrum, it is possible to calculate the transition amplitudes and ultimately the cross section. This latter calculation can be performed on any single-node CPU.

5.2. Atomic photoionisation cross-sections by combination of B-spline-ADC and Stieltjes methods

The main goal here is to test the accuracy of the newly designed and implemented B-spline ADC method at the ADC(1) and ADC(2) levels of *ab-initio* theory for bound-free transitions by calculating a series of total photoionisa-

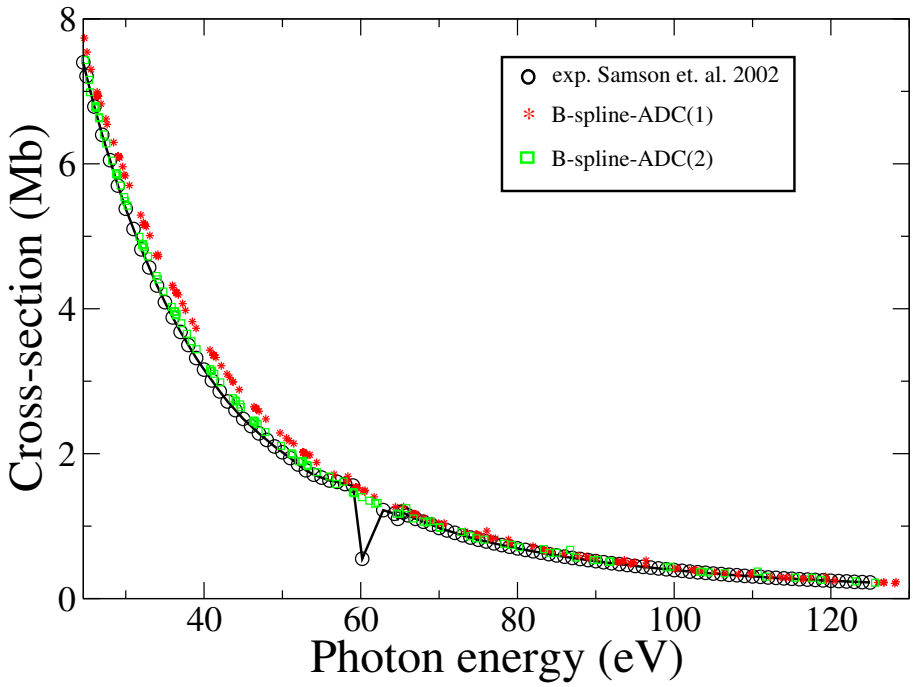

Figure 5.2.: Total photoionisation cross-section of the He atom. Circles – experimental result of Ref. [188], stars – B-spline-ADC(1) result, from Stieltjes order 5 to 34; squares – B-spline-ADC(2)-Lanczos-Stieltjes cross-section, using the Stieltjes orders 5 to 34. B-spline Set 2 was employed (see Table 2.1). With this basis set, the ADC(1) and ADC(2) matrices for He have the dimensions of 88×88 and 96500×96500 respectively. The ADC(2) results was obtained using BL pseudospectrum of 3960 eigenvalues and eigenvectors.

tion cross-sections. A test set of noble gas atom cross-sections for which both very accurate experimental results and a series of GTO-based calculations are available is used. Especially the Ar and Kr atoms provide very good test cases, because their cross-sections contain structured features, such as the Cooper minimum in argon and the $3d$-channel opening in krypton, which so far have been found to be challenging for the GTO calculations.

As in the case of the GTO calculations [104, 146, 165], the Stieltjes imaging (SI) technique [94, 104, 146, 165], which allows one to extract the correctly normalised oscillator-strength density in the electronic continuum, has been used. This also enables us to verify the stability of the B-spline results with respect to the Stieltjes order, providing yet another test of the

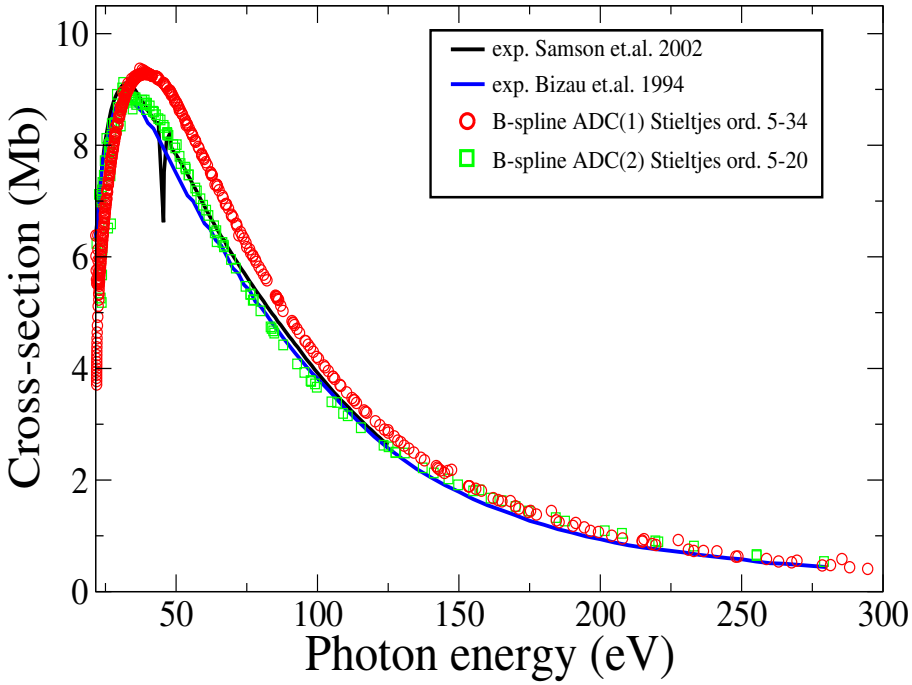

Figure 5.3.: Total photoionisation cross-section of the Ne atom. Full red line – experimental result of Ref. [188], full blue line – experimental result of Ref. [189], circles – B-spline-ADC(1) result, Stieltjes orders 5 to 34; squares – B-spline-ADC(2)-Lanczos-Stieltjes cross-section, Stieltjes orders 5 to 20, obtained using BL pseudospectrum of 26000 eigenvalues and eigenvectors. B-spline Set 2 was employed (see Table 2.1). With this basis set, the dimensions of the ADC(1) and ADC(2) matrices are respectively 472×472 and 379970×379970.

accuracy of the basis set used and of its ability to reproduce the higher spectral moments. Naturally, the accurate representation of these spectral moments is the key factor responsible for the ability to describe such features as Cooper minima. The deviation of the ADC(1) and ADC(2) cross-sections from the experimental ones are quantified by computing their energy-dependent and energy-averaged relative discrepancies over the covered photon energy region.

The radial B-spline basis set used in the following calculations are described in detail in Table 2.1. Figs. 5.2, 5.3 show the experimental total photoionisation cross section Ref. [188, 189] as well as a series of Stieltjes imaging results obtained via full diagonalisation of the ADC(1) Hamiltonian

matrix and Lanczos diagonalisation of the ADC(2) Hamiltonian matrix, of He and Ne atoms.

Checking the convergence with the maximal angular momentum of the spherical harmonics basis, it has been found that it is generally sufficient, as expected for the one-photon absorption processes described in this work, to truncate the angular expansion at values of $L_{\max}$ corresponding to $L_{\max}^{occ}+1$, where $L_{\max}^{\mathrm{occ}}$ is the maximum angular momentum of the occupied orbitals. In the case of He, the results presented are the one for the $L_{max} = 2$ spherical harmonics expansion, while for Ne atom the spherical harmonics expansion used extends up to $L_{\max} = 3$. In the ADC(2) Ne calculations, $1s$ orbital was frozen in both the singly and the doubly excited intermediate states. The starting vectors for the BL scheme were choosen to be the unit vectors corresponding to selected 1h1p intermediate states with the transition moment from the ground state bigger than a fixed threshold value. Throughout this work, the B-spline ADC(2) cross-sections converged with respect to the number of Lanczos iterations are reported.

One can see that the agreement between the experimental and the theoretical cross sections improves with the order of the ADC scheme. The highest-order ADC(2) result for He essentially coincides with the experimental one apart from the $2s$-np ^1P auto-ionisation resonance region around 60 eV. In the Ne calculation the ADC(1) result shows a displacement of the main peak of about 5 eV, consistently with the GTO ADC calculation of Ref. [104]. The ADC(2) result shows good agreement with the experiment. As expected, in the Ne case as well, the use of SI leads to disagreement between the ADC(2) cross-section and the experimental one in the autoionisation resonance region around 45.5 eV due to the $2s$-np autoionising states. This inability of the Stieltjes-Chebyshev moment theory to reproduce very sharp spectral features is well known and apparently persists also in the B-spline implementation.

At a first glance, the B-spline results have comparable accuracy to the one obtained in Ref. [104] with the GTO-based ADC; however, if one looks carefully at the high energy tail of the cross-section, much better agreement with the experiment is obtained with the B-spline basis set. Details of this analysis are given in Fig. 5.4.

The discrepancy in the Gaussian based calculation arose from the inability of the Gaussian basis to provide a correct description for strongly oscillating

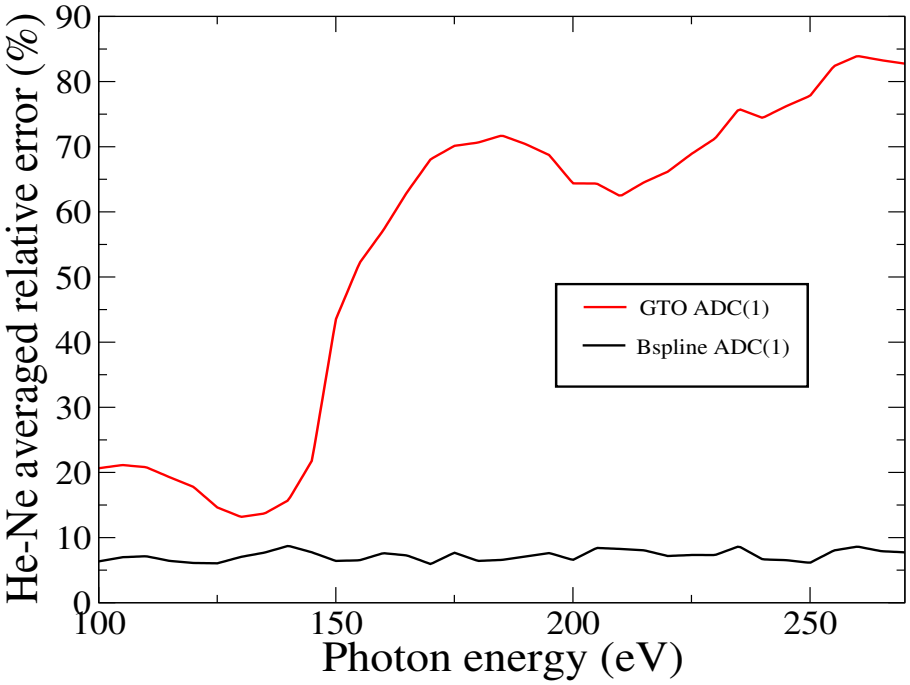

Figure 5.4.: Relative deviations of the calculated ADC-Stieltjes photoionisation cross-sections, averaged over Ne and He atoms, from the experimental result, as a function of the energy in the high energy range, i.e. between 100 eV and 250 eV. Black full line – B-spline-ADC(1)-Stieltjes result, red full line – GTO-ADC(1)-Lanczos-Stieltjes result.

continuum states as well as for high Fourier components of the ground state wave-function [146]. B-splines completely fix this error and give accurate cross-sections up to arbitrary values of the energy, depending on the spatial density on knots used, see discussion in Secs. 2.7 and 5.2.1. Average relative deviations of the computed He and Ne cross-sections from the experimental ones are given in Table 5.2.

The argon photoionisation cross-section is of particular interest for testing the accuracy of the method due to the presence of the Cooper minimum that is known to present a challenge for the GTO calculations. In Fig. 5.5 the B-spline ADC(1) and ADC(2) theoretical photoionisation cross sections of Ar up to 40 eV of photon energy are presented, together with the experimental results of Chang *et al.* [190] and the most recent one of Samson *et al.* [188]. The B-spline basis set parameters used for this calculations are given

ab-initio level	He	Ne	Ar	Kr	average
ADC(1)	6.2 %	12.0 %	11.6 %	7.9 %	9.4 %
ADC(2)	2.5 %	7.5 %	8.1 %	6.0 %	6.0 %

Table 5.2.: Relative deviations of the B-spline ADC-Stieltjes photoionisation cross-sections from the experimental results of Ref. [188] across the energy range of ionisation threshold to 170 eV.

in Table 2.1. The spherical-harmonics expansion extends up to $L_{max} = 3$. In the ADC(2) Ar calculations, the core $1s$, $2s$ and $2p$ orbitals were frozen in both the singly and doubly excited intermediate configurations. Therefore, only the valence holes in the 1h1p and 2h2p state manifold are allowed. One can see that the agreement between the experimental and the theoretical cross sections improves with the order of the ADC scheme. The overall behaviour of the cross-section is very well reproduced with B-splines and the peak position is well reproduced even at the ADC(1) level. The ADC(2) curve, on the other hand, matches better with the experimental data in the energy region from the 3s ionisation limit at 28 eV up to 40 eV. The 3s ionisation limit, which is characterised by the accumulation of autoionisation structures starting from 25 eV up to 28 eV is, however, not resolved by these calculations, as in the case of Ne, due to insufficient energy resolution intrinsic to the SI procedure. The average relative deviations of the computed Ar cross-sections from the experimental ones are given in Table 5.2.

Fig. 5.6 shows the total photoionisation cross section of Ar in the region of the Cooper minimum [191]. The Lanczos convergence of the Cooper minimum shape proved more difficult in this energy region, and it was reached only after almost 30000 iterations. Both ADC(1) and ADC(2) models reproduce the shape of the minimum, with the ADC(2) providing a better quantitative agreement with the experiment in terms of the Cooper minimum position. In fact, ADC(2) gives an almost perfect prediction of the position of the Cooper minimum at 49 eV, while the ADC(1) predicted value is at about 53 eV. The position of the following maximum at 79 eV is overestimated by almost 4 eV from the ADC(1) calculation, while it is underestimated by the nearly the same amount from the ADC(2) one. As it

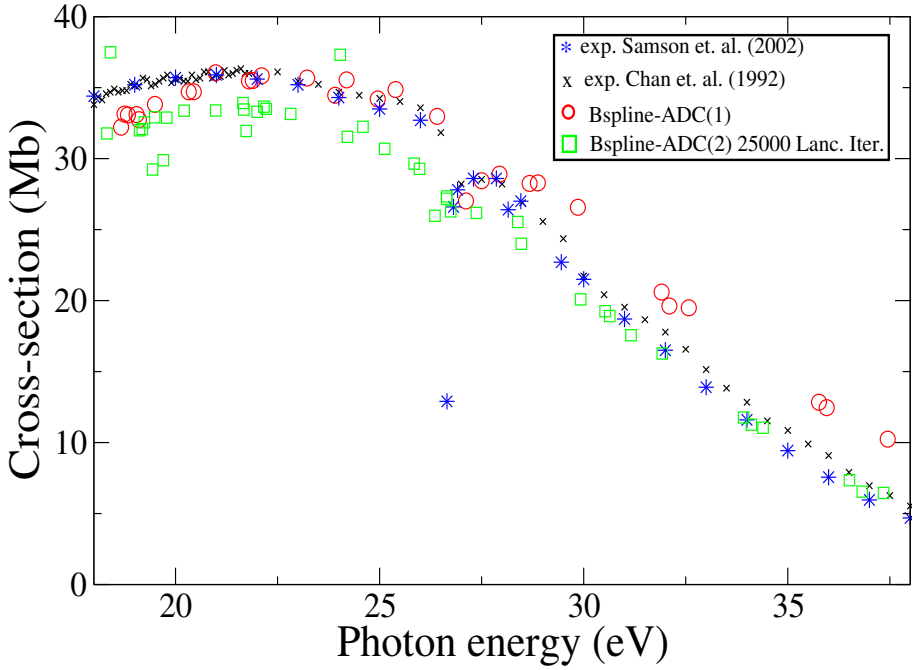

Figure 5.5.: Total photoionisation cross-section of the Ar atom. Stars – experimental result of Ref. [188], crosses – experimental result of Ref. [190], circles – B-spline-ADC(1) result, Stieltjes orders 5 to 18; squares – B-spline-ADC(2)-Lanczos-Stieltjes cross-section, Stieltjes orders 5 to 18, obtained using BL pseudospectrum of 10000 eigenvalues and eigenvectors. B-spline Set 1 was employed (see Table 2.1). With this basis and excitation restrictions, the ADC(1) and ADC(2) matrices have dimension of 602×602 and 396541×396541, while the size of the BL pseudospectrum for which the cross-sections convergence is obtained is 10000.

is possible to notice the ADC(1) result is overall closer to the experimental result of Samson *et al.* [188], while the ADC(2) curve is closer to the experimental result by Chang *et al.* [190]. Both results are also in good agreement with the B-spline TDLDA theoretical calculations in [192], in which the correct normalisation of the final continuum states was performed.

It is worth noting that the Cooper minimum is due to a change of sign of the radial dipole matrix elements, which pass through zero at a certain energy [191], and therefore it is already treatable within one-electron models such as the simple SAE (single active electron approach), as has been verified

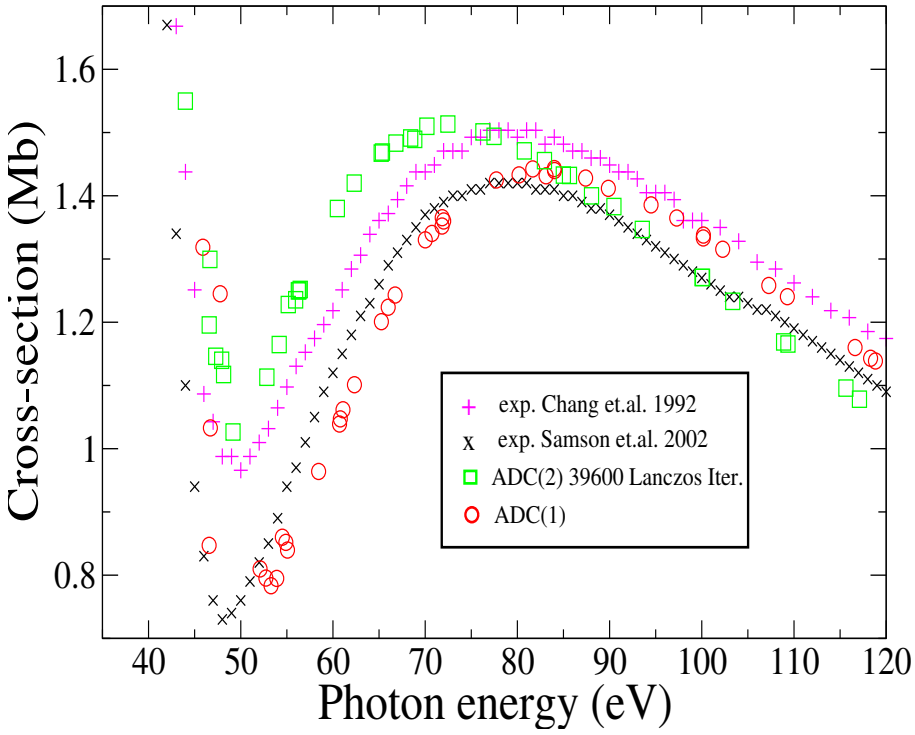

Figure 5.6.: Total photoionisation cross-section of the Ar atom. Crosses – experimental result of Ref. [188], pluses – experimental result of Ref. [190], circles – B-spline-ADC(1) result, Stieltjes orders 25 to 34; squares – B-spline-ADC(2)-Lanczos-Stieltjes cross-section, Stieltjes orders 25 to 34. The size of the BL pseudospectrum for which the cross-sections convergence is obtained is 30000.

within LDA in [192], although its precise energy position may be sensitive to correlation effects. Moreover the possibility of describing properly the Cooper minimum feature is strongly related to the ability of the basis set to properly represent the continuum oscillating single-electron orbitals or, in other words, on the accuracy of the basis set in giving good representation of high order spectral moments in the Stieltjes imaging framework.

In Fig. 5.7 a series of Stieltjes approximations of various orders based on the B-spline ADC(1) and ADC(2) calculation as well as the GTO-based ones are shown for direct comparison. The GTO basis used is the fully uncontracted cc-pCVQZ augmented with 5s7p7d4f KBJ continuum expo-

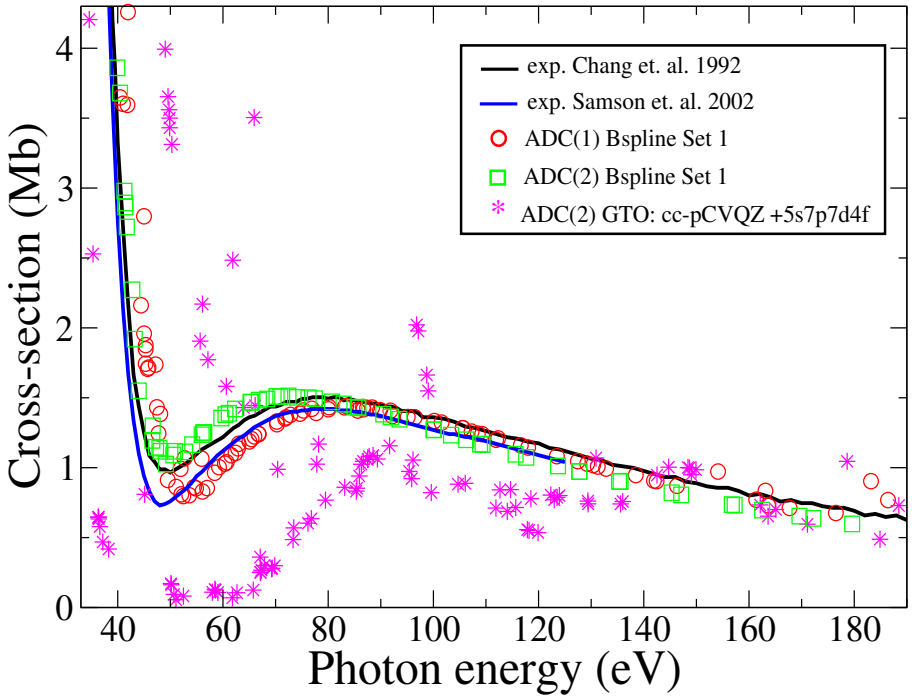

Figure 5.7.: Total photoionisation cross-section of the Ar atom. Full red line – experimental result of Ref. [188], full black line – experimental result of Ref. [190], circles – B-spline-ADC(1) result, from Stieltjes orders 18 to 34; squares – B-spline-ADC(2)-Lanczos-Stieltjes cross-section, from Stieltjes orders 18 to 34, obtained using BL pseudospectrum of 30000 eigenvalues and eigenvectors, stars – GTO ADC(2)-Stieltjes cross-section, from Stieltjes orders 10 to 30.

nents [100]. Importantly, the GTO basis calculation fails completely in this case, in contrast to the present B-spline based one. Clearly, the B-spline calculation shows very good stability of the Stieltjes orders, in contrast to the GTO calculation in which no convergence of the SI procedure can be detected. This, of course, comes at the expense of the much larger size of the B-spline basis that is free of the linear dependency problem.

Finally in Fig. 5.8 the Ar total cross section, in the energy region of the core ionisation from the 2p and 2s orbitals, is presented. As it is possible to notice, good agreement is found in this energy region as well, even if the

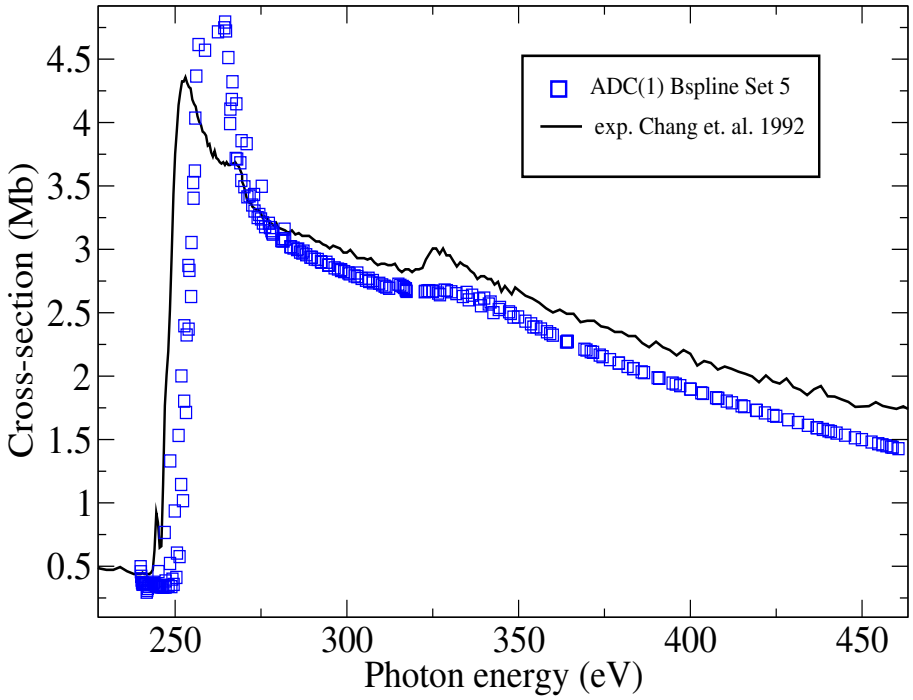

Figure 5.8.: Total photoionisation cross-section of the Ar atom in the inner valence energy region. Full line – experimental result of Ref. [190]; squares – B-spline-ADC(1) result using B-spline Set 4 (see Table 2.1), from Stieltjes order 25 to 34. With this basis, the ADC(1)has dimension of 1728×1728.

position of the peak is shifted to higher energies due to the fact that the core-ionised system is described just as a single hole configuration at the ADC(1) level.

Fig. 5.9 shows the ADC(1) and ADC(2) theoretical photoionisation cross section of Kr in the energy range from 14 eV to 50 eV, together with the experimental results of Chang *et al.* [190] and the most recent ones of Samson *et al.* [188]. The B-spline basis set parameters used for this calculations are given in Table 2.1. The spherical-harmonics expansion extends up to $L_{max} = 3$ both in the ADC(1) and in the ADC(2) cases. In this ADC(2) Kr calculation the $1s$, $2s$, $3s$ and $2p$,$3p$ and $3d$ orbitals, in both the singly and the doubly excited intermediate configuration states, are frozen. Therefore, only single excitations and double excitations from the $4s$ and $4p$ valence orbitals have been allowed. This is enough to describe the outer valence energy region (from the ionisation threshold to 80 eV) completely at the

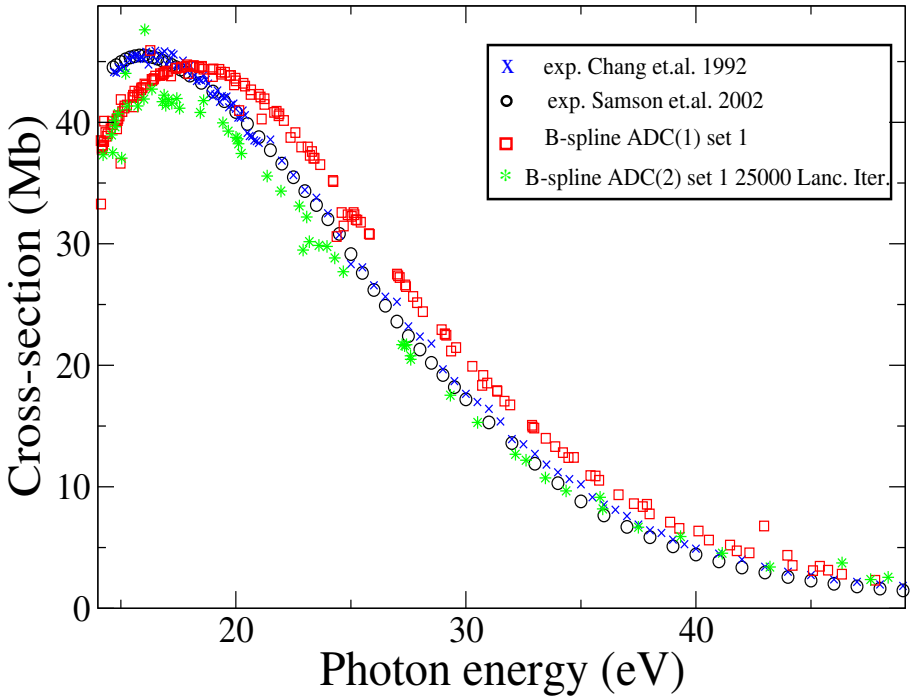

Figure 5.9.: Total photoionisation cross-section of the Kr atom in the outer valence energy region. Circles – experimental result of Ref. [188], stars – experimental result of Ref. [190]; squares – B-spline-ADC(1) result using B-spline Set 4 (see Table 2.1), from Stieltjes order 5 to 18. With this basis, the ADC(1) and ADC(2) matrices have dimension of 1728×1728 and 1921110×1921110 respectively, while the size of the BL pseudospectrum for which the cross-sections convergence was obtained used is 32000.

ADC(2) level.

As in the case of argon, the overall behaviour of the cross-section is very well reproduced with B-spline ADC(1), even if the position of the peak is shifted to higher energy with respect to the experimental one, by about 2 eV. As has already been shown using the GTO calculations [146] this is a general feature of the ADC(1) level of theory that overestimates the final state energies. The decreasing behaviour of the cross-section is correctly displayed by both theoretical curves, but better agreement with the experiment is obtained by the ADC(2) method. Average relative deviations of the computed Kr cross-sections from the experimental one are given in Table 5.2.

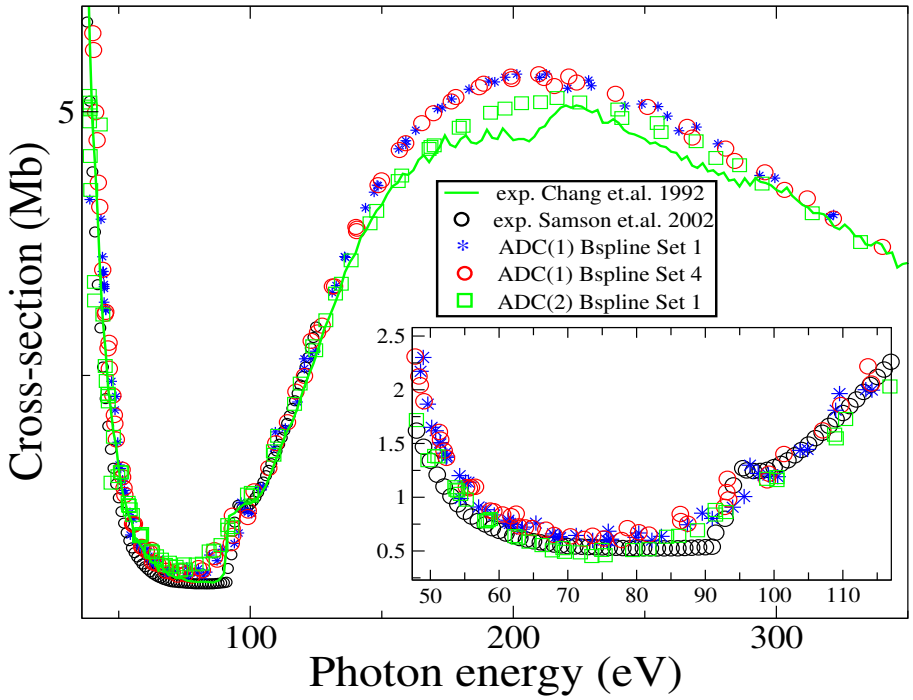

Figure 5.10.: Total photoionisation cross-section of the Kr atom. Circles – experimental result of Ref. [188], full green line – experimental result of Ref. [190]; stars – B-spline-ADC(1) result using B-spline Set 1, from Stieltjes orders 5 to 34; circles – B-spline-ADC(1) result using B-spline Set 4, from Stieltjes orders 5 to 34; squares – B-spline-ADC(2)-Lanczos-Stieltjes cross-section, from Stieltjes orders 18 to 34, obtained using BL pseudospectrum of 30000 eigenvalues and eigenvectors.

Fig. 5.10 shows the ADC(1) and ADC(2) cross-sections for Kr in a higher energy region which includes three inner ionisation limits: $3d$, $3p$ and $3s$. In this ADC(2) Kr calculation the $1s$, $2s$, $3s$ and $2p$ and $3p$ orbitals, in the doubly excited intermediate configuration states, have been frozen. The interval from $3d$ up to $3p$ ionisation is about 100 eV wide and is characterised by an experimental sigmoid shape with a broad maximum just below the $3p$ limit. The theoretical curves in this range have the correct shape, but they are at higher values than the experimental one. Moreover the SI prevents, in this case, the possibility of reproducing the $3p$ and $3s$ channel-opening step. At energies above the $3p$ and $3s$ limits the calculations give an almost linear decreasing curve, with a negative slope that correctly reproduces the

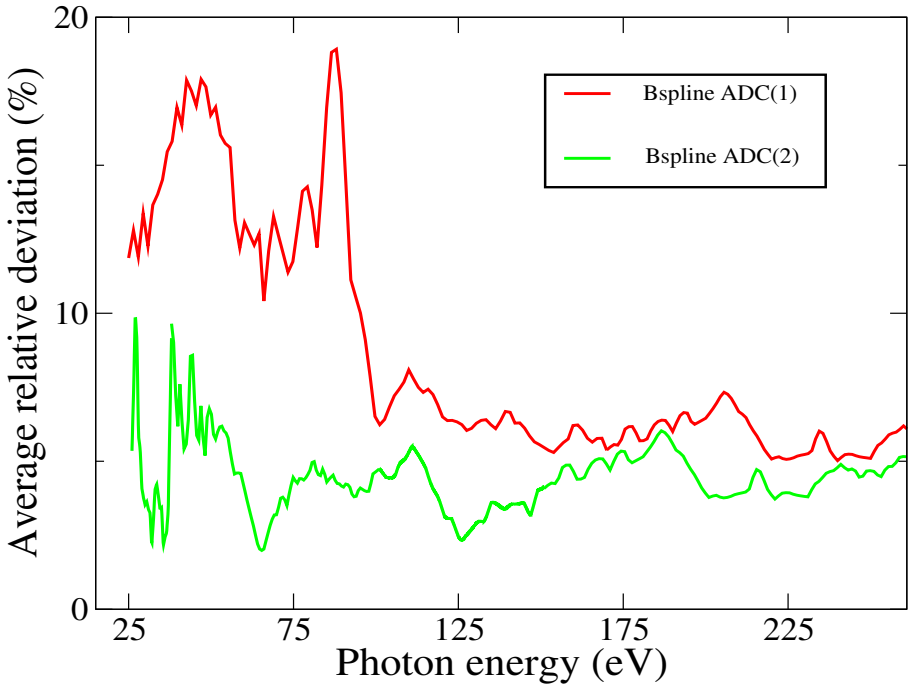

Figure 5.11.: Relative deviations of the B-spline-ADC-Stieltjes photoionisation cross-sections from the experimental results averaged on the four closed shell atoms calculated, namely He, Ne, Ar and Kr, as a function of the energy in the energy range of He ionisation threshold to 260 eV. Green line – ADC(1)-Stieltjes result, red line – ADC(2)-Lanczos-Stieltjes result.

experimental one.

Finally, it is interesting to analyse the relative deviations of the two *ab-initio* methods as a function of the photon energy in the same way it has been already done in [146] for the GTO-ADC calculations. This is done in Fig. 5.11 where one observes that below 100 eV both ADC(1) and ADC(2) methods lead to impressive agreement with experiment with the relative deviations around 14% and 4% respectively. Moreover, the precision deterioration at higher energies typical of the GTO calculations [146] is not present any more, the average error stabilizing around 5% for both methods.

5.2.1. Stieltjes imaging stability

Finally, it is relevant to discuss more about the characteristics of the SI technique when used together with B-splines basis sets. The accuracy of

Stieltjes imaging technique is usually limited by both the ability of the chosen $\mathcal{L}^2$ basis set to represent continuum functions within the interaction volume and by the numerical instability of the computational algorithm of the Stieltjes-Chebyshev moment theory. As already discussed, the B-spline basis set removes the first limitation, accurately representing the continuum functions within the interaction volume and making it possible to correctly reproduce many high-order spectral moments. The immediate consequence of this is that a considerable number of Stieltjes orders becomes reliable and, as a result, the energy resolution is significantly improved. Even if this resolution is in general not yet enough to describe very sharp features, e.g. resulting from series of closely lying autoionisation resonances, the improvement allows one to correctly describe the shape of the Cooper minimum in the argon atom and the $3d$ channel opening in the krypton atom.

Fig. 5.12 shows how the Stieltjes orders converge towards the Cooper minimum in argon; as it is possible to see, low orders smooth out the minimum because of the insufficient resolution while high orders correctly reproduce it. This is why in the GTO calculations, in which only the low orders are accurate, it is very challenging to obtain the correct Cooper minimum shape.

In the following it is shown how the stability of the Stieltjes procedure is affected by the quality of the B-spline basis set. The stability of the Stieltjes results can be quantified by the number of consequent Stieltjes orders that consistently reproduce the same cross-section shape. In Fig. 5.13 the Stieltjes stability is analysed for the Ar cross-section in the energy region from threshold up to 45 eV. The analysis is performed for each of the B-spline sets of Table 2.1. One can see that in the case of Set 1, there are many scattered points present in the set of high orders between $n = 23$ and $n = 34$, i.e. at the same range of orders which gives the convergent Cooper minimum within the same basis set at higher energy. However, when the dimension of the box is increased maintaining the same grid step, a perfect stability up to the last order $n = 34$ is obtained; this is shown in the top-right panel where Set 2 results are plotted and it means that the accuracy of this B-spline basis set is such that the higher Stieltjes orders correctly reproduce the overall shape of the cross-section in an energy range of 170 eV. This happens because when the B-spline basis set changes from Set 1 to Set 2 the density of points, in the energy domain, the continuum is discretised with increases.

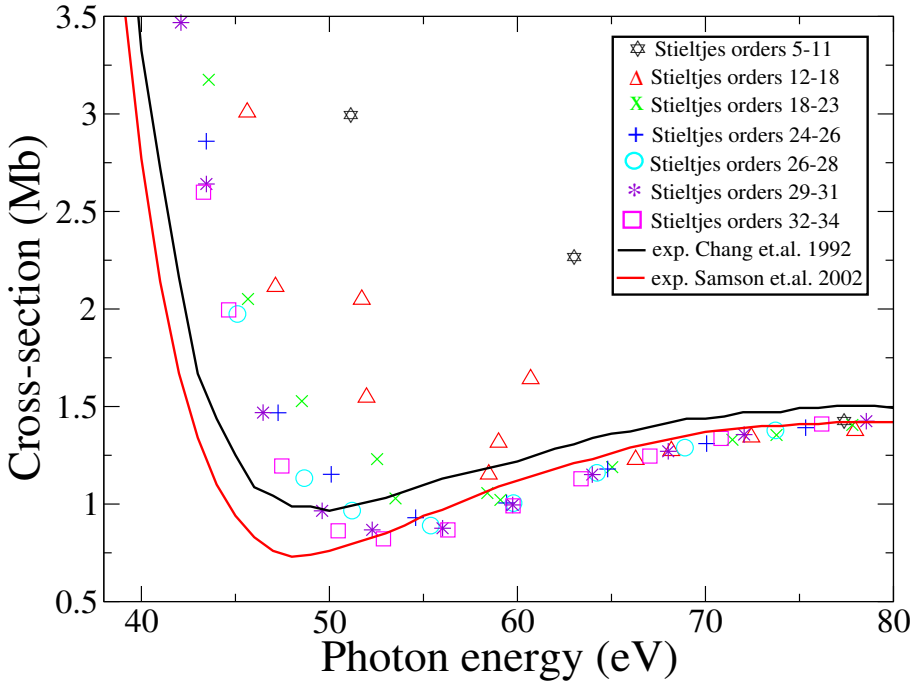

Figure 5.12.: Total photoionisation cross-section of the Ar atom in the Cooper minimum energy region. Convergence with respect to the Stieltjes order n is shown for a B-spline ADC(1) calculation done with B-spline Set 3. Different symbols represent different orders as indicated in the legend. Full red line – experimental result of Ref. [188], full black line – experimental result of Ref. [190].

Stability can be achieved also with a linear grid over the entire radial range. As an example, results obtained using the B-spline Set 3 are shown in the left-bottom panel of Fig. 5.13; they show scattered points at high orders, mostly concentrated near the threshold, up to 22 eV. Set 3 can be considered as an intermediate case, between Set 1 and Set 2, from the point of view of the continuum discretization density. When the density of continuum discretization is increased even more, perfect stability is achieved also with a linear grid, as it is shown in the right-bottom panel of Fig. 5.13, where the results obtained with the Set 4 are shown.

In order to provide a further comparison between the performance of the B-spline basis set with respect to the GTO ones, Fig. 5.14 shows the stability plot for the neon atom in the energy region from threshold up to 300 eV,

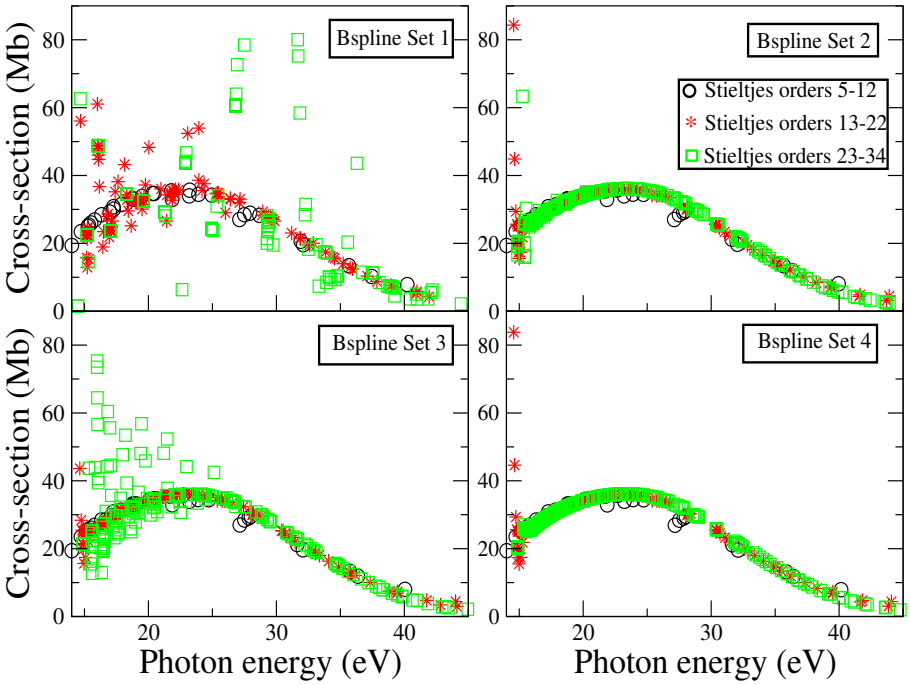

Figure 5.13.: Stability of the photoionisation cross-section Stieltjes orders results for the Ar atom, for the 4 different knots sequences corresponding to B-spline Set 1-4 (see Table 2.1).

both for B-spline Set 4 and for two GTO basis sets. The Stieltjes orders from $n = 10$ to $n = 30$ have been plotted. As is clear form the plot, no Gaussian Stieltjes point stay on the correct profile. In such Gaussian basis sets calculations, the cross-section is obtained only from the orders from $n = 5$ to $n = 9$.

Fig. 5.15 and Fig. 5.16 show respectively the B-spline ADC(1) theoretical photoionisation cross sections of the N_2 and CO_2 molecules in the energy range from the first ionisation threshold to 140 eV, together with the experimental results of Samson *et al.* [193] and the ones of Chan *et al.* [159]. The B-spline basis set parameters used for this calculations are given in Table 2.1. The spherical-harmonics expansion used in the calculation extends up to $L_{max} = 30$ for both molecules.

Also in the case of linear molecules, the B-spline results have comparable accuracy to the one obtained in Ref. [104] with the GTO-based ADC in the energy region close to the first ionisation threshold; however, as for the atomic cross-section calculations, if one looks carefully at the high energy

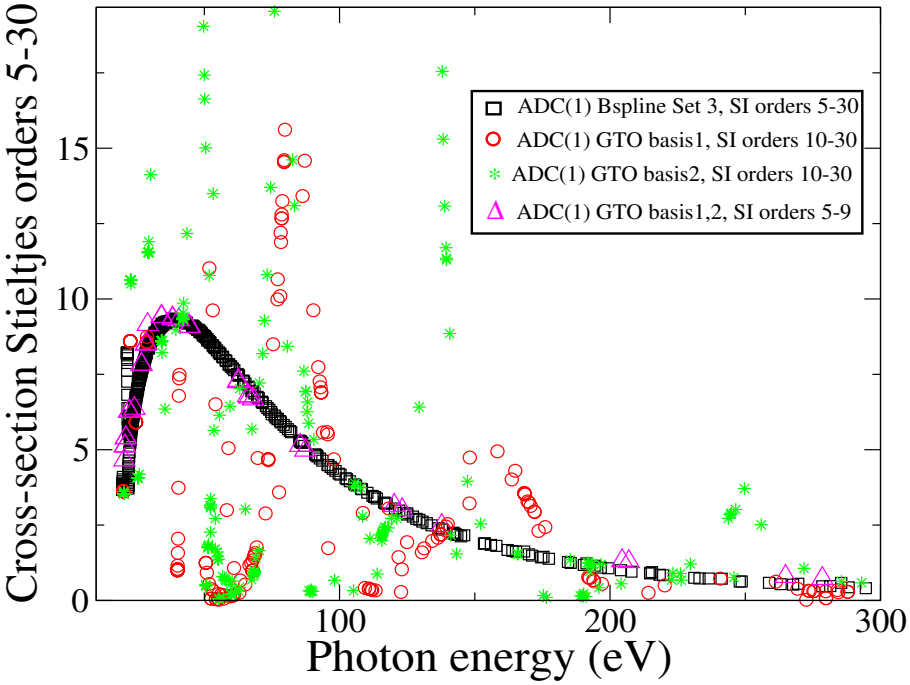

Figure 5.14.: Total photoionisation cross-section of the Ne atom. Squares – B-spline-ADC(1) result using B-spline Set 4, from Stieltjes order 5 to 30, circles– GTO-ADC(1) result, Stieltjes orders 10 to 30 obtained with basis 1, namely cc-pCVTZ basis set augmented by 4s6p4d KBJ diffuse continuumlike functions, stars– GTO-ADC(1) result, Stieltjes orders 10 to 30 obtained with basis 2, namley cc-pCQTZ basis set augmented by 6s7p6d KBJ diffuse continuumlike functions, up triangles– GTO-ADC(1) result, Stieltjes orders 5 to 9 obtained with both GTO basis 1 and 2.

tail of the cross-section, much better agreement with the experiment is obtained with the B-spline basis set.

In the case of the CO_2 molecule, the first plateau which is present in the experimental cross section at a photon energy around 35 eV and which was well reproduced by both GTO-based second order ADC(2) and ADC(2)x methods, see Fig. 3.8, is not reproduced by the B-spline ADC(1) result reported here as its description requires the inclusion of double excitations. On the other hand, the second plateau present in the experimental cross section at around 55 eV, that was missed completely by both the first-order ADC(1) and second-order ADC(2) GTO results, is now fully reproduced by

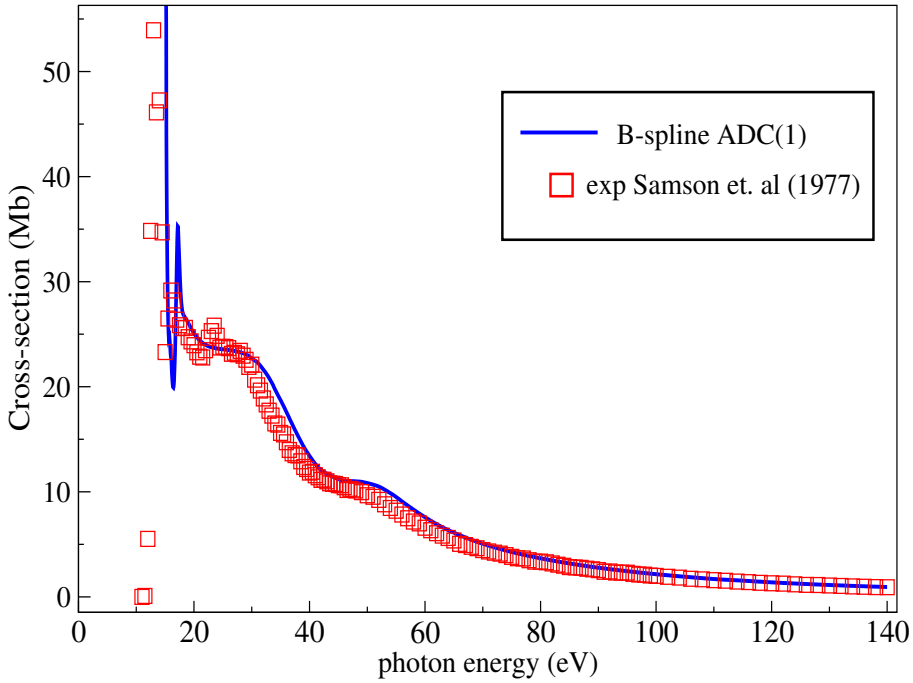

Figure 5.15.: Total photoionisation cross-section of N_2 molecule. Squares – experimental result of Ref. [193], full line – interpolated B-spline-ADC(1) result (Stieltjes orders 25 to 29).

the B-spline first order ADC(1) SI results. This is due to the fact that its description requires just single excitations and that the low resolution of the GTO converged Stieltjes orders, interpolated to obtain the cross-sections, in the 45-65 eV energy range has been considerably improved by the B-spline result. Indeed, while in the GTO calculations the relevant stable Stieltjes orders used to obtain the interpolated cross-section were 6-10, the B-spline Stieltjes orders show much higher stability and the reported cross-section has been obtained interpolating the Stieltjes points accumulating from the Stieltjes orders 25-29.

5.3. Summary

In the present work, the B-spline implementation of the first- and second-order ADC schemes for electronic excitations has been presented. Pho-

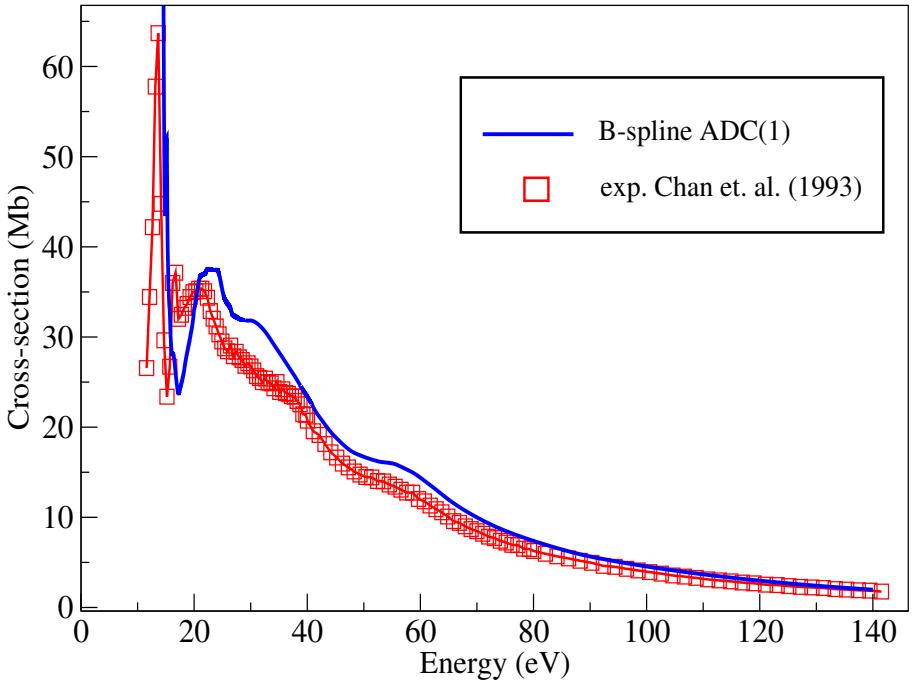

Figure 5.16.: Total photoionisation cross-section of CO_2 molecule. Squares – experimental result of Ref. [159], full line – interpolated B-spline-ADC(1) result (Stieltjes orders 25 to 29).

toionisation cross-sections are natural computational targets for the newly-implemented technique; therefore the advantages of the B-spline ADC have been demonstrated here by performing a series of atomic photoionisation cross-section calculations. In particular, it has been possible to correctly predict the shape and position of the Cooper minimum in the total cross-section of argon, within the SI moment theory technique. The superior accuracy of the newly-implemented basis set is manifested also by its ability to correctly reproduce the high-energy tails of the cross-sections that have been shown to present a notorious difficulty for the GTO-based schemes [146]. They are indeed reproduced by the B-spline ADC in excellent agreement with the experiment. Total B-spline ADC(1) photoionisation cross-sections of N_2 and CO_2 molecules are also presented; as in the case of the noble gas atoms calculations, in the molecular case the high-energy tails are found to be much better reproduced than with the analogous GTO-based

ADC(1) calculations. Apart from the strongly improved accuracy, the B-spline implementation leads to a remarkable stability of the cross-sections with respect to the order of the Stieltjes-Chebyshev moment theory. While the moment theory method leads to a straightforward comparison between the performance of the GTO and B-spline bases, it is no longer a necessity within the B-spline ADC. Indeed, one can obtain directly the correctly normalised continuum eigenstates at arbitrary values of the energy in the electronic continuum by employing methods of Refs. [115, 117]. This should be one of the directions for future work. Another plausible direction of future work is generalisation of the B-spline implementation to calculation of the decay widths within the Fano-Feshbach formalism, see Refs. [99] on the GTO-based Fano-ADC methods.

In view of the large (compared to GTO) size of the B-spline bases, optimised implementation of the B-spline method within the MPI and OpenMP protocols has been realised, making the future calculations of molecular systems entirely possible. The CPU time required for the type of cross-section calculations presented in this thesis is, for example, of the order of a few minutes for the ADC(1) method and of a few hours for the ADC(2) level of theory, when using 20 computational cores.

6. Time-dependent B-spline ADC: many-electron laser driven dynamics

6.1. High-order harmonic generation in Ar atom

In order to apply the correlated ADC schemes to the solution of time-dependent many-electron problems involving ionisation, we have implemented a time-dependent version of the *ab-initio* B-spline ADC method.

The time-dependent problem is solved within TD-ADC making the following ansatz for the time-dependent electronic wave-function:

$$\mid \Psi(t)\rangle = C_0(t) \mid \Psi_0(t)\rangle + \sum_n C_n(t) \mid \Psi_n(t)\rangle \tag{6.1}$$

where the coefficients $C_0(t)$ and $C_n(t)$ refer to the ground-state and to the ECO-CES ADC configuration basis states respectively.

The time-dependent Schrödinger equation (TDSE) for the unknown coefficients C_0, C_n is solved via the short iterative Arnoldi-Lanczos algorithm described in Sec. 2.8. Using this time propagation technique one has to deal at each time step with a repetitive diagonalisation of an upper-Hessenberg matrix much smaller then the full systems Hamiltonian. In this way, the whole scheme becomes applicable to relatively large basis sets, which are practically inaccessible within approaches demanding a full diagonalisation of the secular matrix. The time propagation is parallelised both within the MPI and OpenMP schemes. The allocation of the relevant Hamiltonian and dipole matrices is distributed across the various MPI nodes and within each node the matrix-vector multiplications required to build the Hessenberg matrix are speeded up via OpenMP.

In this section a first application of the newly-implemented B-spline TD-

ADC technique, by calculating the HHG spectrum of the Ar atom, is presented. Here we again concentrate on the effect of the Cooper minimum, since besides its basic importance for photoionisation, it also has recently drawn much attention in connection to the HHG by rare gases [194, 195]. Calculation of the HHG spectrum of the Ar atom interacting with an intense and short infrared (IR) laser pulse allows for the illustration of the effect of the Cooper minimum on the HHG spectrum by a fully *ab-initio* single-atom simulation.

In the following calculation we have used the first-order method of the ADC-hierarchy, namely ADC(1). The HHG spectrum is calculated here via the expectation value of the electric dipole moment $z(t)$, see Eq. (2.173).

The results presented were calculated making explicit use of the atomic spherical symmetry. We used two laser pulses with a carrier frequency $\omega = 0.057$ a.u. (800 nm), a full width at half maximum (FWHM) pulse duration of $\tau = 413$ a.u. (10 fs) and with a peak field strength of $E_{max} = 0.075$ a.u. and $E_{max} = 0.095$ a.u respectively. These two values correspond to peak intensities of $I = 1.5 \times 10^{14}\,\mathrm{W/cm^2}$ and $I = 3.2 \times 10^{14}\,\mathrm{W/cm^2}$ respectively. The time-step used in the calculation is equal to 0.2 a.u. (1/500 of the IR period) at which value the convergence of our final results is obtained.

The intensity profile of the stronger intensity infrared (IR) pulse is shown in Fig. 6.1. The time-dependence of the ground-state depopulation which occurs during the interaction of the Ar atom with the strong IR field is given by $1 - \varrho_0(t) = 1 - \mid C_0(t) \mid^2$ and it is plotted in Fig. 6.1 as well.

In the Ar HHG spectrum calculation, the size of the computational box, R_{max}, is dictated by the semiclassical picture of the process [126], i.e. it must be large enough to contain the longest recolliding electronic trajectories. The classical quiver amplitude of the electron for the higher intensity pulse we are using is $r_{HHG} = \frac{E_{max}}{\omega^2} = 30$ a.u. The calculation is performed using a radial grid radius $R_{max} = 120$ and 200 radial grid points (B-spline basis Set 5, see Table 2.1). A complex absorbing potential (CAP) has been used in order to eliminate wavepacket reflection effects from the grid boundaries. The form of the CAP used was the following:

$$\hat{W} = \eta(r - r_{CAP})^2 \ , \ r \geq r_{CAP} \tag{6.2}$$

and with the addition of the CAP term the form of the total time-dependent

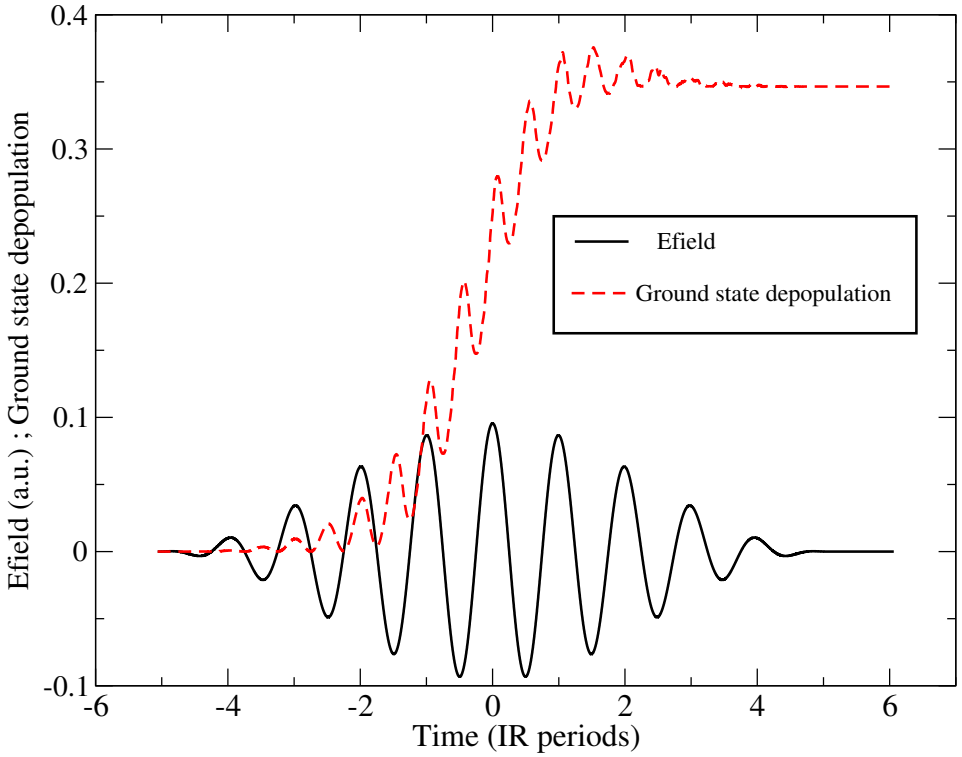

Figure 6.1.: Time dependent IR electric field (in a.u.) used in the calculation. The IR peak intensity is $3.2 \times 10^{14}\,\mathrm{W/cm^2}$. Also shown is ground state depletion (unitless) of the Ar atom.

Hamiltonian of the system reads

$$\hat{H} = \hat{H}_0 + \hat{z}E(t) - i\hat{W} \tag{6.3}$$

where $\hat{H}_0$ is the field-free Hamiltonian and $\hat{z}E(t)$ is the laser-atom interaction in length form and within the dipole approximation. The CAP starts at a radius $r_{CAP} = 100a.u.$ and has a strength $\eta = 0.0005$. The maximum angular momentum employed was $l_{max} = 70$.

The HHG spectral intensity profile is shown in Fig. 6.2, for both the two different IR intensities used. The smaller intensity used gives a cutoff energy for the HHG emission at about 50 eV. The photon energy range of 30-50 eV corresponds to a recollision electron energy range of 15-35 eV and therefore no Cooper minimum is observed in the corresponding HHG spectrum. Conversely, the higher intensity provides higher kinetic energy

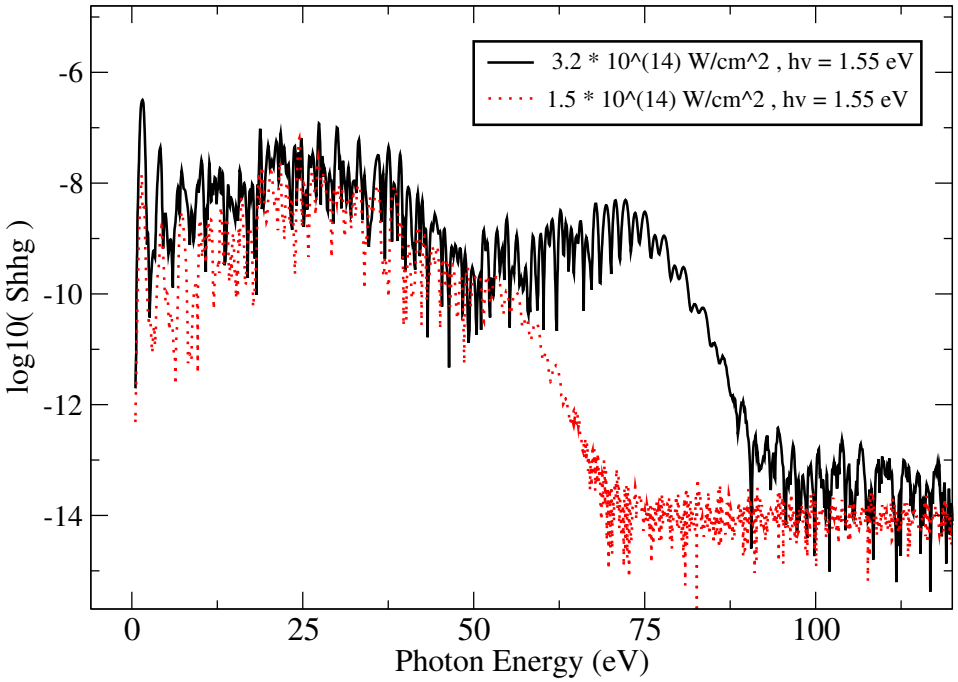

Figure 6.2.: ADC(1) high harmonics generation emission spectrum of the the Ar atom interacting with an IR field. The red and black curves refer to the 1.5×10^{14} W/cm^2 and 3.2×10^{14} W/cm^2 values for the IR peak intensity respectively. The time duration of the IR laser pulse used is about 21 fs and the wavelength is 800 nm.

for the returning electrons, and therefore makes it possible to see the Cooper minimum shape in the HHG spectrum.

Our simulation shows that the Cooper minimum in the HHG spectra can be reproduced by the B-spline TDADC method and its position indeed lies slightly above 50 eV as found in the recent experiments [195]. The results are also in good agreement with those of Ref. [196], obtained using the time-dependent CIS technique. The position of the HHG Cooper minimum is very much consistent with the photoionisation cross-section one. This has to do with the final step of the HHG process [126], where the laser-driven continuum electron recombines into the ground state emitting a single photon in a process that is directly reversed relative to the photoionisation.

6.2. Total and channel resolved ADC(1) high harmonic generation spectra of aligned CO_2 molecule

High-order harmonic generation spectroscopy (HHG) is a powerful technique to resolve ultrafast electron dynamics in atoms and molecules [128, 129, 130, 131, 132, 133, 60, 126, 127]. It has often been assumed that structures in the harmonic spectra reflect the geometry of the highest occupied molecular orbital (HOMO) [128, 130, 134, 197, 198, 199, 200, 201, 202, 203]. Indeed, strong-field ionisation is exponentially sensitive to the ionisation potential I_p, suggesting that after ionisation the molecular ion is left in its ground electronic state (electron removal from HOMO in the Hartree-Fock picture). In this case, even though rearrangement has occurred, only structural information will be recorded in the harmonic spectrum. However, in molecular ions electronic excitations often lie within a couple of electron volts from the ground state, leading to sizeable population amplitudes even for exponential scaling of ionisation rates. The geometry of the molecular orbitals is also crucial [204, 205] and can further increase relative populations of the excited electronic states of the ion (tunnelling from deeper orbitals in the Hartree-Fock picture). The importance of different orbitals in high harmonic generation has been pointed out in various experiments [62, 206]. Moreover, clear evidence for strong-field ionisation from lower orbitals has demonstrated the importance of including multiple orbitals in the description of HHG [60, 62, 207].

Different states of the molecular ion between ionisation and recombination provide different channels for the HHG process. The orbitals relevant for ionisation and recombination are the Dyson orbitals, the overlaps between the multi-electron ground state wave-function of the neutral system and the ground/excited state wave-function of the ion, which, within the ADC(1) method, coincide with the occupied HF orbitals of the neutral system [208].

For each channel, specific electronic structure is encoded onto the amplitude and the phase of the harmonic emission signal. These channels are different pathways that take the system from the same initial to the same final state via different states of the ion. They provide a basis for recording multielectron dynamics, including dynamics of electron rearrangement

upon ionisation. Their interference records the relative phases between the channels by mapping them onto the amplitude modulation in the harmonic spectra. The phases between the channels, accumulated between ionisation and recombination, encode the underlying electronic dynamics with attosecond time resolution. The coherent sum of the multiple channels can thus reveal both structural minima due to the recombination matrix elements or dynamical minima that occur from destructive interferences between channels.

If the minimum is structural as in argon, its position is largely independent of the laser parameters including wavelength and intensity [134, 135, 195, 209]. If the minimum is dynamical, the interference of the orbitals can be controlled directly by the intensity and the wavelength of the IR driving laser field.

In addition to the relative phase of the channels, the structure of the orbitals can lead to a significant phase variation in the recombination matrix element that also affects the observed minimum position.

In the harmonic spectrum of the CO_2 molecule, minima have been found at vastly different positions in different experiments [130, 197, 198, 199, 61]. A spectral minimum observed in CO_2 molecules aligned parallel to the generating laser field was found at 39 eV in [130], at 54 eV in [197], and in a range of intermediate positions, depending on the intensity, in [60, 61]. Even though the structure of the molecule is the same, the minimum appears at different places because it shifts with the laser intensity. Its position and mobility reflect attosecond multielectron dynamics within the ion, including electron rearrangement upon ionisation.

The two most common theoretical approaches for describing molecular HHG are the semiclassical strong-field approximation (SFA) [68], which has been extended to include Coulomb-interaction corrections [135, 210, 211, 212], and the single-active-electron (SAE) approximation [4, 213, 194, 214, 215], where the electron-ion interaction for many-electron systems is described by a model potential [194]. A number of theoretical works based on the SFA approximation and on extensions of this have been performed during the last few years. Recent work suggests that the ionisation from multiple orbitals ($HOMO$ and $HOMO-2$) is responsible for the intensity dependence of the minimum position [60]; other works suggest that the effect of the strong laser field on a single orbital can explain the intensity

dependence [130, 197, 198, 216] in CO_2 molecules aligned parallel to the driving field, whereas another work suggests that both the interference of multiple orbitals and their structural characteristics can affect the position of the minimum [61, 217]. The results presented in [61] show that in addition to the interference of multiple orbitals (HOMO and HOMO-2), the structure of the highest occupied molecular orbital (HOMO) affects the position of the minimum. Indeed, the interference of the recombining electron with the 2-centre HOMO results in strong phase variation of the recombination matrix element with photon energy. It is now generally recognised that the minimum present in the HHG spectrum of CO_2 has a dynamical nature and it is the result of the fact that more than one ionisation channel contributes to the total intensity spectrum.

In this work we perform a fully 3-D *ab-initio* time-dependent calculation for the electron dynamic of the CO_2 molecule interacting with an high-intensity ultra-short infrared (IR) laser pulse, calculating the high-order harmonic generation spectra and quantitatively investigating the effect of its multi-channel nature on the dynamical minimum. The calculation has been performed using the molecular time-dependent version of the *ab-initio* first order ADC(1) many-body Green's function scheme for the polarisation propagator, implemented in the B-spline single-electron basis set.

Our aim, besides testing the accuracy of the newly developed molecular time-dependent code, is to accurately reproduce the experimental observations, for the first time using a completely 3-D *ab initio* method for this purpose, while also understanding if more ionisation channels, other than $HOMO$ and $HOMO-2$, contribute to the total CO_2 HHG spectrum and whether, and to which extent, the effect of the interchannel couplings onto the dynamics of the various ionisation channels influences the position of the dynamical minimum.

The interaction of the liberated electron with the ionic hole state, from which it originates, is referred to as intrachannel interaction and leads for large electron-ion distances to the $1/r$ behaviour of the Coulomb potential. If the liberated electron is influenced by other molecular orbitals (channels) the interaction is referred to as interchannel coupling [218]. Within the ADC(1) scheme, both couplings between the different ionisation channels contributing to the HHG spectrum, the one induced by the electric-field and the one induced by the full Coulomb interaction, are taken into account.

Hence, in this work, the effect onto the interference pattern, which originates from the different phases and intensities of the various harmonic emission channels, due to both the electron rearrangement within the ion driven by the electric field dipole couplings

$$D_{ai,bj}E(t) = -\delta_{a,b}\langle i \mid \hat{d} \mid j\rangle E(t)\ i \neq j\,, \tag{6.4}$$

and the multielectron dynamics driven by the inter-channel Coulomb couplings

$$H^{[1]}_{ai,bj} = -V_{aj[bi]} = -\langle aj \mid\mid bi\rangle\ i \neq j\,, \tag{6.5}$$

is automatically included. Moreover, the residual electron-ion intrachannel interaction is described in detail, including multipole effects. While the couplings driven by the electric field can be included into the SFA approach, Coulomb multichannel interactions [218] go beyond the independent-particle picture and cannot be captured in the language of SFA and SAE.

In order to investigate the role of the different channels, and to better understand the effect of their interaction, the HHG spectrum of CO_2 was calculated not only at the full ADC(1) level of *ab-initio* theory, but also at two different levels of approximation. The first level of approximation consists in setting to zero the interchannel coupling due to the electron-electron Coulomb interaction and will be referred to as *model-2* in the following; the second and lower level of approximation consists of setting to zero both the interchannel couplings due to the Coulomb interaction and the interchannel couplings driven by the ionic dipole transitions induced by the IR electric field and will be referred to as *model-3* in the following.

Additionally, for each of these models, the orbital-resolved contributions to the total HHG spectrum are also calculated. The orbital resolved spectra that are presented in the following are obtained by performing the multichannel simulations, at the various level of approximation described above, and calculating the contributions to the induced dipole coming from the excited configurations corresponding to each specific occupied orbital $\mathbf{i}$ respectively:

$$D^{\mathbf{i}}(t) = \langle \Psi_{\mathbf{i}a,0}(t) \mid \hat{D} \mid \Psi_{\mathbf{i}b,0}(t)\rangle\,, \tag{6.6}$$

where

$$\mid \Psi_{\mathbf{i}a,0}(t)\rangle = C_0(t) \mid \Psi_0\rangle + \sum_a C_{\mathbf{i},a}(t) \mid \Phi^a_{\mathbf{i}}\rangle\,. \tag{6.7}$$

Therefore the single-orbital contributions obtained in *model-3* are of the pure single active electron flavour, while the contributions obtained within the ADC(1) model and within *model-2* take into account, at different levels of accuracy, the effect of the channel couplings on each single-orbital resolved spectrum.

The first step in the calculation is the solution of the discretised closed-shell Hartree-Fock equations (Eq. (2.150)) which, in the molecular case is solved for every irreducible representation (IRREP) of the molecular point symmetry group. In the case of the carbon dioxide molecule, whose point symmetry group is $D_{\infty h}$, the number of spherical harmonics belonging to each IRREP is equal to $L_{max}+1$ for Σ_g and to L_{max} for all the other IRREPS $(\Sigma_u, \Pi_u, \Pi_g, ...)$. Here the maximum angular momentum used in the calculation has been set to be $L_{max} = 50$. Solving Eq. (2.150) self-consistently, we obtain a quasi-complete set of canonical occupied and virtual HF molecular orbitals, expressed in terms of B-spline basis functions. The calculations have been performed using a linear B-spline knot sequence with a radial box radius $R_{max} = 160$ a.u. and 205 radial grid points (B-spline basis Set 6, see Table 2.1). The list of active Hartree-Fock occupied orbitals of the CO_2 molecule used in the following calculations are, in energetically increasing order, $4\sigma_g$, $3\sigma_u$, $1\pi_u$ and $1\pi_g$. Therefore, in this work, we have included a total of four ionisation channels that contribute to harmonic emission of CO_2 molecules; they respectively correspond to creating the CO_2 ion in the ground state $^1\Pi_g$ (channel X), in the first excited state $^1\Pi_u$ (channel A), in the second excited state $^1\Sigma_u^+$ (channel B) and in the third excited state $^1\Sigma_g^+$ (channel C) respectively. Within ADC(1) they respectively consist of, in the molecular orbital picture, the removal of a bound electron from the $HOMO$, $HOMO-1$, $HOMO-2$ and $HOMO-3$ HF orbitals. While the correspoding experimental ionisation potentials are respectively 13.8, 17.3, 18.1 and 19.36 eV [219] and therefore span a 5.56 eV energy range, the ADC(1) ionisation potentials obtained in this calculation are 15.3, 18.81, 19.6 and 20.7 eV spanning a 5.7 eV energy range. In Table 6.1 a comparison between the experimental orbital/ionisation energies of the CO_2 molecule and the theoretical results obtained by means of two HF calculations performed using the B-spline basis Set 6 and the cc-pcvTZ Gaussian basis set respectively is shown. The GTO HF calculation was performed using the MOLPRO quantum chemistry package [220].

Experimental I.P.s (eV) [219]	HF B-splines basis Set 6 I.P.s (eV)	HF cc-pcvTZ GTO basis I.P.s (eV)
13.8	15.03	14.74
17.3	18.81	19.31
18.1	19.6	20.126
19.36	20.7	21.76

Table 6.1.: Orbital/ionisation energies of the CO_2 molecule. Comparison between the experimental values and the theoretical results obtained by means of an HF calculation using the B-spline basis Set 6 and the cc-pcvTZ Gaussian basis set.

In this work, the multi-electron ECO-CES configurations built with the HF orbitals are both spin-adapted and point-symmetry group adapted ones. Therefore we take into account the full symmetry of the molecule, not only in the HF one-particle calculation but also in the many-electron ADC one. The calculations have been performed for the case of a laser field linearly polarised along the molecular axis, and therefore the quantum number M representing the total electronic axial angular momentum is conserved. Consequently, it is enough to consider only the two multi-electron spaces corresponding to the irreducible representations Σ_g^+ and Σ_u^+.

To simulate experimental conditions, the contribution of the 'long trajectories' has been filtered out. Indeed, in a molecular gas propagation of harmonic radiation associated with short and long trajectories is different in terms of both the phase-matching and the divergence. In typical experiments on high harmonic generation, the geometry of the experimental setup suppresses the so-called 'long' trajectories and favours the short ones. To account for this experimental aspect and eliminate from the theoretical spectrum the experimentally unobserved interference effects between the short and long trajectories contributions, which could, in principle, wash out the interference effects between the contributions from the various channels, the absorbing radius, i.e. the radius at which the CAP starts to be different from zero, has been set to approximately coincide with the classical quiver amplitude of the highest return kinetic energy electrons $r_{HHG} = \frac{E_{max}}{\omega^2}$. At this kinetic energy of return the two set of trajectories merge into one; shorter trajectories which contribute to lower emission photon energies are not absorbed while the longer trajectories, which also contribute to lower high harmonic energies, are absorbed by the CAP. Therefore, the CAP acts

as a filter which smoothly removes the long trajectories contribution from the time-dependent calculated dipole $D(t)$, suppressing the signal after the most energetic $\approx U_p$ electron trajectory. The CAP used in this calculation has a strength $\eta = 0.0005$.

Differently from experiments, where the HHG spectrum measured can be considered to be the result of a coherent average over molecular alignment distributions, here the calculation has been performed for CO_2 molecules perfectly aligned along the IR laser field polarisation direction.

The cutoff is determined by the maximum recollision energy E_{kin} and by the ionisation potential I_p as $\Omega_{\text{cutoff}} = 3.17U_p + 1.32I_p$. This means that, as the ionisation energy of the $HOMO-2$ channel in CO_2 is 4.3 eV higher than that of the $HOMO$ channel, the corresponding harmonic cutoff is shifted by nearly 6 eV.

The ADC(1) harmonic spectrum of CO_2 molecule has been calculated for three different laser peak-intensities, namely $I_1 = 0.7 \times 10^{14}\,\text{W/cm}^2, I_2 = 1.1 \times 10^{14}\,\text{W/cm}^2, I_3 = 1.75 \times 10^{14}\,\text{W/cm}^2$. The laser pulses used in the calculation have a carrier frequency of $\omega = 0.057$ a.u. (800 nm) and a full width at half maximum (FWHM) pulse duration of $\tau = 2900$ a.u. (70 fs). The time-step used in the calculation is equal to 0.2 a.u. (1/500 of the IR period) at which value the convergence of our final results has been obtained.

The calculated ADC(1) HHG spectra are shown in Fig. 6.3. As can be seen, the *ab-initio* calculations performed here present a clear minimum in the high harmonic spectrum of CO_2, which shifts to higher orders with increasing intensity, from H_{19} at $I_1 = 0.7 \times 10^{14}\,\text{W/cm}^2$ to H_{27} at $I_3 = 1.75 \times 10^{14}\,\text{W/cm}^2$. Varying the intensity of the fundamental field allows one to vary the relative phase of the high-harmonic emission channels, thereby controlling the photon energy at which the destructive interference occurs. Therefore, the main features of the CO_2 molecule HHG spectra, i.e. the position of the dynimical minimum and its field intensity dependence, are found to be reproduced by the B-spline ADC(1) calculations in very good agreement with the various experiments which have been performed during the past few years [130, 197, 198, 199, 61]. Indeed, experiment [130] confirms that the harmonic minimum shifts approximately linearly with intensity.

In Table 6.2 the calculated positions of the dynamical minimum in the CO_2 HHG spectrum for the three different peak intensities of the IR laser

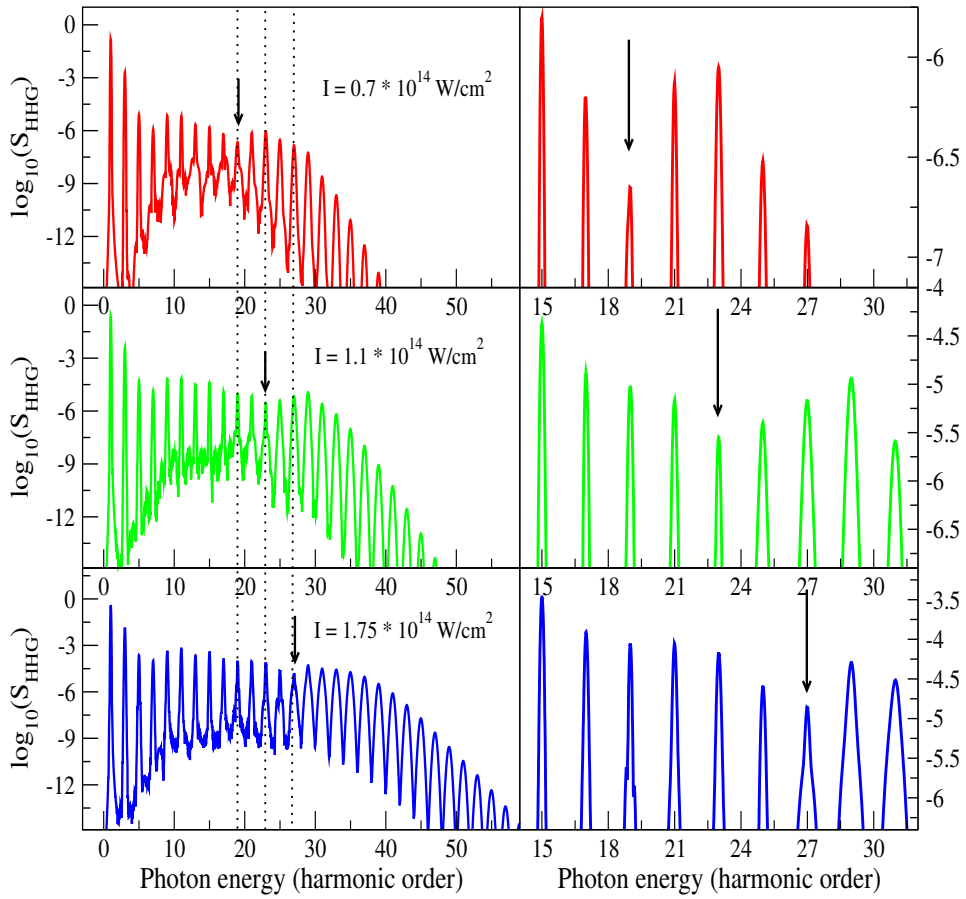

Figure 6.3.: ADC(1) high harmonic generation emission spectrum of the CO_2 molecule interacting with an IR field. The time duration 70 fs and the central wavelength is 800 nm. The laser field is linearly polarised along the molecular axis. Top panel – The peak intensity of the IR laser pulse used is $0.7 \times 10^{14}\,\mathrm{W/cm^2}$; central panel – The peak intensity of the IR laser pulse used is $1.1 \times 10^{14}\,\mathrm{W/cm^2}$; bottom panel – The peak intensity of the IR laser pulse used is $1.75 \times 10^{14}\,\mathrm{W/cm^2}$.

IR peak-intesity	ADC(1)	Model 2	Model 3
$0.7 \times 10^{14}\,\mathrm{W/cm^2}$	19	17	17
$1.1 \times 10^{14}\,\mathrm{W/cm^2}$	23	21	21
$1.75 \times 10^{14}\,\mathrm{W/cm^2}$	27	25	25

Table 6.2.: Calculated positions of the dynamical minimum in the CO_2 HHG spectrum for different peak intensities of the IR laser field and for different level of theoretical approximation.

field and for the three different levels of theoretical approximation are reported. Moreover, as it is possible to notice from Table 6.2, the interchannel couplings play an important role in determining the structure of the spectra and the position of the minimum in general depends on their inclusion in the simulation.

In Fig. 6.4, the integrated high harmonic spectra of CO_2, calculated with respectively ADC(1), *model-2* and *model-3*, are shown for the case of the $I_1 = 0.7 \times 10^{14}\,\mathrm{W/cm^2}$ peak intensity IR laser field. As it is possible to notice, the ADC(1) calculated minimum is shifted to a higher harmonic order, 19, with respect to the minimum calculated with the other two models, which appears at harmonic order 17. Moreover, the ADC(1) plateau harmonics show a smaller intensity with respect to both the *model-2* and *model-3* ones (up to the harmonic order 21). Close to the cutoff region (harmonic orders 23, 25 and 27) the inclusion of the dipole couplings between the ionic channels increases the harmonic intensities with respect to the result obtained with *model-3*, whereas the addition of the Coulomb driven interchannel couplings does not lead to significant modifications to the *model-2* harmonic intensities.

In Fig. 6.5, the integrated orbital-resolved high harmonic generation spectral intensities of CO_2, calculated with respectively ADC(1), *model-2* and *model-3*, are shown for the case of the $I_1 = 0.7 \times 10^{14}\,\mathrm{W/cm^2}$ peak intensity IR laser field.

The relative phases between contributions to the total HHG spectrum from the different emission channels i and j can be extracted from the

calculation in the following way:

$$\Phi_{\mathbf{i},\mathbf{j}} = \arccos\left(Re\left(\frac{\tilde{D}_{\mathbf{i}}(\omega)\,\tilde{D}_{\mathbf{j}}{}^{*}(\omega)}{\mid \tilde{D}_{\mathbf{i}}(\omega) \mid\mid \tilde{D}_{\mathbf{j}}(\omega) \mid}\right)\right). \tag{6.8}$$

In Fig. 6.6, the cosine of the phase differences between the different channel contributions are shown for the cases of the ADC(1), *model-2* and *model-3* calculations respectively.

Within *model-3*, both the influence of the laser field and the effect of the interaction with the ionised electron on the bound electrons in the CO_2 ion are neglected. In contrast to *model-2*, laser-induced transitions in the molecular ion are not considered here and therefore the high-harmonic signal is a coherent sum of the signals generated by ionising from and recombining to the same molecular orbital. The $HOMO$ channel (black curve) dominates the emission for lower harmonics up to harmonic number 15; the $HOMO-2$ channel (green curve) has a comparable contribution (the difference of the contributions is less than an order of magnitude) starting from the harmonic number 17 up to 21, taking over the $HOMO$ contribution at the harmonic number 19.

The cutoff in the harmonic spectrum is determined by the maximum energy of the recombining electron, which is fixed by the electric field amplitude and the laser frequency, plus the ionisation potential I_p of the state into which it recombines; thus, contribution from the deepest orbital with the highest I_p naturally becomes relevant beyond the cutoffs of the harmonics associated with the lower I_p channels. In the case of *model-3*, the $HOMO-3$ channel gives negligible contribution with respect to the $HOMO-2$ channel, i.e. its contribution is always more than an order of magnitude less, up to the harmonic cutoff (harmonic order 27) where the two contributions have the same order of magnitude. Moreover, the $HOMO-1$ channel (red curve) shows even more negligible contribution throughout the spectrum, its intensity being more than three orders of magnitude less than the one of the most contributing channel at each harmonic order. This could be expected because of the following: ionisation from the $HOMO$ orbital along or perpendicular to the molecular axis will be suppressed [204, 205], owing to the destructive interference of currents from the orbital 'lobes' with opposite signs. This effect weakens the contribution of the $HOMO$ orbital, which

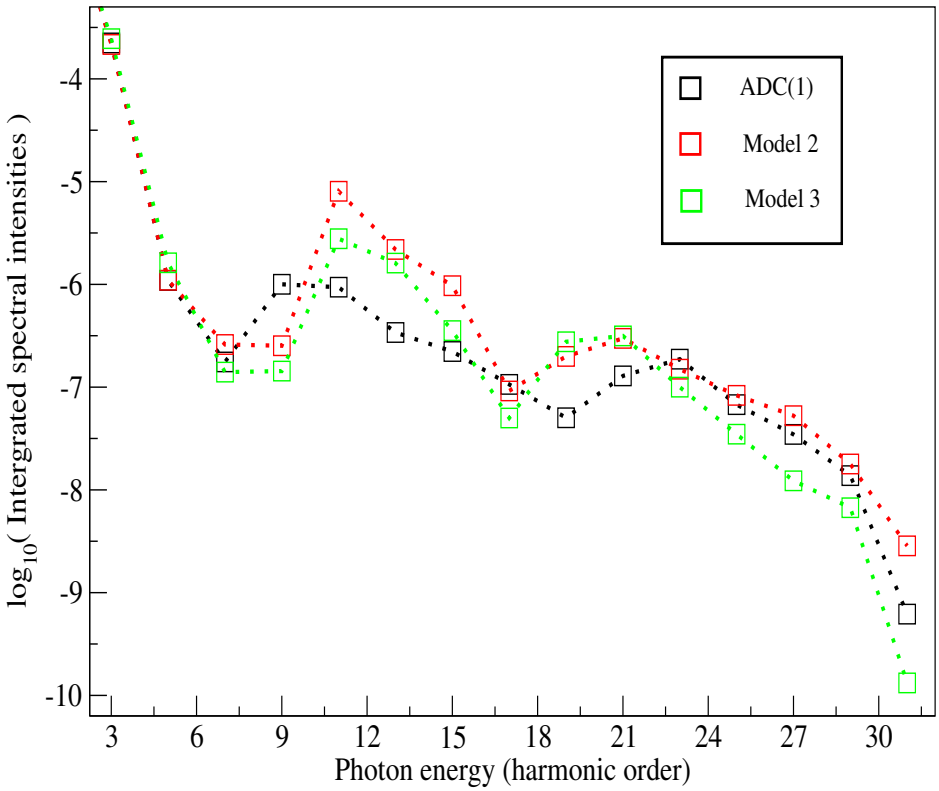

Figure 6.4.: Black squares – high harmonic generation emission spectrum of the CO_2 molecule interacting with an IR field, calculated using the full ADC(1) model with interchannel couplings; red squares – high harmonic generation emission spectrum of the CO_2 molecule interacting with an IR field, calculated using model 2: ADC(1) without interchannel Coulomb couplings; green squares – high harmonic generation emission spectrum of the CO_2 molecule interacting with an IR field, calculated using model 3: ADC(1) without interchannel Coulomb and dipole coupling (single-electron approximation). The peak intensity of the IR laser pulse used is $0.7 \times 10^{14}\,\mathrm{W/cm^2}$, the time duration 70 fs and the central wavelength is 800 nm.

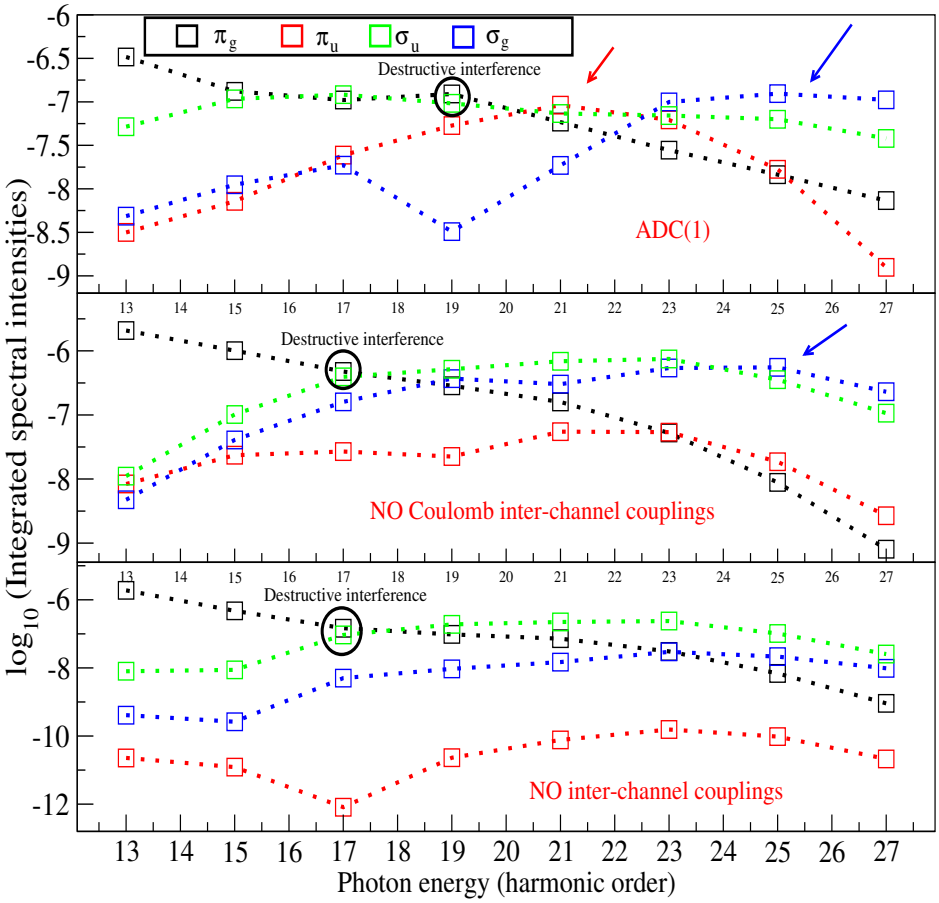

Figure 6.5.: Orbital resolved ADC(1) high harmonic generation emission integrated spectral intensities of the CO_2 molecule interacting with an IR field. Top panel – Full ADC(1) model; central panel – model 2: ADC(1) without interchannel Coulomb couplings; bottom panel – model 3 (independent particle approximation): no Coulomb driven or electric field driven inter-channel couplings. Black curve – intensity of the contribution to the HHG spectrum from the $HOMO$ orbital, π_g; Red curve – intensity of the contribution to the HHG spectrum from the $HOMO-1$ orbital, π_u; Green curve – intensity of the contribution to the HHG spectrum from the $HOMO-2$ orbital, σ_u; Blue curve – intensity of the contribution to the HHG spectrum from the $HOMO-3$ orbital, σ_g. The peak intensity of the IR laser pulse used is $0.7\times10^{14}\,\mathrm{W/cm^2}$, the time duration 70 fs and the central wavelength 800 nm.

otherwise would be completely dominant due to the much lower ionisation potential. For channel A ($HOMO-1$), the molecular orbital favours ionisation perpendicular to the molecular axis, while for channel B ($HOMO-2$) it favours ionisation parallel to the molecular axis. At the independent-electrons level of approximation the angular variation of ionisation rates and recombination dipoles are such that high-harmonic emission for molecules aligned along the laser driving field polarisation direction is dominated by the channels corresponding to $HOMO$ and $HOMO-2$ (contrarily to the perpendicular alignment case where it would be dominated by the $HOMO$ and $HOMO-1$ channels) [60, 221, 222]. Therefore, within the single active electron approximation, it is a good approximation to consider only the two channels given by $HOMO$ and $HOMO-2$ when studying high harmonic emission spectra of CO_2 molecules aligned along the driving laser field polarisation direction.

The total spectrum (Fig. 6.4) records the relative phase between the channels by mapping it into the amplitude modulations. As can be seen in Fig. 6.6, within *model-3* the minimum at harmonic order 17 in the total spectrum corresponds to the destructive interference between the $HOMO$ and $HOMO-2$ channels; at harmonic order 17 $\cos\left(\Phi_{\pi_g,\sigma_u}\right)$ is indeed negative and equal to -0.9. At the same harmonic order, the contribution from $HOMO-3$ interferes constructively and destructively with the one from $HOMO$ and $HOMO-2$ respectively, but this interference does not affect the amplitude modulation of the total HHG spectrum as the intensity of the $HOMO-3$ channel is more than an order of magnitude less than both the $HOMO$ and $HOMO-2$ intensities.

Within the *model-2* orbital resolved spectrum, the influence of the laser field on the bound electrons in the CO_2 ion is still included in the calculations, while the effect of the interaction between the ionised electron and the remaining ion, on the latter, is neglected. While the $HOMO$ channel (black curve) still dominates the emission for lower harmonics up to harmonic order 15, differently from *model-3* here both the $HOMO-3$ (green curve) and the $HOMO-2$ (blue curve) channels give a comparable contribution to the HOMO channel for the harmonic orders 17 and 19 and they both are larger than the $HOMO$ contribution for the higher harmonics starting from order 21. The spectral intensities from the $HOMO-2$ and $HOMO-3$ channels have the same order of magnitude starting from the harmonic or-

der 17 up to the overall harmonic cutoff, where $HOMO-3$ becomes the channel contributing most (at harmonic orders 25 and 27). Therefore, the interchannel dipole coupling between the $HOMO-2$ and $HOMO-3$ channels driven by the IR electric field increases the contribution of the lowest I_p $HOMO-3$ channel. However, even within the *model-2* framework, the $HOMO-1$ channel (red curve) still shows negligible contribution throughout the spectrum.

As can be seen in Fig. 6.6, the minimum at harmonic order 17 in the total HHG spectrum (Fig. 6.4) mainly corresponds to the destructive interference between the $HOMO$ and the $HOMO-2$ channels; at harmonic order 17 the values of the two spectral intensities are very close to each other (Fig. 6.5) and $\cos\left(\Phi_{\pi_g,\sigma_u}\right)$ is negative and equal to -0.7 (Fig. 6.6). Although the value of the spectral intensity for the $HOMO$ channel is three times the one for the $HOMO-3$ channel, contribution to the minimum shape also comes from their destructive interference; at harmonic order 17 $\cos\left(\Phi_{\pi_g,\sigma_g}\right)$ is indeed negative and equal to -1.0 (Fig. 6.6). Correspondingly, the two contributions from $HOMO-3$ and $HOMO-2$ show constructive interference, $\cos\left(\Phi_{\sigma_u,\sigma_g}\right)$ being positive and equal to $+0.5$.

As in the case of the *model-2* and *model-3* calculations, in the ADC(1) orbital resolved spectrum the $HOMO$ channel (black curve) also dominates the emission for low order harmonics up to harmonic number 13; the emission intensity from $HOMO-2$ channel (green curve) gives a comparable contribution for the harmonic numbers 15, 17 and 19 and it takes over the $HOMO$ intensity for the higher order harmonics. In contrast to the non-interacting electron (*model-3*) and the *model-2* results, within the ADC(1) framework, the harmonic emission from the $HOMO-1$ channel (red curve) shows non-negligible contribution for harmonic orders 19, 21 and 23, reaching its maximum specifically at harmonic number 21 where it becomes the mayor contributing channel. The contribution of the $HOMO-3$ channel (blue curve) here is totally irrelevant up to harmonic order 23, from which point $HOMO-3$ becomes the mayor contributing channel up to the harmonic cutoff. Below the position of the minimum and close to the harmonic cutoff, the amplitude of the total HHG spectrum (Fig. 6.4) is predominantly the result of the contributions from two channels; specifically the $HOMO$ and $HOMO-2$ channels at harmonic order 15 and 17 and the $HOMO-2$ and $HOMO-3$ ones at harmonic orders 25 and 27. Conversely, for har-

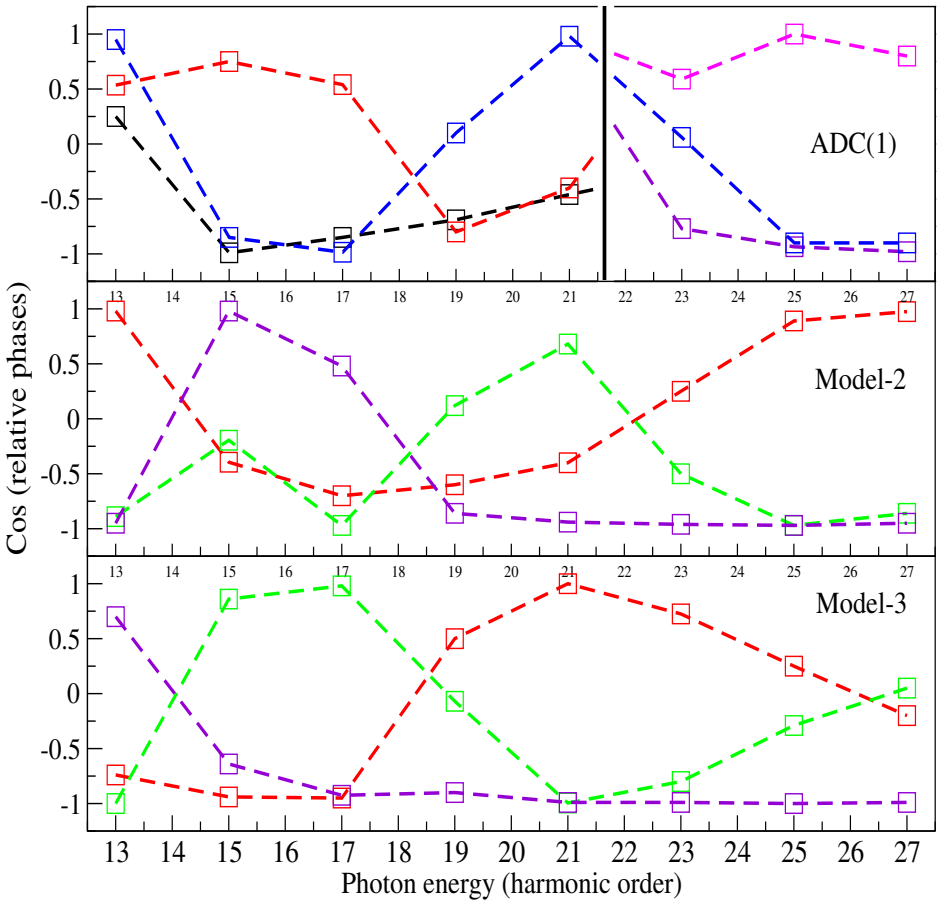

Figure 6.6.: Cosine of the relative phases between the contributions to the HHG emission from the channels of CO_2. Top panel – ADC(1) calculation; central panel – model-2 calculation: ADC(1) without interchannel Coulomb couplings; bottom panel – model-3 calculation: ADC(1) without interchannel Coulomb and dipole coupling (single-electron approximation). Black curve – $\cos\left(\Phi_{\pi_g,\pi_u}\right)$ ($HOMO$ and $HOMO-1$ orbitals); red curve – $\cos\left(\Phi_{\pi_g,\sigma_u}\right)$ ($HOMO$ and $HOMO-2$ orbitals); green curve –$\cos\left(\Phi_{\pi_g,\sigma_g}\right)$ ($HOMO$ and $HOMO-3$ orbitals); blue curve – $\cos\left(\Phi_{\pi_u,\sigma_u}\right)$ ($HOMO-1$ and $HOMO-2$ orbitals); magenta curve – $\cos\left(\Phi_{\pi_u,\sigma_g}\right)$ ($HOMO-1$ and $HOMO-3$ orbitals); violet curve – $\cos\left(\Phi_{\sigma_u,\sigma_g}\right)$ ($HOMO-2$ and $HOMO-3$ orbitals). The peak intensity of the IR laser pulse used is $0.7\times10^{14}\,\mathrm{W/cm^2}$, the time duration 70 fs and the central wavelength is 800 nm.

monic orders 19, 21 and 23, the spectral intensities from three channels have the same order of magnitude and therefore give comparable contribution to the total HHG spectrum. The overall harmonic amplitudes at orders 19 and 21 are the result of the interference between the $HOMO$, $HOMO-1$ and $HOMO-2$ channels. At harmonic order 23, $HOMO-1$, $HOMO-2$ and $HOMO-3$ are the main contributing channels instead. Therefore, in the top panel of Fig. 6.6, for harmonic orders smaller than 23 the three curves corresponding to respectively $\cos\left(\Phi_{\pi_g,\pi_u}\right)$, $\cos\left(\Phi_{\pi_g,\sigma_u}\right)$ and $\cos\left(\Phi_{\pi_u,\sigma_u}\right)$ are plotted, while for harmonic order 23, 25 and 27 we plot the curves corresponding to $\cos\left(\Phi_{\pi_u,\sigma_u}\right)$, $\cos\left(\Phi_{\pi_u,\sigma_g}\right)$ and $\cos\left(\Phi_{\sigma_u,\sigma_g}\right)$. In Fig. 6.6, the two regions are separated by a vertical black line.

As can be seen in Fig. 6.6, in the ADC(1) calculation the minimum at harmonic order 19 in the total spectrum (Fig. 6.4) mainly corresponds to the destructive interference between the $HOMO$ and the $HOMO-2$ channels; at harmonic order 19 the values of the two spectral intensities are very close to each other (Fig. 6.5) and $\cos\left(\Phi_{\pi_g,\sigma_u}\right)$ is negative and equal to -0.8 (Fig. 6.6). Although the value of the spectral intensity for the $HOMO$ channel is 2.5 times the one for the $HOMO-1$ channel, contribution to the minimum shape also comes from their destructive interference; at harmonic order 19 $\cos\left(\Phi_{\pi_g,\pi_u}\right)$ is indeed negative and equal to -0.7 (Fig. 6.6). The two contributions from $HOMO-1$ and $HOMO-2$ channels show a small constructive interference as $\cos\left(\Phi_{\sigma_u,\sigma_g}\right)$ is positive and equal to $+0.15$ (Fig. 6.6).

6.2.1. Summary

In the work presented in this Section we have investigated the relevance of multiple-orbital effects during high-harmonic generation (HHG). We have described the HHG process with the TD B-spline ADC(1) many-body approach and we have studied the impact of the full inclusion of the residual electron-ion interaction on the HHG spectrum of the CO_2 molecule.

We have found that the shape and position of the dynamical minimum in the HHG spectrum of CO_2 changes whether or not interchannel interactions are taken into account, see Fig. 6.4 and Table 6.2. We have also seen that neglecting interchannel interactions can lead to large modifications of up to one order of magnitude in the HHG yield, especially in the plateau region

(see Fig. 6.4). The results presented in this Chapter show that the interchannel couplings can play an important role in determining the relative contributions to the total HHG spectrum from the different ionic channels, also increasing the contribution of channels that would otherwise be negligible in an independent electron model and significantly changing the phase differences between the channel resolved harmonics. Consequently, the argument of low ionisation probability by the end of the pulse is not sufficient to justify ignoring multiple-orbital contributions, such as the ones from the $HOMO-1$ and $HOMO-3$ orbitals. While, after the end of the pulse, the populations of these orbitals are relatively small, their contributions during the pulse are not small and have, indirectly through the interchannel couplings, an impact both on the HHG yield and on the position of the dynamical minimum. In general, the population of an ionic channel at the end of the ionising pulse does not map directly to its relevance in the HHG mechanism.

Moreover, since multichannel effects in the residual electron-ion interaction enter in the HHG spectrum, they cannot generally be neglected but need to be understood in order to successfully use them for tomographic imaging of molecular orbitals [128, 129].

6.3. Nature of the ionic wavepacket resulting from ionisation of aligned CO_2 molecule by femtosecond strong field IR pulses

During an ionisation event, an electron is emitted from the molecular region creating an electronic hole with respect to the neutral parent system. If the initial neutral system was in a pure state, and could then be described by a total N-electrons wave-function, then both the ionisation dynamics driven by the laser field and the following field-free dynamics of the N electrons can be described by a global N-electrons wave-function.

After the emitted electron has travelled a sufficient distance from the parent cation system and therefore can be considered as no longer interacting with the latter, it becomes possible to distinguish, among the initially indistinguishable N electrons, between the photoelectron and the remaining N-1 bound electrons which are still localised in the molecular region

and therefore constitute the ionic electronic cloud. These two physically distinguishable, spatially separated, sub-systems can be considered as non interacting in the sense that the photoelectron basically behaves as a free particle once it is far enough from the parent ionic system, and in turn, the ion system undergoes an internal electron dynamic which can be considered as not influenced by the emitted photoelectron.

Moreover, this type of process gives rise to a molecular ion which does not have to be in an energy eigenstate. As a consequence after photoionisation the state of the molecular ion can undergo an internal non-trivial dynamical evolution, which may take the form of hole migration (i.e. motion of the hole around the molecular frame) [35, 36] or hole decay typically with some non-exponential (oscillatory) behaviour [38]. This will take place on a timescale (< 10 fs) that may be short with respect to the timescale of nuclear motion [44]. Ultrafast hole migration, following sudden ionisation or excitation, is believed to be a universal response of extended molecules. This process occurs due to the electron correlations within many-electron systems, and is predicted to take place typically on the few to sub-femtosecond timescale (i.e. into the attosecond time domain). It is currently a prominent goal in attosecond science [20] to observe and fully characterise the hole migration process in order to improve the understanding of the process and ascertain the role of hole migration in determining photochemical and photophysical outcomes and to prove that experimental methods based on attosecond measurement can address correlation driven dynamics in extended quantum systems such as biomolecules.

In order to follow the dynamical evolution of the system after ionisation, it is essential to know the exact initial state in which the ion is produced, i.e. the exact hole density of the molecular ion. The quantitative understanding of the nature of the ionic state which is produced after the ionisation of the molecular system eliminates any uncertainty about the initial conditions to be fixed for describing and interpreting the post-ionisation electron dynamics in the cation system, i.e. hole migration, as the initial state does not have to be guessed anymore [35, 36].

Coherent population of two or more ionic eigenstates (for example the states resulting from the removal, in the molecular orbital picture, of an electron from the $HOMO$ and $HOMO-1$ orbitals respectively) implies excitation of the bound electronic wavepacket in the ion. In experiments

performed on the ionic system, quantum interference between these channels records the wavepacket dynamics. This multi-state dynamic has two non-trivial parameters: the initial relative phases ϕ between the ionic states that could have been acquired during the ionisation interaction with the laser field and their relative populations.

Moreover, the following questions arise: is the resulting electron dynamic, which occurs within the ionic system, completely coherent? Will the parent ionic produced system be describable by a statistical mixture or by a coherent superposition of ionic eigenstates? When an experimental measurement is performed on the ionic system without considering the photoelectron, does the entanglement within the total N-electron wave-function, between the photoelectron and the N-1 bound electrons constituting the ion, dampen the observable time-dependent ionic electron dynamics? The coherence of the resulting ionic system is crucial to the theoretical interpretation of the dynamical informations that can be obtained in time-resolved (pump-probe) experiments [35, 48]. In general, the entanglement present in the total N-electron wave-function results in the non-separability of the latter into the antisymmetrised product of a single photoelectron wave-function and a (N-1)-electron ionic wave-function. This lack of separability lowers the coherence of the ionic sub-system, which therefore must generally be described by a density matrix instead of a coherent wave-function. Coherence between different ionic (eigen)states requires them to ionise in the same photoelectron continuum, as this leads to the complete separability of the total N-electron wave-function and consequently to the possibility of unambiguosly identifing a (N-1)-electron ionic wave-function.

With a view to achieving our main future goal of performing the study of the coherence and of the nature of the ionic wavepacket resulting from the ionisation by VUV/XUV ultrashort attosecond laser pulses, it is of interest here to investigate the level of coherence and the nature of the ionic wavepacket resulting from the strong field IR ionisation by ultrashort few cycles IR laser pulses with a pulse duration of few femtoseconds. Therefore, in this work, we have used an ultrashort IR laser pulse fixing the pulse duration at 5.2 fs. The time dependent profile of the IR electric field used in the calculation is shown in Fig. 6.7.

In the remaining part of this Chapter, the first calculation of the reduced ionic density matrix (R-IDM) of the cation system produced in the non-

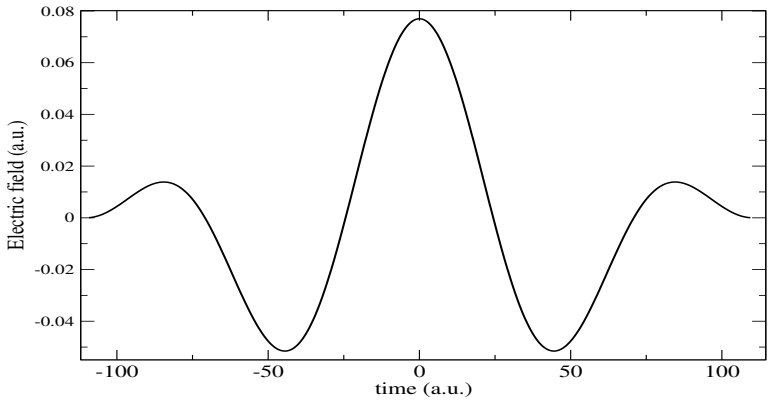

Figure 6.7.: Time dependent profile of the IR electric field (in a.u.) used in the calculation. The IR peak intensity is 1.5×10^{14}W/cm^2.

perturbative ionisation of CO_2 molecules by high-intensity ultra-short IR laser pulses is presented. The R-IDM is obtained by tracing out the photoelectron degree of freedom from the total time-dependent density matrix of the system $\rho^{Ionic}(t) = Tr_a[\hat{\rho}(t)]$. The laser fields used in the following calculations are linearly polarised and it is assumed that the CO_2 molecules are aligned along the electric-field polarisation direction. The IR field intensities used in the calculations vary in the range from 2×10^{13} W/cm^2 to 2×10^{14} W/cm^2 and the IR field carrier frequencies from 0.13 a.u. to 0.038 a.u.. The results presented were obtained by means of a fully *ab-initio* 3-D TDSE calculation which was performed using the recently developed molecular time-dependent B-spline implementation of the algebraic diagrammatic construction (ADC) many-body Green's function method. Specifically, in the following study, the first order ADC(1) scheme of the ADC(n) hierarchy is used. A monocentric B-spline basis set is used to describe single-electron orbitals. The calculations were performed using a linear B-spline knot sequence with a radial box radius $R_{max} = 320$ a.u. and 410 radial grid points (B-spline basis Set 7, see Table 2.1). In order for the photoelectron wavepacket not to be absorbed before the end of the IR laser pulse, the absorbing radius, i.e. the radius at which the CAP starts to be different from zero, has been set to $r_{CAP} = 200$ a.u. The CAP strength has been set to $\eta = 0.0005$.

This newly developed numerical method has made it possible to give a quantitative prediction on the degree of coherence $G_{i,j}(t) = \frac{|\rho^{Ionic}(t)_{i,j}|}{\sqrt{\rho^{Ionic}(t)_{i,i}\rho^{Ionic}(t)_{j,j}}}$

[143] between pairs of final ionic channels i and j formed during the ionisation of the molecular system by the non-perturbative IR laser field. The numerator of the coherence degree between two ionic states i and j is given by the absolute value of the complex off-diagonal $\rho^{Ionic}(t)_{i,j}$ R-IDM matrix element, while the denominator is given by the square-root of the product of the two populations $\sqrt{\rho^{Ionic}(t)_{i,i}\rho^{Ionic}(t)_{j,j}}$. Totally incoherent statistical mixtures result in $G_{i,j}(t) = 0$ while the maximum achievable (perfect) coherence corresponds to $G_{i,j}(t) = 1$.

Additionally, in the cases where the final produced ionic wavepacket shows an appreciable level of coherence, a quantitative prediction of the resulting ionic wave-function coefficients is given. Therefore, the present calculations provide a quantitative understanding about the nature of the ionic states produced after the strong IR field ionisation of the CO_2 molecule in the case of laser fields linearly polarised along the molecular axis.

Coherence between different ionic states requires them to ionise in the same photoelectron continuum; within the geometrical configuration used in this study, where the CO_2 molecular axis is perfectly aligned along the linearly polarised electric field, coherence is possible between two different pairs of ionic states: between the two Π symmetry states, i.e. $\mid \pi_g^{-1}\rangle$ and $\mid \pi_u^{-1}\rangle$, and between the two Σ symmetry states, i.e. $\mid \sigma_u^{-1}\rangle$ and $\mid \sigma_g^{-1}\rangle$. No coherence is possible between ionic states with different axial angular momentum quantum number M. This is because the photons of the aligned laser field do not carry any axial angular momentum, i.e. they have $M = 0$, and therefore M is a conserved quantum number: the initial state of the system is the CO_2 Σ_g^+ ground state, which has $M = 0$, and therefore, in the N-electron configuration states, the Π symmetry ionic states can be coupled only to π symmetry electronic continuum states, while Σ ionic states can only couple to σ symmetry electronic continuum ones. Therefore, ionic states with different M do not share any electronic continuum. Conversely, as the photon field changes the parity of the states, ionic states with different parity (g and u) can share a common electronic continuum and therefore have a certain degree of coherence.

In the cases where the final ionic states produced show a high level of coherence, two normalised ionic wave-functions can be defined: one within

the Π ($\mid M \mid = 1$) symmetry space of the ion

$$\Psi^{\Pi}(t) = C_{\Pi_g} \mid \pi_g^{-1}\rangle + C_{\Pi_u} e^{-i(E_{\pi_u} - E_{\pi_g})t} e^{-i\phi_{\pi_g - \pi_u}} \mid \pi_u^{-1}\rangle \tag{6.9}$$

and one within the Σ ($\mid M \mid = 0$) symmetry space of the ion

$$\Psi^{\Sigma}(t) = C_{\Sigma_u} \mid \sigma_u^{-1}\rangle + C_{\Sigma_g} e^{-i(E_{\Sigma_g} - E_{\Sigma_u})t} e^{-i\phi_{\Sigma_u - \Sigma_g}} \mid \sigma_g^{-1}\rangle \ . \tag{6.10}$$

These resulting ionic wave-function coefficients and phases are given respectively by

$$C_{\Pi_g} = \frac{\sqrt{\rho^{R-IDM}_{\pi_g,\pi_g}}}{Norm_{\Pi}} \ C_{\Pi_u} = \frac{\sqrt{\rho^{R-IDM}_{\pi_u,\pi_u}}}{Norm_{\Pi}} \ e^{-i\phi_{\pi_g - \pi_u}} = \frac{\rho^{R-IDM}_{\pi_g,\pi_u}}{\sqrt{\rho^{R-IDM}_{\pi_g,\pi_g}\rho^{R-IDM}_{\pi_u,\pi_u}}}$$

$$Norm_{\Pi} = \sqrt{\rho^{R-IDM}_{\pi_g,\pi_g} + \rho^{R-IDM}_{\pi_u,\pi_u}} \tag{6.11}$$

for the Π symmetry states of the ion, and by

$$C_{\Sigma_u} = \frac{\sqrt{\rho^{R-IDM}_{\sigma_u,\sigma_u}}}{Norm_{\Sigma}} \ C_{\Sigma_g} = \frac{\sqrt{\rho^{R-IDM}_{\sigma_g,\sigma_g}}}{Norm_{\Sigma}} \ e^{-i\phi_{\Sigma_u - \Sigma_g}} = \frac{\rho^{R-IDM}_{\sigma_u,\sigma_g}}{\sqrt{\rho^{R-IDM}_{\sigma_u,\sigma_u}\rho^{R-IDM}_{\sigma_g,\sigma_g}}}$$

$$Norm_{\Sigma} = \sqrt{\rho^{R-IDM}_{\pi_g,\pi_g} + \rho^{R-IDM}_{\pi_u,\pi_u}} \tag{6.12}$$

for the Σ symmetry states of the ion.

In an intra-channel model, where the Coulomb interchannel coupling has not been included, the degrees of coherence are naturally constants and, after the interaction with the laser field, do not depend on time anymore. This is due to the fact that, within this model, the hole index is a good quantum number and both the hole populations and the coherences can be modified only by the laser electric field. However, in principle, the extension to the exact Coulomb interaction changes the situation. Interchannel coupling causes the hole populations and the degree of coherence to remain nonstationary as long as the photoelectron remains close to the ion. As the distance between the photoelectron and the ion increases, the Coulomb interaction between the photoelectron and the parent ion becomes less important and, consequently, the ionic populations and the degree coherence converge to a stationary value. In the case of strong field IR ionisation stud-

ied in this work, the ionisation amplitude scales exponentially with respect to the electric field and therefore the ionisation events selectively happen at the central highest peaks of the electric field profile, while being completely absent at the tail of the laser pulse where the instantaneous intensity is not strong enough to free any bound electron from the system. In the calculations reported in this Chapter, the numerical simulation was run for a time sufficient for the emitted photoelectrons, which have mainly been produced at the centre of the IR pulse, to reach after the end of the pulse a sufficient distance from the parent ionic system, therefore making sure that the values of the coherence degrees presented here are the final stationary ones.

In Fig. 6.8 we show the dependence of the final degrees of coherence $G_{\pi_g-\pi_u}$ and $G_{\sigma_g-\sigma_u}$ (top left panel) on the IR field peak intensity, together with the corresponding dependencies of the normalised relative populations C_{Π_g} , C_{Π_u} and C_{Σ_u} , C_{Σ_g} of the CO_2 ionic states (bottom panel) and of their relative phases $\phi_{\pi_g-\pi_u}$, $\phi_{\Sigma_u-\Sigma_g}$ (top right panel). The IR central wavelength and the duration of the laser pulse used in the calculation are respectively 800 nm and 5.2 fs. As it is possible to notice, both the G_{π_g,π_u} and G_{σ_g,σ_u} final degrees of coherence have different values depending on the laser pulse peak intensity. The G_{π_g,π_u} degree of coherence shows a rapid increase in the range of peak intensities from $0.2 \times 10^{14}\,\mathrm{W/cm^2}$ to $0.8 \times 10^{14}\,\mathrm{W/cm^2}$, while its value can be considered stable in the very broad range of IR peak intensities starting from $0.9 \times 10^{14}\,\mathrm{W/cm^2}$ to $2.0 \times 10^{14}\,\mathrm{W/cm^2}$. Conversely, the G_{σ_g,σ_u} degree of coherence shows an oscillatory behaviour from $0.2 \times 10^{14}\,\mathrm{W/cm^2}$ to $0.6 \times 10^{14}\,\mathrm{W/cm^2}$, before starting to rapidly increase up to $1.5 \times 10^{14}\,\mathrm{W/cm^2}$ above which its dependence on intensity becomes weaker. Fig. 6.8 shows that a high degree of coherence between both the Π symmetry (π_g and π_u) and the Σ symmetry (σ_g and σ_u) final ionic channels can be obtained using an ultrashort IR laser pulse with a peak intensity in the range from $1.1 \times 10^{14}\,\mathrm{W/cm^2}$ to $2 \times 10^{14}\,\mathrm{W/cm^2}$.

In order to understand the effect of the interchannel Coulomb couplings on the coherence of the final ionic wavepacket, in Fig. 6.9 a comparison is shown between the IR field peak intensity dependencies of the coherence degrees calculated respectively with (ADC(1) and without (intrachannel model) the inclusion of the interchannel couplings. The IR central wavelength and the duration of the laser pulse used in the calculation are respectively 800 nm and 5.2 fs.

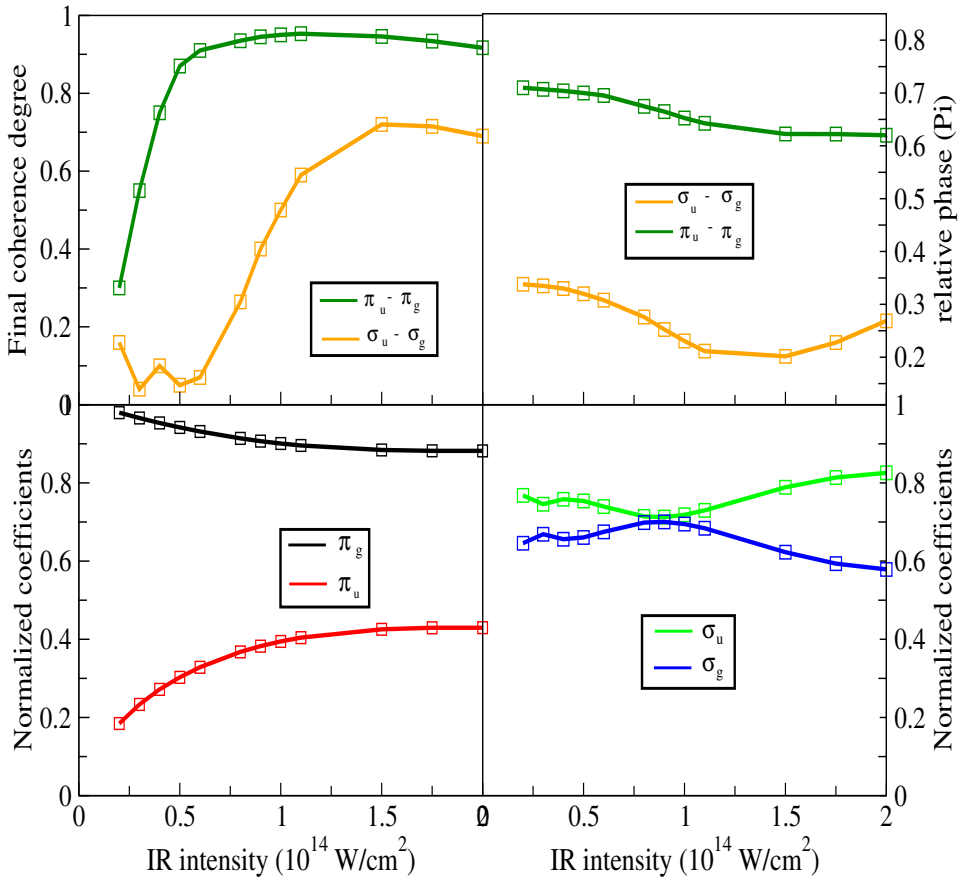

Figure 6.8.: Top panel: Intensity dependence of the final degrees of coherence $G_{\pi_g-\pi_u}$, $G_{\sigma_g-\sigma_u}$ (left figure) and of the relative phases $\phi_{\pi_g-\pi_u}$, $\phi_{\Sigma_u-\Sigma_g}$ in units of π (right figure) between the final ionic states produced during the ionisation of CO_2 by an ultrashort IR laser pulse. Bottom panel: Intensity dependence of the absolute value of the Π symmetry C_{Π_g} C_{Π_u} (left figure) and Σ symmetry C_{Σ_u} C_{Σ_g} (right figure) wave-function normalised coefficients. The IR central wavelength and the duration of the laser pulse used in the calculation are respectively 800 nm and 5.2 fs. The laser field is linearly polarised along the molecular axis.

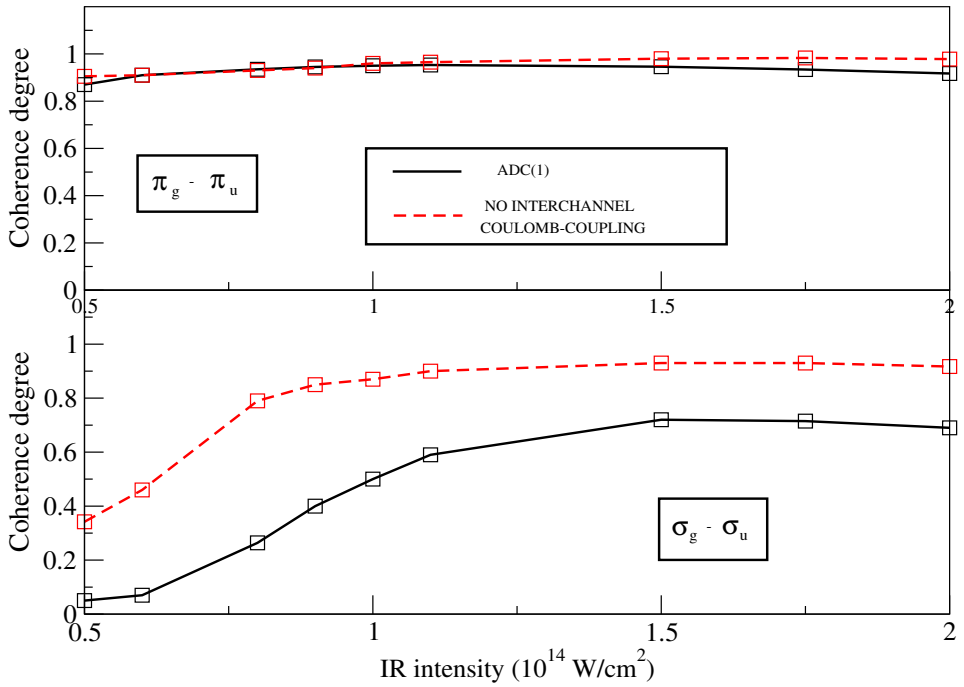

Figure 6.9.: IR peak intensity dependence of the final $G_{\pi_g-\pi_u}$ (top panel) and $G_{\sigma_g-\sigma_u}$ (bottom panel) degrees of coherence between the final ionic states produced during the ionisation of CO_2 by an ultra-short IR laser pulse, computed by means of the full ADC(1) method (black full curve) and of ADC(1) without the inclusion of the interchannel Coulomb couplings (intrachannel model) (red dashed curve). The IR central wavelength and the duration of the laser pulse used in the calculation are respectively 800 nm and 5.2 fs.

As this comparison shows, interchannel coupling affects the coherence in a significant way. As it is possible to see, especially for the case of the $G_{\sigma_g-\sigma_u}$ degree of coherence, interchannel coupling leads to an enhanced entanglement between the photoelectron and the parent ion resulting in a reduced coherence within the ion. When the photoelectron is still in immediate contact with the parent ion, the coherence properties of the ionic system are affected by its interaction with the photoelectron, which can be thought of as a bath. As it is well known [223], the system-bath interaction leads to a reduction in the coherence of the system. With time, as the photoelectron moves further away from the ionic system, the Coulomb interaction

between the parent ion and the photoeletron becomes less important and the coherence converges to a stationary value. The fact that the coherence between the higher lying π_g and π_u hole states is less affected by the interchannel coupling indicates that higher photoelectron kinetic energies lead to a smaller occurrence of system-bath interactions, with a consequent increase in the degree of coherence among the hole states. On the other hand, the interchannel couplings due to the low kinetic energy photoelectrons explain the decrease of the ADC(1) $G_{\sigma_g-\sigma_u}$ degree of coherence with respect to the intrachannel result.

In order to understand how the coherence in the ionic system is achieved, it is possible to identify two different mechanisms that can lead two different ionic states to ionise in the same photoelectron continuum. The first mechanism consists of the direct ionisation from the molecular neutral ground state giving rise, with different probabilities, to both the two different ionic states. Direct ionisation in both channels is then followed by the strong laser field driven acceleration of the respective photoelectrons in the same continuum. Since no interaction between the two ionic states is involved in the formation of the coherence, the one described is an independent-channel process. The Hamiltonian terms responsible for these processes are respectively

$$D_{ai,0}E(t) = \langle \Psi_i^a \mid \hat{D} \mid \Psi_0 \rangle E(t) \ , \tag{6.13}$$

and

$$D_{ai,bj}^{ij}E(t) = +\delta_{i,j}\langle a \mid \hat{d} \mid b \rangle E(t) \ a \neq b \, . \tag{6.14}$$

In Fig. 6.10 a schematic representation of this first mechanism is shown. In the case of an ultrashort laser pulse with broad spectral bandwidth, the absorption of a different number of IR photons from the two different ionic channels can lead to the same final electronic continuum state. The condition to ionise in continuum states with the same final energy is

$$E_i + \sum_k n_k \omega_k = E_f$$

$$E_i - E_{gap}^{i-j} + \sum_l n_l \omega_l = E_f$$

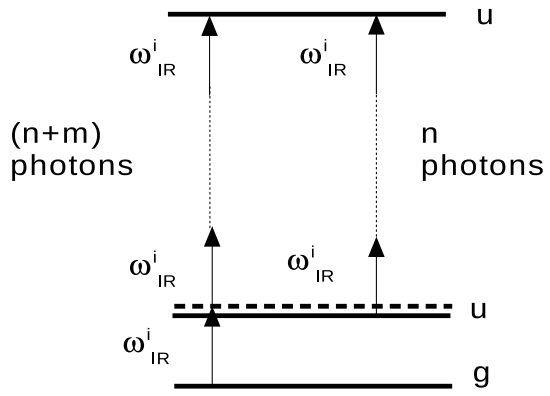

Figure 6.10.: Schematic representation of the first mechanism which can lead two different ionic states to ionise directly in the same photoelectron continuum state.

$$\sum_k n_k = \sum_l n_l - M \qquad M = 0, 1, 2, 3, 4, 5, 6, 7, \ldots \tag{6.15}$$

where both ω_k and ω_l stand for one of the many frequencies components contained in the spectral bandwidth of the pulse and E_{gap}^{i-j} stands for the difference between the ionisation potentials of the two ionic states i and j.

In the case studied in this work where the two different ionic states have different parity, since the absorption of a single photon gives rise to a parity change in the state of the excited electron, in order for the two channels to ionise in a continuum state with the same parity the condition of Eq. (6.15) can extend only to odd values, $1, 3, 5, \ldots$, of the integer M.

The second mechanism consists of the electron rearrangement within the ionic system driven by the coupling between the electric field and the transition dipole matrix element between the ionic eigenstates. The Hamiltonian term responsible for this process is given by

$$D_{ai,bj}^{i \neq j} E(t) = -\delta_{a,b} \langle i \mid \hat{d} \mid j \rangle E(t) \; i \neq j \, . \tag{6.16}$$

This term is responsible for transitions between the different ionic states

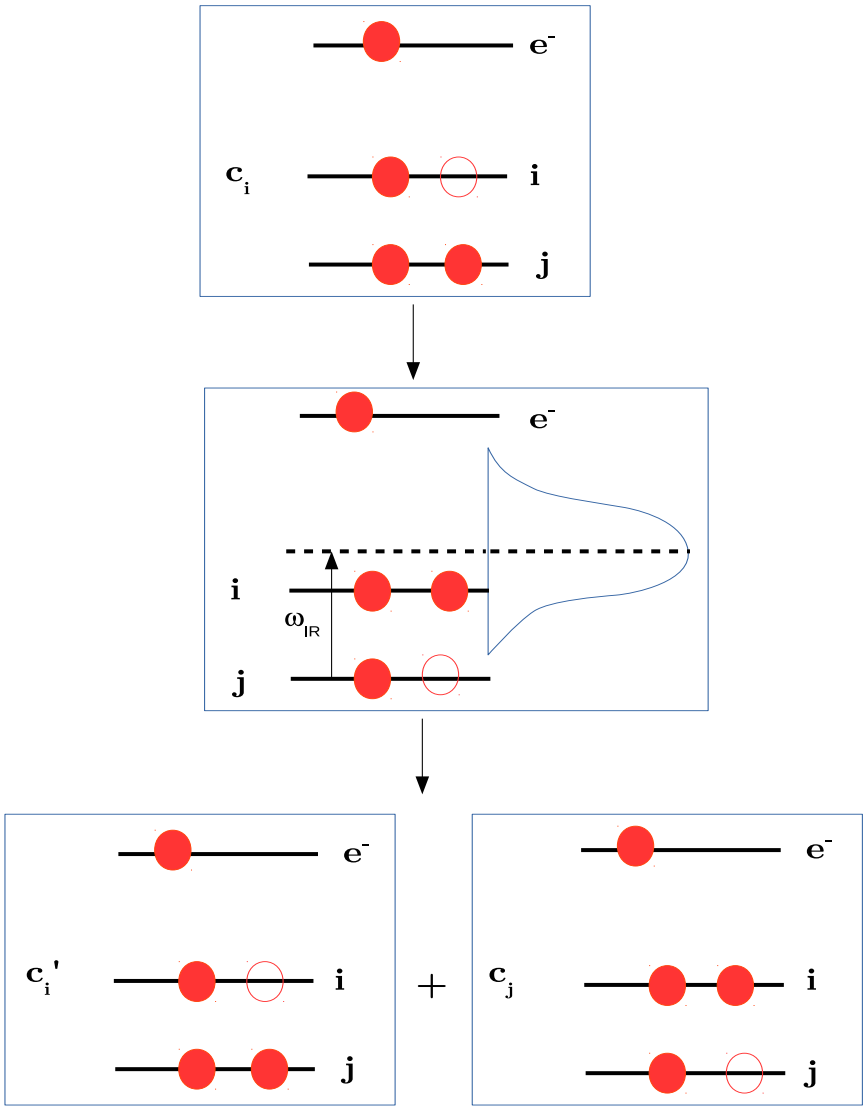

Figure 6.11.: Schematic representation of the second mechanism which can lead two different ionic states to ionise directly in the same photoelectron continuum state. The dipole transitions between the two different ionic states can lead them to share the same electronic continuum.

and does not affect the electron in the continuum, which acts as a spectator. However, this mechanism can change the ionic states the photoelectron is associated with in the configuration expansion of the total wave-function, leading to either an increase or a decrease in the overlap between the electronic continua of the different ionic channels involved in the transition. In Fig. 6.11 a schematic representation of this second mechanism is shown.

In order to investigate the role of the two different mechanisms contributing to the final coherence degree between the produced ionic states, in Fig. 6.12 we show the comparison between the results obtained using the full ADC(1) approach and the ones obtained freezing either the first or the second mechanism respectively.

In Figs. 6.13 and 6.14 we also show the IR peak intensity dependence of the normalised relative final population coefficients of respectively the Π symmetry (π_g and π_u) and Σ symmetry (σ_g and σ_u) ionic channels of CO_2 computed with the three different models. The IR central wavelength and the duration of the laser pulse used in the calculation are respectively 800 nm and 5.2 fs.

When the second mechanism is frozen, no ionic transitions driven by the electric field are possible and the only process that can remove an electron from the occupied π_u (HOMO-1) and σ_g (HOMO-3) orbitals is tunnel ionisation into the continuum. This model will be referred to as model-1. In the second approach only the π_g (HOMO) and σ_u (HOMO-2) occupied orbitals can directly tunnel ionise in the continuum, while the only mechanism that can remove an electron from the lower lying occupied orbitals π_u (HOMO-1) and σ_g (HOMO-3) is the electron rearrangement within the ionic system driven by the electric field. This model will be referred to as model-2. As can be seen in Fig. 6.12, the dependence on intensity of the degrees of coherence predicted by the full ADC(1) model resemble the ones obtained using model-2. In the case of the $G_{\pi_g-\pi_u}$ degree of coherence, the ADC(1) and the model-2 results basically coincide, while the values of the degrees of coherence obtained using model-1 are considerably smaller. In the case of the $G_{\sigma_u-\sigma_g}$ degree of coherence, the values predicted by the ADC(1) calculation are smaller (by about 0.1-0.2) with respect to the ones obtained with the model-2 calculation, but the two curves have the same dependence on intensity. Conversely the dependence on intensity of the $G_{\sigma_u-\sigma_g}$ degree of coherence obtained using model-1 is different. $G_{\sigma_u-\sigma_g}$

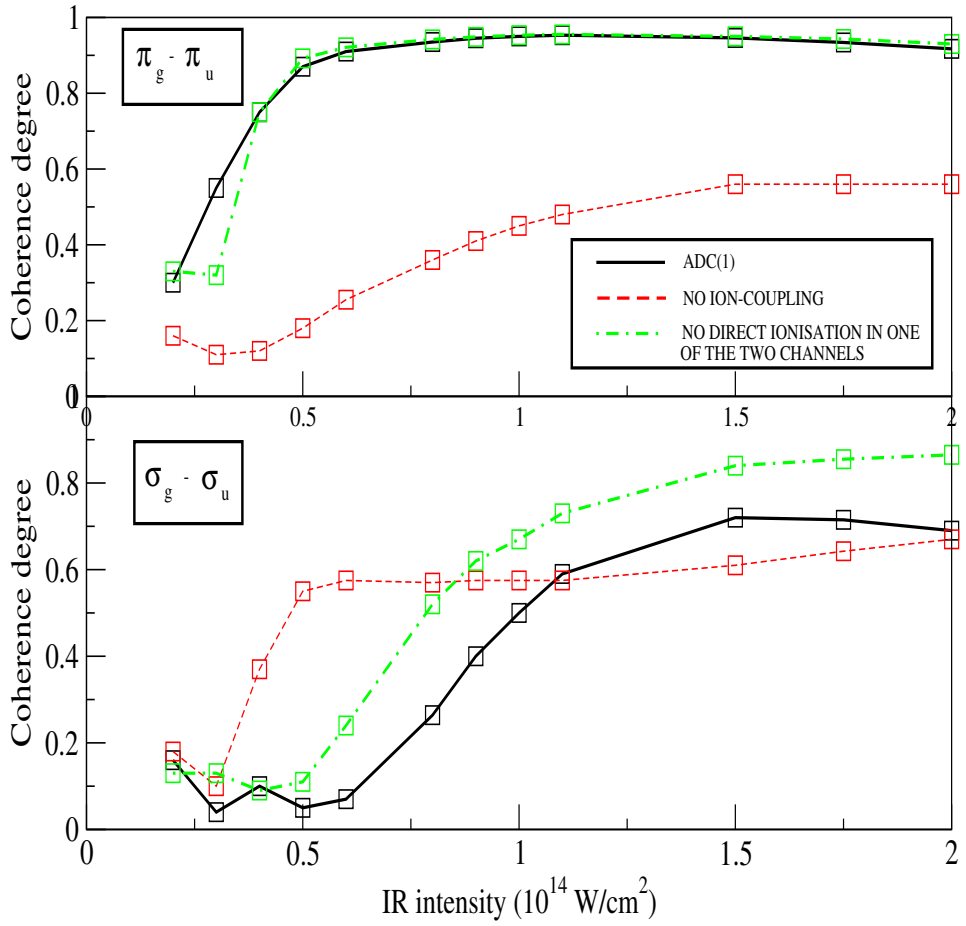

Figure 6.12.: IR peak intensity dependence of the final $G_{\pi_g-\pi_u}$ (top panel) and $G_{\sigma_g-\sigma_u}$ (bottom panel) degrees of coherence between the final ionic states produced during the ionisation of CO_2 by an ultra-short IR laser pulse, computed with the use of the following three different models: Black full curve – Full ADC(1); Red dashed curve – ADC(1) without electric-field induced inter-channel dipole couplings; Green point-dashed curve – ADC(1) with frozen direct ionisation into the continuum from orbitals $HOMO-1$ and $HOMO-3$. The IR central wavelength and the duration of the laser pulse used in the calculation are respectively 800 nm and 5.2 fs.

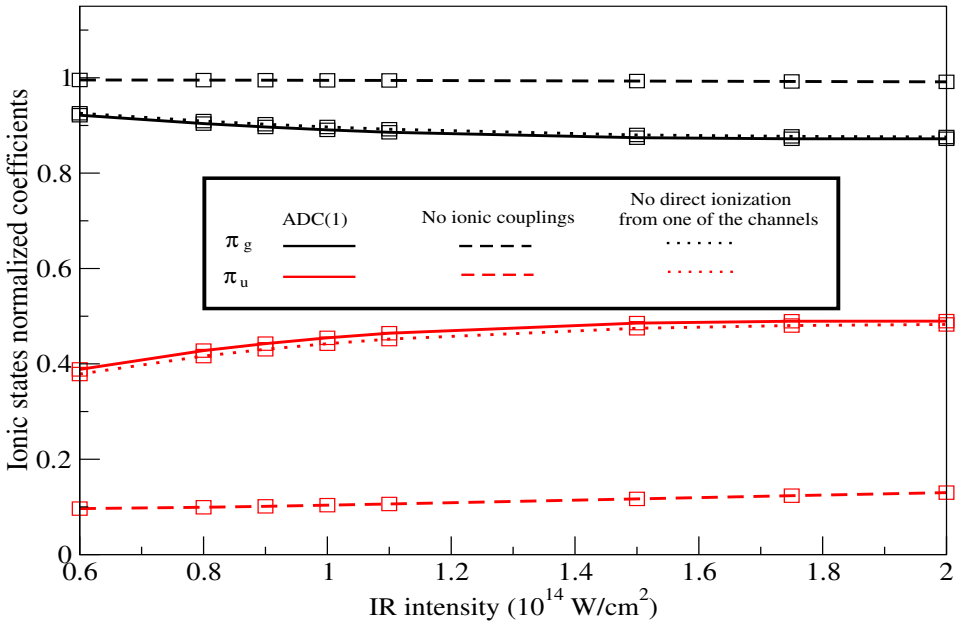

Figure 6.13.: IR peak intensity dependence of the final Π symmetry C_{Π_g} , C_{Π_u} normalised relative population coefficients for the π_g and π_u ionic channels of CO_2, computed with the use of the following three different models: Black full curve – Full ADC(1); Red dashed curve – ADC(1) without electric-field induced interchannel dipole couplings; Green point-dashed curve – ADC(1) with frozen direct (tunnel) ionisation into the continuum from orbitals $HOMO-1$ and $HOMO-3$. The IR central wavelength and the duration of the laser pulse used in the calculation are respectively 800 nm and 5.2 fs.

remains approximately constant in the range of intensities which extends from $0.5\times10^{14}\,\mathrm{W/cm^2}$ to $1.5\times10^{14}\,\mathrm{W/cm^2}$ and it shows a very slow increasing behaviour for higher intensities. Model-1 predicts larger values for the $G_{\sigma_u-\sigma_g}$ degree of coherence with respect to the ADC(1) result, up to the intensity value of $10^{14}\,\mathrm{W/cm^2}$. At higher intensities the difference between the predictions of the two models become smaller and at $2\times10^{14}\mathrm{W/cm^2}$ the first direct mechanism seems to become the predominant one for $G_{\sigma_u-\sigma_g}$. However, in general, the ADC(1) results considerably differ from the ones obtained with model-1. This is due to the fact that, as is seen in Figs. 6.13 and 6.14, in the case of an IR field linearly polarised along the molecular

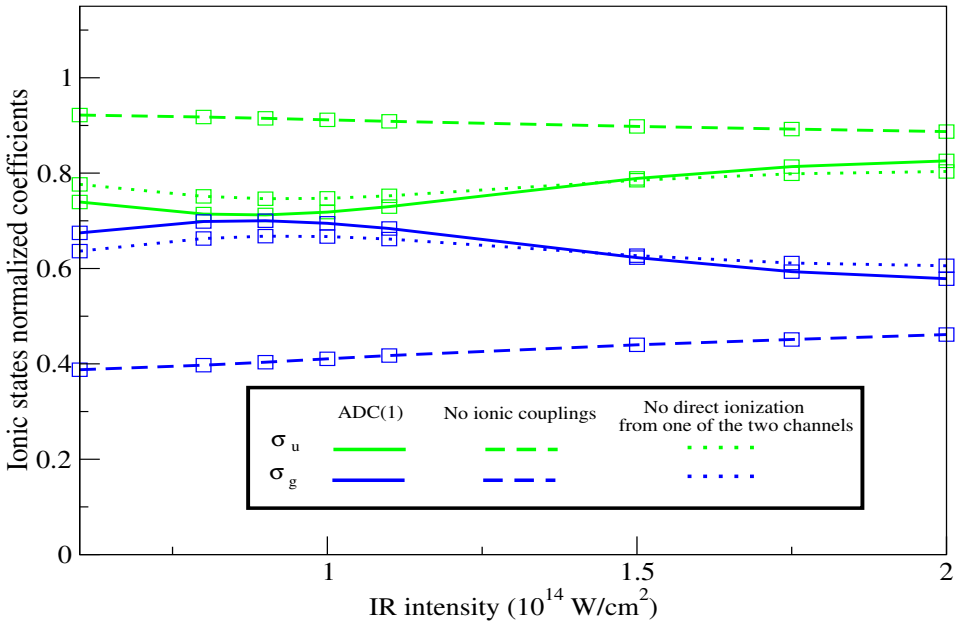

Figure 6.14.: IR peak intensity dependence of the final Σ symmetry C_{Σ_u} , C_{Σ_g} normalised relative population coefficients for the σ_g and σ_u ionic channels of CO_2, computed with the use of the following three different models: Black full curve – Full ADC(1); Red dashed curve – ADC(1) without electric-field induced interchannel dipole couplings; Green point-dashed curve – ADC(1) with frozen direct (tunnel) ionisation into the continuum from orbitals $HOMO - 1$ and $HOMO - 3$. The IR central wavelength and the duration of the laser pulse used in the calculation are respectively 800 nm and 5.2 fs.

axis studied in this work, the main mechanism responsible for the removal of an electron from the lower lying occupied orbitals π_u and σ_g is, especially for the case of π_u, the ionic transitions to the partially empty (as meanwhile they have been tunnel ionised by the strong IR electric field) higher lying π_g and σ_u orbitals driven by the electric field and therefore the formation of the coherence between the ionic states is governed by this second mechanism. Moreover, it is also possible to see that in the case of the $G_{\sigma_g-\sigma_u}$ coherence, the contributions from the two mechanisms show destructive interference, as, at each intensity, the value of the final degree of coherence obtained when both mechanisms are included (ADC(1)) is smaller than the largest

between the values obtained with model-1 and model-2.

Finally in Fig. 6.15 we show the dependence of the final degrees of coherence $G_{\pi_g-\pi_u}$ and $G_{\sigma_g-\sigma_u}$ (top panel) on the central frequency ω of the IR pulse, together with the corresponding dependencies of the normalised relative populations C_{Π_g} , C_{Π_u} and C_{Σ_u} , C_{Σ_g} of the CO_2 ionic states (bottom left panel) and of their relative phases $\phi_{\pi_g-\pi_u}$, $\phi_{\Sigma_u-\Sigma_g}$ (bottom right panel). The laser field is linearly polarised along the molecular axis. The IR peak intensity used in the calculation is $0.8\times10^{14}\,\mathrm{W/cm^2}$ and the pulses remain 'single cycled' as the carrier frequency ω is changed. As it is possible to notice, the G_{Σ_g,Σ_u} degree of coherence increases at longer wavelengths, starting from 800 nm, while the G_{π_g,π_u} coherence shows a much weaker dependence onto the central frequency of the IR laser pulse, remaining almost constant in the range of frequencies from 0.4 a.u. to 0.7 a.u.

6.3.1. Summary

In this Section we have calculated the final degree of coherence between the ionic states of CO_2 formed after ionisation by an intense ultrashort IR laser pulse linearly polarised along the molecular axis. In the cases where the final ionic states produced show an appreciable level of coherence, we have been able to give a quantitative prediction of the resulting ionic wave-function coefficients. We studied the dependence on intensity of the coherences and of the final populations of the ionic states, showing that a high degree of coherence between both the Π symmetry (π_g and π_u) and the Σ symmetry (σ_g and σ_u) ionic channels can be obtained using an ultrashort IR laser pulse with a peak intensity in the range from $1.1\times10^{14}\,\mathrm{W/cm^2}$ to $2\times10^{14}\,\mathrm{W/cm^2}$.

Additionally, we find that interchannel coupling leads to an enhanced entanglement between the photoelectron and the parent ion resulting in a reduced coherence within the ion. Therefore, interchannel coupling accompanying the hole creation process can be expected to affect attosecond experiments investigating hole migration processes in photoionised systems. Moreover, we were able to identify the main mechanism responsible for the establishment of the final coherence; we found that the formation of the coherence between the ionic states of CO_2 is governed by the electron rearrangement within the ionic system caused by the dipole transitions between the different ionic states driven by the IR electric field. Finally it was shown

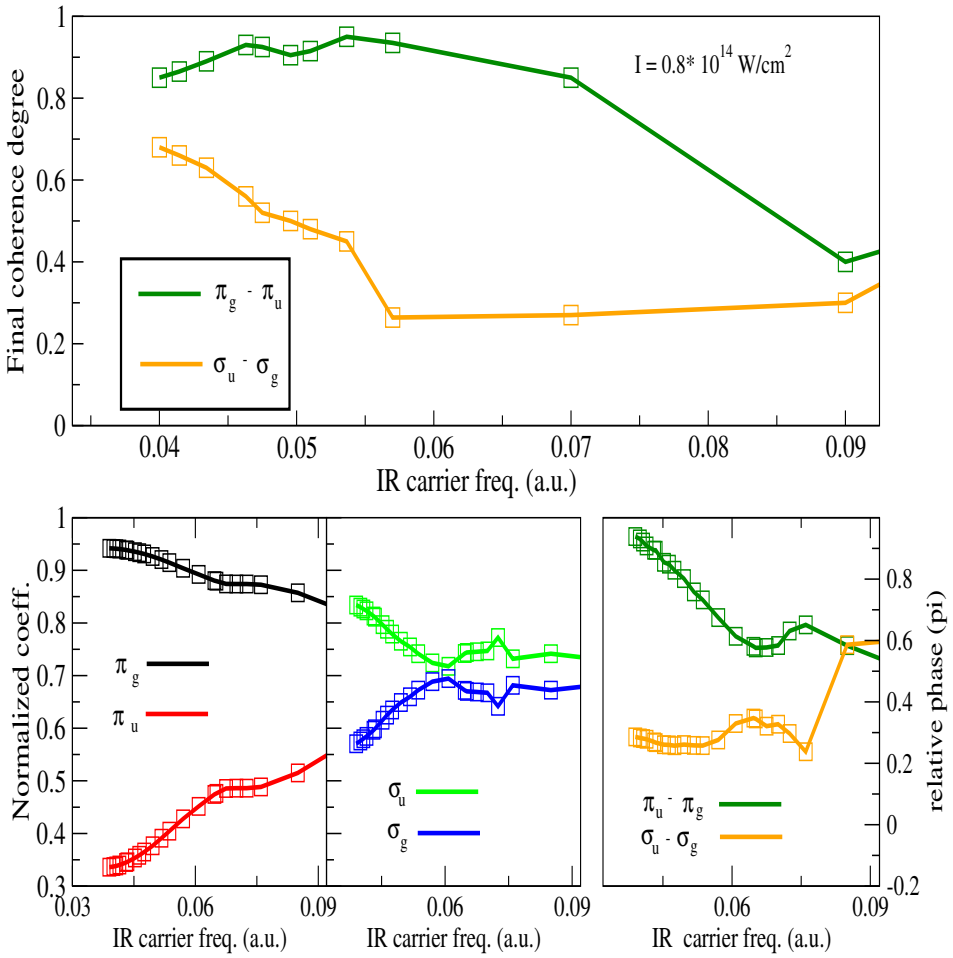

Figure 6.15.: Top panel – central frequency dependence of the final degrees of coherence $G_{\pi_g-\pi_u}$ and $G_{\sigma_g-\sigma_u}$ between the final ionic states produced during the ionisation of CO_2 by an ultra-short IR laser pulse. Bottom panel – Absolute value of the normalised coefficients C_{Π_g} and C_{Π_u} for the Π symmetry ionic wave-function (left figure); Absolute value of the normalised coefficients C_{Σ_u} and C_{Σ_g} for the Σ symmetry ionic wave-function (central figure); Relative phases $\phi_{\pi_g-\pi_u}$ and $\phi_{\Sigma_u-\Sigma_g}$, in units of π, for the Π and Σ symmetry ionic wave-functions (right figure). The IR peak intensity and the pulse duration used in the calculation are respectively $0.8 \times 10^{14}\,\mathrm{W/cm^2}$ and 5.2 fs.

that the $\pi_g - \pi_u$ final coherence is weakly affected by the central frequency of the ultrashort pulse in the frequency range from 0.4 a.u. from to 0.7 a.u., while using wavelengths longer than 800 nm leads to higher degrees of coherence between the Σ_g and Σ_u hole ionic states. This study paves the way to the general theoretical understanding of the initial conditions that drive the time-dependent electron dynamics that can be induced in the ionic system produced after photoionisation.

7. Conclusion and perspectives

The aim of this thesis has been the implementation of an efficient first-principles theoretical and numerical method based on the many-electron algebraic diagrammatic construction [ADC(n)] schemes, in order to describe the correlated multi-electron ionisation dynamics induced in atomic and molecular systems by laser pulses both in the perturbative and non-perturbative regime. The basic theoretical problem in the description of atomic and molecular photoionisation is the need to take into account both the scattering character of the photoionised electron continuum wave-function and the electron correlation responsible for the many-electron effects. Within the ADC(n) framework it is possible to describe the electron correlation at different levels of approximation depending on the specific ADC method n used within the ADC hierarchy. The ADC(n) schemes have originally been developed and applied in the Quantum Chemistry (QC) community to the calculation of properties of bound electronic systems using, as single-particle basis set, the Gaussian Type Orbitals which have notorious limitations when used to describe continuum wave-functions of ionised electrons.

However, with the use of the ADC-Lanczos-Stieltjes technique introduced in [104] and based on the application of the Stieltjes-Imaging moment theory to the Lanczos pseudospectra of the GTO-based ADC electronic Hamiltonian, one of the main basic observables describing the electron dynamics of an atom or molecule interacting with an ionising electric field and which can be, at the same time, measured in experiments and predicted theoretically, i.e. the single photon total photoionisation cross-section, becomes accessible (with reasonable accuracy) also with the use of a GTO basis set. Therefore, with the aim of comparing the accuracy of the different ADC(n) schemes in describing the effects of electron correlation in the ionisation dynamics and of establishing the ADC-Lanczos-Stieltjes method introduced in [104] as an efficient and reasonably accurate *ab-initio* tool for theoretical predic-

tion of total molecular photoionisation cross-sections in the valence energy region, a series of total photoionisation cross-sections calculations have been presented in Chapter 3. The accuracy of this method has been established by comparing the ADC-Lanczos-Stieltjes ground state cross-sections calculated at different levels of the *ab-initio* many-body theory, i.e. ADC(1), ADC(2) and ADC(2)x, in the valence ionisation region, to the experimental ones for a series of eight molecules of first row elements for which high-quality experimental cross-sections are available in the literature: HF, NH_3, H_2O, CO_2, H_2CO, CH_4, C_2H_2, and C_2H_4 [146]. Stieltjes imaging has been long established as an efficient way of calculation of total photoionisation cross-sections using discretised continuum pseudospectra of the final states. However, the accuracy of this technique is limited by both the ability of the chosen $\mathcal{L}^2$ basis set to represent continuum functions within the interaction volume and the numerical instability of the computational algorithm of the Stieltjes-Chebyshev moment theory. In view of these limitations, it could be doubted that improving the many-body theoretical description of the ionised system leads to significantly better cross-sections justifying the required higher numerical effort. Indeed, the resulting difference in the calculated cross-sections might fall within the margins of the inaccuracy incurred by the basis set and the Stieltjes imaging procedure. The first results on ADC-Lanczos-Stieltjes method presented [104], indicated that this is actually not the case and full inclusion of double electronic excitations does lead to more accurate Stieltjes imaging cross-sections. However, the initial work dealt only with two atomic and one molecular system. In the present work, it has been shown beyond doubt that the trend seen in Ref. [104] is characteristic of molecules of first row atoms in the valence energy region. It is shown that, within the specific family of post-HF many-electron methods used here (ADC), the second-order ADC technique [ADC(2)] that includes double electronic excitations leads to clear, substantial systematic improvement over the first-order single-excitation ADC(1) theory for all the molecules considered and to very good agreement with experiment for photon energies below 80 eV, while for some of them, use of a more demanding ADC(2)x level of theory leads to better agreement with the available experimental data (see Table 3.2). On average, the precision gain achieved with ADC(2)x relative to ADC(2) in the energy window considered (from ionisation threshold up to 100 eV) is about twice smaller than the preci-

sion gain of ADC(2) relative to the single-excitation ADC(1) method. The analysis of the relative deviations of the three *ab-initio* methods as function of photon energy has shown that below 60 eV both ADC(2) and ADC(2)x methods lead to impressive agreement with experiment with the relative deviations below 10%. At higher photon energies, the inaccuracy of all the ADC schemes grows, reaching the 20% level around 80 eV. Since above 80 eV photon energy all three methods lead to significant deviations from the experimental values, this behaviour does not depend on the level of *ab-initio* theory; the inaccuracy in this photon energy range is attributed to the limitations inherent to the use of the Gaussian single-electron basis sets, which are not adequate to represent the rapidly oscillating continuum states of high kinetic energy ionised electrons as present, rapidly increasing, numerical linear dependencies as the basis set increases. In summary, the work presented in Chapter 3 has established the ADC(2)-Lanczos-Stieltjes technique as an efficient and reasonably accurate *ab-initio* tool for theoretical prediction of total molecular photoionisation cross-sections in the valence energy region. Indeed, even within an unoptimised straightforward implementation of the method on the Intel Core i7-2600 processor, typical CPU time required for the cross-section calculations presented here is of the order of a few hours.

Moreover, we extended the $\mathcal{L}^2$ *ab-initio* ADC-Lanczos-Stieltjes method to the calculation of total photoionisation cross-sections of molecules in electronically excited states [165]. Comparison of the series of excited state cross-sections for the CO, N_2 and H_2O molecules, computed both at the ground state and the excited state equilibrium geometries and at different levels of the *ab-initio* many-body theory, i.e. ADC(1), ADC(2) and ADC(2)x, led us to conclude that, in contrast to the ground state photoionisation case, the single excitation ADC(1) method is inadequate for the description of the excited state photoionisation even at the qualitative level and that the inclusion of double electronic excitations for description of excited state photoionisation is essential. The reason for the inapplicability of the first-order scheme is that many of the final states of the process have double excitation (2h2p) character and this class of possible final states is completely omitted by the single-excitation ADC(1) method. While this feature is fully expected on the basis of the simple Slater-Condon rule analysis, the extent to which the double excitations change the cross-section

could be seen only in a quantitative study such as the one performed here. The numerical results reported in Chapter 4 show beyond doubt that the full inclusion of double electronic excitations is absolutely necessary in order to produce even a qualitatively accurate photoionisation cross-section. Moreover, it is found that it is important to include the coupling between the double excitations into the theory. Indeed, within the ADC family of methods used here ADC(2)x leads to clear, substantial difference from the strict second-order ADC(2) theory for all molecules and all geometries considered. This is in sharp contrast to the case of the ground state cross-sections, where ADC(2) and ADC(2)x results were found to be in much better agreement [146]. Since the doubly excited final states of the excited state photoionisation are much better described by the ADC(2)x theory, it is assumed that the ADC(2)x cross-sections represent a major improvement over the ADC(2) results. In summary, the calculations reported in Chapter 4 demonstrated that a theoretical modelling of photoionisation of excited states requires an intrinsically double excitation theory with respect to the ground state and can not be achieved by the standard single excitation methods.

There is no reason to assume that the failure of the single-excitation theory for the excited state photoionisation is unique to the ADC(1) scheme. Indeed, these results imply that any method that does not fully include the 2h2p final states, such as configuration interaction singles (CIS), Tamm-Dancoff approximation (TDA), random phase approximation (RPA), linear response TDDFT, etc. can not be expected to provide a correct description of the process. A separate issue is whether the non-perturbative TDDFT calculations, such as performed in Ref. [164] can describe ionisation of a many-electron wavepacket consisting of the ground and a series of excited states. For the exchange-correlation functionals used in Ref. [164], one would expect that in general the contribution of the double excitation relative to that of the singles is subject to non-physical constraints stemming from the single-determinant description and as a result the XUV ionisation probability should not be given correctly. Indeed, artefacts arising from the single determinant character of the wave-function have been extensively discussed in the context of the related time-dependent HF (TDHF) method [184]. However, if the exciting IR field can be considered as an adiabatic perturbation, the initial (approximately HF, i.e. single-determinant) ground state

would physically evolve into a TDHF-like state under the influence of the IR field. XUV ionisation of such an adiabatic TDHF state should be given correctly by the TDHF or TDDFT theory as long as the XUV intensity is in the perturbative regime. From the cross-section analysis presented in Chapter 4, it is clear however that careful benchmarking of the performance of the non-perturbative TDDFT with various exchange-correlation functionals in the time-dependent modelling of excitation-ionisation schemes is highly warranted.

The main focus of research in my PhD has been dedicated to overcoming the difficulty of representing the ionisation continuum inherent to the use of the GTO basis set, by abandoning the GTO L^2 approach and successfully constructing and computationally optimising the first B-spline implementation of the first- [ADC(1)] and second-order [ADC(2)] schemes for electronic excitations, which has been presented in the second part of this thesis and applied to the *ab-initio* calculation of photoionisation cross-sections, which are natural computational targets for the newly-implemented technique and dynamic quantities (high-order harmonic generation spectra, reduced ionic density matrices).

The implementation of the time-dependent version of the B-spline method has been based on the solution of the TDSE via the Arnoldi Lanczos algorithm. The advantages of using the B-spline basis set is that the B-splines basis functions give an accurate representation of the true electronic continuum, making it possible to describe highly oscillating discretised continuum wave-functions and therefore overcoming the limitations inherent to the use of Gaussians.

By performing a series of atomic photoionisation cross-section calculations, we have demonstrated the advantages of the B-spline ADC showing that the cross-section features that pose a challenge for the Gaussian basis calculations are found to be reproduced by the B-spline ADC in excellent agreement with the experiment [55]. In particular, we have been able to correctly predict the argon Cooper minimum shape and position in the total cross-section within the moment theory technique. The superior accuracy of the newly implemented basis set is also manifested by the ability to correctly reproduce the high-energy tails of the cross-sections that we have shown to present a notorious difficulty for the GTO-based schemes [146]. Total B-spline ADC(1) photoionisation cross-sections of N_2 and CO_2 molecules are

also presented; as in the case of the noble gas atoms calculations, also in the molecular case the high-energy tails are found to be much better reproduced with respect to the analogous GTO-based ADC(1) calculations. Apart from the strongly improved accuracy, the B-spline implementation leads to a remarkable stability of the cross-sections with respect to the order of the Stieltjes-Chebyshev moment theory. While the moment theory method leads to the straightforward comparison between the performance of the GTO and B-spline bases, it is no longer a necessity within the B-spline ADC. Indeed, one can obtain directly the correctly normalised continuum eigenstates at arbitrary values of the energy in the electronic continuum by employing methods of Refs. [115, 117]. This should be one of the directions for future work. Another plausible direction for future research is generalisation of the B-spline implementation to calculation of the decay widths within the Fano-Feshbach formalism, see Refs. [99] on the GTO-based Fano-ADC methods. In view of the large (compared to GTO) size of the B-spline bases, optimised implementation of the B-spline method, both the time-independent and -dependent versions, within the MPI and OpenMP protocols has been realised, making the future calculations of molecular systems entirely possible. A lot of optimisation, both regarding the time consumption and the dynamical memory requirements and issues, was performed on the two-electron integral transformation from the primitive monocentric B-spline basis set functions to the HF canonical orbitals required within the ADC formalism. The CPU time required for the type of cross-section calculations presented in this thesis is, for example, of the order of a few minutes for the ADC(1) method and of a few hours for the ADC(2) level of theory, when using 20 computer cores.

By calculating the high-order harmonic generation spectrum of the Ar atom we presented the first strong-field time-dependent application of the new *ab-initio* B-spline ADC technique [55], showing that the effect of the Cooper minimum on the high-order harmonic generation spectrum of Ar is correctly predicted by the time-dependent ADC calculation in the B-spline basis.

We also performed a fully time-dependent *ab-initio* calculation for the electron dynamic of the CO_2 molecule interacting with an high-intensity ultra-short infrared (IR) laser pulse, calculating the high-order harmonic generation spectra for different field intensities and quantitatively investi-

gating the multi-channel effects on its dynamical minimum. The results presented in Chapter 6 show that the main features of the CO_2 molecule HHG spectra, i.e. the position of the dynamical minimum and its field intensity dependence, are found to be reproduced by the B-spline ADC(1) calculations in a very good agreement with the various experiments which have been performed during the past few years [130, 197, 198, 199, 61]. Indeed, the calculated ADC(1) HHG spectra calculations performed here present a clear minimum in the high harmonic spectrum of CO_2, which shifts, almost linearly, to higher orders with increasing intensity, from H_{19} at $I_1 = 0.7 \times 10^{14}\,\mathrm{W/cm^2}$ to H_{27} at $I_3 = 1.75 \times 10^{14}\,\mathrm{W/cm^2}$. We have investigated the origin of the minimum by performing an orbital resolved analysis of the CO_2 HHG spectrum, taking into account the inter-channel couplings driven by the Coulomb interaction and the ionic dipole transitions induced by the IR electric field. We have found that the inter-channel couplings can play an important role in determining the relative contributions to the total HHG spectrum from the different ionic channels, and consequently its overall structure, increasing the contribution of channels that would otherwise be negligible in an independent-electron model. We also found that the position of the minimum in general depends on their inclusion in the simulation and that neglecting these multichannel interactions can lead to large modifications of up to one order of magnitude in the HHG yield, especially in the plateau region (see Fig. 6.4). These calculations demonstrate that many-body effects enter in the HHG spectrum and therefore they cannot generally be neglected but need to be understood in order to successfully use them for tomographic imaging of molecular orbitals [128, 129].

As a last application of the newly-implemented TD B-spline ADC code, we performed a study about the nature and internal coherence of the ionic wavepacket formed after strong field ionisation of the CO_2 molecule. We calculated the final degree of coherence between the ionic states of CO_2 formed after ionisation by an intense ultrashort IR laser pulse linearly polarised along the molecular axis. In the cases where the final ionic states produced show an appreciable level of coherence, we were able to give a quantitative prediction on the resulting ionic wave-function coefficients. We studied the intensity dependencies of the coherences and of the final populations of the ionic states, showing that a high degree of coherence between both the Π symmetry (π_g and π_u) and the Σ symmetry (σ_g and σ_u) ionic channels

can be obtained using an ultrashort IR laser pulse with a peak intensity in the range from $1.1 \times 10^{14}\,\mathrm{W/cm^2}$ to $2 \times 10^{14}\,\mathrm{W/cm^2}$. Additionally, we have found that interchannel coupling leads to an enhanced entanglement between the photoelectron and the parent ion resulting in a reduced coherence within the ion. Therefore, interchannel coupling accompanying the hole creation process can be expected to affect attosecond experiments investigating hole migration processes in photoionised systems. Moreover, we were able to identify the main mechanism responsible for the establishment of the final coherence; we have found that the formation of the coherence between the ionic states of CO_2 is governed by the electron rearrangement within the ionic system caused by the dipole transitions between the different ionic states driven by the IR electric field. Finally it was shown that the $\pi_g - \pi_u$ final coherence is weakly affected by the central frequency of the ultrashort pulse in the frequency range from 0.4 a.u. from to 0.7 a.u., while using wavelengths longer than 800 nm leads to higher degrees of coherence between the Σ_g and Σ_u hole ionic states. The present calculations provide a quantitative understanding about the nature of the ionic states produced after the strong IR field ionisation of the CO_2 molecule in the case of laser fields linearly polarised along the molecular axis.

This study paves the way to the general theoretical understanding of the initial conditions that drive the time-dependent electron dynamics that can be induced in the ionic system produced after IR ionisation and measured in pump-probe scheme based experiments. Indeed, after photoionisation, the state of the molecular ion can consist of a superposition of different ionic eigenstates and can therefore undergo an internal non-trivial dynamical evolution, such as hole-migration [35, 36], Auger decay and so forth. These processes are the focus of the major attosecond electron dynamics research within the attosecond scientific community [20]. In order to follow the dynamical evolution of the system after ionisation, it is essential to know the exact initial state in which the ion is produced, i.e. the exact hole density of the molecular ion. The quantitative understanding of the nature of the ionic state which is produced after the ionisation of the molecular system eliminates the uncertainty about the initial conditions to be fixed for describing and interpreting the post-ionisation electron dynamics in the cation system, i.e. hole migration, as the initial state does not have to be guessed anymore. Moreover, the coherence of the resulting ionic system is

crucial to the theoretical interpretation of the dynamical informations that can be obtained in time-resolved (pump-probe) experiments [48].

The groundbreaking development of the attosecond laser pulse [19] in the extreme ultraviolet (XUV) spectrum where atoms and molecules can be ionised has enabled the experimental study of attosecond physics [20], i.e. the study of ultrafast motions of electrons in atoms, molecules and condensed matter, which can be resolved on a femtosecond or attosecond timescale.

Our main goal for future works is the application of the newly-developed time-dependent many-electron B-spline ADC theory for atomic and molecular interaction with strong IR and attosecond XUV laser pulses to the *ab-initio* description of strong field multiphoton ionisation, creation of ionic state wavepackets by sudden single-photon ionisation, high-order harmonic generation, above-threshold ionisation, electron correlation-driven hole migration, etc.

The advancement of attosecond physics requires new time-resolving methods and new attosecond spectroscopies. Therefore, future perspective also include the application of the time-dependent B-spline ADC method to two new types of attosecond spectroscopies of electron-hole dynamics, high-order harmonic generation (HHG) based spectroscopy [224] and single-photon laser-enabled Auger decay (spLEAD) spectroscopy [225].

Auger decay is one of the main relaxation processes of an inner-shell hole in the atom or molecule. A valence electron fills the vacancy in the inner shell and raises the energy of the system, which in turn ionises another valence electron. In summary, it is an autoionisation process of which the net result is the emission of an electron from the system. Auger decay typically takes place in a few femtoseconds to hundreds of attoseconds and the rate can be measured accurately by streaking [31]. Attosecond streaking [31] is a state-of-the-art technique used to resolve ultrafast electron dynamics. It relies on the emission of electrons from the system triggered by attosecond pulses, and driving those electrons with phase-controlled IR field. By sampling the time evolution of the electron signal as a function of the phase delay between the IR field and the attosecond pulse, one can retrace the process back to the dynamics of the system that leads to the emission. In some cases of electron-hole dynamics such as hole migration [35, 36], no secondary electron is emitted, and therefore streaking is unable to trace the

dynamics. Other attosecond techniques have been introduced recently, for example attosecond transient absorption [32], but so far it is limited to electron dynamics in the valence shell, because the initial ionisation happens through tunneling effect.

The HHG spectroscopy of Auger-type transitions has been proposed theoretically by Leeuwenburgh *et al.* [224]. In the XIHHG process, while one electron is emitted from the atomic or molecular system through either tunneling or photoionisation and then accelerated in the IR field, another core electron is ionised by the XUV pulse. Recombination of the electron driven back to the parent ion by the IR field and consequent production of HHG radiation can occur only if, meanwhile, the excited ionic system has not undergone Auger decay or an Auger-type transition, as the core hole would not exist anymore and therefore recombination would be suppressed and no HHG photon would be emitted. Since the energy of the emitted HHG photon is mapped to the time elapsed after the ionisation [226] and the intensity of the HHG radiation varies linearly with the survival probability of the initial hole, a profile for the attosecond electron hole dynamics of the ion can be constructed. In the work presented in [224], the survival probability in krypton and the electron-hole dynamics in trans-butadiene and propanal were reconstructed from the simulated HHG spectrum. The reconstructed curve fit the original one well. However the calculation was based on the plane wave approximation for the description of the electronic continuum wave-function, even though the kinetic energy of the electron may not be high enough to justify this approximation. Performing a calculation using the time-dependent B-spline ADC method, one can get a better description of the wave-function in the continuum and hence a more accurate result and understanding of the underlying physical processes.

The electron-hole dynamics in an inner-valence ionised molecule with energy below the double ionisation potential (DIP) can be probed by inducing Auger decay with a single photon. The photon provides energy to an outer-valence electron so that it is energetic enough to go through Auger decay. The technique of laser-enabled Auger decay (LEAD) has already been realised experimentally on argon ion in the multiphoton regime [227]. The difference between LEAD and spLEAD is that the latter one is more sensitive to the initial configuration mixing of the ion as many transitions are forbidden by the many-body selection rules. On the other hand, multi-

photon absorption makes many more transitions possible with the result that the final Auger decay can arise from many different configurations, therefore losing the information regarding the initial electron-hole dynamics. Within a certain range of energy, spLEAD is the only possible process that is able to produce a doubly charged ion starting from a singly charged one. Therefore measuring the probability of double ionisation is equivalent to measuring the probability of the spLEAD transition. A theoretical calculation of the spLEAD probability and the survival probability of the initial state has been performed by Cooper and Averbukh [225]. The results indicate a correspondence between the two quantities in terms of the time evolution pattern. Since the calculation was done with the use of a GTO L^2 single-electron basis set, the theoretical model did not include a description and the effects of the phase component of the dipole. With the use of the time-dependent B-spline ADC numerical tool, the phase of the matrix elements can be accurately calculated and naturally included in the calculation, therefore obtaining a real *ab-initio* simulation of the spLEAD based pump-probe spectroscopy.

Initially, we plan to apply the TD B-spline ADC method to the HHG and spLEAD spectroscopies of ultrafast atomic processes, such as Auger decay in neon $1s$ and spLEAD in neon $2s$, to test the methodology. As a second step, we plan to simulate the electron-hole dynamics of molecular systems, such as glycine, where we expect the results to uncover effects, such as the molecular-orbital (MO) picture breakdown [228], which would never appear in a simplified theoretical model. The strong electron correlation in an ion with energy near DIP causes the excited state configurations to overwhelm the ground state in the wave-function of the ion. The electrons no longer have well-defined orbitals, and the MO picture of the ionisation breaks down. The time dependence of the wave-function becomes significant due to the abundance of the excited state configurations. Theoretical studies of such molecules with TD B-spline ADC may also help us understand attosecond hole migration in large molecules such as peptides, short chains of aminoacids, as suggested in [35]. So far the phenomenon has not been observed experimentally, but hopefully this work will lead to the very first experimental verification of the electron-correlation-driven hole migration.

In order to be able to apply the TD B-spline ADC method to molecules as large as glycine, we plan to extend the actual implementation based on a

One Centre Expansion (OCE), where the functions are centred on a single origin, to a multicentre basis set approach. The multicentre approach consists of adding off-centre functions, located at non-equivalent nuclei, to the B-spline expansion and permits to improves dramatically the convergence of the calculation for most molecules [229]. Two different types of approach are possible: a mixed B-spline/GTO, where the added off-centre radial functions are GTO's or a full multicentre B-spline basis approach, where all the radial functions located at the different centres are represented as B-splines. Traditionally, a multicentre basis set is constituted by GTO or STO functions that yield fast convergence for the lowest bound states with a limited number of basis functions. Increasing the basis represents a difficult task because numerical linear dependencies rapidly come up. This is due to the large overlap between functions on different centres. One of the advantages of using a complete spherical B-spline functions approach lies on the fact that their local nature permits to control the overlap between functions and avoid numerical linear dependence problems [57]. In this approach the radial and angular parts of the basis set are expanded over several suitable centres to correctly describe bound and continuum states. These centres are:

- The centre of mass of the molecule, associated with a large spherical box of radius R^O_{max} to correctly describe the long range behaviour of the continuum wave-functions.

- The position occupied by each nucleus i, associated with smaller spherical boxes of radius R^i_{max}; this boxes are generally quite small (1 a.u.) in order to avoid significant overlap with the expansions performed on neighbouring centres.

The addition of these off-centre basis functions will solve the convergence problem that the spherical harmonics monocentric expansion presents when applied to the description of orbitals localised in distant off-centre atomic nuclei. Our goal is to efficiently implement the calculation of the two-electron integrals in this multicentre B-spline basis set, and consequently apply the TD B-spline ADC correlated method to large molecules, such as benzene and amino-acids.

In summary, the present development paves the way to the *ab-initio* study of these phenomena not only in atoms but also in molecular systems and

beyond single excitation theory (e.g., TDCIS [64, 143, 196]), as is indeed essential, e.g. [165], in order to describe the dynamical phenomena involving photoabsorption from excited states of the system and will allow the possibility to accurately describe a series of many-electron phenomena in the time-resolved fashion on the atto-second scale.

Publications

- M. Ruberti, R. Yun, K. Gokhberg, S. Kopelke, L. S. Cederbaum, F. Tarantelli and V. Averbukh, J. Chem. Phys. **139**, 144107 (2013).
- M. Ruberti, R. Yun, K. Gokhberg, S. Kopelke, L. S. Cederbaum, F. Tarantelli and V. Averbukh, J. Chem. Phys. **140**, 184107 (2014).
- M. Ruberti, V. Averbukh and P. Decleva, J. Chem. Phys. **141**, 164126 (2014).
- M. Ruberti, V. Averbukh and P. Decleva, "Total and channel resolved *ab-initio* ADC(1) high harmonic generation spectra of aligned CO_2 molecule", to be submitted to J. Chem. Phys.
- M. Ruberti, V. Averbukh and P. Decleva, "Nature of the ionic wavepacket resulting from ionisation of aligned CO_2 molecule by femtosecond strong field IR pulses", to be submitted to J. Chem. Phys.

Bibliography

[1] U. Fano and J. W. Cooper, Rev. Mod. Phys. **40**, 441 (1968).

[2] M. Schultze, M. Fiess, N. Karpowicz, J. Gagnon, M. Korbman, M. Hofstetter, S. Neppl, A. L. Cavalieri, Y. Komninos, T. Mercouris *et al.*, Science **328**, 1658 (2010).

[3] G. Sansone, F. Kelkensberg, J. F. Perez-Torres, F. Morales, M. F. Kling, W. Siu, O. Ghafur, P. Johnsson, M. Swoboda, E. Benedetti *et al.*, Nature (London) **465**, 763 (2010).

[4] K. J. Schafer, B. Yang, L. F. Di Mauro, and K. C. Kulander, Phys. Rev. Lett. **70**, 1599 (1993).

[5] M. Lein, J. P. Marangos, and P. L. Knight, Phys. Rev. A **66**, 051404 (2002).

[6] C. I. Blaga, F. Catoire, P. Colosimo, G. G. Paulus, H. G. Muller, P. Agostini, and L. F. DiMauro, Nat. Phys. **5**, 335 (2009).

[7] A. Fleischer, H. J. Wörner, L. Arissian, L. R. Liu, M. Meckel, A. Rippert, R. Dörner, D. M. Villeneuve, P. B. Corkum, and A. Staudte, Phys. Rev. Lett. **107**, 113003 (2011).

[8] R. Murray, M. Spanner, S. Patchkovskii, and M. Y. Ivanov, Phys. Rev. Lett. **106**, 173001 (2011).

[9] A. N. Pfeiffer, C. Cirelli, M. Smolarski, R. Dorner, and U. Keller, Nat. Phys. **7**, 428 (2011).

[10]

[11] G. Doumy *et al.*, Phys. Rev. Lett. **102**, 093002 (2009).

[12] N. Dudovich *et al.*, Nature Phys. **2**, 781 (2006).

[13] E. A. Gibson *et al.*, Phys. Rev. Lett. **92**, 033001 (2004).

[14] E. Goulielmakis *et al.*, Science **320**, 1614 (2008).

[15] D. Fabris, T. Witting, W. A. Okell, D. J. Walke, P. Matia-Hernando, J. Henkel, T. R. Barillot, M. Lein, J. P. Marangos and J. W. G. Tisch, Nature Photonics **9**, 383-387 (2015).

[16] P. B. Corkum and F. Krausz, Nat. Phys. **3**, 381 (2007).

[17] A.-T. Le, R. D. Picca, P. D. Fainstein, D. A. Telnov, M. Lein, and C. D. Lin, J. Phys. B **41**, 081002 (2008).

[18] J. P. Marangos *et al.*, Phys. Chem. Chem. Phys. **10**, 35 (2008).

[19] M. Hentschel , R. Kienberger, Ch. Spielmann, G. A. Reider, N. Milosevic, T. Brabec, P Corkum, U. Heinzmann, M. Drescher and F. Krausz, Nature **414**, 509 (2001).

[20] F. Krausz and M. Ivanov, Rev. Mod. Phys. **81**, 163 (2009).

[21] L. Cederbaum and J. Zobeley, Chem. Phys. Lett. **307**, 205 (1999).

[22] J. Mauritsson, P. Johnsson, E. Mansten, M. Swoboda, T. Ruchon, A. LHuillier, and K. J. Schafer, Phys. Rev. Lett. **100**, 073003 (2008).

[23] P. Eckle, A. N. Pfeiffer, C. Cirelli, A. Staudte, R. Dörner, H. G. Muller, M. Büttiker, and U. Keller, Science **322**, 1525 (2008).

[24] C. Ott, A. Kaldun, P. Raith, K. Meyer, M. Laux, J. Evers, C. H. Keitel, C. H. Greene, and T. Pfeifer, Science **340**, 716 (2013).

[25] M. Schultze, K. Ramasesha, C. Pemmaraju, S. Sato, D. Whitmore, A. Gandman, J. S. Prell, L. J. Borja, D. Prendergast, K. Yabana, D. M. Neumark, and S. R. Leone, Science **346**, 1348 (2014).

[26] M. C. H. Wong, A.-T. Le, A. F. Alharbi, A. E. Boguslavskiy, R. R. Lucchese, J.-P. Brichta, C. D. Lin, and V. R. Bhardwaj, Phys. Rev. Lett. **110**, 033006 (2013).

[27] I. Petersen, J. Henkel, and M. Lein, Phys. Rev. Lett. **114**, 103004 (2015).

[28] S. Haessler *et al.*, Nature Phys. **6**, 200 (2010).

[29] J. Mauritsson *et al.*, Phys. Rev. Lett. **105**, 053001 (2010).

[30] E. Skantzakis *et al.*, Phys. Rev. Lett. **105**, 043902 (2010).

[31] M. Drescher, M. Hentschel, R. Kienberger, M. Uiberacker, V. Yakovlev, A. Scrinzi, Th. Westerwalbesloh, U. Kleineberg, U. Heinzmann and F. Krausz, Nature **419**, 803 (2002).

[32] E. Goulielmakis, Z. Loh, A. Wirth, R. Santra, N. Rohringer, V. S. Yakovlev, S. Zherebtsov, T. Pfeifer, A. M. Azzeer, M. F. Kling, S. R. Leone and F. Krausz, Nature **466**, 739 (2010).

[33] A. Wirth, M. T. Hassan, I. Grguras, J. Gagnon, A. Moulet, T. T. Luu, S. Pabst, R. Santra, Z. A. Alahmed, A. M. Azzeer, V. S. Yakovlev, V. Pervak, F. Krausz, and E. Goulielmakis, Science **334**, 195 (2011).

[34] K. Schnorr, A. Senftleben, M. Kurka, A. Rudenko, L. Foucar, G. Schmid, A. Broska, T. Pfeifer, K. Meyer, D. Anielski, R. Boll, D. Rolles, M. Kübel, M. F. Kling, Y. H. Jiang, S. Mondal, T. Tachibana, K. Ueda, T. Marchenko, M. Simon, G. Brenner, R. Treusch, S. Scheit, V. Averbukh, J. Ullrich, C. D. Schröter and R. Moshammer, Phys. Rev. Lett. **111**, 093402 (2013).

[35] F. Remacle and R. D. Levine, Proceedings of the National Academy of Science **103**, 6793 (2006).

[36] J. Breidbach and L. S. Cederbaum, J. Chem. Phys. **118**, 3983 (2003); A. I. Kuleff and A. Dreuw, J. Chem. Phys. **130**, 034102 (2009); H. Eshuis and T. van Voorhis, Phys. Chem. Chem. Phys. **11**, 10293 (2009); S. Lunnemann, A. I. Kuleff, and L. S. Cederbaum, J. Chem. Phys. **129**, 104305 (2008); M. Nest, F. Remacle, and R. D. Levine, New J. Phys. **10**, 025019 (2008); A. I. Kuleff, S. Lunnemann, and L. S. Cederbaum, J. Phys. Chem. A **114**, 8676 (2010); A. I. Kuleff and L. S. Cederbaum, Phys. Rev. Lett. **106**, 053001 (2011).

[37] P. M. Kraus, A. Rupenyan, J. Schneider, D. Baykusheva, and H. J. Wörner, 4th International Conference on Attosecond Physics (2013).

[38] V. Averbukh, U. Saalmann and J. M. Rost, Phys. Rev. Lett. **104**, 233002 (2010); J. Craigie, A. Hammad, B. Cooper and V. Averbukh, J. Chem. Phys. **141**, 014105 (2014).

[39] C. Ott, A. Kaldun, L. Argenti, P. Raith, K. Meyer, M. Laux, Y. Zhang, A. Blattermann, S. Hagstotz, T. Ding, R. Heck, J. Madronero, F. Martin, and T. Pfeifer, Nature **516**, 374 (2014).

[40] H. J. Wörner and P. B. Corkum, Journal of Physics B: Atomic, Molecular and Optical Physics **44**, 041001 (2011).

[41] P. M. Kraus, S. B. Zhang, A. Gijsbertsen, R. R. Lucchese, N. Rohringer, and H. J. Wörner, Phys. Rev. Lett. **111**, 243005 (2013).

[42] D. Baykusheva, P. M. Kraus, S. B. Zhang, N. Rohringer, and H. J. Wörner, Faraday Discussions (2014).

[43] S. B. Zhang, D. Baykusheva, P. M. Kraus, H. J. Wörner, and N. Rohringer, Phys. Rev. A **91**, 023421 (2015).

[44] D. Mendive-Tapia, M. Vacher, M. J. Bearpark and M. A. Robb, J. Chem. Phys. **139**, 044110 (2013).

[45] Louise Belshaw, Francesca Calegari, Martin J. Duffy, Andrea Trabattoni, Luca Poletto, Mauro Nisoli, and Jason B. Greenwood, J. Phys. Chem. Lett. **3**, 3751 (2012).

[46] R. Weinkauf *et al.*, J. Phys. Chem. A **101**, 7702 (1997).

[47] E. W. Schlag *et al.*, Angew. Chem., Int. Ed. **46**, 3196 (2007).

[48] B. Cooper, P. Kolorenč, L. J. Frasinski, V. Averbukh and J. P. Marangos, Faraday Discuss. **171**, 93-111 (2014).

[49] A. Szabo and N. S. Ostlund, *Modern Quantum Chemistry: Introduction to Advanced Electronic Structure Theory* (Dover, New York, 1996).

[50] R. J. W. Henry and L. Lipsky, Phys. Rev. **153**, 51 (1967); H. P. Kelly, Chem. Phys. Lett. **20**, 547 (1973); M. Ya. Amusia, in Atomic Physics 5, edited by R. Marrus, M. Prior and H. Shugart (Plenum, New York, 1977), pp. 537-565; S. T. Manson and A. F. Starace, Rev. Mod. Phys. **54**, 389 (1982).

[51] G. Fronzoni, M. Stener, P. Decleva, Chem. Phys. **298**, 141 (2004); Xi Chu, Phys. Rev. A **82**, 023407 (2010); N. Rohringer, A. Gordon, and R. Santra, Phys. Rev. A **74**, 043420 (2006).

[52] C. M. Oana and A. I. Krylov, J. Chem. Phys. **127**, 234106 (2007).

[53] H. Nakatsuji and K. Hirao, J. Chem. Phys. **68**, 2053 (1978).

[54] J. F. Stanton and R. J. Bartlett, J. Chem. Phys. **98**, 7029 (1993).

[55] M. Ruberti, V. Averbukh and P. Decleva, J. Chem. Phys. **141**, 164126 (2014). "Reproduced with permission from ["B-spline algebraic diagrammatic construction: Application to photoionization cross-sections and high-order harmonic generation", M. Ruberti, V. Averbukh and P. Decleva, J. Chem. Phys. 141, 164126 (2014). http://dx.doi.org/10.1063/1.4900444]. Copyright [2014], AIP Publishing LLC.

[56] J. Schirmer, Phys. Rev. A **26**, 2395 (1982).

[57] H. Bachau, E. Cormier, P. Decleva, J. E. Hansen and F. Martin, Rep. Prog. Phys. **64**, 1815 (2001).

[58] G. N. Gibson, R. R. Freeman, and T. J. McIlrath, Phys. Rev. Lett. **67**, 1230 (1991).

[59] H. Akagi, L. Arissian, J. B. Bertrand, P. B. Corkum, M. Gertsvolf, D. Pavici c, D. M. Rayner, C. Smeenk, A. Staudte, D. M. Villeneuve, and H. J. Wörner, Laser Physics **19**, 1697 (2009).

[60] O. Smirnova, Y. Mairesse, S. Patchkovskii, N. Dudovich, D. Villeneuve, P. Corkum, and M. Y. Ivanov, Nature (London) **460**, 972 (2009).

[61] H. J. Wörner, J. B. Bertrand, P. Hockett, P. B. Corkum, and D. M. Villeneuve, Phys. Rev. Lett. **104**, 233904 (2010).

[62] B. K. McFarland, J. P. Farrell, P. H. Bucksbaum, and M. Guhr, Science **322**, 1232 (2008).

[63] H. F. Rey and H. W. van der Hart, Phys. Rev. A **90**, 033402 (2014).

[64] N. Rohringer, A. Gordon and R. Santra, Phys. Rev. A **74**, 043420 (2006).

[65] P. Dennery and A. Krzywicki, *Mathematics for Physicists* (Dover Books on Physics 1996).

[66] Ed. by U. Becker and D. A. Shirley, *VUV and Soft X-Ray Photoionization*, Plenum Press, 1996.

[67] *Polycyclic Aromatic Hydrocarbons and Astrophysics*, edited by A. Leger, L. Dhendecourt, and N. Boccara Reidel, Dordrecht, 1987.

[68] M. Lewenstein, Ph. Balcou, M. Yu. Ivanov, A. LHuillier and P. B. Corkum, Phys. Rev. A **49**, 2117 (1994).

[69] J. Oddershede and P. Jrgensen, J. Chem. Phys. **66**, 1541 (1977).

[70] E. S. Nielsen, P. Jrgensen, and J. Oddershede, J. Chem. Phys. **73**, 6238 (1980).

[71] H. Koch and P. Jörgensen, J. Chem. Phys. **93**, 3333 (1990); A. B. Trofimov, I. L. Krivdina, J. Weller, J. Schirmer, Chemical Physics **329**, 1-10 (2006).

[72] R. D. Mattuck, *A Guide to Feynmann Diagrams in the Many-Body Problem* (McGraw-Hill, New York, 1967).

[73] A. A. Abrikosov, L. P. Gorkov, and I. E. Dzyaloshinski, *Methods of Quantum Field Theory in Statistical Physics* (Prentice-Hall, Englewood Cliffs, N. J. 1963).

[74] P. Nozieres, *Interacting Fermi Systems* (Benjamin, New York, 1964).

[75] A. B. Migdal, *Theory of Finite Fermi Systems* (Wiley-Interscience, New York, 1967).

[76] D. A. Pines, *The Many-Body Problem* (Benjamin, London, 1962).

[77] A. L. Fetter and J. D. Walecka, *Quantum Theory of Many-Particle Systems* (McGraw-Hill, New York, 1971).

[78] P. C. Martin and J. Schwinger, Phys. Rev. **115**, 1342 (1959).

[79] E. E. Salpeter and H. A. Bethe, Phys. Rev. **84**, 1232 (1951).

[80] L. S. Cederbaum, in *The Encyclopaedia of Computational Chemistry*, edited by P. v. R. Schleyer, N. L. Allinger, T. Clask, J. Gasteiger, P. A. Kollmann, H. F. Schaefer III, and P. R. Schreiner (Wiley, Chichester, 1998).

[81] J. Schirmer and A. Barth, Z. Phys. A **317**, 267 (1984); A. Tarantelli and L.S. Cederbaum, Phys. Rev. A **39**, 1656 (1989).

[82] A. Tarantelli and L. S. Cederbaum, Phys. Rev. A **46**, 81 (1992).

[83] A. B. Trofimov, G. Stelter, and J. Schirmer, J. Chem. Phys. **111**, 9982 (1999)

[84] J. Schirmer, Phys. Rev. A **43**, 4647 (1991).

[85] J. Schirmer and A. B. Trofimov, J. Chem. Phys. **120**, 11449 (2004).

[86] E. Dalgaard, Int. J. Quantum Chem. **15**, 169 (1979).

[87] C. Hattig, in: Electronic Structure: Hartree-Fock and Correlation Methods, eds Multiscale Simulation Methods in Molecular Sciences, J. Grotendorst, N. Attig, S. Blugel, D. Marx (Eds.) Vol. **42**, pp. 77-120, (2009).

[88] M. Head-Gordon, M. Oumi, and D. Maurice, Mol. Phys. **96**, 593574, 1999.

[89] P.-O. Löwdin, Phys. Rev. **97**, 1474 (1955).

[90] F. Mertins, J. Schirmer and A. Tarantelli, Phys. Rev. A **53**, 2153 (1996); F. Mertins and J. Schirmer, Phys. Rev. A **53**, 2140 (1996); J. Schirmer and F. Mertins, J. Phys. B **29**, 3559 (1996).

[91] A. B. Trofimov and J. Schirmer, J. Chem. Phys. **123**, 144115 (2005).

[92] Y. Velkov, T. Miteva, N. Sisourat and J. Schirmer J. Chem. Phys. **135**, 154113 (2011).

[93] A. I. Kuleff and L.S. Cederbaum, Phys. Rev.Lett. **98**, 083201 (2007); J. Breidbach and L. S. Cederbaum, J. Chem. Phys. **118**, 3983 (2003); H. Hennig, J. Breidbach, and L. S. Cederbaum J. Chem. Phys. **122**, 134104 (2005).

[94] P. Langhoff, Chem. Phys. Lett. **22**, 60 (1973); P. Langhoff, in *Electron-Molecule and Photon-Molecule Collisions*, edited by T. Rescigno, V. McKoy, and B. Schneider (Plenum, New York, 1979) p. 183; P. W. Langhoff, in *Theory and Application of Moment Methods in Many-Fermion Systems*, edited by B. J. Dalton, S. M. Grimes, J. P. Vary, and S. A. Williams (Plenum, New York, 1980) p. 191; R. R. Whitehead, in *Theory and Applications of Moment Methods in Many-Fermion Systems*, edited by B. J. Dalton, S. M. Grimes, and J. P. Vary (Plenum, New York, 1980) p. 235; P. W. Langhoff and C. T. Corcoran, J. Chem. Phys. **61**, 146 (1974).

[95] P. K. Kabir and E. E. Salpeter, Phys. Rev. **108**, 1256 (1957).

[96] F. Müller-Plathe and G. Diercksen, in *Electronic Structure of Atoms, Molecules and Solids*, edited by S. Canuto, J. D. e Castro, and F. J. Paixão (World Scientific, Singapore, 1990).

[97] P. W. Langhoff, C. T. Corcoran, J. S. Sims, F. Weinhold, and R. M. Glover, Phys. Rev. A **14**, 1042 (1976).

[98] S. Kopelke, K. Gokhberg, L. S. Cederbaum, F. Tarantelli and V. Averbukh, J. Chem. Phys. **134**, 024106 (2011); S. Kopelke, K. Gokhberg, V. Averbukh, F. Tarantelli, and L. S. Cederbaum, J. Chem. Phys. **134**, 094107 (2011).

[99] V. Averbukh and L. S. Cederbaum, J. Chem. Phys. **123**, 204107 (2005); K. Gokhberg, V. Averbukh, and L. S. Cederbaum, J. Chem. Phys. **126**, 154107 (2007); P. Kolorenč, V. Averbukh, K. Gokhberg, and L. S. Cederbaum, J. Chem. Phys. **129**, 244102 (2008).

[100] K. Kaufmann, W. Baumeister, and M. Jungen, J. Phys. B **22**, 2223 (1989).

[101] R. K. Nesbet, Phys. Rev. A **14**, 1065 (1976).

[102] V. V. Ivanov and A. V. Luzanov, J. Struct. Chem. **38**, 10 (1997).

[103] H. Ågren, V. Carravetta, H. J. A. Jensen, P. Jårgensen and J. Olsen, Phys. Rev. A **47**, 5 (1993); H. Ågren, V. Carravetta and Yi Luo, Chem. Phys. **174**, 141 (1993).

[104] K. Gokhberg, V. Vysotskiy, L. S. Cederbaum, L. Storchi, F. Tarantelli, and V. Averbukh, J. Chem. Phys. **130**, 064104 (2009).

[105] J. Cukras, S. Coriani, P. Decleva, O. Christiansen and P. Norman, J. Chem. Phys. **139**, 094103 (2013).

[106] B. N. Parlett, *The Symmetric Eigenvalue Problem* (Prentice-Hall, NJ, 1980).

[107] H.-D. Meyer and S. Pal, J. Chem. Phys. **91**, 6195 (1989).

[108] H.-G. Weikert, H.-D. Meyer, L. S. Cederbaum and F. Tarantelli, J. Chem. Phys. **104**, 7122 (1996).

[109] C. Bottcher, Phys. Rev. Lett. **48**, 85 (1982).

[110] B. W. Shore, J. Chem. Phys. **58**, 3855 (1973).

[111] C. Froese Fischer and M. Idrees, Comput. Phys. **3**, 53 (1989); C. Froese Fischer and W. Guo, J. Comput. Phys. **90**, 486 (1990); C. Froese Fischer, W. Guo and Z. Shen, Int. J. Quantum Chem. **42**, 849 (1992); C. Froese Fischer and M. Idrees, J. Phys. B: At. Mol. Opt. Phys. **23**, 679 (1990); T. Brage, C. Froese Fischer and G. Miecznik, J. Phys. B: At. Mol. Opt. Phys. **25**, 5289 (1992); M. Brosolo and P. Decleva, Chem. Phys. **159**, 185 (1992); M. Brosolo, P. Decleva and A. Lisini, J. Phys. B: At. Mol. Opt. Phys. **25**, 3345 (1992); T. N. Chang and T. K. Fang, Phys. Rev. A **52**, 2638 (1995); D. P. Carrol, H. J. Silverstone and R. M. Metzger, J. Chem. Phys. **71**, 4142 (1979); W. R. Johnson, S. A. Blundell and J. Sapirstein, Phys. Rev. A **37**, 307 (1988); T. N. Chang, Phys. Rev. A **39**, 4946 (1989); T. N. Chang, Phys. Rev. A **47**, 705 (1993); T. N. Chang, Phys. Rev. A **47**, 3441 (1993); T. N. Chang and X. Tang, Phys. Rev. A **44**, 232 (1991); T. N. Chang and M. Zhen, Phys. Rev. A **47**, 4849 (1993); J. C. Morrison, C. Bottcher and G. Bottrell, Theor. Chim. Acta **80**, 245 (1991); J. C. Morrison and C. Bottcher, J. Phys. B: At. Mol. Opt. Phys. **26**, 3999 (1993); Y.-T. Shen, M. Landtman and J. E. Hansen, J. Phys. B: At. Mol. Opt. Phys. **23**, L121 (1990); W. H. van der Hart and J. E. Hansen, J. Phys. B: At. Mol. Opt. Phys. **25**, 41 (1992); W. H. van der Hart and J. E. Hansen, J. Phys. B: At. Mol. Opt. Phys. **26**, 641 (1993); M. Landtman and J.

E. Hansen, J. Phys. B: At. Mol. Opt. Phys. **26**, 3189 (1993); M.-K. Chen and C.-S. Hsue, J. Phys. B: At. Mol. Opt. Phys. **25**, 4059 (1992); P. Decleva, A. Lisini and M. Venuti, Int. J. Quantum Chem. **56**, 27 (1995).

[112] P. Lambropoulos, P. Maragakis and J. Zhang, Phys. Reports **305**, 203 (1998); E. Cormier and P. Lambropoulos, J. Phys. B: At. Mol. Opt. Phys. **30**, 77 (1997); X. Tang, H. Rudolph and P. Lambropoulos, Phys. Rev. Lett. **65**, 3269 (1990); E. Cormier and P. Lambropoulos, J. Phys. B: At. Mol. Opt. Phys. **28**, 1667 (1996); E. Cormier and P. Lambropoulos, J. Phys. B: At. Mol. Opt. Phys. **30**, 3095 (1997); R. Hasbani, E. Cormier and H. Bachau, J. Opt. Soc. Am. B **16**, 1880 (1999); P. Lambropoulos, P. Maragakis and E. Cormier, Laser Phys. **8**, 625 (1998); L. A. A. Nikolopoulos and P. Lambropoulos, Phys. Rev. Lett. **82**, 3771 (1999); S. J. Van Enk, J. Zhang and P. Lambropoulos, J. Phys. B: At. Mol. Opt. Phys. **30**, L17 (1997); J. Zhang and P. Lambropoulos, Phys. Rev. Lett. **77**, 2186 (1996); E. Cormier and M. Lewenstein, Eur. Phys. J. D **12**, 227 (2000); U. Andiel, G. D. Tsakiris, E. Cormier and K. Witte, Eur. Lett. **47**, 42 (1999); P. Maragakis, E. Cormier and P. Lambropoulos, Phys. Rev. A **60**, 4718 (1999); G. Duchateau, C. Illescas, B. Pons, E. Cormier and R. Gayet, J. Phys. B: At. Mol. Opt. Phys. **33**, L571 (2000); R. Hasbani, E. Cormier and H. Bachau, J. Phys. B: At. Mol. Opt. Phys. **33**, 2101 (2000); G. Lagmago Kamta, T. Grosges, B. Piraux, R. Hasbani, E. Cormier and H. Bachau, J. Phys. B: At. Mol. Opt. Phys. **34**, 857 (2001); E. Cormier, D. Garzella, P. Breger, P. Agostini, G. Chriaux and C. Leblanc, J. Phys. B: At. Mol. Opt. Phys. **34**, L9 (2001).

[113] C. de Boor, *A Practical Guide to Splines*. Springer, New York, 1978.

[114] J. R. Rice 1983 *Numerical Methods, Software and Analysis* (Singapore: McGraw-Hill) J. Stoer and R. Bulirsch 1983 *Introduction to Numerical Analysis* (New York: Springer).

[115] P. Decleva, A. Lisini and M. Venuti, J. Phys. B: At. Mol. Opt. Phys. **27**, 4867 (1994).

[116] M. Landtman M and J. E. Hansen, J. Phys. B: At. Mol. Opt. Phys. **26**, 3189 1993.

[117] F. Martin, Phys. Rev. A **48**, 331 (1993); M. Cortes and F. Martin, J. Phys. B: At. Mol. Opt. Phys. **27**, 5741 (1994); M. Venuti, P. Decleva and A. Lisini, J. Phys. B: At. Mol. Opt. Phys. **29**, 5315 (1996); M. Venuti and P. Decleva, J. Phys. B: At. Mol. Opt. Phys. **30**, 4839 (1997); L. Argenti and R. Moccia, J. Phys. B: At. Mol. Opt. Phys. **39**, 2773 (2006).

[118] U. V. Riss and H.-D. Meyer, J. Phys. B **26**, 4503 (1993).

[119] W. E. Arnoldi, Q. Appl. Math. **9**, 17 (1951).

[120] R. A. Friesner, L. S. Tuckerman, B. C. Dornblaser, and T. V. Russo, J. Sci. Comput. **4**, 327 (1989).

[121] C. Leforestier, R. H. Bisseling, C. Cerjan *et al.*, J. Comput. Phys. **94**, 59 (1991).

[122] T. J. Park and J. C. Light, J. Chem. Phys. **85**, 5870 (1986).

[123] G. Jolicard and E. Austin, J. Chem. Phys. **95**, 5056 (1991).

[124] M. H. Beck, A. Jnckle, J. A. Worth, and H.-D. Meyer, Phys. Rep. **324**, 1 (2001).

[125] T. J. Park and J. C. Light, J. Chem. Phys. **85**, 5870 (1986).

[126] P. B. Corkum, Phys. Rev. Lett. **71**, 1994 (1993).

[127] Y. Mairesse et. al., Phys. Rev. Lett. **104**, 213601 (2010).

[128] J. Itatani, J. Levesque, D. Zeidler, H. Niikura, H. Pepin, J. Kieffer, P. Corkum, and D. Villeneuve, Nature (London) **432**, 867 (2004).

[129] C. Vozzi *et al.*, Nature Physics **7**, 822826 (2011).

[130] T. Kanai, S. Minemoto, and H. Sakai, Nature (London) **435**, 470 (2005).

[131] S. Baker *et al.*, Science **312**, 424 (2006).

[132] J. P. Marangos *et al.*, Phys. Chem. Chem. Phys. **10**, 35-48 (2008).

[133] C. Vozzi *et al.*, Appl. Phys. Lett. **97**, 241103 (2010).

[134] T. Morishita, A.-T. Le, Z. Chen, and C. D. Lin, Phys. Rev. Lett. **100**, 013903 (2008).

[135] A.-T. Le, R. R. Lucchese, S. Tonzani, T. Morishita, and C. D. Lin, Phys. Rev. A **80**, 013401 (2009).

[136] M. V. Frolov *et al.*, Phys. Rev. Lett. **102**, 243901 (2009).

[137] Y. Mairesse, J. Levesque, N. Dudovich, P. B. Corkum, and D. M. Villeneuve, J. Mod. Opt. **55**, 2591 (2008).

[138] S. Baker *et al.*, Phys. Rev. Lett. **101**, 053901 (2008).

[139] Y. Mairesse *et al.*, Science **302**, 15401543 (2003).

[140] M. Lein, Phys. Rev. Lett. **94**, 053004 (2005).

[141] P. Agostini and L. F. Di Mauro, Rep. Prog. Phys. **67**, 813 (2004); Nature Physics, Vol. **4**, p. 545, (2008).

[142] A. Gordon and F. Kärtner, Opt. Express **13**, 2941 (2005).

[143] L. Greenman, P.J. Ho, S. Pabst, E. Kamarchik, D. A. Mazziotti and R. Santra, Phys. Rev. A **82**, 023406 (2010).

[144] F. Aquilante, L. De Vico, N. Ferré, G. Ghigo, P.-Å. Malmqvist, P. Neogrády, T. B. Pedersen, M. Pitonak, M. Reiher, B. O. Roos, L. Serrano-Andrés, M. Urban, V. Veryazov, R. Lindh, J. Comp. Chem. **31**, 224 (2010).

[145] Extensible Computational Chemistry Environment Basis Set Database, Version 02/25/04, developed and distributed by the Molecular Science Computing Facility, Environmental and Molecular Sciences Laboratory which is part of the Pacific Northwest Laboratory, P.O. Box 999, Rich- land, Washington 99352, USA.

[146] M. Ruberti, R. Yun, K. Gokhberg, S. Kopelke, L. S. Cederbaum, F. Tarantelli and V. Averbukh, J. Chem. Phys. **139**, 144107 (2013). "Reproduced with permission from ["Total molecular photoionization cross-sections by algebraic diagrammatic construction-Stieltjes-Lanczos method: Benchmark calculations", M. Ruberti,

R. Yun, K. Gokhberg, S. Kopelke, L. S. Cederbaum, F. Tarantelli and V. Averbukh, J. Chem. Phys. 139, 144107 (2013). http://dx.doi.org/10.1063/1.4824431]. Copyright [2013], AIP Publishing LLC.

[147] K. H. Tan, C. E. Brion *et al.*, Chem. Phys. **29**, 299 (1978).

[148] W.F. Chan, G. Cooper, C.E. Brion, Chem. Phys. **178**, 387 (1993).

[149] G. N. Haddad and J. A. R. Samson, J. Chem. Phys. **84**, 6623 (1986).

[150] F. Carnovale, R. Tseng, and C. E. Brion, J. Phys. B **14**, 4771 (1981).

[151] I. Cacelli, V. Carravetta, R. Moccia and A. Rizzo, J. Phys. Chem. **92**, 979-982 (1988).

[152] G. R. Burton, W. F. Chan, G. Cooper, and C. E. Brion, Chem. Phys. **177**, 217 (1993).

[153] J. A. R. Samson, G. N. Haddad, and L. D. Kilcoyne, J. Chem. Phys. **87**, 6416 (1987).

[154] W. Au, G. Cooper, G. R. Burton, T. N. Olney and C.E. Brion, Chem. Phys. **173**, 209 (1993).

[155] Raffaele Montuoro and Roberto Moccia, Chemical Physics **293** (2003) 281-308.

[156] G. Cooper, T. Ibuki, *et al.*, Chem. Phys. **125**, 307 (1988).

[157] G. Cooper, T.N. Olney, and C.E. Brion, Chem. Phys. **194**, 175 (1995).

[158] G. Cooper, J.E. Anderson, and C.E. Brion, Chem. Phys. **209**, 61 (1996).

[159] W. F. Chan, G. Cooper, and C. E. Brion, Chem. Phys. **178**, 401 (1993).

[160] W. F. Chan, G. Cooper, and C. E. Brion, Chem. Phys. **178**, 387 (1993); G. Cooper, G. R. Burton, and C. E. Brion, J. Electron Spectrosc. Relat. Phenom. **73**, 139 (1995).

[161] *Molecular Fluorescence: Principles and Applications*, edited by B. Valeur (Wiley, Weinheim, 2001).

[162] L. S. Cederbaum, H. Köppel and W. Domcke, Int. J. Quantum Chem. **20**, 251 (1981); *Conical Intersections: Electronic Structure, Dynamics and Spectroscopy*, edited by W. Domcke, D. Yarkony and H. Köppel (World Scientific, London, 2004).

[163] M. A. Kalyar, M. Rafiq, Sami-ul-Haq and M. A. Baig, J. Phys. B: At. Mol. Opt. Phys. **40** 2307 (2007); V. L. Sukhorukov, I. D. Petrov, M. Schafer, F. Merkt, M.-W. Ruf and H. Hotop, J. Phys. B: At. Mol. Opt. Phys. **45** (2012) 092001; R. Cong, Y. Cheng, J. Yang, J. Fan, G. Yao, X. Ji, X. Zheng and Z. Cui, J. Appl. Phys. **106**, 013103 (2009); M. Gisselbrecht, D. Descamps, C. Lynga, A. L'Huillier, C.-G. Wahlström and M. Meyer, Phys. Rev. Lett. **82**, 4607 (1999); T. N. Chang and T. K. Fang, Phys. Rev. A **52**, 2052 (1995); **52**, 2638 (1995); H. A. Hyman, Appl. Phys. Lett. **31**, 14 (1977).

[164] Ch. Neidel, J. Klei, C. H. Yang, A. Rouzee, and M. J. J. Vrakking, K. Klunder, M. Miranda, C. L. Arnold, T. Fordell, A. L'Huillier, M. Gisselbrecht, P. Johnsson, M. P. Dinh, E. Suraud, P. G. Reinhard, V. Despre, M. A. L. Marques, and F. Lepine, Phys. Rev. Lett. **111**, 033001 (2013).

[165] M. Ruberti, R. Yun, K. Gokhberg, S. Kopelke, L. S. Cederbaum, F. Tarantelli and V. Averbukh, J. Chem. Phys. **140**, 184107 (2014). "Reproduced with permission from ["Total photoionization cross-sections of excited electronic states by the algebraic diagrammatic construction-Stieltjes-Lanczos method", M. Ruberti, R. Yun, K. Gokhberg, S. Kopelke, L. S. Cederbaum, F. Tarantelli and V. Averbukh, J. Chem. Phys. 140, 184107 (2014). http://dx.doi.org/10.1063/1.4874269]. Copyright [2014], AIP Publishing LLC.

[166] K. Yuan, R. N. Dixon, and X. Yang, Acc. Chem. Res. **44**, 369 (2011); T. Harb, W. Kedzierski and J. W. McConkey, J. Chem. Phys. **115**, 5507 (2001); P. Andresen, V. Beushausen, D. Hausler, H. W. Lulf, E. W. Rothe, J. Chem. Phys. **83**, 1429 (1985); D. Hausler, P. Andresen, R. Schinke, J. Chem. Phys. **87**, 3949 (1987); R. Schinke, R. L. Vanderwal,

J. L. Scott, F. F. Crim, J. Chem. Phys. **94**, 283 (1991); V. Engel, V. Staemmler, R. L. Vanderwal, F. F. Crim, R. J. Sension, B. Hudson, P. Andresen, S. Hennig, Weide, K.; Schinke, R., J. Phys. Chem. **96**, 3201 (1992); M. Brouard, S. R. Langford, D. E. Manolopoulos, J. Chem. Phys. **101**, 7458 (1994); A. U. Grunewald, K. H. Gericke, F. J. Comes, Chem. Phys. Lett. **133**, 501 (1987); D. W. Hwang, X. F. Yang, X. M. Yang, J. Chem. Phys. **110**, 4119 (1999); X. F. Yang, D. W. Hwang, J. J. Lin, X. M. Ying, J. Chem. Phys. **113**, 10597 (2000).

[167] P. Farmanara, O. Steinkellner, M. T. Wick, M. Wittmann, G. Korn, V. Stert, and W. Radloff, J. Chem. Phys. **111**, 6264 (1999); O. Steinkellner, F. Noack, H.-H. Ritze, W. Radloff and V. Hertel, J. Chem. Phys. **121**, 1765 (2004).

[168] R. van Harrevelt and M. C. van Hemert, J. Chem. Phys. **112**, 5777, 5787 (2000); G. Theodorakopoulos, I. D. Petsalakis, and R. J. Buenker, Chem. Phys. **96**, 217 (1985); R. van Harrevelt and M. C. van Hemert, J. Chem. Phys. **114**, 9453 (2001); G. Theodorakopoulos, C. A. Nikolaides, R. J. Buenker and S. D. Peyerimhoff, Chem. Phys. Lett. **89**, 164 (1982); G. Theodorakopoulos, I. D. Petsalakis, R. J. Buenker, and S. D. Peyerimhoff, Chem. Phys. Lett. **105**, 253 (1984); J. H. Fillion, R. van Harrevelt, J. Ruiz, M. Castillejo, A. H. Zanganeh, J.-L. Lemaire, M. C. van Hemert and F. Rostas, J. Phys. Chem. A **105**, 11414 (2001); J. D. Gorfinkiel, L. A. Morgan and J. Tennyson, J. Phys. B **35**, 543 (2002).

[169] A. Chutjian, R. I. Hall and S. Trajmar, J. Chem. Phys. **63**, 892 (1975).

[170] R. Thomas, S. Rosen, F. Hellberg, A. Derkatch, M. Larsson, S. Datz, R. Dixon and W. J. van der Zande, Phys. Rev. A **66**, 032715 (2002); J.-H. Fillion, J. Ruiz, X.-F. Yang, M. Castillejo, F. Rostas and J.-L. Lemaire, J. Chem. Phys. **120**, 6531 (2004).

[171] A. B. Trofimov, G. Stelter, and J. Schirmer, J. Chem. Phys. **117**, 6402 (2002); A. B. Trofimov and J. Schirmer, J. Phys. B: At. Mol. Opt. Phys. **28**, 2299 (1995).

[172] S. Trajmar, W. Williams and A. Kuppermann, J. Chem. Phys. **58**, 2521 (1973).

[173] P. Gurtler, V. Saile, and E. E. Koch, Chem. Phys. Lett. **51**, 386 (1977).

[174] A. Skerbele, V. D. Meyer and E. N. Lassettre, J. Chem. Phys. **43**, 817 (1965).

[175] R. Mota, R. Parafita, A. Giuliani, M.J. Hubin-Franskin, J. M. C. Lourenco, G. Garcia, S. V. Hoffmann, N. J. Mason, P. A. Ribeiro, M. Raposo and P. Limao-Vieira, Chem. Phys. Lett. **416**, 152 (2005).

[176] E. S. Nielsen, P. Jorgensen and J. Oddershede, J. Chem. Phys. **73**, 6238 (1980);

[177] K. P. Huber and G. Herzberg, *Molecular Spectra and Molecular Structure IV. Constants of Diatomic Molecules* (Van Nostrand Reinhold, New York, 1979).

[178] J. Oddershede, N. E. Griiner and G. H. F. Diercksen, Chem. Phys. **97**, 303 (1985).

[179] M. E. Rosenkrantz, and K. Kirby, J. Chem. Phys. **90**, 6528 (1989); D.-H. Shi, W.-T. Li, J.-F. Sun, and Z.-L. Zhu, Int. J. Quantum Chem. **113**, 934 (2013).

[180] L. S. Cederbaum and W. Domcke, Adv. Chem. Phys. **36**, 205 (1977).

[181] O. Christiansen, H. Koch, P. Jorgensen, J. Olsen, Chem. Phys. Lett. **256**, 185 (1996); S.B. Ben-Shlomo, U. Kaldor, J. Chem. Phys. **92**, 3680 (1990); R. Buenker and S. D. Peyerimhoff, Chem. Phys. Letters **29**, 253 (1974).

[182] J. Páleníková , M. Kraus , P. Neogrády , V. Kellö and M. Urban, Mol. Phys. **106**, 2333 (2008); X. Z. Li and J. Paldus, Mol. Phys. **104**, 661 (2006); Z. L. Cai, D. J. Tozer, and J. R. Reimers, J. Chem. Phys. **113**, 7084 (2000); M. Rubio, L. Serrano-Andres and M. Merchan, J. Chem. Phys. **128**, 104305 (2008).

[183] J. Schirmer and O. Walter, Chem. Phys. **78**, 201 (1983).

[184] K. Kulander, Phys. Rev. A **36**, 2726 (1987); M. S. Pindzola, D. C. Griffin and C. Bottcher, Phys. Rev. Lett. **66**, 2305 (1991).

[185] I. Cacelli, V. Carravetta, A. Rizzo, and R. Moccia, Phys. Rep. **205**, 283 (1991).

[186] B. Chapman, G. Jost and R. van der Pas, *Using OpenMP: Portable Shared Memory Parallel Programming* (The MIT Press Cambridge, Massachusetts, 2007).

[187] M. Snir, S. Otto, S. Huss-Lederman, D. Walker, and J. Dongarra, *MPI: The Complete Reference* (The MIT Press Cambridge, Massachusetts, 1996).

[188] J. A. R. Samson and W. C. Stolte, J. Electron Spectrosc. Relat. Phenom. **123**, 265 (2002).

[189] J.M. Bizau and F.J. Wuilleumier, J. Elec. Spec. Rel. Phen. **71**, 205 (1995).

[190] Chan W. F., Cooper G., Guo X., Burton G. R. and Brion C. E., Phys. Rev. A **46**, 149 (1992).

[191] Starace A. F. 1982, Theory of atomic photoionization Handbuch der Physik, Vol. 31 ed S Flügge (Berlin:Springer).

[192] M. Stener, P. Decleva and A. Lisini, J. Phys. B: At. Mol. Opt. Phys. **28**, 4973 (1995).

[193] J. A. R. Samson, G. N. Haddad, and J. L. Gardner, J. Phys. B **10**, 1749 (1977).

[194] J. Higuet, H. Ruf, N. Thiré, R. Cireasa, E. Constant, E. Cormier, D. Descamps, E. Mvel, S. Petit, B. Pons, Y. Mairesse, and B. Fabre, Phys. Rev. A **83**, 053401 (2011).

[195] A. D. Shiner, B. E. Schmidt, C. Trallero-Herrero, P. B. Corkum, J.-C. Kieffer, F. Legare and D. M. Villeneuve, J. Phys. B: At. Mol. Opt. Phys. **45**, 074010 (2012). H. J. Wörner, H. Niikura, J. B. Bertrand, P. B. Corkum, and D. M. Villeneuve, Phys. Rev. Lett. **102**, 103901 (2009). J. P. Farrell, L. S. Spector, B. K. McFarland, P. H. Bucksbaum, M. Guhr, M. B. Gaarde, and K. J. Schafer, Phys. Rev. A **83**, 023420 (2011).

[196] S. Pabst, L. Greenman, D. A. Mazziotti and R. Santra, Phys. Rev. A **85**, 023411 (2012).

[197] C. Vozzi *et al.*, Phys. Rev. Lett. **95**, 153902 (2005).

[198] W. Boutu *et al.*, Nature Phys. **4**, 545549 (2008).

[199] X. Zhou *et al.*, Phys. Rev. Lett. **100**, 073902 (2008).

[200] A. T. Le, T. Morishita and C. D. Lin, Phys. Rev. A **78**, 023814 (2008).

[201] V. H. Le, A. T. Le, R. H. Xie and C. D. Lin, Phys. Rev. A **76**, 013414 (2007).

[202] A. T. Le, X. M. Tong and C. D. Lin, Phys. Rev. A **73**, 041402 (2006).

[203] M. Lein, J. Phys. B **40**, R135R173 (2007).

[204] X. M. Tong, Z. X. Zhao and C. D. Lin, Phys. Rev. Lett. **66**, 033402 (2002).

[205] J. Muth-Bohm, A. Becker and F. H. M. Faisal, Phys. Rev. Lett. **85**, 22802283 (2000).

[206] W. Li *et al.*, Science **322**, 12071211 (2006).

[207] A.-T. Le, R. R. Lucchese, and C. D. Lin, J. Phys. B **42**, 211001 (2009).

[208] J. V. Ortiz, Int. J. Quantum Chem. **95**, 593599 (2003).

[209] S. Minemoto et al., Phys. Rev. A **78**, 061402(R) (2008).

[210] J. Z. Kaminski and F. Ehlotzky, Phys.Rev.A **54**, 3678 (1996).

[211] O. Smirnova, A. S. Mouritzen, S. Patchkovskii, and M. Y. Ivanov, J. Phys. B **40**, F197 (2007).

[212] A. Abdurrouf and F. H. M. Faisal, Phys.Rev.A **79**, 023405 (2009).

[213] K. C. Kulander, K. J. Schafer, and J. L. Krause, Int. J. Quantum Chem. **40**, 415 (1991).

[214] M. Awasthi, Y. V. Vanne, A. Saenz, A. Castro, and P. Decleva, Phys. Rev. A **77**, 063403 (2008).

[215] I. A. Ivanov and A. S. Kheifets, Phys. Rev. A **79**, 053827 (2009).

[216] P. Wei *et al.*, Phys. Rev. A **79**, 053814 (2009).

[217] R. Torres, T. Siegel, L. Brugnera, I. Procino, J. G. Underwood, C. Altucci, R. Velotta, E. Springate, C. Froud, I. C. E. Turcu, S. Patchkovskii, M. Yu. Ivanov, O. Smirnova and J. P. Marangos, Phys. Rev. A **81**, 051802 (2010).

[218] A. F. Starace, in Handbuch der Physik, Vol. **31**, edited by W. Mehlhorn (Springer, Berlin, 1980), pp. 1121.

[219] K. Kimura, S. Katsumata, Y. Achiba, T. Yamazaki, and S. Iwata, Handbook of HeI Photoelectron Spectra (Japan Scientific Societies Press, Tokyo, 1981).

[220] MOLPRO, version 2012.1, a package of ab initio programs, H.-J. Werner, P. J. Knowles, G. Knizia, F. R. Manby, M. Schutz and others, see http://www.molpro.net.

[221] O. Smirnova *et al.*, Phys. Rev. Lett. **102**, 063601 (2009).

[222] O. Smirnova, S. Patchkovskii, Y. Mairesse, N. Dudovich, and M. Y. Ivanov, Proc. Natl. Acad. Sci. U.S.A. **106**, 16556 (2009).

[223] H.-P. Breuer and F. Petruccione, *The Theory of Open Quantum Systems* (Oxford University Press, 2002).

[224] J. Leeuwenburgh, B. Cooper, V. Averbukh, J. P. Marangos and M. Ivanov, Phys. Rev. Lett. **111**, 123002 (2013).

[225] B. Cooper and V. Averbukh, Phys. Rev. Lett. **111**, 083004 (2013).

[226] Y. Mairesse, A. de Bohan, L. J. Frasinski, H. Merdji, L. C. Dinu, P. Monchicourt, P. Breger, M. Kovaev, R. Taeb, B. Carr, H. G. Muller, P. Agostini and P. Salires, Science **302**, 1540 (2003).

[227] P. Ranitovic, X. M. Tong, C. W. Hogle, X. Zhou, Y. Liu, N. Toshima, M. M. Murnane and H. C. Kapteyn, Phys. Rev. Lett. **106**, 053002 (2011).

[228] L. S. Cederbaum, W. Domcke, J. Schirmer and W. Von Niessen, Adv. Chem. Phys. **65**, 115 (1986).

[229] D. Toffoli, M. Stener, G. Fronzoni, and P. Decleva, Chem. Phys. **276**, 25 (2002).

RE: RIGHTS FOR MATERIAL IN PHD THESIS

AIPRights Permissions [Rights@aip.org]

Inviato: venerdì 7 agosto 2015 15.20
A: Ruberti, Marco

Dear Dr. Ruberti:

Thank you for requesting permission to reproduce material from AIP Publishing LLC publications.

Material to be reproduced:

"Total molecular photoionization cross-sections by algebraic diagrammatic construction-Stieltjes-Lanczos method: Benchmark calculations"

M. Ruberti, R. Yun, K. Gokhberg, S. Kopelke, L. S. Cederbaum, F. Tarantelli and V. Averbukh, J. Chem. Phys. 139, 144107 (2013).
http://dx.doi.org/10.1063/1.4824431

"Total photoionization cross-sections of excited electronic states by the algebraic diagrammatic construction-Stieltjes-Lanczos method"
M. Ruberti, R. Yun, K. Gokhberg, S. Kopelke, L. S. Cederbaum, F. Tarantelli and V. Averbukh, J. Chem. Phys. 140, 184107 (2014).
http://dx.doi.org/10.1063/1.4874269

"B-spline algebraic diagrammatic construction: Application to photoionization cross-sections and high-order harmonic generation"
M. Ruberti, V. Averbukh and P. Decleva, J. Chem. Phys. 141, 164126 (2014).
http://dx.doi.org/10.1063/1.4900444

For use in the following manner:

Reproduced in your PhD thesis at Imperial College London.

Permission is granted subject to these conditions:

1. AIP Publishing LLC grants you non-exclusive world rights in all languages and media. This permission extends to all subsequent and future editions of the new work.

2. The following copyright notice must appear with the material (please fill in the information indicated by capital letters):

"Reproduced with permission from [FULL CITATION]. Copyright [PUBLICATION YEAR], AIP Publishing LLC."

When reusing a full article, the copyright notice must be printed on the first page of the reprinted article or book chapter. When reusing figures, photographs, covers, or tables,

the notice may appear in the caption, in a footnote, or in the reference list.

In cases where the new publication is licensed under a Creative Commons license, the full copyright notice as stated above must appear with the reproduced material.

3. If the material is published in electronic format, we ask that a link be created pointing back to the abstract of the article on the journal website. This can be accomplished through the use of the article's DOI.
4. This permission does not apply to any materials credited to another source.

Please let us know if you have any questions.

Sincerely,
Susann Brailey

Manager, Rights and Permissions
AIP Publishing LLC
1305 Walt Whitman Road
Suite 300
Melville, NY 11747-4300

Tel. +1 516-576-2268
rights@aip.org